Design, Fabrication and Assessment of 2D Photonic Crystals

A thesis by

Sascha Klengel

Submitted for the degree of
Ph.D. and D.I.C.

Centre for Electronic Materials and Devices,
Imperial College London,
December 2003

Abstract

Two dimensional photonic crystals (2D PhCs) in a GaAs/AlGaAs environment were studied experimentally. Emphasis was placed on evaluating the loss characteristics of these structures.

Fabrication of 2D PhCs was carried out using a combination of electron beam lithography, reactive ion and electron cyclotron resonance etching techniques. This work was carried out at the Sharp Laboratories of Europe. Excellent control over the more than fifty necessary processing steps was demonstrated and further improvements suggested.

An optical laser-based characterization experiment was set up to study the transmission, reflection and scattering properties of 2D PhCs embedded in ridge waveguides. These passive structures were designed to operate around 1.55 μm. Many of the difficulties involved in characterizing structures with dimensions of the order of microns, were overcome to obtain reproducible results.

The characterization results obtained in the spectral and Fourier domain demonstrated unambiguously the existence of photonic bandgaps. Fourier analysis was shown to be a particularly useful tool for obtaining physical parameters of the structures, such as propagation loss coefficients and structural information of the sample. A number of loss mechanisms inside photonic crystals were identified. The overall PhC loss was found to be crucially dependent on the etch depth of the holes that constitute the photonic crystal.

Work was carried out to show the possibility of producing large fill factor 2D photonic crystals, which could potentially be an ideal environment to embed quantum dots in. Further more, patterns with small hole diameters were created, which could be used in conjunction with active organic semi-conducting material. Passive 1D microcavities defined by 2D photonic crystals in ridge guides were analyzed.

Contents

Acknowledgements 10

1 Introduction 12
- 1.1 Theoretical developments . . . 13
  - 1.1.1 What are photonic crystals? . . . 14
  - 1.1.2 Theory . . . 15
- 1.2 Early fabrication . . . 17
- 1.3 Outlook . . . 21
- 1.4 Current state . . . 24
- 1.5 Outline of Thesis . . . 26

2 Fabrication 34
- 2.1 Introduction . . . 35
  - 2.1.1 Host material . . . 37
  - 2.1.2 Structural characterization . . . 40
- 2.2 Sample preparation . . . 43
  - 2.2.1 PECVD . . . 43
  - 2.2.2 Photoresist . . . 44
  - 2.2.3 Pattern design . . . 46
- 2.3 Electron beam lithography . . . 50
  - 2.3.1 Description of electron beam writer and set-up . . . 51
  - 2.3.2 Limitations . . . 57
  - 2.3.3 Proximity effect . . . 61
  - 2.3.4 Stitching error . . . 64
  - 2.3.5 Development and rinse . . . 65
- 2.4 Dry etching . . . 67
  - 2.4.1 Reactive Ion Etching . . . 67
  - 2.4.2 Electron cyclotron resonance etching . . . 74
- 2.5 Photolithography . . . 86
  - 2.5.1 Lithography preparation . . . 86
  - 2.5.2 Photoresist . . . 87
  - 2.5.3 Application . . . 88
  - 2.5.4 Mask, Exposure and Development . . . 88
  - 2.5.5 Stripping . . . 90
  - 2.5.6 Cleaving . . . 90

2.5.7 Limitations . . . 93
2.6 Conclusion . . . 96

3 Theoretical considerations **100**
3.1 Introduction . . . 101
3.2 Designing photonic crystals . . . 101
3.2.1 Pattern geometry . . . 102
3.2.2 Band structure calculation . . . 104
3.2.3 Device modelling . . . 107
3.3 Waveguide design . . . 110
3.3.1 The wave equation . . . 113
3.3.2 `MultiLayer` . . . 116
3.3.3 Ridge waveguide . . . 117
3.4 Fourier Analysis . . . 118
3.4.1 Decomposition of transmission signal in a single cavity . . . 118
3.4.2 The Fourier Transform . . . 122
3.4.3 Single Fabry-Pérot cavity . . . 126
3.4.4 Derivation of Fourier coefficients in Transmission . . . 127
3.4.5 Extracting cavity dimensions from the Fourier picture . . . 134
3.5 Conclusion . . . 136

4 Characterization **140**
4.1 Description of problem . . . 141
4.1.1 Requirements for characterization set-up . . . 141
4.2 White light spectroscopy . . . 142
4.2.1 The Source . . . 143
4.2.2 General set-up . . . 144
4.2.3 Spot size . . . 147
4.2.4 Losses . . . 149
4.2.5 Output facet . . . 151
4.3 Laser-based characterization . . . 155
4.3.1 Description of laser . . . 155
4.3.2 Experimental set-up . . . 156
4.3.3 Polarizer . . . 158
4.3.4 Scattering measurements . . . 161
4.4 Loss analysis of characterization set-up . . . 164
4.4.1 Details . . . 165
4.4.2 Estimation of overall losses . . . 169
4.4.3 Other difficulties . . . 170
4.5 Conclusion . . . 173

5 Optical characterization results **175**
5.1 Presentation of key results . . . 176
5.1.1 Observation of PBG-effect . . . 176
5.1.2 Results in spectral domain . . . 180

5.1.3 Results in Fourier domain . . . 186
5.1.4 Waveguide propagation losses . . . 189
5.2 Discussion . . . 190
5.2.1 Experimental photonic crystal loss coefficient results . . . 190
5.2.2 Comparing two methods for extracting the PhC loss coefficient . 191
5.2.3 Key factors of losses in photonic crystals . . . 193
5.2.4 Linear response . . . 198
5.2.5 Quantitative analysis of visibility . . . 199
5.3 Other issues . . . 201
5.3.1 Richness of Fourier representation . . . 201
5.3.2 Reflection measurements . . . 203
5.3.3 Loss mechanisms . . . 205

6 Other photonic bandgap structures **211**
6.1 Large fill factor work . . . 212
6.1.1 Rationale for large fill factors . . . 213
6.1.2 Fabrication of large fill factor 2D photonic crystals . . . 216
6.1.3 Conclusion . . . 218
6.2 Organic materials with photonic crystals . . . 219
6.2.1 Fundamentals . . . 220
6.2.2 Design considerations . . . 221
6.2.3 Band structures . . . 223
6.2.4 Fabrication of 2D photonic crystals with active organic materials 224
6.2.5 Optical characterization . . . 226
6.2.6 Conclusion . . . 227
6.3 Photonic crystal microcavity in ridge waveguides . . . 227
6.3.1 Fabrication . . . 228
6.3.2 Cavity design . . . 229
6.3.3 Optical characterization . . . 230
6.3.4 Conclusion . . . 231

7 Conclusions **236**
7.1 Summary . . . 237
7.2 Conlusions . . . 239
7.3 Future work . . . 242

A Detailed processing steps **244**

B Fabry-Pérot Equation **246**

C Sample catalogue **248**

D Publications **249**

List of Figures

1.1 1D, 2D, 3D Photonic crystals 14
1.2 Yablonovite 18

2.1 Key processing steps in fabrication of PhCs in ridge waveguides 36
2.2 Planar waveguide structure of wafers 38
2.3 Reflection spectra of good region of wafer QT1598UP 39
2.4 Reflection spectra of poor region of wafer QT1598UP 40
2.5 Calibration results of α-step 41
2.6 SEM image of a sample showing PMMA and SiO_2 thicknesses 45
2.7 Band diagram of inflnite 2D photonic crystal 47
2.8 Illustration of flll factor concept 49
2.9 Diagram of typical 2D PhC dimensions 49
2.10 SEM image of 3D PhC produced by deep x-ray lithography 50
2.11 Diagram of EBL set-up. 51
2.12 Diagram of EBL apparatus. 52
2.13 Chromatic and spherical aberration in electron optics 53
2.14 Example of a misshaped pattern due to too short dwell time 58
2.15 Effect of pixel spacing change 59
2.16 Example of high quality hole pattern 60
2.17 Effect of low and high-energy electrons 61
2.18 Measured hole diameters across various square patterns 63
2.19 SEM showing proximity effect on 4×4 μm pattern 63
2.20 Plan view of 20row PhC pattern on a ridge 64
2.21 Stitching error 65
2.22 Characteristics of PMMA development 66
2.23 Example of state-of-the-art etch results by Bosch 68
2.24 Pattern layout of RIE test sample 70
2.25 Etch rate determination for silica RIE 70
2.26 Cross section before SiO_2 etch 71
2.27 After 4 min of SiO_2 etch 71
2.28 After 6 min of SiO_2 etch 71
2.29 After 7.5 min of SiO_2 etch 71
2.30 After 7.5 min of SiO_2 etch, tilted at 45° 71
2.31 Cross section after 400 s ECR etch 71
2.32 Rough PMMA caused by RIE 73
2.33 Variation of PMMA across a PhC pattern after RIE 73

2.34 Good ECR etch profile 76
2.35 Hole depth as a function of hole-top diameter 77
2.36 Estimated etch depth-hole diameter relationship for ECR etches 78
2.37 SEM image typical hole profile in InP 80
2.38 SEM image of large fill factor PhC cross section 80
2.39 Holes overlapping below surface - 1 82
2.40 Holes overlapping below surface - 2 82
2.41 SEM image of a ridge showing epilayers. 83
2.42 Basic L.E.P.D. set-up. 83
2.43 Reflections at layer interfaces - LEPD 2 84
2.44 Experimental LEPD trace 85
2.45 Grass on sample surface 87
2.46 Effects of beading 89
2.47 SEM image of entire sample prior to cleaving. 91
2.48 SEM image of a poorly cleaved ridge facet. 91
2.49 SEM image of an immaculate ridge facet 92
2.50 SEM image showing ridge with rough sidewall. 94
2.51 SEM image of a defective ridge. 95
2.52 High quality PhC patterns of different lengths. 96
2.53 Several different aspects of a fully processed sample. 97

3.1 Definition of polarization 102
3.2 Square lattice 103
3.3 a) Triangular, b) Kagomé, c) Graphite lattice 103
3.4 Real space vs. reciprocal space. 104
3.5 Convergence for band diagram calculation 106
3.6 Gap map for triangular lattice of air holes 106
3.7 Band structure for f=50%, air holes in GaAs, triangular lattice 107
3.8 Ray diagram of general slab waveguide 111
3.9 The first and second guided modes in a slab waveguide. 115
3.10 Wave propagating in the guiding layer and the substrate. 115
3.11 Planar waveguide structure 116
3.12 `FWave` simulation of two different ridge heights 118
3.13 Diagram of Fabry-Pérot cavity - Transmission 119
3.14 Decomposition of spectral data into Fourier components. 122
3.15 Effect of finite sampling window in spectral domain. 123
3.16 Effect of finite sampling window in Fourier domain. 123
3.17 Fourier representation of transmission spectrum for FP cavity 127
3.18 fwhm of I_1 as function of a) scan range, b) step length. 128
3.19 Extraction of waveguide loss from simulated data. 130
3.20 Modelled FT-transmission spectrum of waveguide with PhC 132
3.21 Schematic representation of ridge with PhC. 132
3.22 Extraction accuracy of α_p from simulated data 133
3.23 Definition of visibility. 134

4.1 Emission spectrum of Xenon arc lamp . . . 143
4.2 First set-up for white light characterization. . . . 145
4.3 Investigation of fibre coupling efficiency . . . 146
4.4 Layout with two further MOGs added . . . 146
4.5 How to achieve the smallest spot size . . . 147
4.6 Set-up used to record image of the sample's surface . . . 148
4.7 Image of light scattered at the input facet of a ridge waveguide . . . 149
4.8 CCD camera image of the output facet. . . . 150
4.9 Set-up for white light measurements with MOG at output facet. . . . 151
4.10 Imaging the output facet. . . . 152
4.11 Variation of power away from output facet . . . 153
4.12 Escape routes for light not coupled into input facet . . . 153
4.13 Illustration of set-up with SMF at output facet . . . 154
4.14 Repeatability check of white light measurements . . . 155
4.15 Set-up for laser-based characterization. . . . 157
4.16 Photographs of the characterization set-up . . . 157
4.17 Glan-Thompson polarizing prism. . . . 159
4.18 Measurement of light scattered vertically out of PhC . . . 161
4.19 Scan along top of ridge waveguide with PhC pattern. . . . 162
4.20 Limit of scattered light detection . . . 163
4.21 Scattering loss due to poor PhC termination. . . . 163
4.22 Characterization set-up as used in the loss analysis. . . . 164
4.23 Set-up for beamsplitter characterization. . . . 166
4.24 Coupling loss at input facet . . . 167
4.25 FC/PC adaptor . . . 169
4.26 Stability test . . . 171

5.1 SEM image of 10 row PhC in a ridge waveguide . . . 176
5.2 Calculation of PhC transmission . . . 177
5.3 Trans. and Refl. scans of unpatterned ridge . . . 178
5.4 Experimental demonstration of PBG effect . . . 179
5.5 5 row and 20 row PhC transmission spectra . . . 181
5.6 Normalized average transmitted power for different PhC lenghts . . . 182
5.7 Results from polarization mixing tests . . . 185
5.8 Fourier representation of transmission for 5 row PhC . . . 187
5.9 Transmission and reflection for normal and reversed 20 row PhC . . . 189
5.10 α_p extracted from various photonic crystal lengths . . . 191
5.11 PhC loss coefficient as a function of hole depth . . . 194
5.12 PhC loss coefficient as a function of fill factor . . . 196
5.13 PhC loss coefficient as function of ridge height . . . 198
5.14 Transmission spectra for different input powers . . . 199
5.15 Visibility as function of PhC length . . . 200
5.16 Fourier representation of TM reflection from 10 row PhC . . . 203
5.17 Visibility from reflection measurements . . . 204
5.18 Loss mechanisms in photonic crystals . . . 205

6.1 Diagram of a H1 photonic crystal defect cavity 214
6.2 Proposed experiment to characterize quantum dots in PhCs 215
6.3 SEM image of large fill factor SiO_2 mask 216
6.4 SEM image of H1 cavity in 50x50 μm pattern 217
6.5 SEM image of H3 cavity in 50x50 μm pattern 218
6.6 Diagram of a photonic crystal with organic gain material 219
6.7 SEM image of 1D photonic crystal microcavity 228
6.8 SEM image of 50 row 'defect' PhC cavity 230

List of Tables

2.1 PECVD gas flow rates for silica deposition 44
2.2 Summary of RIE conditions for SiO_2 under PMMA etch 69
2.3 RIE characteristics for SiO_2 under PMMA etch 72
2.4 Summary of typical ECR conditions for PhC pattern etch. 75
2.5 Wafer composition 76
2.6 Summary of ECR conditions for ridge etches. 81
2.7 Calibration of LEPD chart 85

3.1 Parameters used for `FWave` simulation 117
3.2 Spatial coherence length data 125
3.3 Parameters for FP-cavity transmission calculation. 126

5.1 Transmission results for 20 row PhC structure 181
5.2 Physical parameters of two PhC samples 183
5.3 Cavity lengths of 5 row sample extracted from Fourier picture 188

6.1 Structural parameters for PhC with organic material 224

A.1 Photonic crystal processing steps 244
A.2 Processing steps for creating ridge waveguides 245
A.3 Processing steps for thinning the substrate by wet etching 245

C.1 Catalogue of fabricated samples 248

Acknowledgements

First and foremost I would like to thank my supervisor Prof. G. Parry for his invaluable advice and guidance over the past three years. I would like to extend my thanks to Dr. P. N. Stavrinou for his constant support, help and numerous fruitful discussions. I am grateful for his contributions to the theory part of this work, as well as for the occasional golf lesson.

I thank EPSRC for the financial assistance they provided for this project, carried out under the Ultrafast Photonics Collaboration.

Thank you to the members of the Advanced Optoelectronic Devices group at Sharp Laboratories of Europe in Oxford for giving me time on their equipment as well as the support I received during the many months I spent with them. Special thanks go to Dr. B. Poole and Dr. J. Heffernan for their support, help and encouragement.

To Youssef Saied Jalili and Pierre Caillaud, thanks for the entertainment and all the welcome distractions.

A big THANK YOU also goes to the friends that looked after my emotional well-being and who were there for me when I needed them, particularly the St. Clare's crew.

Finally, I am most grateful for the continuous moral support I received from my family, especially my parents, who never doubted me and who supported all my dreams and ambitions. You two are a big inspiration for me.

To my parents

Chapter 1

Introduction

1.1 Theoretical developments

Throughout history, scientists and philosophers have tried to understand the nature of this most fundamental of natural phenomena: Light. As early as 280 B.C. Greek scholars like Euclid and later Ptolemy studied the behaviour of light and concluded that it was governed by simple geometrical rules. A ray pictures was developed, which adequately described many optical phenomena including reflection. Around 1000 A.D. the Arab scholar Abu Ali Mohamed Ibn Al Hasan Ign Al Haytham studied the properties of light extensively. The next significant advances in the understanding of optics were made in the 16th century by the likes of Galileo and Kepler. During the 17th century the nature of light was the subject of much debate. Descartes and Newton were the most notorious advocates of the corpuscular theory of light, i.e. that it consists of streams of particles. Huygens and others rejected this and proposed that light is a disturbance or pulse in a medium. Young's work at the start of the 19th century clearly showed the wave nature of light in the historic double-slit experiment.

Following on from the work of Coulomb, Fizeau, Faraday and others, James C. Maxwell, the hero of our tale, in 1865 came to the conclusion that light is an electromagnetic wave. In his momentous work Maxwell synthesized the hitherto separate subjects of optics and electromagnetism, summarized concisely in four laws. Apart from describing naturally occurring phenomena Maxwell's equations lay the foundations for radio, TV and all modern telecommunication. Mankind has begun to learn how to control and exploit optical processes. Guiding light in arbitrary directions, blocking, polarizing, localizing and storing light are some of the functions we would like to have perfect control over. Much progress has been made in most of these areas. More work is necessary to truly reap the benefits of optical technology. Photonic crystals (PhC) are materials, which we believe have the potential to solve most of these problems.

The study of photonic crystal only really began in 1987 with a paper by Eli

Yablonovitch [1]. Since then the number of people interested in this field has increased exponentially, as reflected by the number of publications on the subject. Many of the concepts and much of the terminology come from the semiconductor physics. It is assumed that the reader is familiar with fundamental solid state physics concepts.

1.1.1 What are photonic crystals?

A photonic crystal is a medium with periodically varying dielectric constant. An analogy with electronic materials is useful. A regular arrangement of atoms presents a variation of potential energy between the nuclei and inter-nuclear space. The properties of the lattice govern the conduction properties of electrons in the lattice, leading to the formation of energy bands in which electrons can propagate freely and bandgaps, where no electron states are allowed. In optical systems the variation in potential energy is replaced by a variation in dielectric constant. Instead of regions of high and low potential energy a photonic crystal consists of regions of high and low dielectric constant. The physical properties of such a photonic crystal determine the photonic band structure of the material. Photonic bandgaps (PBG) exist in materials with periodically varying dielectric constants. Such periodic variation of dielectric constant can occur in one, two or three orthogonal directions, leading to the classification of 1, 2 and 3-dimensional photonic crystals as shown in Fig. 1.1.

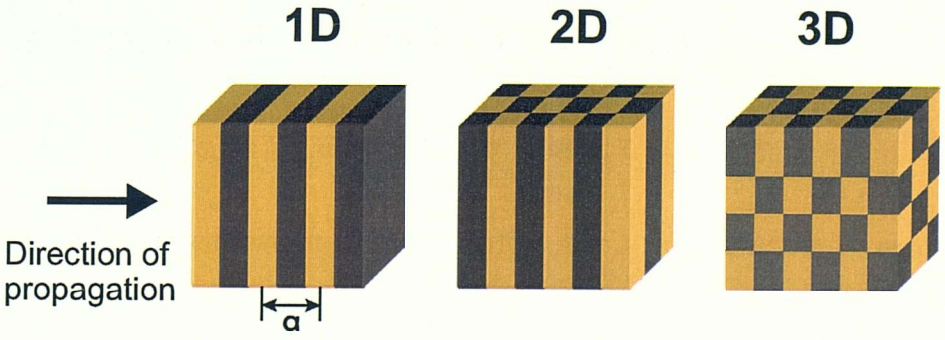


Figure 1.1: Schematic representation of one, two and three dimensional photonic crystals. Different colours indicate different dielectric constants.

PhCs are not novel materials. They occur in nature, where they cause some of the

most spectacular colour effects. Opals are perhaps the most familiar example of a 3D PhC. Members of the Lepidoptera, such as the *Polyommatus daphnis* butterfly often exhibit striking coloured patches, which were found to be photonic bandgap material [2, 3]. The dimensions and quality of these and other naturally occurring PhC structures can not be reproduced with the best of today's technology. Nonetheless, useful structures have been fabricated with sub-micron dimensions, as described below and in Chapter 2. When creating artificial photonic crystals one has nearly total control over the physical properties of the lattice and material. This opens the possibility to design structures that affect light in a predetermined manner. Light will be under man's control once this is perfected.

1.1.2 Theory

In order to explain the formation of photonic bands and bandgaps in photonic crystals one can start by looking at the one-dimensional Helmholtz or wave equation[1]:

$$\frac{c^2}{\epsilon(x)}\frac{\partial^2 E}{\partial x^2} = \frac{\partial^2 E}{\partial t^2} \tag{1.1}$$

c is the speed of light in vacuum. For mathematical convenience the electric field is expressed as a complex function $E(x,t)$, but it is understood that any measured E-field is an entirely real quantity given by the real part of $E(x,t)$. The dielectric function $\epsilon(x)$ is position-dependent and periodic along the direction of propagation. Hence,

$$\epsilon(x+a) = \epsilon(x), \tag{1.2}$$

where a is the lattice constant as shown in Fig. 1.1. $\epsilon^{-1}(x)$ can then be expanded in a Fourier series.

$$\epsilon^{-1}(x) = \sum_{m=-\infty}^{\infty} c_m exp\left(i\frac{2\pi m}{a}x\right) \tag{1.3}$$

[1]See any standard Optics text book, such as Ref. [4] for the derivation of the 1D wave equation.

m = integer and c_m are the Fourier coefficients. Assuming infinite periodicity one can invoke Bloch's theorem and express the eigenmodes of the electric field in a 1D periodic structure as

$$E_k(x,t) = \sum_{m=-\infty}^{\infty} E_m exp\left\{i\left(k + \frac{2\pi m}{a}\right)x - i\omega_k t\right\} \tag{1.4}$$

E_k is the eigen energy, E_m are Fourier expansion coefficients, k is the wave number and ω_k is the eigen-angular frequency. By inserting Eqns. 1.3 and 1.4 into Eqn. 1.1 and considering only the first few expansion coefficients ($m = 0, \pm 1, \pm 2$) it can be shown through some lengthy but straightforward algebra, as in Ref. [5], that E_0 and E_{-1} dominate the Fourier expansion in Eqn. 1.4. Thus, considering only these two coefficients leads to two coupled equations:

$$(\omega_k^2 - c_0 c^2 k^2)E_0 - c_1 c^2 \left(k - \frac{2\pi}{a}\right)^2 E_{-1} = 0 \tag{1.5}$$

$$-c_{-1}c^2k^2E_0 + \left\{\omega_k^2 - c_0c^2\left(k - \frac{2\pi}{a}\right)^2\right\}E_{-1} = 0 \tag{1.6}$$

Nontrivial solutions exist when the determinant of coefficients vanishes. This, finally, leads to the condition that no modes exist in the frequency interval where

$$\frac{\pi c}{a}\sqrt{c_0 - |c_1|} < \omega < \frac{\pi c}{a}\sqrt{c_0 + |c_1|} \tag{1.7}$$

This equation describes the frequency region where the first photonic bandgap occurs. The gap disappears when $c_1 = 0$. There are an infinite number of bandgaps in the entire spectrum, but the fundamental gap spans the widest frequency range.

No propagating modes exist inside the bandgap. The wave vector is purely imaginary. For photonic crystals with small dielectric contrast, modes below (above) the fundamental bandgap have maximal field intensity in the high (low) dielectric constant material. With this pattern of field localization in mind the lowest band of eigenmodes is referred to as the *dielectric band* and the band above the fundamental gap is called the *air band.*[2] All this is rather intuitive in nature, but can formally be described using

[2]In the case of large difference in dielectric constant the fields of both the lower and upper band

the *electromagnetic variational theorem* [6].

Several excellent articles can be found in the literature, which describe field localization in photonic crystals in a very clear and detailed way [7, 8]. The effect of introducing deliberate defects into an otherwise perfect crystal has been investigated theoretically and experimentally. A lattice defect, such as a single layer in a 1D PhC being thicker than the others, results in a breakdown of the perfect crystal periodicity. In terms of the band structure a lattice defect creates an allowed photon state inside a bandgap. This can lead to highly localized wave functions with mode volumes as low as $\sim 0.1(\lambda/2)^3$ [9, 10, 11] in the case of point defects in 2D PhCs. Line defects in 2D photonic crystals have been used to provide tight lateral mode confinement to create very compact waveguides [12, 13, 14, 15, 16].

The idea of localized electromagnetic fields led John [17] and Yablonovitch [1] to investigate the possibility of influencing the behaviour of an excited atom by placing it in a photonic bandgap surrounding. Purcell [18] and Kleppner [19] also discussed how spontaneous emission would be affected by manipulating the available photon modes. Much of this early theoretical work has been verified experimentally and has led to a number of beautiful devices [20, 21, 22, 23].

1.2 Early fabrication

Following theoretical investigations of photonic crystal properties it was necessary to prove the concept experimentally. In 1989 Yablonovitch and Gmitter [24] produced the first man-made three-dimensional photonic crystal. Due to technological constraints they chose to design their structure to operate in the microwave regime, which allowed them to create a structure with large dimensions. Conventional machine tools were used to drill hemispheres in slabs of high dielectric constant material and a number

are concentrated in the high index region, but the lower frequency band is more concentrated.

of identical slabs were stacked such that the hemispheres face one another. These hemispheres were several millimetres in diameter. Once assembled, this created a dielectric structure with a regular, face-centred-cubic (fcc) array of spherical air holes. As Maxwell's equations, which govern the properties of photonic crystals, have no inherent dimensional dependence, the behaviour of these structures in the microwave regime must be equivalent to the appropriately scaled PhCs in the infrared, visible and any other region of the electromagnetic spectrum.

In 1991 Yablonovitch *et al* [25] fabricated a 3D PhC with nonspherical atoms and demonstrated that this structure has an omni-directional photonic bandgap. The advantage of that structure lay in the relative ease of fabrication. A mask of two-dimensional holes in a triangular lattice was laid on the material and each hole was drilled through as shown in Fig. 1.2.

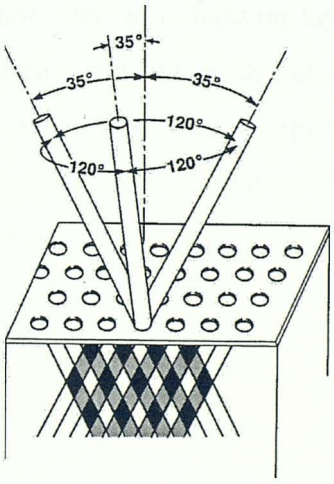


Figure 1.2: Holes drilled into a dielectric to create a full photonic bandgap in the microwave regime. The overlap of different holes creates 'atoms' of air inside a dielectric surrounding. Taken from Ref. [25].

Yablonovite, which is how the structure shown in Fig. 1.2 became known as, lends itself to fabrication using dry etching techniques. This technology enables one to access the very small length scales required to produce PhCs for operation with infrared light. Sub-micron features can be produced with excellent accuracy and repeatability.

In 1995 Cheng and Scherer [26] used a chemically assisted ion beam etching set-up (CAIBE) to realize the Yablonovite structure in GaAs. The centre to centre spacing was 350 nm, which is a reduction in size of around 4 orders of magnitude compared with the original work in Ref. [25].

Other designs for 3D photonic crystals were proposed [27] and realized [28, 29, 30, 31, 32] and this is still a very active field of research. However, due to their complexity and difficulties in fabricating 3D PhCs, let alone integrating them in a systems environment, the majority of photonic bandgap research in the last decade has been focused on two-dimensional photonic crystals.

A 2D PhC presents a periodic variation[3] of dielectric constant in the direction of propagation of an electromagnetic wave. Lateral confinement of the wave can be provided in a conventional slab waveguide configuration, where the refractive index difference between the waveguide core and cladding layers confines the wave through total internal reflection. Therefore, a 2D PhC with a slab waveguide structure is an environment in which a suitably launched EM wave experiences a photonic crystal effect in the direction of propagation. A selection of early modelling work of two-dimensional PhC structures is presented in Refs. [34, 35, 36]. One of the first experimental studies of 2D PhCs was reported by Robertson *et al* [37]. It was carried out in the microwave regime and involved 10 cm long alumina-ceramic rods (0.74 mm in diameter) arranged in a square array with lattice constant 1.87 mm.

The wavelengths of interest for telecommunications applications are 1.3 and 1.55 μm. Today a great deal of research into PBG materials is carried out at these wavelengths. The current state of photolithography and etching equipment cater well for the required feature sizes for these wavelengths, which are as small as $\sim$100 nm. Feature sizes of the order of 10 nm have been achieved in PMMA [38], which is now

[3]Photonic crystals need not consist of a periodic structure. Fibonacci sequence patterns can also form photonic bandgaps. See Ref.[33]

the standard resist used in electron beam lithography (EBL) - see Chapter 2.

Gourley *et al* [39] in 1994 etched sub-micron holes in (Al,Ga)As material to produce a triangular lattice of air holes in a III-V compound using reactive ion etching (RIE). In order to improve vertical photon confinement suspending slab waveguides in air has been investigated. Villeneuve *et al* fabricated a series of air bridges in silicon as well as in (Al,Ga)As [40]. These were patterned with a PhC structure, which contained microcavities. Strong field confinement was calculated for the 'defects'. In Ref. [41] transmission measurements for air-bridge structures with varying defect sizes were reported. Strong mode confinement was achieved and spontaneous emission enhancement up to a factor of 72 was observed. Other groups also investigated air-bridge structures, eg. Refs. [42, 43, 35].

By introducing a line defect in a triangular lattice PhC Noda *et al* produced a low-loss dielectric waveguide [44]. Similar effects were reported in Ref. [45]. Also, in Ref. [44] it was shown that photons can be trapped by small crystal defects close to the line defect. These defects can then act as resonant cavities and couple photons efficiently in and out of the PhC. This could be the basis of add-drop filters for optical communication [46, 47].

To measure the optical properties of 2D PhCs internal light sources in the form of quantum wells and quantum dots have been used, as in Refs. [48, 49]. In the latter report a laser diode was used to excite the active regions and some of the radiative recombination (30-40%) was channeled into the waveguide mode. This is a very elegant way of illuminating the sample. Transmission, reflection and diffraction properties of PhC patterns were successfully measured and efficient light confinement demonstrated. In Ref. [48] the difference in guiding between ΓM and ΓK crystal symmetry directions (defined in Section 3.2.1 on Page 102) was also demonstrated.

Efficiently coupling light into and out of photonic crystal waveguides is a problem,

which must be solved if these structures are to be used in integrated optics applications. Several groups reported numerical investigations of coupling from ridge waveguides to PhC waveguides. Happ *et al* [50] found improved coupling when a tapered input end was created in the PhC waveguide and the taper's performance was found to be very tolerant to small variations in PhC parameters as well as alignment. Xu *et al* reported calculations of efficient coupling from tapered slab waveguides to PhC waveguides and back with transmission efficiencies up to 80% [51]. Talneau *et al* demonstrated a 150% enhancement of coupling between ridge waveguide modes and PhC waveguide modes when a suitable taper section was used [52].

O'Brien *et al* [53] fabricated one of the earliest devices making use of 2D photonic crystals. Two photonic crystal 'mirrors' were etched at either end of a laser cavity and would have very high reflectance for frequencies inside the photonic bandgap. Photonic bandgap materials are also being used to create more efficient LEDs and VCSELs (vertical cavity surface emitting lasers), since they improve the light out-coupling (and in-coupling) at the surface, as demonstrated in Refs. [54, 55, 56, 57, 58].

1.3 Outlook

Photonic bandgap materials are likely to play a significant part in future telecommunications and data-communications applications, as well as in other fields that are currently emerging.

Miniaturization is one of the key advantages of photonic crystals. Taking a step back, it is well known that Moore's law [59] describes the increase in transistor density on a chip. This empirical law was based on Moore's observation of industry trends in 1965, just four years after the first planar integrated circuit was created. It has held true remarkably well until today. Greater transistor density results in shorter gate distances and greater switching speeds. This rapid increase in microprocessor power

brought about significant changes in the way western society operates. Powerful computers and convenient communication tools are ubiquitous today in developed countries and have lead to greater productivity and improved standards of living. Moore's law, however, cannot be sustained with current technology much beyond 2010, primarily due to thermodynamical effects and power dissipation [60]. Nonetheless, a computer's performance depends on more than just the microprocessor's speed. The speed at which data is transferred between the various components that make up the computer also has a huge effect. In future these connections will all be fully optical - photons rather than electrons will carry information through circuits.

Optical integrated circuits (OIC) have many advantages over electronic ones. Increased bandwidth is one such advantage. The bandwidth of fibre-optic communication systems is typically of the order of one terahertz, while that of electronic systems is only a few hundred kilohertz [61]. OICs can be made smaller, lighter and have lower power consumption than electronic circuits [62]. In spite of the numerous advantages of photons, all-optical circuits have yet to be commercially available on a large scale. The major disadvantage is the high cost of developing new fabrication technology. Photonic crystals are an exciting new technology and have the potential to become the building blocks of tomorrow's optical circuits. For instance, PhCs can be used to make very small filters and polarizers (few microns in length) and short photonic crystal 'waveguides' ($<$100 μm long) can be used to steer light around corners. Combining PhCs with active materials such as quantum dots or organic polymers opens the door to creating efficient light sources. It is easy to envisage how these and other ideas will lead to monolithic optical integrated circuits. As fabrication techniques improve these will be able to compete directly with today's technology.

An entirely different use for photonic crystals lies in their novel properties. The applications mentioned above are exciting because of the great potential for miniaturization, which ultimately translates to cost reduction and greater portability. In terms of technology, however, miniaturization adds nothing new to the devices. The real

strength of PhCs will become apparent when their unique properties are exploited. In particular the ability to tailor the photonic band structure (see Chapter 3) of PhCs to suit a particular application is an exciting prospect. One application, which is currently being studied experimentally, is dispersion compensation with photonic crystals [63, 64]. As pulses of light travel through optical fibre they spread due to the normal dispersion properties of the fibre. With single mode fibre the pulses need to be reshaped approximately every 50 km [65]. This is conventionally done using an optoelectronic device comprising a detector, amplifier and emitter. These devices are a significant cost to cable network operators, especially if they need to be installed at the bottom of the ocean, as with the trans-Atlantic cables. Passing a dispersed pulse through a short length of photonic crystal can have the same effect as these active 'repeater stations' at a significantly reduced price. Photonic crystals can easily be created with the desired amount of negative dispersion required for that application.

The context in which photonic crystals were originally proposed in 1987 by Yablonovitch [1] is yet another area where PhCs will have a significant impact. It was recognized that the spontaneous emission of atoms is governed by the interaction of the radiation field with the surrounding matter [18]. The radiation field of an atom, or atom-like structures such as quantum dots, can be modified in a controlled manner by placing the emitter in a photonic crystal environment. This can lead to suppression or enhancement of spontaneous emission, as discussed in Chapter 6. The possibility of creating very compact efficient light sources based on this effect has generated much interest in this field [9, 56, 66, 67, 68, 69].

The first PhC-based device that has been commercialized is a gas sensor developed by Mesophotonics. More and more sensor-type application are appearing [22, 70], with the aim of producing ultra-small, robust, cheap 'labs on a chip'. Again the advantage of having total control over the photonic band structure of the PhC devices and their inherent small size make them attractive candidates for these applications.

1.4 Current state

Theoretical work on photonic bandgap structures has been a very active field of research in recent decades. Exciting phenomena, such as suppression and enhancement of spontaneous emission and dispersion compensation have been predicted. A variety of tools have been developed with which ever more complex devices can be modelled. Models such as 3 dimensional FDTD (finite difference time domain) and RCWA (rigorous coupled wave analysis) are becoming more sophisticated and can model real devices more accurately, offering insight into how PBG structures work, their limitations and possible application.

Much of this theoretical work still remains to be verified experimentally. Until recently the available fabrication technology did not allow an investigation of sub-micron structures. However, lithography and dry etching techniques have seen significant improvements, which have enabled experimental studies of 1, 2 and 3 dimensional photonic crystal structures. The necessary equipment is costly and difficult to operate, which is why high quality experimental work on PhCs is only carried out in few facilities worldwide. Anyone with a computer can investigate photonic bandgap effects theoretically. Few have access to appropriate facilities for experimental work on these structures. This state of affairs will continue, but the theory-fabrication gap will decrease as fabrication techniques become cheaper and more widely accessible.

A significant problem for today's photonic crystal community is that there is no killer application for photonic crystals yet. Everything that has been realized with PhCs has already been done with other devices. For instance, filters, polarizers and optical waveguides have been fabricated for decades with conventional materials. Efficient dispersion compensation is available. The superprism fabricated by Wu *et al* [71] is an attempt to emulate the arrayed waveguide gratings (AWG), which have been commercially available since the mid 1990s. Today's PhC superprisms win over AWGs in terms of size, but their performance is far inferior to that of modern AWGs [72].

If a killer application can be found, something that can exclusively be achieved with photonic crystals, or if PhCs can be shown to be significantly cheaper and better than conventional components, then the future for photonic crystals will be bright.

Not only is photonic crystal technology more costly than conventional technology, but PhCs cannot yet compete in terms of performance either. This is because they are inherently lossy structures. There is a real shortage of data in the literature that discusses losses in photonic crystals. A number of poor and ambiguous experimental results highlight the situation of recent years. However, in the last 2-3 years more and more publications have appeared, which address the loss issue. This is a positive development. It is imperative to identify the causes of the poor performance of PhC devices. As a starting point, an unambiguous and repeatable way of characterizing these structures is required.

Extrinsic losses due to fabrication-related issues are reduced as the technology advances. Nonetheless, we believe that there are a number of intrinsic losses, which will always limit the performance of PhC devices. A number of authors have discussed various loss mechanisms recently [73, 74, 75, 76]. Much experimental work needs to be done to gain better understanding of the PhC-related losses, how to optimize the design of the PhCs and their environment and the factors that will ultimately limit the performance of photonic crystal devices. This is the motivation for the study presented here.

1.5 Outline of Thesis

The work is presented in the following Chapters can be summarized as follows:

- Chapter 2: a detailed account of the fabrication techniques used in making the photonic crystal structures
- Chapter 3: theoretical background is given and various modelling and data analysis tools are presented
- Chapter 4: optical characterization issues are discussed and our approach is presented
- Chapter 5: spectral results of characterization experiments are discussed and in the second part results from Fourier-transformed data is presented
- Chapter 6: other photonic crystal structures that were investigated are discussed - large fill factor work, PhC with organic materials and microcavity structures
- Chapter 7: conclusions are drawn on the overall project and future work is proposed

Bibliography

[1] E. Yablonivitch. Inhibited spontaneous emission in solid-state physics and electronics. *Phys. Rev. Lett.*, 58(20):2059–2062, May 1987.

[2] H. Ghiradella. Light and color on the wing: structural colors in butterflies and moths. *Appl. Opt.*, 30(24):3492–3500, August 1991.

[3] L. P. Biró. Role of photonic-crystal-type structures in the thermal regulation of a Lycaenid butterfly sister species pair. *Phys. Rev. E*, 67:021907, February 2003.

[4] E. Hecht. *Optics.* Addison-Wesley, 2nd edition, 1987.

[5] K. Sakoda. *Optical properties of photonic crystals.* Optical Sciences. Springer Verlag, 2001.

[6] J. D. Joannopoulos, R. D. Meade, and J. N. Winn. *Photonics Crystals, Molding the Flow of Light.* Princeton University Press, Princeton, 1995.

[7] R. D. Meade, A. M. Rappe, K. D. Brommer, and J. D. Joannopoulos. Nature of the photonic band gap: some insights from a field analysis. *J. Opt. Soc. Am. B*, 10(2):328–332, February 1993.

[8] R. De La Rue and C. Smith. On the threshold of success. *Nature*, 408:653–656, December 2000.

[9] M. Lončar, T. Yoshie, A. Scherer, P. Gogna, and Y. Qiu. Low-threshold photonic crystal laser. *Appl. Phys. Lett.*, 81(15):2680–2682, October 2002.

[10] K. Okamoto, M. Lončar, T. Yoshie, A. Scherer, Y. Qiu, and P. Gogna. Near-field scanning optical microscopy of photonic crystal nanocavities. *Appl. Phys. Lett.*, 82(11):1676–1678, March 2003.

[11] O. J. Painter, J. Vučković, and A. Scherer. Defect modes of a two-dimensional photonic crystal in an optically thin dielectric slab. *J. Opt. Soc .Am. B*, 16(2):275–285, February 1999.

[12] A. Talneau, L. Le Gouezigou, N. Bouadma, M. Kafesaki, C. M. Soukoulis, and M. Agio. Photonic-crystal ultra short bends with improved transmission and refiection at 1.55μm. *Appl. Phys. Lett.*, 80(4):547–549, January 2002.

[13] A. Sharkawy, S. Shi, and D. W. Prather. Multichannel wavelength division multiplexing with photonic crystals. *Appl. Opt.*, 40(14):2247–2252, May 2001.

[14] J. Moosburger, M. Kamp, and A. Forchel. Enhanced transmission through photonic-crystal-based bent waveguides by bend engineering. *Appl. Phys. Lett.*, 79(22):3579–3581, November 2001.

[15] C. J. M. Smith, H. Benisty, S. Olivier, M. Rattier, C. Weisbuch, T. F. Krauss, R. M. De La Rue, R. Houdré, and U. Oesterle. Low-loss channel waveguides with two-dimensional photonic crystal boundaries. *Appl. Phys. Lett.*, 77(18):2813–2815, October 2000.

[16] M. Tokushima, H. Kosaka, A. Tomita, and H. Yamada. Lightwave propagation through a 120 degree sharply bent single-line-defect photonic crystal waveguide. *Appl. Phys. Lett.*, 76(8):952–954, February 2000.

[17] S. John. Strong localization of photoncs in certain disordered dielectric superlattices. *Phys. Rev. Lett.*, 58(23):2486–2489, June 1987.

[18] E. M. Purcell. Spontaneous emission probabilities at radio frequencies. *Phys. Rev.*, 69(11,12):681–681, 1946.

[19] D. Kleppner. Inhibited spontaneous emission. *Phys. Rev. Lett.*, 47(4):233–236, July 1981.

[20] B. Gayral and J. M. Gérard. Strong Purcell effect for InAs quantum boxes in high-Q wet-etched microdisks. *Physica E*, 7:641–645, 2000.

[21] O. J. Painter, R. K. Lee, A. Scherer, A. Yariv, J. D. O'Brien, P. D. Dapkus, and I. Kim. Two-dimensional photonic band-gap defect mode laser. *Science*, 284:1819–1821, June 1999.

[22] M. Lončar, A. Scherer, and Y. Qiu. Photonic crystal laser sources for chemical detection. *Appl. Phys. Lett.*, 82(26):4648–4650, June 2003.

[23] T. Asano and S. Noda. Characterization of channel add/drop functions using donor/acceptor point defects in two dimensional photonic crystal slabs. *Proc. CLEO*, JWB6, June 2003.

[24] E. Yablonovitch and T. J. Gmitter. Photonic band structure: The face-centred-cubic case. *Phys. Rev. Lett.*, 63(18):1950–1953, October 1989.

[25] E. Yablonovitch, T. J. Gmitter, and K. M. Leung. Photonic band structure: The face-centred-cubic case employing nonspherical atoms. *Phys. Rev. Lett.*, 67(17):2295–2298, October 1991.

[26] C. C. Cheng and A. Scherer. Fabrication of photonic band-gap crystals. *J. Vac. Sci. Technol. B*, 13(6):2696–2700, Nov/Dec 1995.

[27] S. Fan, P. R. Villeneuve, R. D. Meade, and J. D. Joannopoulos. Design of three-dimensional photonic crystals at submicron lengthscales. *Appl. Phys. Lett.*, 65(11):1466–1468, September 1994.

[28] C. C. Cheng, A. Scherer, V. Arbet-Engels, and E. Yablonovitch. Lithographic band gap tuning in photonic band gap crystals. *J. Vac. Sci. Technol. B*, 14(6):4110–4114, Nov/Dec 1996.

[29] C. C. Cheng, A. Scherer, R.-C. Tyan, Y. Fainman, G. Witzgall, and E. Yablonovitch. New fabrication techniques for high quality photonic crystals. *J. Vac. Sci. Technol. B*, 15(6):2764–2767, Nov/Dec 1997.

[30] G. Feiertag, W. Ehrfeld, H. Freimuth, H. Kolle, H. Lehr, M. Schmidt, Sigalas, C. M. Soukoulis, G. Kiriakidis, T. Pedersen, J. Kuhl, and W. Koenig. Fabrication of photonic crystals by deep x-ray lithography. *Appl. Phys. Lett.*, 71:1441–1443, September 1997.

[31] H. Kosaka, T. Kawashima, A. Tomita, M. Notomi, T. Tamamura, T. Sato, and S. Kawakami. Superprism phenomena in photonic crystals. *Phys. Rev. B*, 58(16):R10096–R10099, October 1998.

[32] S. Y. Lin, J. G. Fleming, D. L. Hetherington, B. K. Smith, R. Biswas, K. M. Ho, M. M. Siglas, W. Zubrzycki, S. R. Kurtz, and J. Bur. A three-dimensional photonic crystal operating at infrared wavelengths. *Nature (London)*, 394:251–253, July 1998.

[33] L. Dal Negro. Light transport through the band-edge states of Fibonacci quasicrystals. *Phys. Rev. Lett.*, 90(5):55501, February 2003.

[34] R. D. Meade, A. Devenyi, J. D. Joannopoulos, O. L. Alerhand, D. A. Smith, and K. Kash. Novel application of photonic band gap materials: Low-loss bends and high Q cavities. *J. Appl. Phys.*, 75(9):4753–4755, May 1994.

[35] J. C. Chen, H. A. Haus, S. Fan, P. R. Villeneuve, and J. D. Joannopoulos. Optical filters from photonic band gap air bridge. *J. Lightwave Technol.*, 14(11):2575–2580, November 1996.

[36] A. Mekis, J. C. Chen, I. Kurland, S. Fan, P. R. Villeneuve, and J. D. Joannopoulos. High transmission through sharp bends in photonic crystal waveguides. *Phys. Rev. Lett.*, 77(18):3787–3790, October 1996.

[37] W. M. Robertson, G. Arjavalingam, R. D. Meade, K. D. Brommer, A. M. Rappe, and J. D. Joannopoulos. Measurement of photonic band structure in a two-dimensional periodic dielectric array. *Phys. Rev. Lett.*, 68(13):2023–2026, March 1992.

[38] O. Dial, C. C. Cheng, and A. Scherer. Fabrication of high-density nanostructures by electron beam lithography. *J. Vac. Sci. Technol. B*, 16(6):3887–3890, November 1998.

[39] P. L. Gourley, J. R. Wendt, G. A. Vawter, T. M. Brennan, and B. E. Hammons. Optical properties of two-dimensional photonic lattices fabricated as honeycomb nanostructures in compound semiconductors. *Appl. Phys. Lett.*, 64(6):687–689, February 1994.

[40] P. R. Villeneuve, S. Fan, J. D. Joannopoulos, K.-Y. Lim, G. S. Petrich, L. A. Kolodziejski, and R. Reif. Air-bridge microcavities. *Appl. Phys. Lett.*, 67(2):167–169, July 1995.

[41] D. J. Ripin, K.-Y. Lim, G. S. Petrich, P. R. Villeneuve, S. Fan, E. R. Thoen, J. D. Joannopoulos, E. P. Ippen, and L. A. Kolodziejski. One-dimensional photonic bandgap microcavities from strong optical confinement in GaAs and GaAs/Al(x)O(y) semiconductor waveguides. *J. Lightwave Technol.*, 17(11):2152–2160, November 1999.

[42] M. Kanskar, P. Paddon, V. Pacradouni, R. Morin, A. Busch, J. F. Young, S. R. Johnson, J. MacKenzie, and T. Tiedje. Observation of leaky slab modes in an air-bridge semiconductor waveguide with two-dimensional photonic lattice. *Appl. Phys. Lett.*, 70(11):1438–1440, March 1997.

[43] J. S. Foresi, P. R. Villeneuve, J. Ferrara, E. R. Thoen, G. Steinmeyer, S. Fan, J. D. Joannopoulos, L. C. Kimerling, H. I. Smith, and E. P. Ippen. Photonic-bandgap microcavities in optical waveguides. *Nature (London)*, 390:143–145, November 1997.

[44] S. Noda, A. Chutinan, and M. Imada. Trapping and emission of photons by a single defect in a photonic bandgap structure. *Nature (London)*, 407:608–610, October 2000.

[45] S. Y. Lin, E. Chow, S. G. Johnson, and J. D. Joannopoulos. Demonstration of highly efficient waveguiding in a photonic crystal slab at the 1.5μm wavelength. *Opt. Lett.*, 25(17):1297–1299, September 2000.

[46] T. Asano, S. Noda, K. Kiyota, Y. Tanaka, Y. Akahane, B.-S. Song, M. Mochizuki, and M. Imada. Channel-add operation of a device using defects in a two-dimensional photonic crystal slab. *Proc. MRS*, 722:363 (L2.3), April 2002.

[47] T. Asano, B.-S. Song, Y. Tanaka, and S. Noda. Investigation of a channel-add/drop-filtering device using acceptor-type point defects in a two-dimensional photonic-crystal slab. *Appl. Phys. Lett.*, 83(3):407–409, July 2003.

[48] D. Labilloy, H. Benisty, C. Weisbuch, T. F. Krauss, R. Houdré, and U. Oesterle. Use of guided spontaneous emission of a semiconductor to probe the optical properties of two-dimensional photonic crystals. *Appl. Phys. Lett.*, 71(6):738–740, August 1997.

[49] H. Benisty, C. Weisbuch, D. Labilloy, M. Rattier, C. J. M. Smith, T. F. Krauss, R. De La Rue, R. Houdré, U. Oesterle, C. Jouanin, and D. Cassagne. Optical

and confinement properties of two-dimensional photonic crystals. *J. Lightwave Technol.*, 17(11):2063–2077, November 1999.

[50] T. D. Happ, M. Kamp, and A. Forchel. Photonic crystal tapers for ultracompact mode conversion. *Opt. Lett.*, 26(14):1102–1104, July 2001.

[51] Y. Xu, R. K. Lee, and A. Yariv. Adiabatic coupling between conventional dielectric waveguides and waveguides with discrete translational symmetry. *Opt. Lett.*, 25(10):755–757, May 2000.

[52] A. Talneau, M. Mulot, S. Anand, and Ph. Lalanne. Compound cavity measurement of transmission and reflection of a tapered single-line photonic-crystal waveguide. *Appl. Phys. Lett.*, 82(16):2577–2579, April 2003.

[53] J. O'Brien, O. Painter, R. Lee, C. C. Cheng, A. Yariv, and A. Scherer. Lasers incorporating 2D photonic bandgap mirrors. *Electron. Lett.*, 32(24):2243–2244, November 1996.

[54] S. Fan, P. R. Villeneuve, J. D. Joannopoulos, and E. F. Schubert. High extraction efficiency of spontaneous emission from slabs of photonic crystals. *Phys. Rev. Lett.*, 78(17):3294–3297, April 1997.

[55] A. A. Erchak, D. J. Ripin, S. Fan, P. Rakich, J. D. Joannopoulos, E. P. Ippen, G. S. Petrich, and L. A. Kolodziejski. Enhanced coupling to vertical radiation using a two-dimensional photonic crystal in a semiconductor light-emitting diode. *Appl. Phys. Lett.*, 78(5):563–565, January 2001.

[56] C. Reese. Photonic crystal microcavities with self-assembled InAs quantum dots as active emitters. *Appl. Phys. Lett.*, 78(16):2279–2281, April 2001.

[57] K.-H. Lee, D.-S. Song, Y.-J. Lee, H.-G. Park, S.-H. Kim, and Y.-H. Lee. Polarization-controlled, single-mode photonic-crystal vertical cavity surface emitting lasers. *Proc. CLEO*, CThP2, June 2003.

[58] A. J. Danner, N. Yokouchi, and K. D. Choquette. Single mode photonic crystal vertical cavity lasers incorporating etch depth dependence. *Proc. CLEO*, CThP3, June 2003.

[59] G. Moore. Cramming more components onto integrated circuits. *Electronics*, 38(8), April 1965.

[60] L. B. Kish. End of Moore's law: thermal (noise) death of integration in micro and nano electronics. *Phys. Lett. A*, 305:144–149, December 2002.

[61] J. D. Joannopoulos, P. R. Villeneuve, and S. Fan. Photonic crystals: putting a new twist on light. *Nature (London)*, 386:143–149, March 1997.

[62] R. G. Hunsperger. *Integrated Optics.* Springer, 4th edition, 1995.

[63] M. Notomi, K. Yamada, A. Shinya, J. Takahashi, C. Takahashi, and I. Yokohama. Extremely large group-velocity dispersion of line-defect waveguides in photonic crystal slabs. *Phys. Rev. Lett.*, 87(25):253902:1–4, December 2001.

[64] G. Parker. Photonic integration takes things forward. *Fibersystems Europe*, 7(2):9, February 2003.

[65] P. Bayvel. Future high-capacity optical telecommunication networks. *Phil. Trans. R. Soc. Lond. A*, 358:303–329, 2000.

[66] O. J. Painter, A. Husain, A. Scherer, P. T. Lee, I. Kim, J. D. O'Brien, and P. D. Dapkus. Lithographic tuning of a two-dimensional photonic crystal laser array. *IEEE Phot. Technol. Lett.*, 12(9):1126–1128, September 2000.

[67] O. J. Painter, A. Husain, A. Scherer, J. D. O'Brien, I. Kim, and P. D. Dapkus. Room temperature photonic crystal defect lasers at near-infrared wavelengths in InGaAsP. *J. Lightwave Technol.*, 17(11):2082–2088, November 1999.

[68] H. Y. Ryu, Y. H. Lee, R. L. Sellin, and D. Bimberg. Over 30-fold enhancement of light extraction from free-standing photonic crystal slabs with InGaAs quantum dots at low temperature. *Appl. Phys. Lett.*, 79(22):3573–3575, November 2001.

[69] T. Yoshie, A. Scherer, H. Chen, D. Huffaker, and D. Deppe. High quality two-dimensional photonic crystal slab cavities. *Appl. Phys. Lett.*, 79(26):4289–4291, December 2001.

[70] J. Topol'ančik, P. Bhattacharya, J. Sbarinathan, and P.-C. Yu. Fluid detection with photonic crystal-based multichannel waveguides. *Appl. Phys. Lett.*, 82(8):1143–1145, February 2003.

[71] L. Wu, M. Mazilu, T. Karle, and T. F. Krauss. Superprism phenomena in planar photonic crystals. *IEEE J. Quantum Electron.*, 38(7):915–918, July 2002.

[72] Y. Hida. Fabrication of low-loss and polarisation-insensitive 256 channel arrayed-waveguide grating with 25GHz spacing using 1.5% δ waveguides. *Electron. Lett.*, 36(9):820–821, April 2000.

[73] R. Ferrini, B. Lombardet, B. Wild, R. Houdré, and G.-H. Duan. Hole depth- and shape-induced radiation losses in two-dimensional photonic crystals. *Appl. Phys. Lett.*, 82(7):1009–1011, February 2003.

[74] H. Benisty, D. Labilloy, C. Weisbuch, C. J. M. Smith, T. F. Krauss, D. Cassagne, A. Béraud, and C. Jouanin. Radiation losses of waveguide-based two-dimensional photonic crystals: Positive role of the substrate. *Appl. Phys. Lett.*, 76(5):532–534, January 2000.

[75] H. Benisty, Ph. Lalanne, S. Olivier, M. Rattier, C. Weisbuch, C. J. M. Smith, T. F. Krauss, C. Jouanin, and D. Cassagne. Finite-depth and intrinsic losses in vertically etched two-dimensional photonic crystals. *Opt. Quantum Electron.*, 34:205–215, 2002.

[76] L. C. Andreani and M. Agio. Intrinsic diffraction losses in photonic crystal waveguides with line defects. *Appl. Phys. Lett.*, 82(13):2011–2013, March 2003.

Chapter 2

Fabrication

2.1 Introduction

In this Chapter a detailed account is given of how photonic crystal structures were produced. This proved to be an incredibly delicate and time-consuming part of the overall project. Many of the processing steps involved temperamental cutting-edge technology and processes that are not perfectly understood. Several months were spent on detailed calibrations of equipment, which turned out to be a key component to the eventual success and high quality of the fabricated photonic crystal structures.

The first Section is a brief overview in which a justification for using the chosen host material is given. Key parts of any fabrication work are the characterization and analysis tools, with which to assess the structural properties and quality of samples. These tools are also introduced in the first Section.

The fabrication of photonic crystals in ridge waveguides can be broken down into four parts, each of which will be described in a separate Section. These are:

- **sample preparation**: deposition of masking layers
- **electron beam lithography**: initial transfer of patterns into PMMA - the most critical part of the entire process
- **dry etching**: transfer of patterns into mask and epilayers
- **ridge lithography**: defining ridge waveguides.

The order of these Sections reflects the order in which the processing of PhCs in ridge waveguides is performed, as shown in Fig. 2.1. Other structures that were fabricated, which are discussed in Chapter 6 involved minor variations of these steps and some steps were omitted entirely.

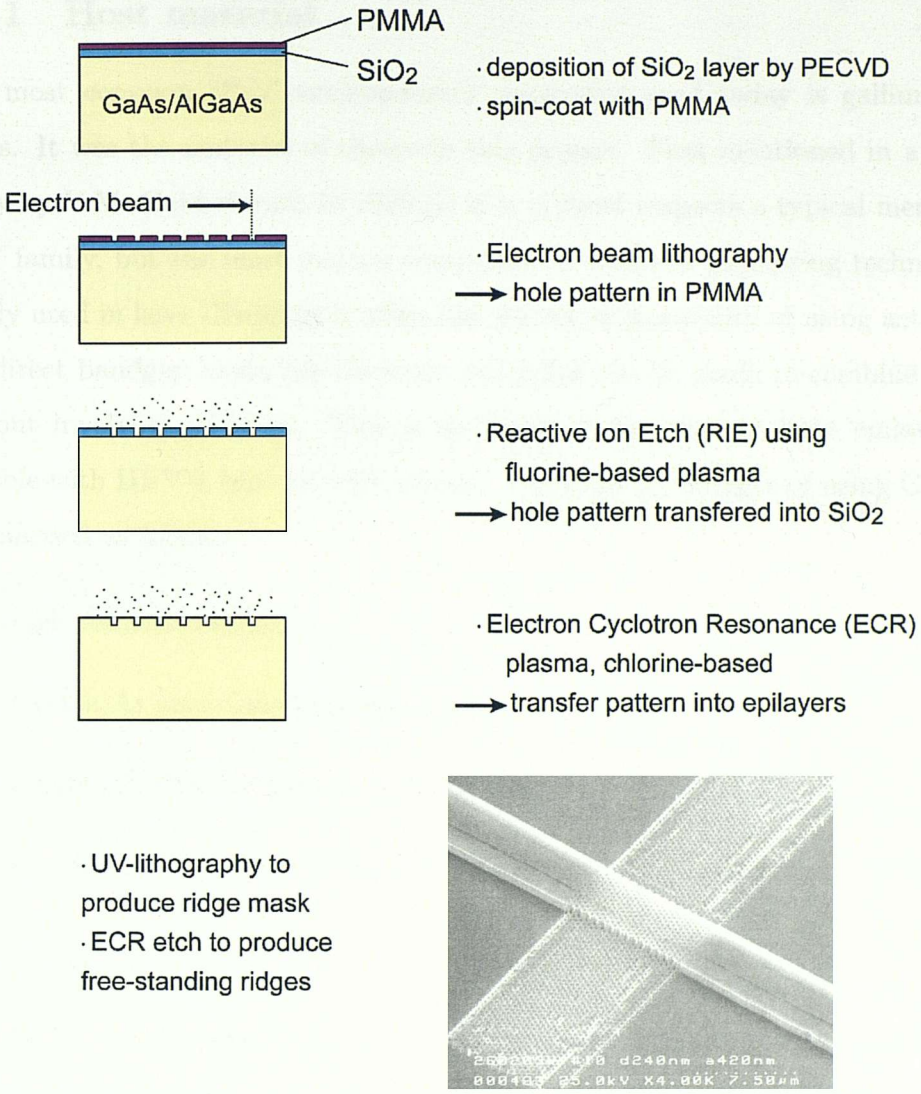


Figure 2.1: Overview of key processing steps for producing PhC in ridge waveguides.

All fabrication work was carried out at Sharp Laboratories of Europe (SLE) in the Oxford Science Park.

2.1.1 Host material

The most common III-V semiconductor compound used today is gallium arsenide, GaAs. It was the material of choice in this project. First mentioned in a theoretical study by V.M. Goldschmidt in 1929 [1] it is in most respects a typical member of the III-V family, but the most mature compound in terms of processing technology. It is widely used in laser diodes as it offers the attractive possibility of using active regions. For direct bandgap materials electrons and holes can be made to combine radiatively without involving phonons. This is the basis of the efficient light emission that is possible with III-V's, but not with silicon. The main advantages of using GaAs can be summarised as follows:

- high refractive index
- (Al,Ga)As established system
- highly suitable for waveguide structures
- low absorption (2-3 dB/cm, [2, 3]) at wavelength of interest

Properties

Gallium (Ga) and arsenic (As) are mainly covalently bonded in a cubic sphalerite lattice, also known as the zincblende lattice structure. A small part of the bonding force is of ionic nature (~4 %, [4]) due to the small difference in electronegativity between Ga and As. This makes the compound polar.

GaAs, as all III-V semiconductors, has a direct bandgap, which means that on an E-k diagram the conduction band edge and the valence band edge both occur at $k = 0$. The minimum energy required for a photon to be absorbed in a direct bandgap material is simply the difference between the conduction and valence band edges. For indirect bandgap materials, photon absorption is typically assisted by phonons, quanta of lattice vibration, which supply the required momentum to reach the k-value of the bottom of the conduction band. Unassisted photon absorption is possible for indirect

bandgap materials, but relatively large photon energies are necessary (at room temperature ~3.5 eV for Si at the Brillouin zone centre vs. ~1.42 eV for GaAs [5]).

Growth

The two main wafers (QT1598UP and QT1598DOWN) used in this project were grown at Sheffield University by John Roberts, using metalorganic chemical vapour deposition (MOCVD). In this technique the substrate is heated and exposed to a laminar flow of gas precursors for the materials to be grown. The gas flow is tightly controlled. The gases dissociate into atomic species at the heated surface of the wafer and get deposited to form epitaxial layers. Typical growth rates are 10-30 nm/min [4].

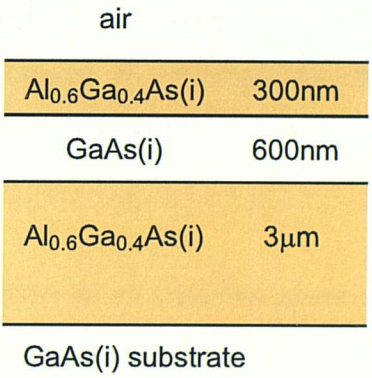


Figure 2.2: Planar waveguide structure of wafers. All materials were undoped.

Figure 2.2 shows the structural composition of wafers QT1598UP and QT1598DOWN. Reflection measurements were performed on different parts of these wafers using a broadband halogen light source. A theoretical reflection spectrum for the nominal wafer structure was calculated using `Multilayer` [6]. Figure 2.3 shows the measurement from an area of the wafer, which gave the best match visually with the modelled result for the nominal wafer structure.

The reflection spectra from most regions of the wafers showed similar trends to those of Fig. 2.3. Measurements on some edge regions of the wafer indicated that the

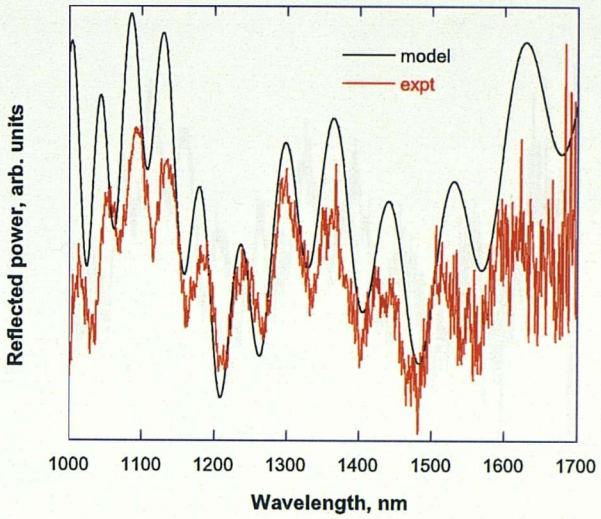


Figure 2.3: Reflection spectra recorded on MOCVD-grown wafer QT1598UP. The theoretical curve was calculated using `Multilayer` and is plotted in black.

growth process was not homogenous across the wafer, see Fig. 2.4. This is no surprise with the MOCVD growth technique. Nonetheless, the wafers were judged to have been successfully grown very close to the specifications and all parts of the wafer were used without reservations.

Other wafers, such as U20067, which contains layers of quantum dots and was used in the large fill factor[1] study described in Chapter 6, were grown by MBE at Imperial College London, by Christine Roberts. Very high film purity can be achieved with MBE. The layer thickness can also be controlled precisely. MBE growth is carried out under very high vacuum conditions, typically 10^{-8} to 10^{-9} Pa. Semiconductor components are evaporated inside high-temperature effusion cells creating molecular beams that are directed onto a wafer, which is heated to 500-700°C. Typical growth rates are one monolayer per second ($\sim$1 μm/hr).

[1]See Section 2.2.3 for a definition of the fill factor.

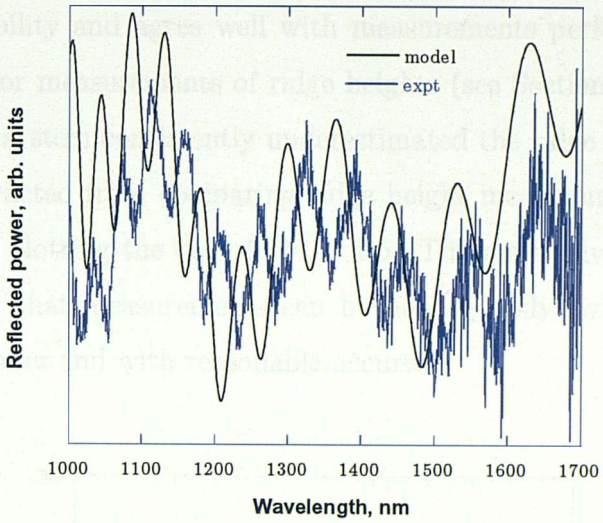


Figure 2.4: Reflection spectra recorded on MOCVD-grown wafer QT1598UP. Measured spectrum varies somewhat from theoretical curve, indicating inhomogenous growth conditions across wafer.

2.1.2 Structural characterization

Optical microscope

A high magnification optical microscope (Olympus AH3) was available to inspect the samples. The features of a photonic crystal pattern designed to have a photonic bandgap in the near infrared spectrum, around 1550 nm, are typically 100-300 nm. These dimensions are unresolvable with common optical microscopes, due to the classical diffraction limit, given in Eqn. 4.1 on Page 147. Nonetheless, the overall morphology of the etched patterns can be analysed very quickly in a high magnification optical microscope. Ridge waveguides described in Section 2.5 were several micrometers wide, which was easily resolvable under the available microscope. After every processing step in the cleanroom the samples were analysed under the optical microscope.

Alpha-step

The Tencor alpha-step 200 is a stylus-based surface profiler. It measures the difference in thickness across a sample and it was used to measure ridge heights. Measurements

show good repeatability and agree well with measurements performed by SEM (see next subsection). For measurements of ridge heights (see Section 2.4.2) it was found that the alpha-step system consistently underestimated the ridge height by ~200 nm. This value was extracted from comparing ridge height measurements with the SEM and the α-step and plotting the data in Fig. 2.5. The main advantage of using this measuring device is that measurements can be done quickly (within minutes), in a non-destructive manner and with reasonable accuracy.

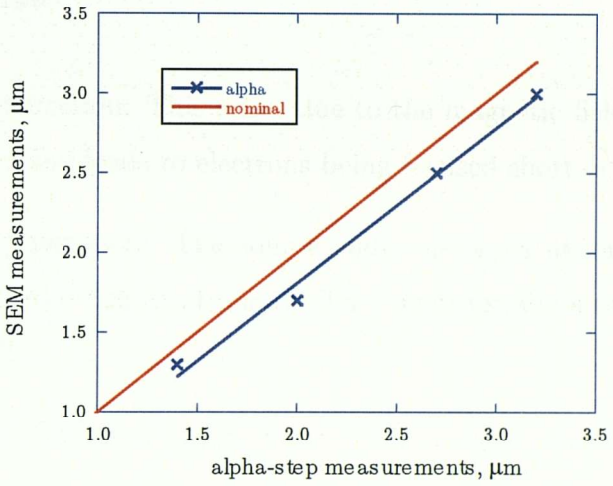


Figure 2.5: Calibration results of α-step profiler. Ridge height was compared with SEM measurements, which have an accuracy of ± 5 nm.

SEM

The Hitachi S4000 'cold cathode field emission' Scanning Electron Microscope (SEM) was used to obtain ultra-high magnification images of the fabricated structures. An electron beam is generated by applying a large potential difference (extraction voltage, V_{ext} ~4 kV) between a V-shaped tungsten filament cathode and an anode. This pulls electrons away from the filament. A second potential difference, the accelerating voltage (V_{acc}) is applied between the filament and a second anode. V_{acc} can be varied between 0.5 and 25 kV. This is used to select the final energy of the electrons, which can be as high as 100 keV [7]. High accelerating voltage is used to obtain high resolution,

whereas low V_{acc} allows one to observe surface texture. Some common limitations of SEMs are given below. The beam is cleaned up, shaped and focused onto the sample. Impinging electrons cause the sample to emit low energy electrons, known as secondary electrons. Some electrons are reflected. These are backscattered electrons. Electrons hitting the sample also generate X-rays. The secondary electrons are collected by a photo-multiplier tube (PMT), which boosts the electronic signal. This is then converted to an intensity map of the field of view and imaged in real time on a monitor.

Lens Aberrations

- Spherical Aberration: This arises due to the magnetic field distribution created by the lenses and leads to electrons being focused short or long.
- Chromatic Aberration: The source emits electrons at various energies, which become focused on different planes. This is not usually a serious problem in field emission SEM.
- Astigmatism: This is a result of the beam emerging from the source not being spherical. Also, some components of the electron optics system are likely to be not perfectly symmetrical due to machining imperfections. This contributes to astigmatism.

2.2 Sample preparation

A fundamental step in the processing of semiconductor devices is the transfer of designs from a computer aided design (CAD) drawing into the semiconductor. Sub-micron features are commonly created using dry etching techniques, an example being plasma etching. Other etch techniques are discussed in Section 2.4. This Section is a description of the necessary sample preparation for etching holes with diameters of the order of 200 nm into GaAs/AlGaAs epilayers using an electron cyclotron resonance plasma, which is the subject of Section 2.4.2.

A two-mask process was used to transfer the designed hole pattern into the semiconductor epilayers. The standard method employed by the vast majority of research groups in this field consists of depositing a layer of silicon dioxide (silica, SiO_2) on top of the semiconductor, followed by an application of photoresist. These two steps are discussed in the following Sections.

The use of a nickel mask as an alternative to silica has been reported [8].

2.2.1 PECVD

Plasma-enhanced chemical vapour deposition (PECVD) was used to deposit a layer of silica atop the GaAs/AlGaAs samples. In essence the PECVD reactor is a parallel plate configuration [4], in which gas-phase precursors such as silane (SiH_4), nitrous oxide (N_2O) and nitrogen (N_2) are pumped into the chamber at precisely controlled flow rates, see Table 2.1. The plasma is ignited by a radio frequency (RF) discharge between two electrodes. In this process the sample is heated to 300°C. The STS 310 PECVD tool by Surface Technology Systems plc (STS) was used. Performing a series of carefully timed plasma etches, described in Section 2.4.1 the rate of deposition was determined. For the process conditions used here, this was found to be ~25 nm/min. Silica was deposited on large semiconductor pieces; either full 2in wafers, or quarter

wafers. This ensures that all samples obtained from cleaving up this large piece have the same mask thickness, i.e. the same initial processing conditions.

Gas	N_2	N_2O	SiH_4
Flow rate, sccm	200	500	5
P_{ch}, mT	650		
Temperature, °C,	300		
RF power, W	10		
dep. rate, nm/min	~26		

Table 2.1: PECVD gas flow rates for silica deposition

2.2.2 Photoresist

A photoresist is a light-sensitive material, usually consisting of polymer chains, which when exposed to certain forms of radiation incurs physical changes. Apart from photons the photoresist can also be exposed by more energetic particles, such as H^+, He^+, O^+ ions and electrons [9]. In this study beams of electrons were used to expose the photoresist. The details of the electron beam lithography (EBL) process are given in Section 2.3.

There are two types of photoresist: positive and negative. Bombarding positive photoresist with electrons breaks the polymer chains in exposed areas. The broken polymer chains have a lower molecular weight and are easily removed with an appropriate solvent.

The exposure of a negative photoresist results in more cross linkage of polymer chains, rendering the exposed areas less soluble than the unexposed regions.

The fabrication of sub-micron diameter holes in a semiconductor is most easily accomplished using a positive photoresist. The standard photoresist used today in photonic crystal fabrication is polymethyl methacrylate (PMMA, commonly known

as Plexiglas ®, chemical formula of monomer: $C_5H_8O_2$). The "950 PMMA C4" by MicroChem Corp. (MCC) was selected for this work. The molecular weight of the PMMA was 950,000 and it was dissolved in chlorobenzene.

Before applying PMMA onto the silica-coated semiconductor, it is imperative to ensure that the sample surface is very clean. Careful rinsing in acetone, methanol and de-ionised water, followed by blow-drying with nitrogen was carried out to remove surface contamination. The entire sample was then covered with PMMA and spun at 4500 rpm for 30 seconds, which results in a film thickness of ~310±5 nm, with good reproducibility. Figure 2.6 is a high resolution SEM image of the cross section of a sample after electron beam lithography. The PMMA was exposed by electron beam lithography (see Section 2.3), developed (described in Section 2.3.5) and the sample was cleaved through the exposed patterns, as described in Section 2.5.6. To view PMMA in an SEM a film of gold was sputtered on.

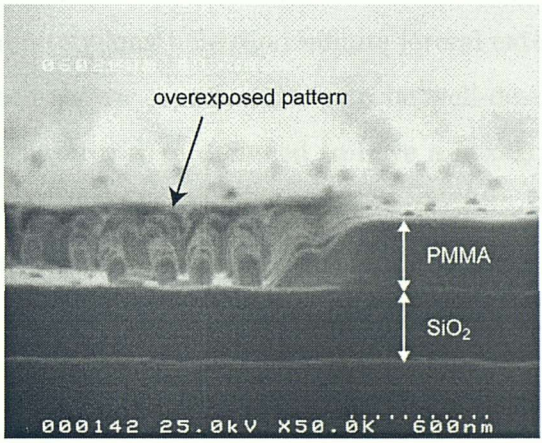


Figure 2.6: An SEM image of a sample cross section showing the thicknesses of the PMMA and SiO_2 layers. Gold was sputtered on to the sample prior to analysing it in the SEM.

In Fig. 2.6 one can see the remains of a totally overexposed pattern on the left hand side of the picture. On the right hand side three distinct layers can be identified: the top layer is unexposed PMMA, below that is a layer of silica and below that is the top part of the GaAs/AlGaAs structure. The calibration bar is 600 nm long, which

indicates the height of the unexposed PMMA, i.e. the initial film thickness, to be ~310 nm. Furthermore, using the same SEM image the thickness of the silica layer was measured to be ~260±5 nm.

It is necessary to bake the sample once the PMMA is spun on to remove the solvent. This post-bake was done on a hotplate at 180°C for 90 seconds. Using a hotplate was found to result in a more homogenous film morphology than baking the sample in an oven. Once the sample was baked the PMMA was not found to deteriorate with time. Consistent EBL (Section 2.3) performance was obtained for over 12 months with the same PMMA film.

2.2.3 Pattern design

Band diagrams discussed in Section 3.2.2 on Page 104 are an essential tool for the design of photonic crystal patterns. Although calculated for plane waves propagating inside a crystal with infinitely long holes and infinite lateral extent, the band structure of real 2D PhC has been shown experimentally to be well-described by this approximation [10]. All our structures were designed to have a hexagonal lattice of air holes in semiconductor, usually a GaAs/AlGaAs heterostructure. In this system there is a large refractive index contrast between the hole material (n_{air} ~1.0) and the host material (n_{GaAs} ~3.4 for light around 1550 nm). This results in photonic bandgaps along certain crystal direction over certain frequency ranges.

As explained in Section 3.2 on Page 101 the band structure is highly polarization dependent, which has the result that frequency bands can be identified on a band diagram where light of one polarization experiences a photonic bandgap while orthogonally polarized light can propagate freely. This is depicted in Fig. 2.7. The definitions of TE and TM polarization used in this project are described in Section 3.2. In the shaded frequency band propagation modes exist for TE-polarized light, but TM-polarized light is evanescent. The crystal lattice does not support TM propagating modes at those

photon energies.

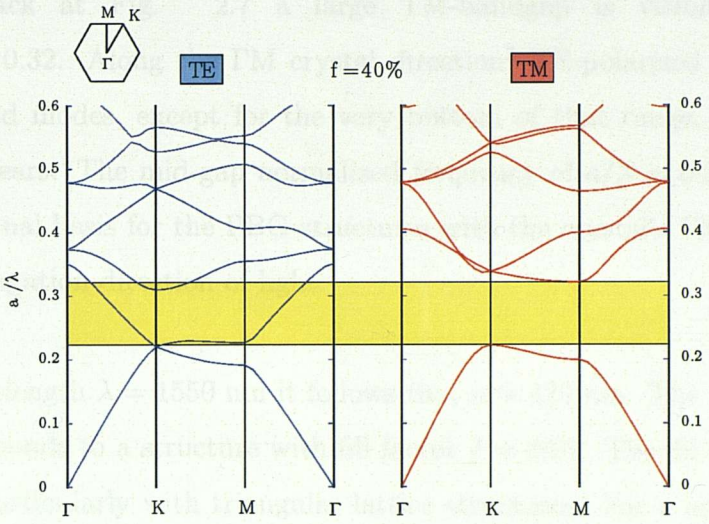


Figure 2.7: Band structure of an infinite 2D photonic crystal lattice calculated with 721 plane waves. Over the highlighted frequency range high transmission is predicted for TE-polarized light and a photonic bandgap exists for TM polarization.

From an experimental point of view this is a very interesting setting: for TE-polarized light of the correct energy the structure is transparent, but it is completely opaque to light of TM polarization at the same energy.

The vertical axis on band diagrams is given by the normalized frequency, a/λ, where a is the lattice constant of the triangular lattice. λ is the wavelength of light inside the photonic crystal. A band diagram is scalable to all imaginable dimensions, as Maxwell's equations do not contain any length scales.

We chose to design structures, which would operate around 1550 nm, the centre of the ITU (International Telecommunication Union) C-band (~1520-1570 nm). The reasons are that a) the required PhC feature sizes are realisable with current nano-fabrication technology; b) these structures may one day be incorporated into devices used in long-haul telecommunications applications, which is carried out primarily in the C-band where silica-based optical fibre experiences least dispersion. Some possible

future applications for photonic crystals were outlined in Section 1.3, Page 21.

Looking back at Fig. 2.7 a large TM-bandgap is visible in the range $0.22 < a/\lambda < 0.32$. Along the ΓM crystal direction[2] TE-polarized light can propagate in air-band modes, except for the very bottom of that range, where the lower band edge appears. The mid-gap normalized frequency of $a/\lambda = 0.27$ was chosen to be the operational basis for the PBG structures with the crystal's ΓM symmetry axis along the propagation direction of light.

At the wavelength $\lambda = 1550$ nm it follows that $a \approx 420$ nm. The band diagram in Fig. 2.7 corresponds to a structure with fill factor $f = 40\%$. The fill factor is a useful concept [11], particularly with triangular lattice structures. For a unit cell with area A_c it is defined as the fraction of the unit cell that is taken up by holes of area A_h; see Fig. 2.8. Hence, for a tringular lattice of holes with radius r this can be expressed as

$$\begin{aligned} f &= \frac{A_h}{A_c} \\ &= \frac{2 \times \pi r^2}{a \times \sqrt{3}a} \\ &= \frac{2\pi r^2}{\sqrt{3}a^2} \end{aligned} \tag{2.1}$$

The expression for the fill factor in Eqn. 2.1 can be rearranged to give the hole diameter d, which using $a = 420$ nm and $f = 40\%$ is found to be

$$\begin{aligned} d &= 2a\left(\frac{\sqrt{3}f}{2\pi}\right)^{\frac{1}{2}} \\ &= 2 \times 420\left(\frac{\sqrt{3} \times 0.4}{2\pi}\right)^{\frac{1}{2}} \\ &\approx 280 \text{ nm} \end{aligned} \tag{2.2}$$

The minimum feature size in a crystal pattern with lattice constant $a = 420$ nm and hole diameter $d = 280$ nm is given by the minimum wall thickness between nearest

[2]See Section 3.2 on Page 101 for an explanation of the ΓM symmetry

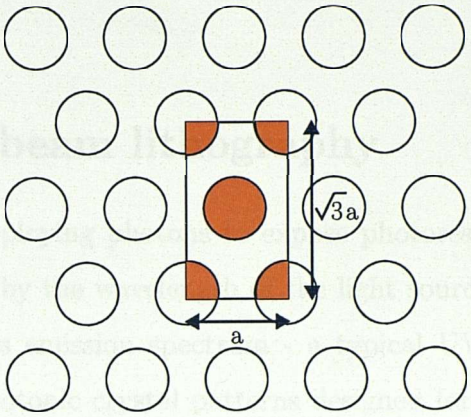


Figure 2.8: Illustration of the concept of fill factor as used with triangular lattices.

neighbour holes. In this case it corresponds to 140 nm - see Fig. 2.9.

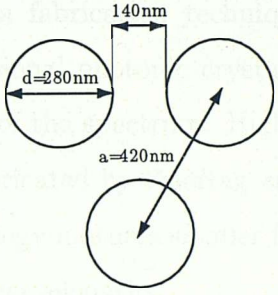


Figure 2.9: Schematic representation of typical dimensions used for triangular patterns.

These dimensions are readily realisable with today's nano-fabrication technology.

Pattern drawing

The graphics design package `AutoCAD` was used to create pattern files in the `DXF` format, which can be read by the e-beam writer software. The `AutoCAD` software tool is very versatile and any imaginable pattern can be drawn with great precision. The only limitation, which had nothing to do with `AutoCAD`, was that the maximum size of the pattern file could not be greater than 8 MB. This was due to limited onboard memory on the electron-beam control card, through which the PC and e-beam writer communicated, as described in Section 2.3.1.

2.3 Electron beam lithography

Optical lithography, employing photons to expose photoresist, has a resolution limit approximately dictated by the wavelength of the light source. For example, the i-line of a mercury arc lamp's emission spectrum - a typical UV light source - occurs at 365 nm. Features in photonic crystal patterns designed for operation in the near infrared spectrum are typically of the order of 100 nm, which can not be achieved with optical lithography.

Deep x-ray lithography is a fabrication technique, which can possibly be used to create complex three-dimensional photonic crystals at the dimensions required for bandgaps in the infra-red part of the spectrum. Highly regular 3D lattices of ceramic rods in air (Fig. 2.10) were fabricated by Feiertag *et al* [12], which showed bandgaps around 125 μm. As this technology matures smaller feature sizes will become possible, leading to bandgaps at shorter wavelengths.

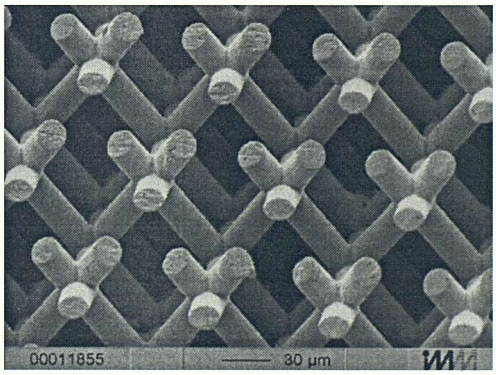


Figure 2.10: SEM image of 3D PhC lattice produced by deep x-ray lithography, taken from Ref. [12].

2.3.1 Description of electron beam writer and set-up

Figure 2.11 shows the set-up used to perform electron beam lithography. The e-beam writer is a converted scanning electron microscope (Cambridge Leica Stereoscan 360). Software controlled beam blanking equipment allows accurate bombardment of the sample's surface by a focused beam of electrons. The control software and specialised signal generator card (ELPHY) installed on a PC were produced by RAITH GmbH. It has an onboard RAM of 8 MB. This determines the maximum pattern file size as the entire pattern file has to be loaded into the card's memory prior to the launch of the e-beam control routine.

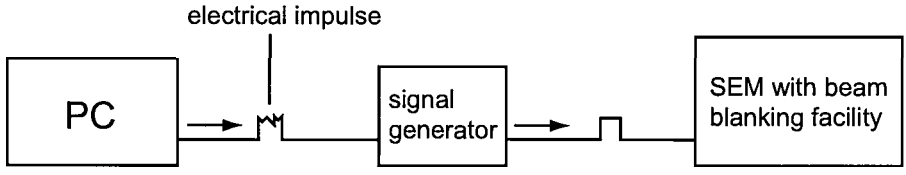


Figure 2.11: Diagram of EBL set-up.

The signal generated by the RAITH card is of poor quality. It is supposed to be a square pulse, but it is very noisy and misshaped. A 50 MHz signal generator (HP 8116A) was connected between the PC and the e-beam writer in order to clean up the PC-generated pulse. The width of the pulse leaving the signal generator was set manually on the signal generator. Pulse widths of ~60 ns were found to be the limit of what the signal generator was capable of producing.

A thermionic emission-type electron beam writer was used. A 'filament', which acts as a cathode, is heated to incandescence at ~1600°C by passing a large current through a refractory metal strip soldered to it. A large potential difference across the anode and the cathode accelerates electrons away from the filament. In our case a Lanthanum Hexaboride (LaB_6) rod was chosen as the cathode. This compound material has a lower work function than tungsten, which is conventionally used as filament material in SEMs. A LaB_6 rod is able to produce approximately 10 times the brightness

(emission current density) of a tungsten filament [7]. The set-up of the electron beam accelerator is shown in Fig. 2.12.

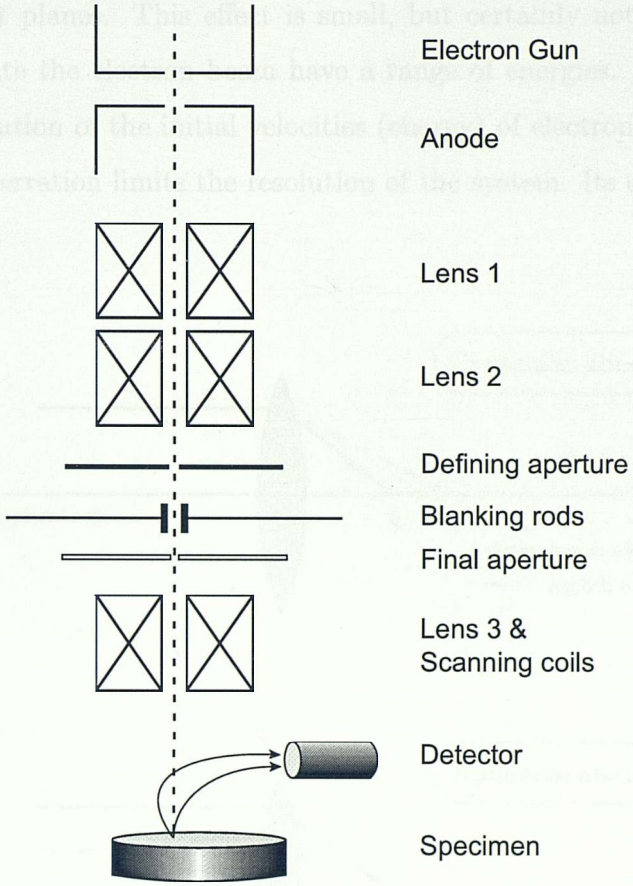


Figure 2.12: Diagram of EBL apparatus.

Two sets of electro-magnets (condenser lenses) significantly reduce the electron beam diameter before it impinges on the final aperture. A very small aperture of 10 μm diameter was used as the final aperture. This gives a very clean beam of nearly perfectly collimated electrons. This beam is then focused onto the sample by a final set of electro-magnets (objective lens).

There are many similarities between electron-optics and conventional electro-magnetic wave optics. Beams of electrons can be deflected, focused, scattered just like EM waves. The concept of chromatic aberration can also be used in the context of

electron optics. Chromatic aberration in conventional optics is a nuisance that arises when photons with different energies are focused. The refractive index of the focusing lens is a function of photon energy, which means photons of different energies are focused to different planes. This effect is small, but certainly noticeable. The electrons that constitute the electron beam have a range of energies. This is due to the Maxwellian distribution of the initial velocities (energy) of electrons leaving the cathode. Chromatic aberration limits the resolution of the system. Its effects are depicted in Fig. 2.13a.

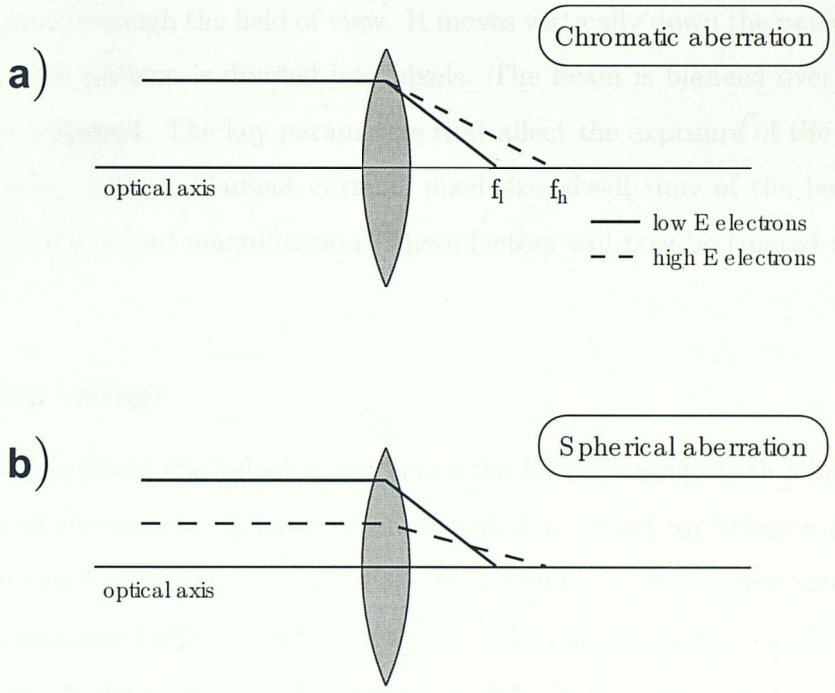


Figure 2.13: (a) Chromatic and (b) spherical aberration effects in electron optics. The 'lens' is a set of electromagnets.

Spherical aberration is another factor that limits the resolution of the electron beam focusing system - see Fig. 2.13b. The further the path of electrons is away from the optical axis of the system, the stronger they are focused. The effect of spherical aberration can be minimised by using a small final aperture, the approach taken here.

When electrons impinge on the surface of the sample some electrons are backscat-

tered while others cause atoms in the sample to emit secondary electrons. It is primarily the secondary electrons that are accelerated towards the detector, which consists of a scintillator. The light output from the scintillator is directed towards a photomultiplier tube, whose output drives the video system. Running the e-beam writer in *Emission Image* mode allows the exact shape of the electron beam to be imaged. This was used to shape the beam into a round spot of even brightness.

The patterns were drawn using `AutoCAD` as described in Section 5 and converted to the native file format of the e-beam control software. During the exposure the electron beam is scanned through the field of view. It moves vertically down the pattern, column by column. The pattern is divided into pixels. The beam is blanked over pixels that are not to be exposed. The key parameters that affect the exposure of the photoresist are accelerating voltage, filament current, pixel size, dwell time of the beam at each pixel, probe current and magnification. These factors will now be treated in turn.

Accelerating voltage

This parameter affects the velocity and hence the kinetic energy with which the electrons arrive at the sample. A large potential difference is set up between the electron gun and the anode before the column. Fast, high energy electrons are desirable, as this reduces the proximity effect - see Section 2.3.3. Top of the range e-beam writers are capable of generating an accelerating voltage of 100 kV [13]. The machine used in this project was able to produce an accelerating voltage of 30 kV.

Filament current

The filament current (I_{fil}) is the current flowing through the tungsten strip heating the filament (LaB_6 rod in our case). Once the LaB_6 rod is heated above a certain threshold temperature, electrons will escape from it, which constitutes the electron beam. As I_{fil} is ramped up the beam of electrons hitting the sample was clearly seen to pass through

two points of maximum intensity and smallest spot diameter. The first maximum occurred around I_{fil}=1.95 A and the second around 2.20 A. These values increase with the age of the filament. Higher filament current means the filament is hotter. Heating the rod to the second emission maximum results in the highest possible resolution of the electron beam as this gives the minimum spot size. However, operating the filament at that high temperature severely reduces its lifetime. Therefore, the filament was operated near its first emission maximum.

Very small changes in I_{fil} have a large effect on the current density of the electron beam and thus the electron dose at the sample. Therefore, it is imperative that the filament current supply is extremely stable.

Pixel size

Another critical variable is the spacing between exposure points in the pattern. The pattern to be exposed is divided into pixels. The maximum number of pixels available is governed by the capacity of the digital to analogue converter (DAC) on the RAITH e-beam control card. The card installed in the system used here had a 16 bit DAC, which means a pattern can be represented by a maximum of 65536 pixels.

To obtain smooth pattern features the pixel spacing (ps) should be smaller than the size of the focused electron beam on the surface of the sample. Therefore, it is desirable to operate at the maximum pixel spacing for which no decrease in pattern quality is noticeable. A pixel spacing of 15 nm gave as high quality hole patterns as a ps of 6 nm or smaller. Larger pixel spacing allows one to pattern a larger area on the sample at constant magnification.

It must be remembered that for multiple exposures the electron dose at the sample is roughly inversely proportional to the square of the pixel spacing, due to the overlap of the exposure regions. Thus,

$$D \propto \frac{1}{ps^2}$$

where D = electron dose on sample. One of the main problems encountered was that patterns were consistently overexposed. The realization that an increase in the pixel spacing reduces the dose significantly without affecting the pattern quality much, was a great step forward to determining the optimum exposure conditions of the EBL step.

Magnification

The magnification determines the field of view of the electron beam writer. The highest resolution is achieved at the highest magnification, but only over a small area. Large, coarsely resolved areas can be patterned at low magnification. This was one parameter that was never varied. A magnification of $\times 1526$ was always used.

Dwell time

One of the most important parameters in the e-beam lithography process is the dwell time (t_d) of the electron beam. This determines the duration a pixel is exposed to the stream of electrons. Dwell time was the parameter that gave the greatest flexibility and repeatability for varying the electron dose arriving at the sample. This was the key parameter used to choose the electron dose primarily because it could be selected with great precision on the digital signal generator. The filament current also has a great effect on the electron dose, but it was next to impossible to change the dose by small amounts in a reproducible manner and the built-in detection mechanism for the filament current was very crude (± 10 mA).

Probe current

The probe current I_{probe} was varied by altering the bias voltage inside the electron gun unit of the e-beam writer. As the beam current was increased, the current density arriving on the surface of the sample increased, hence the electron dose increased.

With the accelerating voltage, probe current, magnification and pixel spacing fixed a series of patterns was exposed at different electron doses by varying the dwell time from pattern to pattern, typically in the range 0.6-1.4 μs.

2.3.2 Limitations

It had previously been found that the pulse generated by the computer does not have a sufficiently accurate shape. It is a very noisy signal and its accuracy is limited by the CPU's clock speed to $\sim$5 μs. That is why a pulse generator was set up between the computer and the e-beam writer. This produced a perfectly square pulse whenever a rising edge was detected from the computer input. A 50 MHz signal generator was used, which was capable of producing good quality square pulses as short as $\sim$60 ns. The output of the signal generator was monitored on a cathode ray oscilloscope.

The beam-blanking unit consisted of a set of electromagnets that deflected the e-beam over an aperture when a pixel in the pattern was to be left unexposed. The response time of this unit was quoted by the manufacturer as better than 30 ns, but it was found that the minimum pulse duration necessary to produce high quality patterns was >60 ns. For shorter dwell times deformed patterns, such as Fig. 2.14 were obtained. The most likely cause of this phenomenon is that as the dwell time was shorter than the response time of the beam-blanking unit the electron beam was constantly swept to and fro over the beam-blanking aperture. Hence the consistent and repeatable directionality of the hole deformation. The beam never came to rest long enough on a pixel to produce a spatially even exposure.

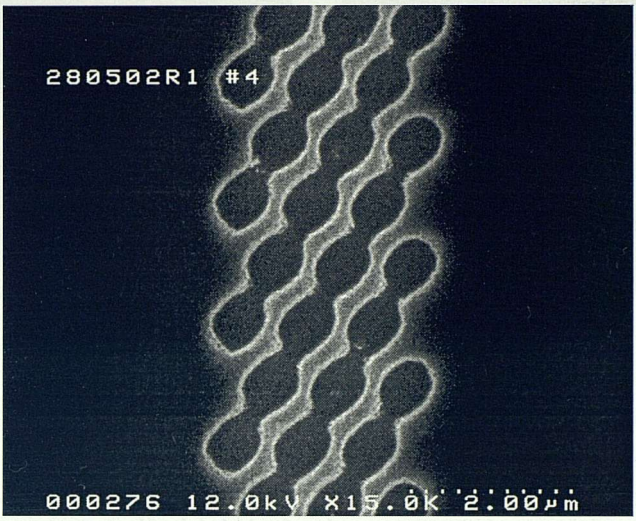
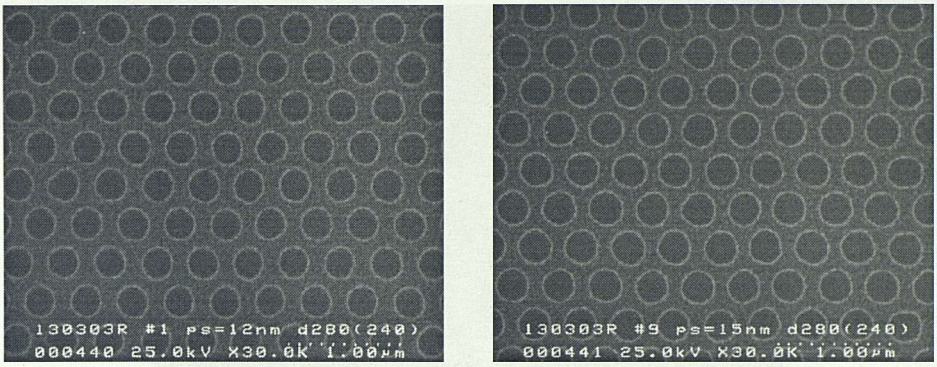


Figure 2.14: Example of a misshaped pattern due to too short dwell time. This is an SEM image of a sample after the exposed pattern was transfered into silica by RIE, described in Section 2.4.1

Finding ways to reduce the electron beam intensity without deteriorating the beam profile or spot size proved to be a challenge. Operating the electron beam at reasonably long dwell times was possible by settling for a modest filament current close to the first (lower) emission peak of the LaB_6 filament, a low probe current of 30 pA, and choosing a large pixel spacing. Initially patterns were written with pixel spacing as small as 3 nm. This was increased to 15nm without any deterioration in pattern quality. Figures 2.15a and b are patterns on the same sample, one written with a pixel spacing of 12 nm and the other with ps = 15 nm. The dwell time was increased from 0.6 μs to 1.0 μs to maintain a similar electron dose. Quite clearly there is no significant difference in quality between the two patterns, but the exposure conditions of the second pattern offer much greater flexibility with dwell time.

Those were found to be the key factors for writing very high quality photonic crystal patterns with ~100 nm features, as the one shown in Fig. 2.16.

The two key parameters of a pattern that are set by the EBL process and which



(a) (b)

Figure 2.15: Effect of pixel spacing (ps) change. SEM image of two patterns on the same sample, showing PhC patterns etched into the silica mask. (a) ps=12 nm, dwell time(t_d)=0.6 μs (b) ps=15 nm, t_d=1.0 μs. Electron dose was approximately constant and pattern quality was equally high in both cases.

affect the photonic crystal's band structure are the lattice constant, a, and the hole diameter, d. Under the correct magnification the lattice constant was always transferred with great accuracy ($\pm$5 nm, due to accuracy of SEM) from the pattern file to the sample. This parameter is largely independent of the electron dose during exposure. The hole diameter, however, was critically dependent on the exposure dose. Too large a dose would overexpose the pattern, even to the point where the entire lattice collapsed. If the electron dose was too small the pattern was underexposed. The tolerance in exposure dose was very small. This made writing PhC patterns with small feature sizes $\sim$50 nm particularly difficult, but these were necessary for large fill factor structures discussed in Chapter 6.

The key problem was that certain parameters of the e-beam lithography process could not be kept constant between exposures of different samples. The focus of the electron beam on the sample was one such parameter. The focus was manually adjusted for each new sample that was loaded. This is a somewhat subjective process, which depended on the particular sample and the operator's personal judgement. Furthermore, the pressure inside the e-beam column and chamber was never exactly the same for different samples. Obtaining the minimum spot size in *Emission Image* mode (see

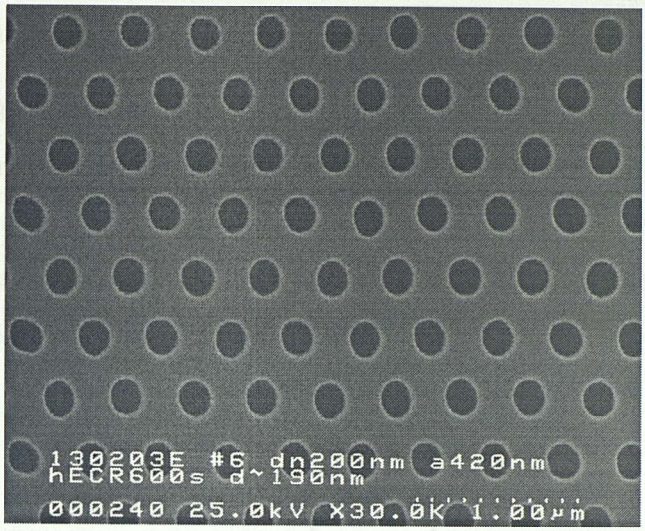


Figure 2.16: Example of a high quality hole pattern. The SEM image shows a pattern of holes with ~190 nm diameters after ECR etching, described in Section 2.4.2

Section 2.3.1) was another subjective process carried out with every new sample. Apart from these there were parameters, such as the probe current and the dwell time, which were set to a precise value. The dwell time was checked for each exposure by feeding the signal produced by the pulse generator into an oscilloscope and it was always found that the output signal matched the desired pulse width with great accuracy. However, there was no direct way of measuring the probe current.

It was found that more flexibility and tolerance in exposure conditions could be obtained by drawing pattern files with exactly the desired lattice constant, but smaller hole diameter than desired. The patterns were then, in essence, overexposed to give the required hole diameter. To produce a pattern with 280 nm diameter holes a pattern file with 240 nm diameter holes would be written. The reason why this works so well is that overexposure is a limited process, meaning exposing a single pixel for an infinite period of time will not expose the entire sample, but a finite radius around the pixel. The exposure effect of an electron beam decays in time for a given pixel, much like the effect of developing PMMA shown in Fig. 2.22. Operating on the shallow gradient part of that curve renders the entire process more tolerant to fluctuations in the electron beam.

2.3.3 Proximity effect

One problem that is ubiquitous in all electron beam lithography apparatus is the proximity effect. As mentioned earlier, electrons incident on the surface of the sample will often pass through the PMMA layer and get backscattered by the underlying SiO_2 layer. These reflected electrons can interact with the PMMA, effectively exposing it further. The situation is depicted in Fig. 2.17.

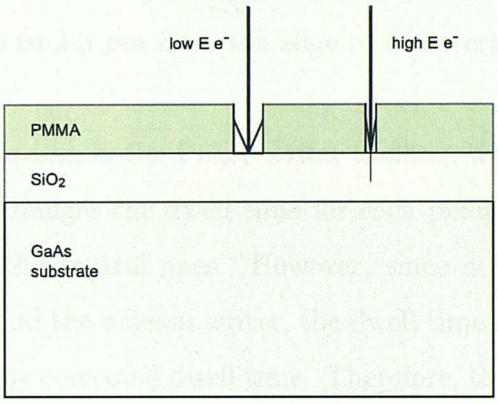


Figure 2.17: Effect of low and high-energy electrons. Low-energy electrons are much more likely to be backscattered off the SiO_2 to expose a larger area than intended. High-energy electrons get buried in the SiO_2 and are less likely to be reflected, resulting in the exposure of a small region.

It is evident from the diagram that the exposed area is actually larger than intended. The angle through which the electrons can be backscattered is a function of their energy, with low-energy electrons being most affected.

Any given pixel to be exposed will experience a contribution of exposing electrons from all neighboring pixels, and even from exposure points several micrometers away. For pixels near the centre of the field this is not a problem, as the entire area will effectively receive a homogenous average electron dose. The problem arises in regions near the edge of the pattern. Taking the extreme case of a pixel on the very last row of a pattern, it is clear that it will only experience a contribution of electrons from one side, as there are no pixels to be exposed beyond the edge of the pattern. Hence,

the average dose received by pixels near the edge will be up to half as much as for pixels near the centre, and even lower for pixels near the corners of the pattern. This was investigated by exposing square patterns of 2×2, 4×4, 6×6, 8×8 and 10×10 μm. Figures 2.18 and 2.19 show the results of this analysis.

Holes near the centre are much larger than near the edges. For the 8×8 and 10×10 μm patterns a central region with holes of equal diameter is visible. Under the given exposure conditions it was found that the proximity effect causes hole size variations in regions up to 2-3 μm from the edge of a pattern.

There is a software option in the Proxy-writer toolbox, which performs a proximity effect correction. This changes the dwell time for each pixel, exposing the pixels near the edges longer than the central ones. However, since a pulse generator was used between the computer and the e-beam writer, the dwell time set on the pulse generator would simply override the corrected dwell time. Therefore, this feature cannot be used.

There are a number of ways to overcome this problem. If a large patterned field is required one only needs to design in a 'buffer zone' of about 3 μm on each edge, in which the holes will not have the desired diameter. For narrow patterns with few periods of holes, the proximity effect does not have as significant an impact, as the 2×2 μm test field showed (Fig. 2.18).

The study of photonic crystals in ridge waveguides discussed in Chapter 5 is the worst case scenario for working without proximity correction. The main part of the work was carried out on 20 rows of PhC's with lattice spacing a=420 nm, giving a pattern length of ~7.27 μm. Figure 2.20 is a typical pattern with these dimensions. The nominal hole diameter is 280 nm, but at the centre d_c=260 nm and on the edge row of the pattern d_e=220 nm, ±5 nm.

Another way to counteract the proximity effect is to manually design patterns,

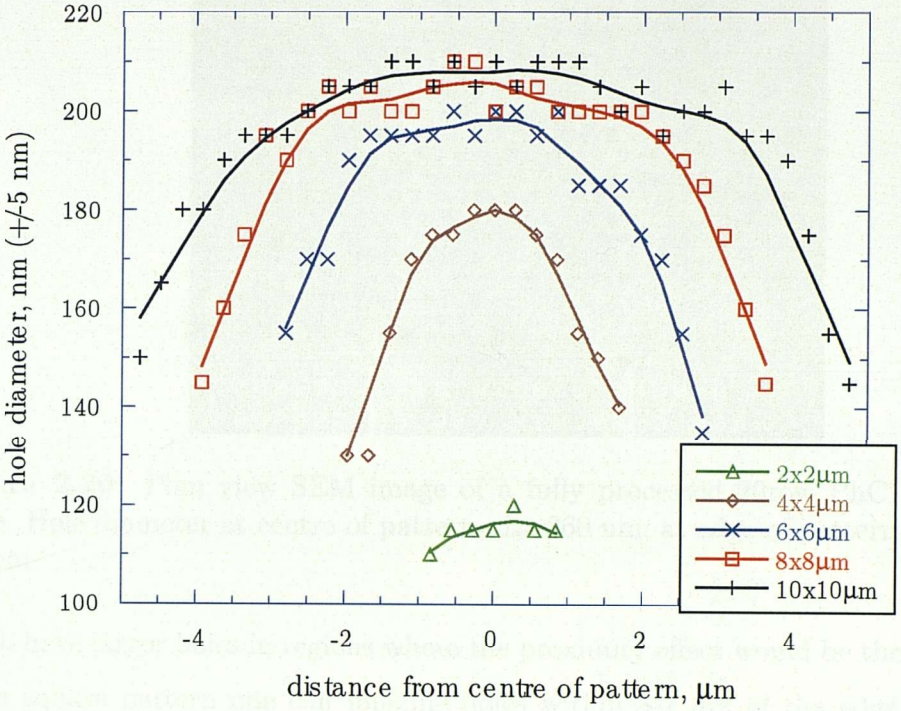


Figure 2.18: Measured hole diameters across various square patterns

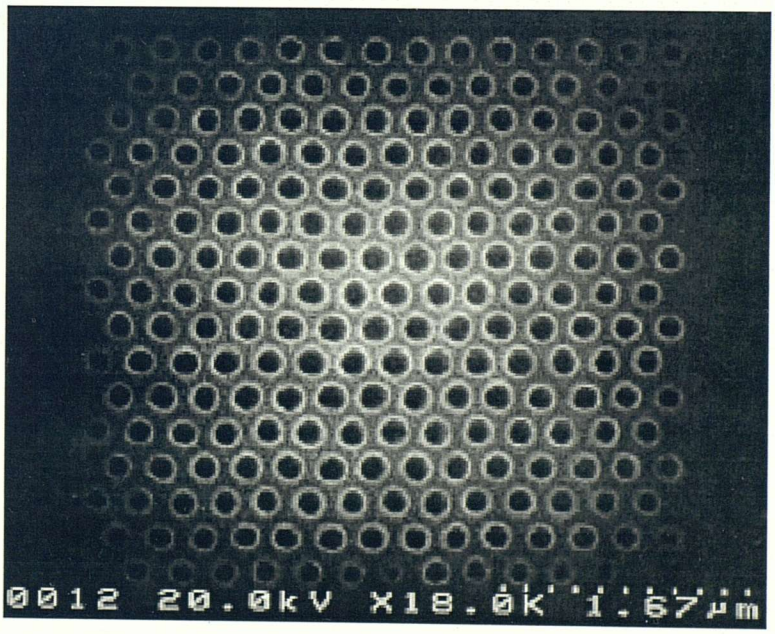


Figure 2.19: SEM showing proximity effect on 4×4 μm pattern

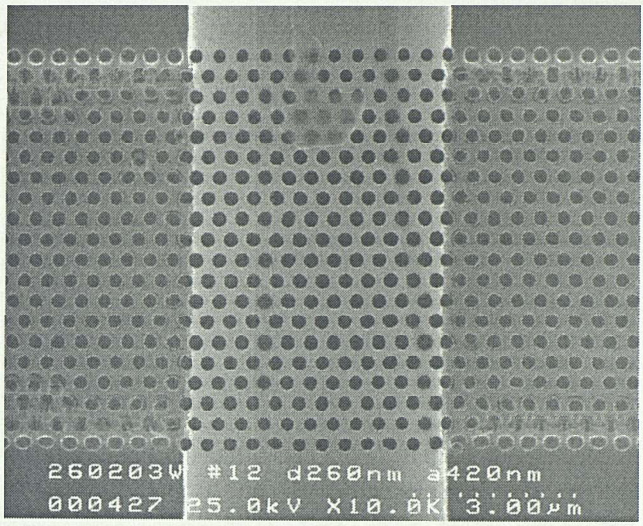


Figure 2.20: Plan view SEM image of a fully processed 20row PhC pattern on a ridge. Hole diameter at centre of pattern, d_c=260 nm, at edge of pattern, d_e=220 nm, ±5 nm.

which have larger holes in regions where the proximity effect would be the most severe. For a square pattern one can imagine holes within ~2 μm of the edge to be larger than ones in the central region by a certain percentage and holes near the corner of the pattern would be even larger. These hole enlargements could be graded gradually to further improve the overall pattern homogeneity. This or any other form of proximity correction was not performed. It is merely noted that there is the possibility for systematic proximity correction without any software aids.

2.3.4 Stitching error

Patterns are exposed by stepping the electron beam from one pixel to the next one down in the same column. When the end of the column is reached the beam is moved right across the pattern while being blanked, to the top of the adjacent column. The success of this method of exposure depends on very high precision in the beam control unit as well as excellent mechanical stability of the whole e-beam unit. Stitching errors can occur when these conditions are not given for the entire duration of the pattern exposure. Figure 2.21 is an example of a failed pattern due to stitching error. It is

noted, though, that this type of error rarely occurred.

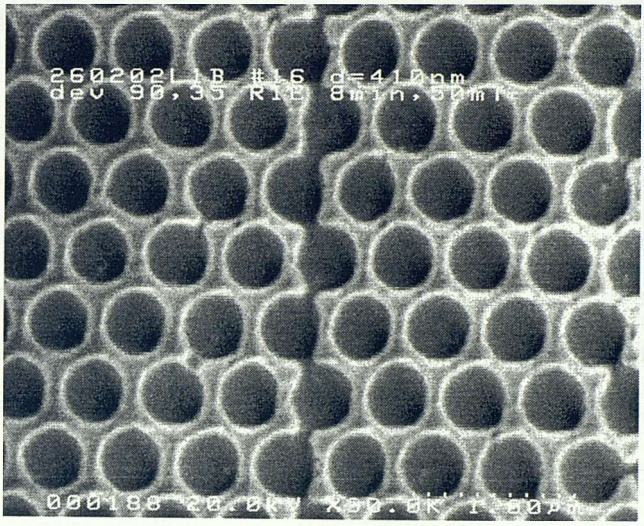


Figure 2.21: SEM image of a pattern with stitching error caused by a slight misalignment of the e-beam during exposure.

There is another type of stitching error, although this was not applicable here. This occurs when an area, larger than the field of view of the electron beam, is patterned. To write such a pattern it is common practice to expose smaller areas, manually move the electron beam a short distance and write another small segment of the overall pattern. Stitching errors between segments are very common and difficult to avoid even with state-of-the-art electron beam writers.

2.3.5 Development and rinse

After exposing the PMMA on the sample to an electron beam the photoresist was developed and rinsed. For a positive photoresist such as PMMA this means that photoresist in the exposed areas is dissolved away. The manufacturer of the chosen PMMA (MicroChem Corp.) recommended using a 1:3 mixture of MIBK (Methyl Iso Butyl Ketone, a solvent often used as silver paint diluent) and IPA (Iso Propyl Alcohol) to achieve the highest pattern resolution. Immersing an e-beam exposed sample in this

mixture for up to 3 minutes produced no change at all in the PMMA. Neat MIBK, however, worked very well for developing exposed patterns. This development step was followed by rinsing the sample in the MIBK:IPA [1:3] mixture.

Initially samples were developed in MIBK for 35 s and rinsed in MIBK:IPA[1:3] for 30 s. This produced high resolution patterns with appropriate e-beam exposures, but not with the desired reproducibility. It was decided to extend the development time to 60 s without changing the rinse time. After calibrating the e-beam exposure conditions it was found that this increased development time produced high quality patterns with excellent repeatability. Figure 2.22 is believed to represent the characteristics of the development step.

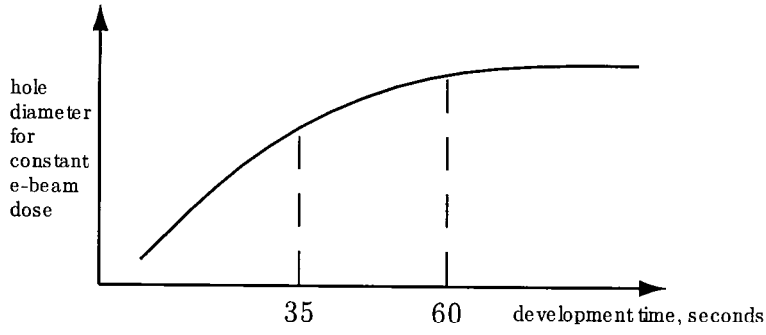


Figure 2.22: Characteristics of PMMA development. This is one possible relationship between hole diameter and development time of PMMA in MIBK after electron beam exposure.

With a development time of 35 seconds one probably operates on a steep gradient part of the development curve, where small variations in development time have a relatively large effect on developed area. At 60 s the resulting hole diameter seems to be much more tolerant to small fluctuations in development time, suggesting that the curve has levelled off. A thorough study of this processing step can certainly yield further improvements in pattern quality and process repeatability.

2.4 Dry etching

Etch technology can generally be divided into wet and dry etching. Wet etching typically involves immersing the sample in a liquid oxidising agent and dissolving the oxides formed at the sample's surface. It is a purely chemical process and etching occurs primarily along crystal planes, resulting in very smooth surfaces. Dry etching typically makes use of a plasma to etch the surface. There are chemical as well as physical etch components that contribute to the etch. Vertical or anisotropic etch profiles are typically obtained [4], but the etched surfaces are usually rougher than ones obtained by wet etching. Good control over etch depths can be achieved with both techniques.

Dry etching technology is required to achieve structures with micron and sub-micron scale features. Micro Electro Mechanical Systems (MEMS) have recently generated much interest. For example, at Robert Bosch GmbH in Germany 50 million MEMS are produced each year for the automotive industry [14]. Figure 2.23 is an example of the high quality deep etches routinely achieved at Bosch. Chips for the biomedical-MEMS market are also made in large volumes. The only way of producing these devices with extremely low manufacturing tolerances in large volumes is to employ dry etching techniques.

The following Sections describe two types of plasma etches that were used in making two dimensional photonic crystal structures.

2.4.1 Reactive Ion Etching

A reactive ion etch RIE reactor consists of a sealed chamber into which the etch sample is loaded. Gases are pumped into the chamber at precisely controlled flow rates and a plasma is formed by an alternating current (ac) discharge.

RIE is a type of plasma etch, in which the physical and chemical aspects are signifi-

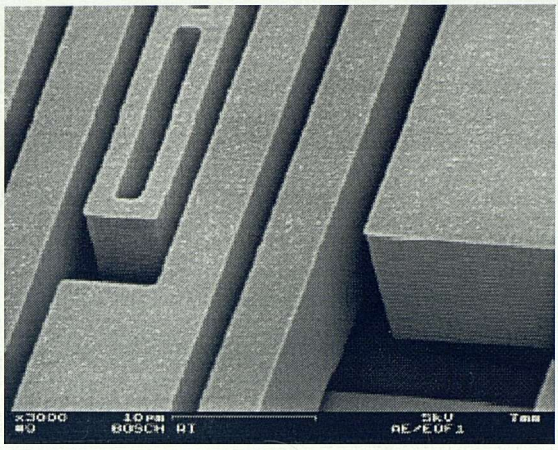


Figure 2.23: Example of state-of-the-art etch results, courtesy of Robert Bosch GmbH, Germany. Shown is a structure etched in silicon using deep reactive ion etching (DRIE). This component forms part of an acceleration sensing element. Picture taken from Ref. [14].

cant. Reactive radicals from the plasma combine with surface atoms on the sample and these newly formed compounds are removed from the sample. The surface chemistry involved is extremely complicated and much work is in progress in that field, see for example Ref. [15].

The reactor effectively consists of two parallel plates connected to an ac generator running at a fixed radio frequency (RF). An electric field is set up between the plates. The sample rests on the cathode onto which ions from the plasma are accelerated. A small number of atoms on the sample's surface are sputtered away by this ion bombardment. The primary factors that control the etch conditions are the ion species, gas flow rate, chamber pressure and RF power.

A mask is provided by the patterned PMMA. The next task is to transfer this pattern into the underlying silica layer. A number of studies were undertaken to find the optimum etch conditions. First, the chamber bias voltage (V_{ch}) was investigated. Four identical patterns were exposed by EBL on a sample. The sample was developed as outlined in Section 2.3.5 and cleaved (see Section 2.5.6) into four pieces. These

four identical[3] samples were etched in the RIE reactor under different chamber bias voltages. Upon inspection in the SEM it was determined that $V_{ch} = 330 \pm 5$ V provides the best pattern transfer into silica. The key criteria used to make this judgement were trueness of dimensions compared to the nominal pattern, smoothness of features and general surface damage.

The chamber pressure (P_{ch}) is regulated by adjusting the position of a throttle valve above the extraction pump. P_{ch} was set to 50 mT.

Table 2.2 is a summary of the etch conditions used to transfer the EBL-written pattern from PMMA into the underlying silica.

Gas	CF_4	H_2
Flow rate, sccm	32	10
P_{ch}, mT	50	
V_{ch}, V	330	
RF power, W	150	
Time, min	8	

Table 2.2: Summary of RIE conditions for transferring PhC pattern from PMMA mask into 260 nm thick SiO_2

The only remaining etch parameter that needed to be determined was the etch duration. This depends on the etch rate of the process under the set conditions. Once the etch rate was determined and the thickness of the silica layer was known, the etch duration can easily be determined. A sample was prepared with five sets of three PhC patterns exposed in PMMA by EBL as shown in Fig. 2.24.

The three patterns in each set were exposed to different doses of electron to give a range of hole diameters. The aim of this study was to monitor the evolution of etch depth into silica. The sample was etched for two minutes, cleaved through one set of patterns and the hole profile was analysed in an SEM. The rest of the sample was

[3]limited by the reproducibility of the electron beam lithography step

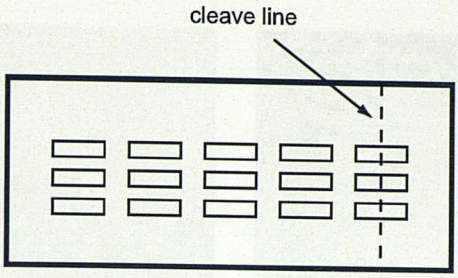


Figure 2.24: A diagramatic representation of the pattern arrangement on a sample used to determine the etch rate in silica using RIE.

etch for another two minutes, etc. Figures 2.26 - 2.31 are scanning electron microscope images of the various stages of the study. The samples were always coated with gold prior to imaging the profiles in the SEM. The information gathered from Figs. 2.26 - 2.29 was plotted in Fig. 2.25. Note that measurements of the hole depths were limited by the resolution limit and image stability of the SEM and can be assumed to be ± 5 nm. Also, the difference between the hole diameters in the PMMA mask and the silica layer was found to be negligible, i.e. mask erosion was not found to be a problem.

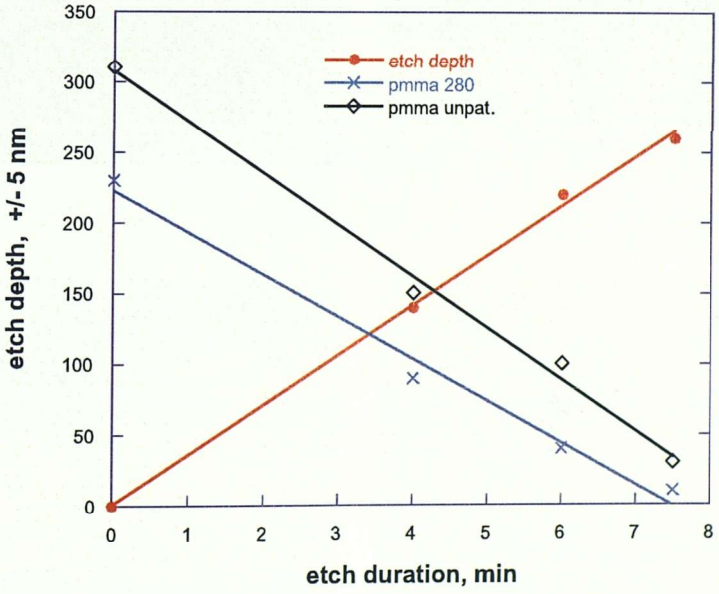


Figure 2.25: Etch rate determination of fluorine-based RIE in silica. Change in etch depth with time is plotted. "pmma 280" is the thickness of PMMA on patterns with 280 nm hole diameters.



Figure 2.26: After EBL, pre SiO_2 etch

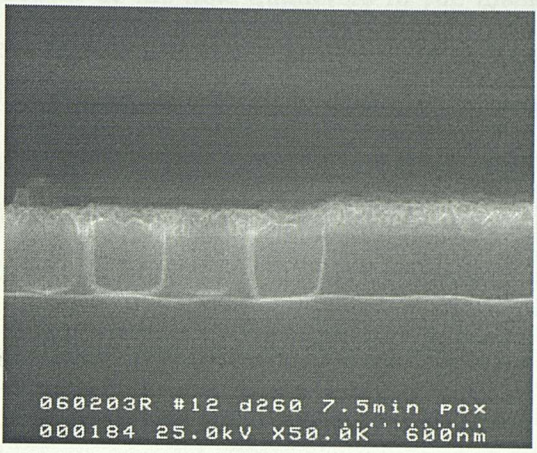


Figure 2.29: After 7.5 min of SiO_2 etch

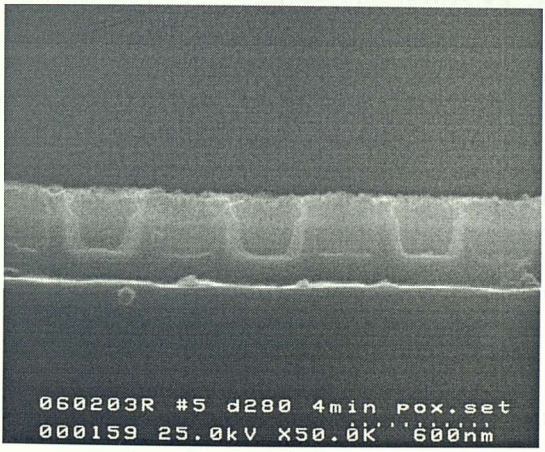


Figure 2.27: After 4 min of SiO_2 etch

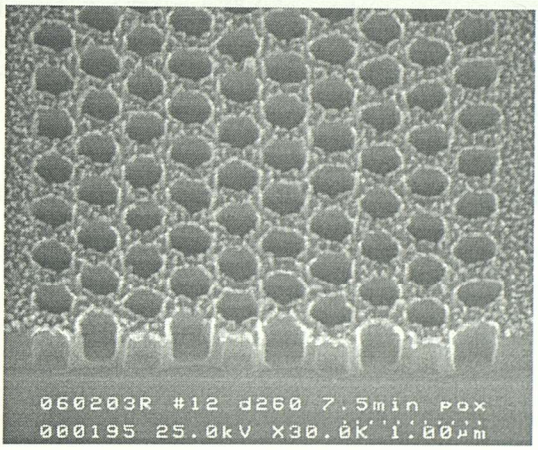


Figure 2.30: Same sample as in Fig. 2.29

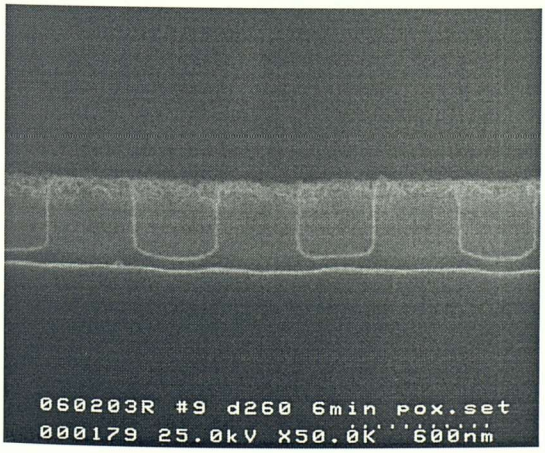


Figure 2.28: After 6 min of SiO_2 etch

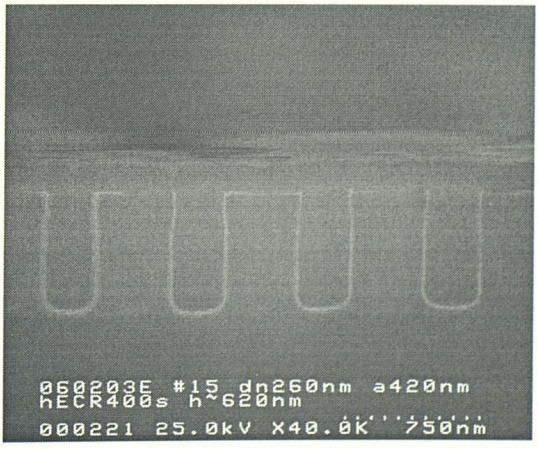


Figure 2.31: After 400 s ECR etch

Hole etch rates were found to be independent of the hole diameters in the mask. This was unexpected. For smaller diameters (<100 nm) this relationship is not expected to hold. Judging by numerous SEM images of pattern cross sections the most important criterion for achieving good pattern transfer from the PMMA mask to silica is the quality of the PMMA mask. The silica etch rate for patterns with such dimensions and all other information extracted from Figs. 2.26 - 2.25 is summarized in Table 2.3.

initial PMMA thickness, nm	310±5
initial SiO_2 layer thickness, nm	260±5
sputtering rate of PMMA, nm/min	30±1
etch rate of SiO_2(d=300 nm), nm/min	35±1

Table 2.3: RIE characteristics for SiO_2 under PMMA etch

Therefore, for hole patterns with diameter = 280 nm to be transferred from a perfect PMMA pattern into 260 nm of silica with fluorine-based RIE, samples need to be etched for at least 7.5 min.

What is apparent from the above pictures and highlighted in Fig. 2.32 is that the surface of the PMMA is made very rough by the reactive ion etch of silica. The polymer chains that constitute the PMMA are an inhomogeneous medium and this results in very uneven surface morphology during RIE.

The thicknesses of layers PMMA plotted in Fig. 2.25 are a measure of the minimum PMMA thickness. The thickness of the PMMA film also varies across the hole pattern. Perforating the PMMA film weakens it. As there is always a non-zero lateral etch component, the exposed sidewalls of holes in the PMMA layer are attacked. Larger holes have more inner wall surface area than smaller holes, hence a larger area for attack by ion bombardment. The proximity effect discussed in Section 2.3.3 results in holes away from the pattern edge to be larger than ones near the edge. That effect is exacerbated during the reactive ion etch of silica. Figure 2.33 is a clear example of the PMMA in

central pattern regions being worn away more quickly than the pattern edges and the unpatterned regions.

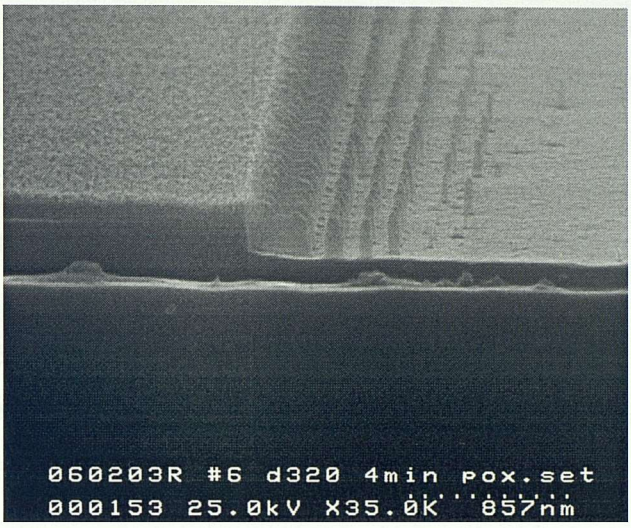


Figure 2.32: Rough PMMA caused by RIE. The PhC pattern on the right hand side of the picture is totally overexposed.

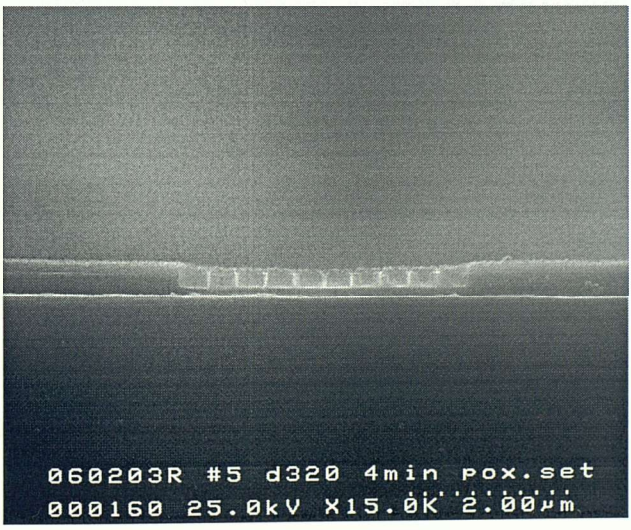


Figure 2.33: Variation of PMMA across a PhC pattern after 4 minutes of RIE. At the centre of the pattern all the PMMA is sputtered away.

This variation of PMMA thickness across a patterned region is less pronounced for smaller fill factor patterns. The effect was found to be negligible for patterns with hole diameters less than ~220 nm.

The surface of the PMMA was found to become very rough and uneven during the reactive ion etch. If the etch progresses for too long, the roughness of the PMMA is transferred to the underlying silica layer. This was found to be the root cause of the surface roughness ("grass") of the fully processed samples, as discussed in Section 2.5.1. For future work we suggest using a thicker PMMA layer. This would then require a change in the EBL conditions as a thicker layer of polymer chains would have to be broken by the electron beam in order to fully expose the PMMA.

It is essential to clean the remaining PMMA off the sample. It was found that placing the sample in acetone in an ultrasonic bath for 3 min, rinsing with methanol and deionised water and drying with nitrogen cleaned the sample sufficiently.

2.4.2 Electron cyclotron resonance etching

Electron Cyclotron Resonance (ECR) etching is a sophisticated dry etching technique. As in RIE, a plasma is formed by the application of an RF source. In ECR, resonance between electrons in a static magnetic field (electromagnetic solenoid coils around the ECR chamber) and a time-varying electric field (produced by a microwave source) allows efficient energy transfer to the plasma, resulting in much higher ion densities than with RIE. Because of that, the ECR process can be run at a lower DC bias voltage than RIE, which reduces damage to the sample. Some of the advantages of ECR over other techniques are:

- low surface damage
- high plasma density
- reduced chamber pressure
- better anisotropic nature

One of the disadvantages of ECR plasma etching is the relative difficulty with which the microwave source is tuned to the magnetic field. This tuning is done manually and requires optimisation for different plasmas. This is one of the strengths of the competing technology - ICP (Inductively Coupled Plasma). Another disadvantage of the particular ECR apparatus used is the relatively slow turnaround time. The actual etch typically takes less than 10 min for GaAs/AlGaAs structures, but the process requires a high vacuum ($<1\times10^{-8}$ T) , which is only achieved by long pump-down times of the order of hours. The ECR etch conditions used to transfer the photonic crystal patterns from the silica mask into the (Al,Ga)As structure are given in Table 2.4.

Gas	$SiCl_4$
Flow rate, sccm	20
P_{ch}, mT	0.1
V_{ch}, V	103
RF power, W	127
Microwave power, W	250
Time, min	~13

Table 2.4: Summary of typical ECR conditions for PhC pattern etch.

Etch depth vs. hole diameter

In order to calibrate the ECR plasma reactor for the hole pattern etch, the influence of the hole diameter on the maximum etch depth was investigated. It is obvious that for a given etch duration and at constant etch conditions the maximum achievable etch depth increases with hole diameter. The wider the opening, the faster the physical and chemical etch components can remove material under the mask.

A series of triangular lattice patterns with lattice constant, a=420 nm, and a range of diameters (200-320 nm) was exposed onto PMMA using electron beam lithography, as described in Section 2.3. The electron dose was varied considerably during the exposures, to give a large range of hole diameters. Once exposed the patterns were

transferred into the underlying silica by reactive ion etching; see Section 2.4.1. The samples were then etched for different lengths of time in a Plasmaquest ECR reactor. After cleaving through the patterns, mounting one of the cleave products edge-on on an SEM stub, the cross section of the etched hole pattern was analysed in an SEM, as described in Section 2.1.2. Figure 2.34 shows a typical hole profile.

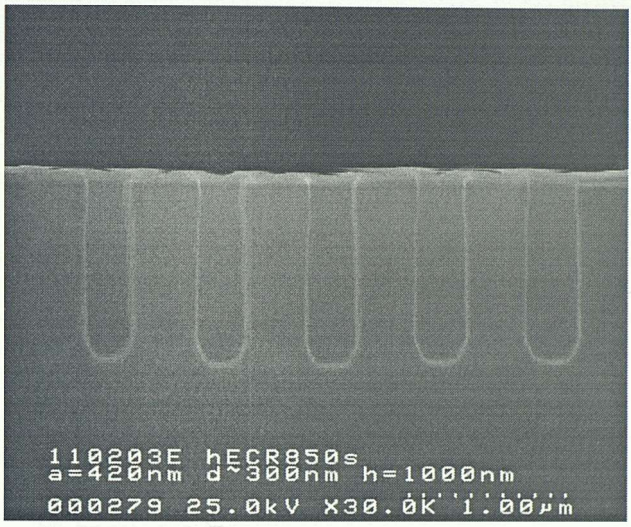


Figure 2.34: SEM image showing etch profile of 300 nm diameter hole after 850 s of ECR etching. Etch depth ~1.0 μm.

What is apparent is that although the sidewalls are reasonably vertical and the etch is anisotropic, the top of the hole is somewhat narrower than the bottom. All samples used in this investigation came from the same wafer, which consisted of a planar waveguide as shown in Table 2.5.

Thickness	Material	Purpose
5 nm	GaAs(i)	cap
300 nm	$Al_{0.6}Ga_{0.4}As$(i)	upper cladding
600 nm	GaAs(i)	waveguide core
3 μm	$Al_{0.6}Ga_{0.4}As$(i)	lower cladding
~400 μm	GaAs(i)	substrate

Table 2.5: Wafer composition

The widening of the holes as the etch progresses into the semiconductor is related

to the composition of the epilayers. In the AlGaAs region the etch is slightly slower than in the GaAs region. It is believed that the lateral etch component has therefore more time to act on the sidewalls. Once in the GaAs layer, the etch is nearly vertical. Therefore, in most cases the diameter of the holes is larger at the bottom than at the top. The narrower top is clearly the limiting factor to the etch rate. Hence the dependence of the etch depth on the *top* hole diameter was analysed.

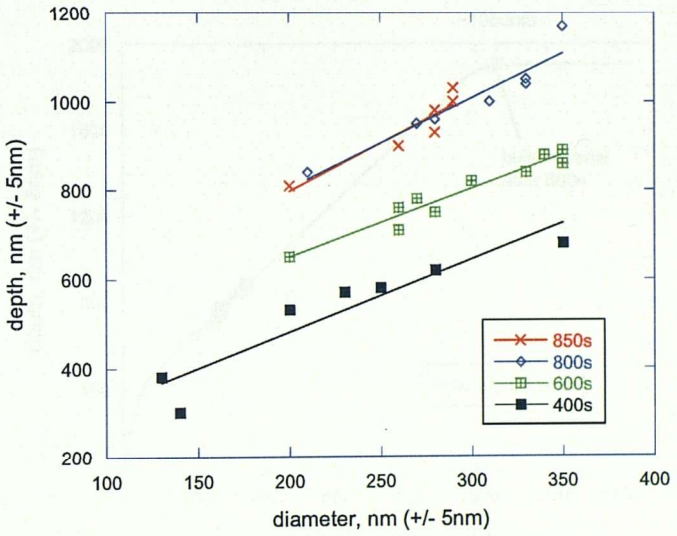


Figure 2.35: Hole depth as a function of hole-top diameter

Shown in Fig. 2.35 is a plot of hole depth vs. top hole diameter. Four different sets of data corresponding to different etch times are shown. A linear fit was applied to the data sets. There does seem to be a linear relationship between hole etch depth h and hole diameter d, given by

$$h = md + c \tag{2.3}$$

where m is the slope and c is the line's y-intercept. Smaller holes are not etched as deep as larger holes, under constant etch conditions. This relationship breaks down in the extreme cases of very small and very large holes. The y-intercept of all shown data sets is greater than zero, which is nonsensical. Also, as the hole diameter becomes very large (>500 μm) the etch rate is given by that of bulk $Al_{0.6}Ga_{0.4}As/GaAs$. This is a constant, found to be $\sim$75$\pm$1 nm/min for $\sim$280 nm diameter patterns under typical

process conditions. The etch rate for bulk material was found to be 185±1 nm/min. Beyond a certain hole diameter the etch rate does not increase with diameter. To determine this diameter beyond which the etch behaviour is like that of bulk material, one curve from Fig. 2.35 was extrapolated to the etch depth of bulk material. Figure 2.36 schematically depicts the obtained etch depth-hole diameter relationship. The behaviour at the low-diameter end of the curve is estimated.

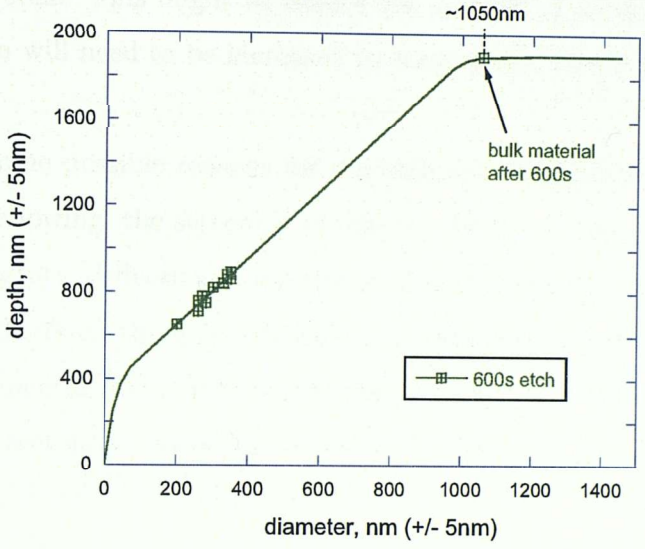


Figure 2.36: Diagram of estimated etch depth - hole diameter function for ECR etches of GaAs/AlGaAs.

The from Fig. 2.36 it was found that beyond hole diameter $d \geq 1050$ nm the etch behaviour is expected to resemble that of bulk material. This was verified by examining the other curves in Fig. 2.35. The dimensions of patterns in the work presented here are significantly smaller than 1000 nm, so the etch rate must be treated as a function of hole diameter.

For the hole diameter that was aimed for, d=280 nm, the deepest holes that were successfully etched were $\sim$1.06 μm deep. Less than 30 nm of the silica mask was remaining on the record pattern at the end of the ECR etch. The walls of the holes were always of very smooth. It is believed that the ECR etch process was not pushed

to its absolute limit. Hole depths of about 1.5 μm ought to be possible with an optimised process recipe while maintaining the same silica mask thickness. D'Urso *et al* [16] reported etches up to 2 μm in AlGaAs using RIE. Their hole sidewalls were of poor quality, but the etch depth is impressive nonetheless. This is encouraging and indicates that with an ECR-generated plasma, which is superior to conventional RIE in many ways, we ought to be able to achieve greater etch depths than we currently are by optimising the etch conditions. For future work we suggest reducing the RF power during the ECR etch. This ought to reduce the sputtering away of the silica mask. The etch duration will need to be increased to compensate for the reduced etch rate.

In Ref. [17] some possible reasons for the etch rate dependence on hole diameter are given. Ion shadowing, the screening of ions by the mask edge, is one such reason. Another is electrostatic deflection of ion species due to charging of the mask. Redeposition of etch products on the hole sidewalls is yet another possible factor that would have a more detrimental effect on the etch rate for small diameter holes than for large ones. All of these factors are likely to be present in the work here presented.

Large fill factor etches

The difficulties in writing masks for large fill factor patterns were outlined in Section 2.3.2. Once a pattern was successfully created in silica the next challenge was the transfer into GaAs/AlGaAs using an ECR plasma. Extremely small feature sizes can be generated. The walls between neighboring holes can be as narrow as tens of nanometers.

The primary difficulty was the verticality of hole sidewalls. The lateral etch component must be as close to zero as possible. A common problem of etching AlGaAs structures is that holes tend to become wider the longer the etch progresses. This is quite different to the 'carrot-shaped' hole profiles typically obtained in dry-etching InP structures; see Fig. 2.37.

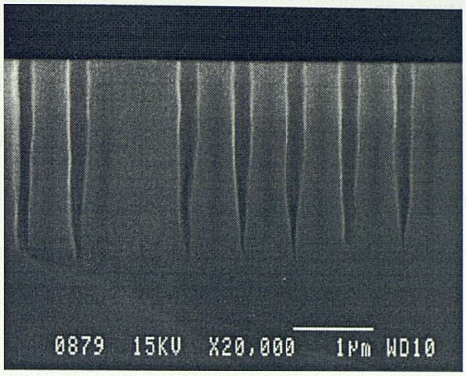


Figure 2.37: SEM image of a typical hole profile in InP taken from Ref. [18].

The best large fill factor hole cross section that was produced is shown in Fig. 2.38. It shows a series of near-vertical holes, diameter = 380 nm, depth = 700 nm. The smallest feature size obtained is 30 nm and corresponds to the wall thickness at the bottom two adjacent holes.

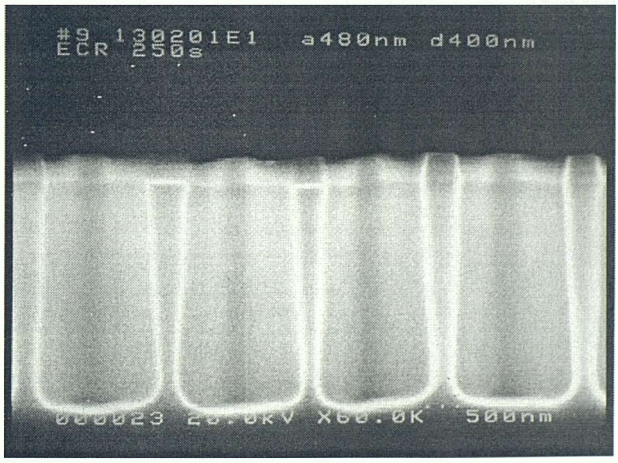


Figure 2.38: SEM image of large fill factor PhC cross section. Silica can be seen on top of the pattern.

A longer etch would have resulted in the overlap of holes, as was found in the test sample shown in Fig. 2.39, which was tilted 20 degrees. This can lead to the total collapse of the photonic crystal lattice. Figure 2.40 is a further illustration of the overlap problem due to non-vertical hole sidewalls. The proximity effect discussed in Section 2.3.3 played a part in that pattern and exacerbated the problem.

Figures 2.39 and 2.40 also show clearly that merely looking at a processed PhC pattern in plan view can be misleading. Tilting the sample in the SEM can often reveal hole overlap below the surface. However, the only reliable way to determine the quality and profile of a pattern is to destroy the sample by cleaving through the PhC pattern and looking at it edge on in an SEM.

Ridge etch

Following ridge lithography described in Section 2.5 the sample was dry-etched in an ECR-generated plasma. Silicon-tetrachloride was used as the input gas in the ECR reactor, as in the hole-etch process. The condition for the ridge etch were slightly different to those of the hole etch. Typical etch conditions are given in Table 2.6. The other difference compared with the hole etch was that the etch depth could be monitored in real time as the etch progressed.

Gas	$SiCl_4$
Flow rate, sccm	20
P_{ch}, mT	0.4
V_{ch}, V	46
RF power, W	43.4
Microwave power, W	250
Time, min	$\sim$2

Table 2.6: Summary of ECR conditions for ridge etches.

Figure 2.41 is an SEM image of a cleaved sample with a ridge etched. The epilayers of the waveguide are clearly seen, as well as a smooth front facet.

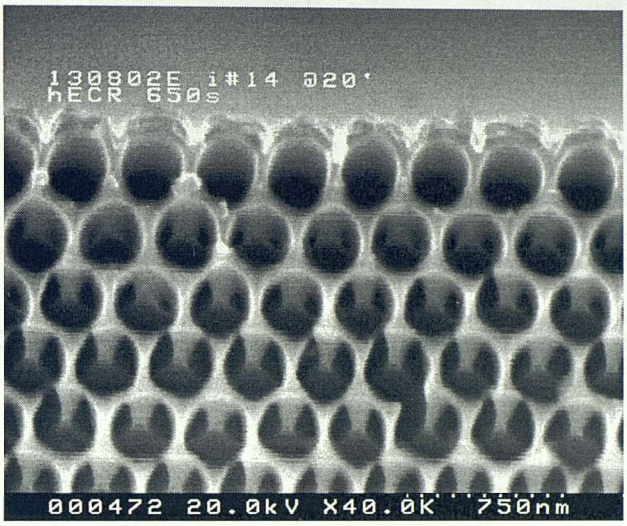


Figure 2.39: An SEM image of large fill factor PhC sample tilted 20 degrees. Hole overlap below the surface is clearly visible.

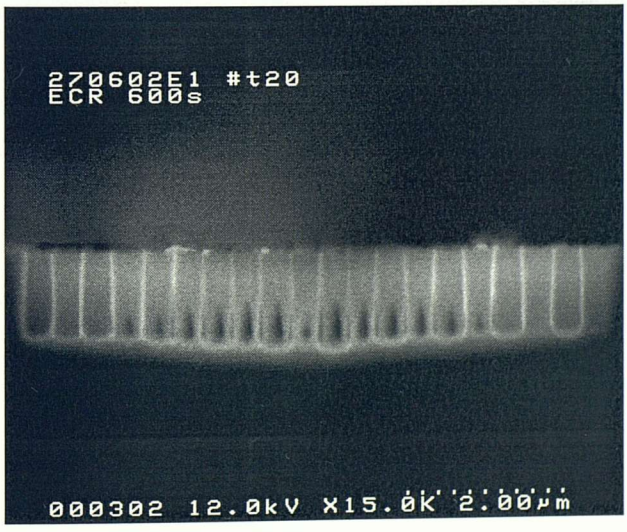


Figure 2.40: Cross section of a large fill factor PhC pattern. The holes overlap below the surface near the centre of the pattern due to the proximity effect.

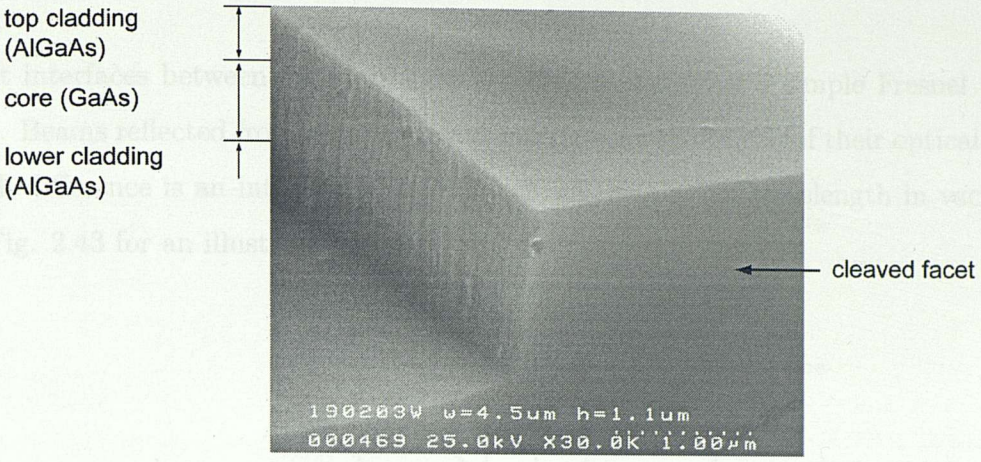


Figure 2.41: SEM image of a ridge showing epilayers.

L.E.P.D

Laser end-point detection (LEPD) is a standard technique used for in situ monitoring of dry etching processes [19]. A laser is reflected off the surface of the etch sample, as shown in Fig. 2.42.

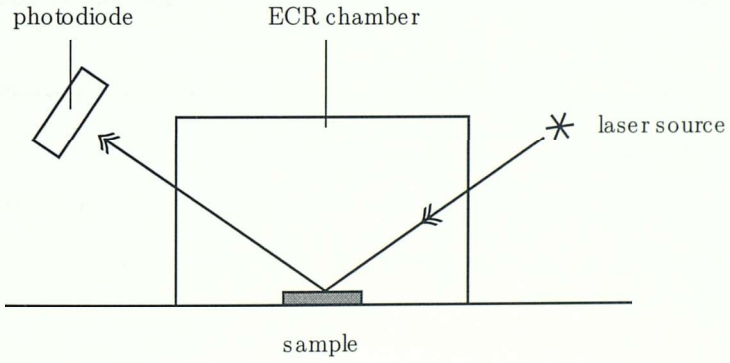


Figure 2.42: Basic L.E.P.D. set-up.

In the case of most GaAs/AlGaAs structures a simple red laser diode can be used, depending on the AlGaAs composition. GaAs strongly absorbs photons with wavelengths below ~800 nm. $Al_{0.6}Ga_{0.4}As$ was used in the planar waveguide structure of our samples. This has a bandgap energy of 2.198 eV [20], which corresponds to a wavelength of ~565 nm in vacuum. Light from a red laser is strongly reflected by the AlGaAs layers and absorbed by the GaAs waveguide core and substrate.

At interfaces between epilayers light is reflected, following a simple Fresnel argument. Beams reflected from different layers interfere constructively if their optical path length difference is an integer multiple of $\lambda/2$, where λ is the wavelength in vacuum. See Fig. 2.43 for an illustration.

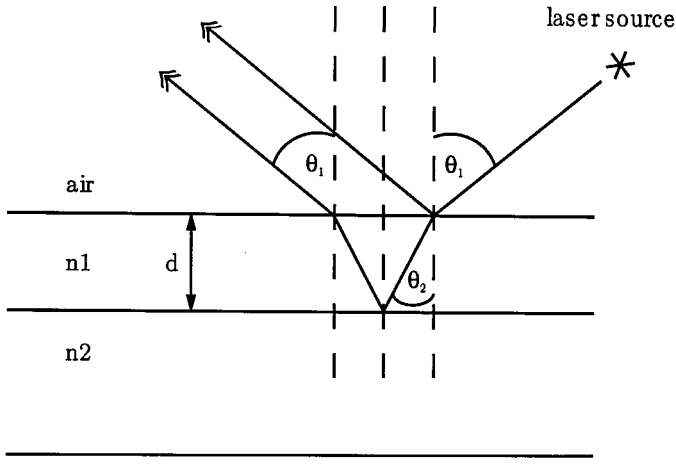


Figure 2.43: Reflections at adjacent layer interfaces form the basis of LEPD.

As the thickness of the top layer is gradually reduced during the etch, the reflected light experiences conditions of constructive and destructive interference. These were recorded on a chart recorder via a photodiode connected to a power meter. This set-up was used to monitor the etch depth during ridge etches. A typical trace for a deep ridge etch is shown in Fig. 2.44.

The Fabry-Pérot equation,

$$m\lambda = 2nd\cos\theta_i \tag{2.4}$$

was used to calculate the material thickness that corresponds to one cycle on the recorded chart. m=integer, n=refractive index, d=distance, θ_i=angle i as in Fig. 2.43. Using Snell's law θ_2 was calculated. Rearranging Eqn. 2.4 for d, using the appropriate value for n and inserting the calculated value of θ_2 gives the results shown in Table 2.7.

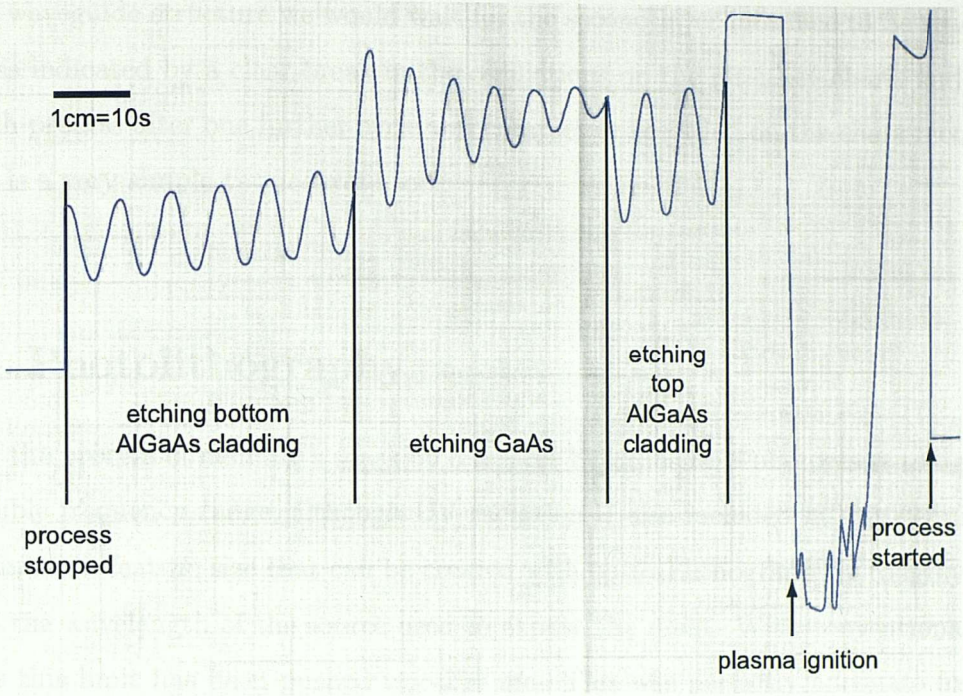


Figure 2.44: Trace obtained by LEPD during ECR etching of ridges.

Thickness corresponding to one oscillation in LEPD	
$Al_{0.6}Ga_{0.4}As$	107 nm
GaAs	95 nm

Table 2.7: Calibration of LEPD chart

The thickness of the first AlGaAs layer (upper cladding) was known to be 300 nm and as expected from the above calculation less than 3 complete cycles were recorded during the etch of that layer. GaAs strongly absorbs the red light emitted by the laser, but as the layer decreases in thickness the amplitude of the recorded signal was seen to increase and the expected oscillations on the chart recorder became more pronounced. Just over 6 cycles were visible in the GaAs region, as expected from theory. These two experimental confirmations of the calculated etch distance strengthened the case for using LEPD to monitor and control the etch depth during the ridge etch process.

The calibrated cycle lengths of the chart recorder traces allowed us to determine exactly when to stop the ECR etch to achieve the desired etch depth. For instance, to produce 1.0 μm high ridges in the usual 300-600-3000 nm AlGaAs-GaAs-AlGaAs

planar waveguide structure we would wait for the second layer interface to be reached, which is indicated by a clear break in the oscillations on the intensity chart, and stop the etch process after one further cycle was completely recorded on the chart recorder. LEPD is a very simple yet accurate tool.

2.5 Photolithography

This is the process of defining a mask on a sample by exposing a photoresist to light in the visible frequency range, although UV radiation is also included in this definition. The minimum feature size that can be created with optical lithography is roughly limited to the wavelength of the source used to expose the resist. With conventional UV sources this limit has been pushed to ~250 nm. This was perfectly adequate for our purpose of defining ridge waveguides.

Photolithography is a series of processing steps, which are described in the following Sections.

2.5.1 Lithography preparation

In the last processing step photonic crystal patterns were transferred from a silica mask into the underlying semiconductor epilayers. Before performing the next processing step in line, ridge lithography, it was found to be absolutely imperative to clean the surface of the sample thoroughly. Most important of all, the remains of the silica mask left over from the hole etch process must be removed completely. When this was not done, then a) the etch did not progress as intended because of the silica layer covering the surface unevenly. It was impossible to monitor the etch depth of the ridges accurately and this would vary somewhat across the sample b) "grass" was found all over the surface of the sample. Figure 2.45 is a high magnification SEM image of a grassy surface.

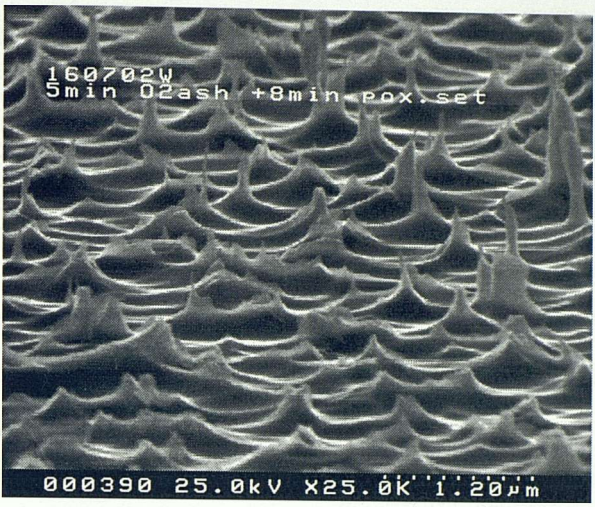


Figure 2.45: High magnification SEM image of improperly processed surface, clearly showing "grass".

The origins of the grass were determined to be as follows: Dry etching silica in a reactive ion etch with a PMMA mask can transfer the very granular nature of the photoresist into the surface of silica. During the ECR hole etch the silica mask is sputtered away, depending on how long the etch is carried out for. If the silica mask remnants are not removed before the ridge lithography step, then the rough silica mask morphology is transferred into the GaAs/AlGaAs epilayers. Running a sufficiently long fluorine-based RIE process cleans up the surface of the sample.

2.5.2 Photoresist

Optical lithography makes use of a prefabricated mask to transfer the pattern of the mask to the photoresist. Two positive photoresists, S1813 and S1818, were investigated. These are standard resists and are commercially available. S1818 is the thicker, more viscous of the two resists. Very similar results were obtained with both resists.

2.5.3 Application

Prior to spinning on the photoresist the sample was coated with hexamethyldisilazane (chemical formula: $C_6H_{19}NSi_2$), and spun for ~5 seconds. This acts as an adhesion promoter. The photoresist was applied to the cleaned, dried sample by spin coating. As the sample was spun at 4000 rpm the centrifugal force pushed the photoresist to the sample's edge. This inevitable build up of resist, especially in the corners of the sample, is known as *beading*. This was found to be more pronounced with the S1818, as it is more viscous that S1813. Following 40 s of spinning the sample was pre-baked on a hotplate at 109°C for 60 s.

2.5.4 Mask, Exposure and Development

Unlike electron beam lithography (see Section 2.3) or ion beam lithography, where the patterns are written directly into the photoresist, optical lithography requires a mask to transfer the pattern to the photoresist on the wafer. These masks are usually created by electron beam lithography as they need to be very accurate. The waveguide mask consisted of a glass plate with chrome strips on it. These chrome strips had the dimensions of the waveguides to be etched into the wafer. Theoretically a mask can be used for an infinite number of exposures, but realistically the mask lifetime is limited to hundreds of exposures.

The resist-coated sample was placed on a mask aligner (Karl Suss MJB3) and the waveguide patterns of the mask are laid over the photonic crystal patterns. It was with this alignment in mind that the PhC patterns were designed to be 50 μm wide, as this leaves sufficient room to find a mask position for which the waveguides overlap the majority of PhC patterns. The PhC patterns were never all perfectly in line due to inaccuracies in the stage control of the e-beam writer.

Once in place, the sample was brought in hard contact with the mask. Beading,

which occurred during spin-coating prevented perfect contact between the resist and the mask. This could result in a shadowing effect, which would explain why the exposed ridges were ususally slightly wider than their nominal width (~5.0 μm vs. 4.5 μm on mask). Figure 2.46 is an illustration of the beading effect. Beading was expected to be somewhat less strong with S1813 as this is the less viscous of the two photoresists. No noticeable difference was found though between S1813 and S1818.

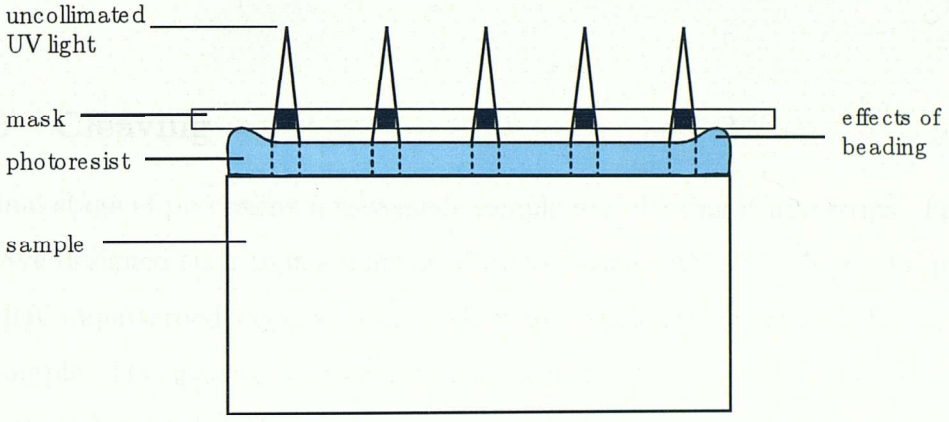


Figure 2.46: Beading prevents contact between mask and most of photoresist layer. This results in incorrect translation of mask pattern to photoresist.

The mask and sample were flooded with UV light for 2.8 s. The areas protected by the strip mask received the same pattern as the mask, because a positive resist was used. Following the exposure the sample was post-baked on a hotplate at 115°C for 10 min.

As a final step of the photolithography the resist was developed. This was accomplished by immersing the sample in "351 developer", a commercially available product, under gentle agitation for 45 s immediately followed by a further 45 s in a separate container with clean 351 developer. Then, the sample was rinsed thoroughly in deionised water and blown dry with nitrogen.

2.5.5 Stripping

With photoresist in the shape of ridge waveguides on the sample, the next step was to transfer this ridge pattern into the sample by dry etching in an ECR generated plasma, as described in Section 2.4.2. The etch depth was monitored by laser end-point detection. Following the ECR etch the remains of the photoresist were stripped from the ridges in an oxygen plasma. This process is usually known as *descum* and was carried out in an RIE reactor.

2.5.6 Cleaving

The final stage of processing a waveguide sample was cleaving it into strips. The samples were designed such that a number of ridges, some with photonic crystal patterns some left unpatterned, would be on each strip. Typically about 10 ridges are on a final sample. The spacing between ridges is fixed to 250 μm by the strip mask used to define the ridges with UV lithography, as described in the previous Section. The sample dimensions are dictated largely by the size of the sample holder inside the e-beam writer, where samples can not be larger than $\sim 1 \times 1$ cm^2. This is more than sufficient to produce 2-3 usable samples and there is also sufficient space for test patterns. It is essential to have a number of test patterns of each sample to monitor the processing steps. Some characterization techniques are destructive, such as imaging the cross section of a pattern in the SEM. This requires some sacrificial patterns that can be cleaved through. Shown in Fig. 2.47 is an example of a completely processed sample, prior to cleaving, with ridges going through regions of photonic crystals.

To facilitate cleaving and to give good quality facets it is important to thin the sample. It is extremely difficult - if not impossible - to cleave a sample into strips which are narrower than the sample's thickness. The facets are likely to chip, which can render the sample useless for spectral characterisation. A poorly cleaved facet is shown in Fig. 2.48.

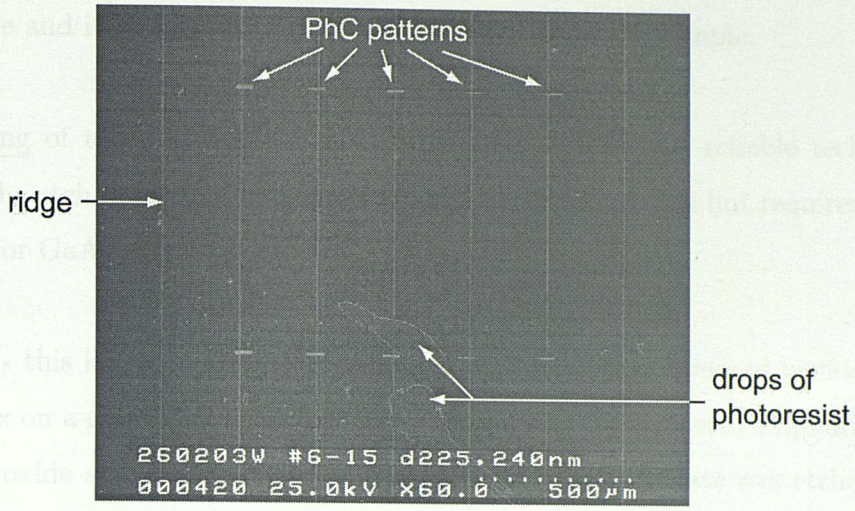


Figure 2.47: SEM image of entire sample prior to cleaving.

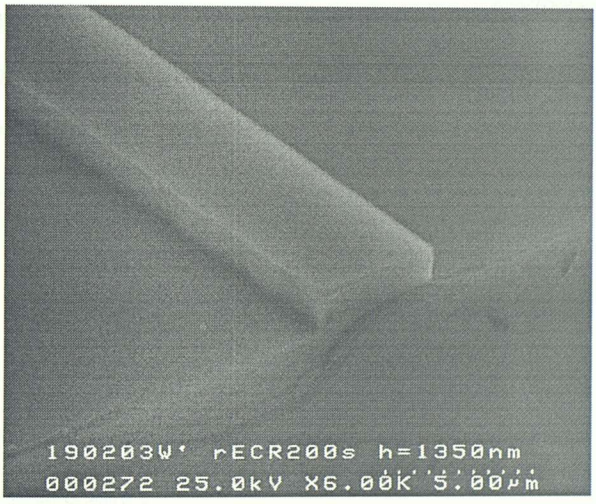


Figure 2.48: SEM image of a poorly cleaved ridge facet.

Thinning the substrate

The GaAs substrates of the samples used in this investigation were typically ~400 μm thick. There are several methods for reducing the thickness of these substrates.

Mechanical lapping using Al_2O_3 - this can give highly reproducible results, but is a very messy technique, which requires sacrificial samples to produce a level back surface

on the sample and it is difficult to monitor the thickness of the sample.

Dry etching of the upside-down mounted sample - clean and reliable technique. Monitoring the etch depth can be done using LEPD (Section 2.4.2) but requires an IR laser source for GaAs samples.

Wet etch - this is the technique used here. The sample was mounted upside-down in melted wax on a glass slide and immersed in mixture of concentrated sulphuric acid, hydrogen peroxide and water under constant stirring. The substrate was etched very homogenously if care was taken to remove excess wax from the edges. The etch rate was constant, but depended on the exact mixture, which differed slightly each time the mixture was prepared. Typical etch rates were 100±10 μm in 5 min. Thinning the sample to ~250 μm was found to be sufficient for producing high quality facets upon cleaving, such as the one shown in Fig. 2.49. After rinsing the sample in deionised water it was removed from the glass slide by heating it to ~150°C. The wax was washed off in an acetone bath.

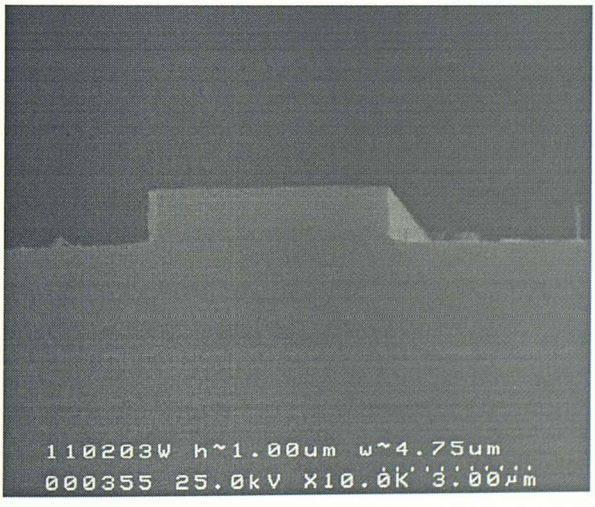


Figure 2.49: SEM image of an immaculate ridge facet. Sample was thinned to 250 μm before cleaving.

The sample was then ready to be cleaved into strips as narrow as ~300 μm. The

sample was placed on a scribing stage, where a line was scored along the intended cleave line using a diamond scribe. The score line can be placed to within ~20 μm of the intended position. This was crucial because in order to view the profile of an etched pattern the sample has to be cleaved through a pattern and the patterns were typically 50 μm wide. After scoring the sample it was cleaved over a razor blade on a special stage by applying gentle pressure to the corners of the sample. After thinning down the sample it was very fragile and easily cleaved. To avoid the sample breaking along unintended lines, such as the corners where the pressure was applyed it was found useful to lay a transparent, flexible piece of plastic, such as a piece of overhead transparency film cut approximately to the size of the sample, over the sample and gently apply pressure to the entire plastic piece. Thus, the pressure was distributed evenly over the entire sample and the cleave was more likely to occur along the direction dictated by the scribe mark.

This resulted in strips of samples containing a number of ridge waveguides (typcially ~10), some of which were unpatterned, while others contained photonic crystal patterns of various fill factors due to different electron doses during the electron beam lithography step. The strips were then glued onto specially prepared SEM stubs, for which a holder had been constructed that was integrated into the characterization setup described in Chapter 4.

2.5.7 Limitations

Etching ridges as described above has the disadvantage of creating somewhat uneven sidewalls. A typical example is shown in Fig. 2.50. The photoresist used to define a mask for the ridges consists of polymer chains such as PMMA described in Section 2.2.2. As these chains are broken during UV exposure, it is inevitable that cut ends of these chains create an uneven interface between the exposed and unexposed regions. This unevenness is transferred into the underlying epilayers during the ECR etch. In fact, this is a common problem in all forms of dry etching, as they are highly direc-

tional. In wet etching, surface roughness is gradually removed as the etch progresses, but at the cost of isotropic etch profiles.

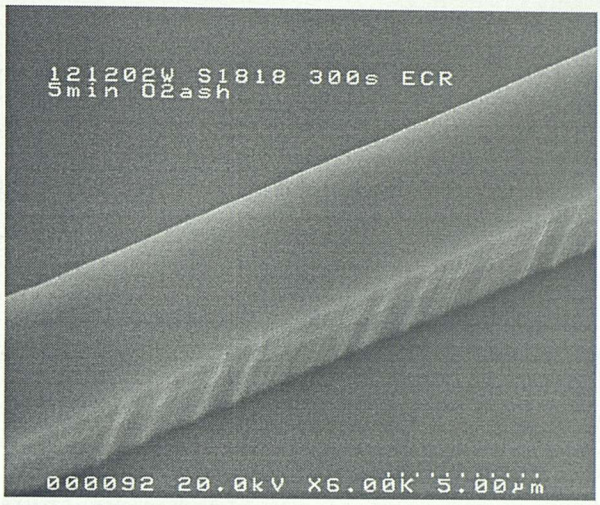


Figure 2.50: SEM image showing ridge with rough sidewall.

This sidewall roughness presents scattering sites to light travelling through these ridges. There are a number of possibilities for reducing this effect, which should be considered in future work.

The first option involves depositing an intermediate mask layer, such as silica, between the photoresist and the sample. This only needs to be thin (<100 nm for silica) for shallow ridge etches (<1 μm) in (Al,Ga)As structures. The transfer to the silica mask will lessen the roughness of the polymer mask. This is will reduce the roughness of the final ridge sidewalls, but it will not remove it completely.

The second possibility is carrying out a short wet etch once the ridges have been etched. The dry etch duration needs to be adjusted to avoid vertically overetching the ridges.

Furthermore, the possibility of only wet etching the sample should be considered. This will result in slanted sidewalls as wet etching primarily takes place along crystal

planes, but whether or not this has a detrimental effect on the guiding properties of the ridge or not will need to be investigated.

Another factor that caused defects in the ridges was the state of the mask used for UV lithography. Over time patches of photoresist start building up on the edges of the metal strips that define the ridges. The particular mask used here was nearly 10 years old. Gently cleaning it did not remove much of the photoresist. These imperfections in the mask were responsible for random ridge defects, such as that shown in Fig. 2.51.

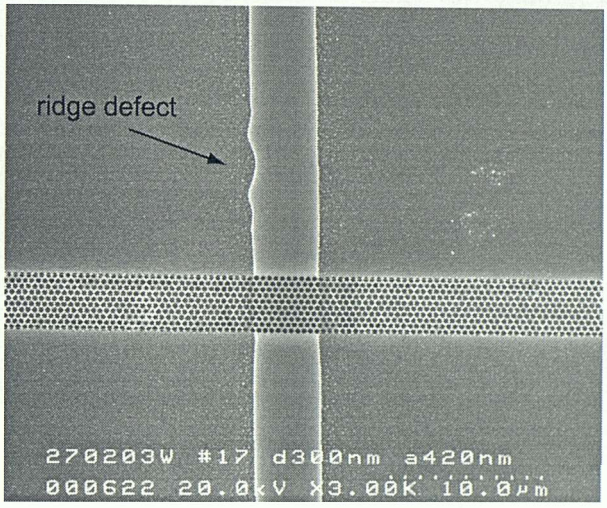


Figure 2.51: SEM image of a defective ridge caused by a defect in the mask.

A new mask should solve this problem, as fewer defects will present fewer scattering sites for EM waves propagating through the ridges, which will reduce the waveguide losses.

2.6 Conclusion

The fabrication of 2 dimensional photonic crystals with sub-micron features is a non-trivial task. Approximately 50 processing steps are required to produce 2D PhCs embedded in ridge waveguides, which is the structure that was focused on in this project. Each processing step bears the potential to ruin the sample.

Nonetheless we have successfully processed a range of samples with different parameters such as the PhC pattern fill factor, hole depth, hole diameter and ridge height. Figures 2.52 show a series of PhC patterns in ridge waveguides, all fabricated on the same sample.

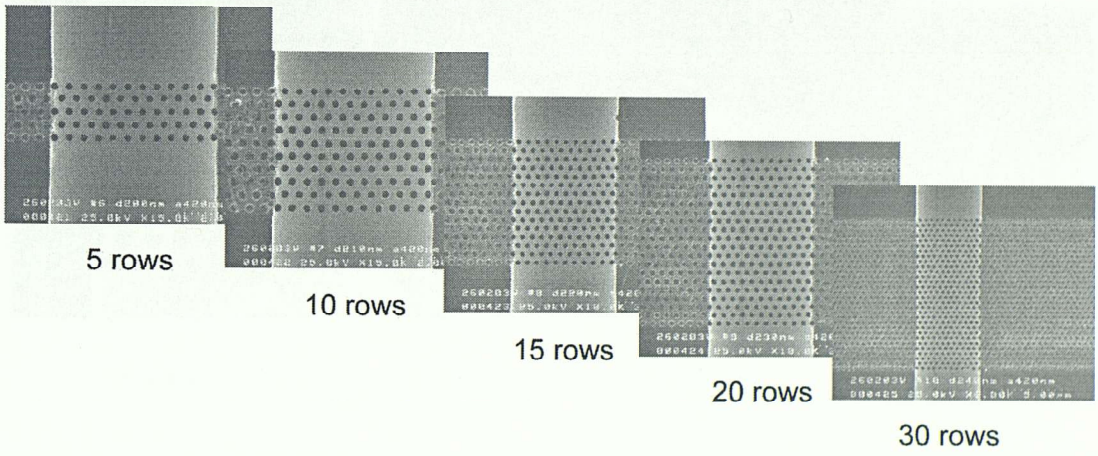


Figure 2.52: High quality PhC patterns of different lengths.

Figure 2.53 shows a fully processed sample with excellent pattern quality.

We have demonstrated good control over all aspects of the fabrication processes and it is believed that further quality improvements can be achieved by investigating certain key processing steps. In particular the ECR etching of the PhC pattern has optimization potential. The etch depth of the hole patterns can possibly be increased to $\sim$1.5 μm by running a 'gentler' etch, i.e. lower RF power but longer etch duration, without changing the thickness of the silica mask. The overall system used here was

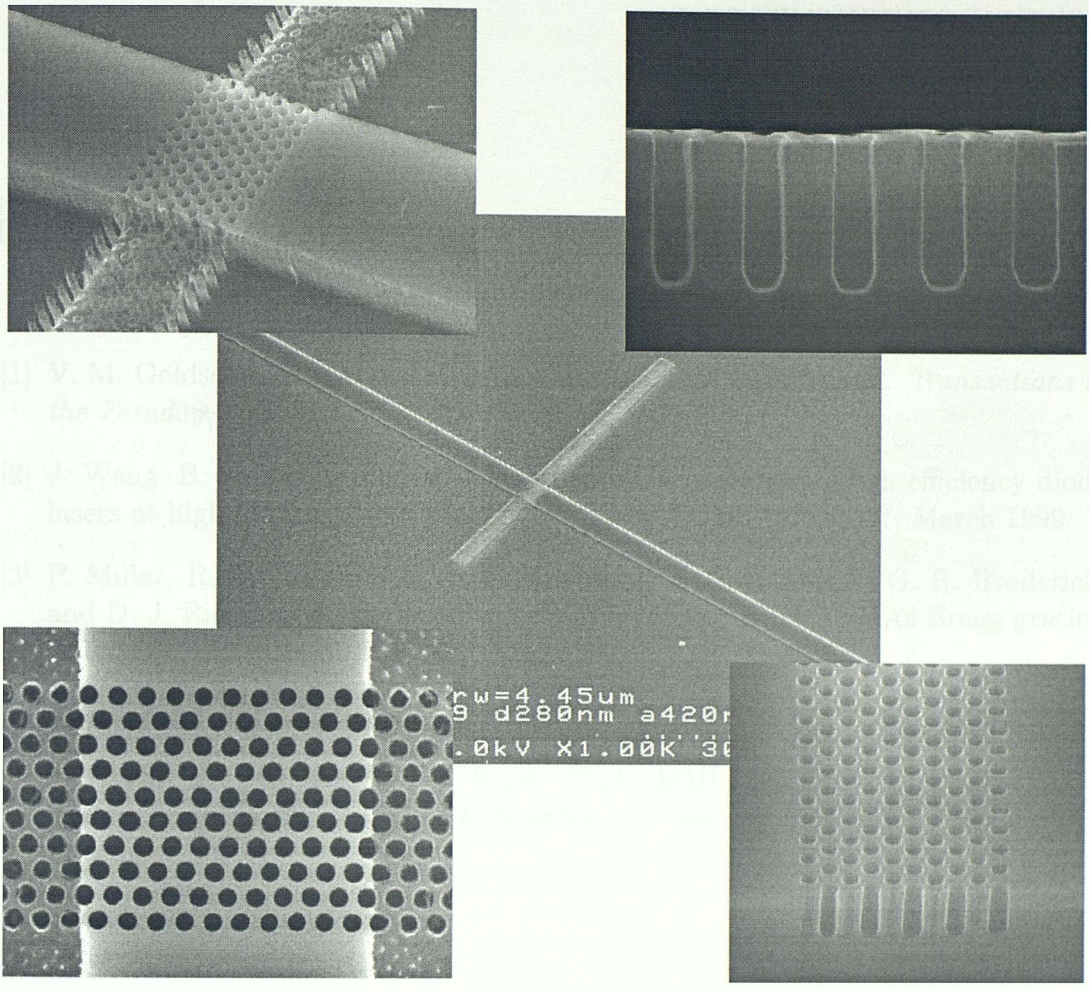


Figure 2.53: Several different aspects of a fully processed sample.

very well suited for research purposes. Electron beam lithography allows great flexibility in pattern design and we have shown that RIE/ECR plasma etching can be used to produce high quality patterns.

This part of the project was very time consuming, but after etching approximately 3.5 million holes over three years we believe to have gained significant expertise in most of the fabrication issues. The overall success of this study was largely attributed to the achievements at this stage.

Bibliography

[1] V. M. Goldschmidt. Crystal structure and chemical constitution. *Transactions of the Faraday Society*, 25:253–283, December 1929.

[2] J. Wang, B. Smith, X. Xie, X. Wang, and G. T. Burnham. High-efficiency diode lasers at high output power. *Appl. Phys. Lett.*, 74(11):1525–1527, March 1999.

[3] P. Millar, R. M. De La Rue, T. F. Krauss, J. S. Aitchison, N. G. R. Broderick, and D. J. Richardson. Nonlinear propagation effects in an AlGaAs Bragg grating filter. *Opt. Lett.*, 24(10):685–687, May 1999.

[4] H. P. Zappe. *Introduction to semiconductor integrated optics.* Artech House, 1995.

[5] S. Kayali, G. Ponchak, and R. Shaw. GaAs MMIC reliability assurance guideline for space applications. *Jet Propulsion Laboratory publication*, 96-25:1–221, December 1996.

[6] provided by M. Whitehead, with permission of R. Geels at University of California, Santa Barbara.

[7] J. I. Goldstein. *Practical Scanning Electron Microscopy.* Plenum, New York, 1975.

[8] B. Gayral and J. M. Gérard. Strong Purcell effect for InAs quantum boxes in high-Q wet-etched microdisks. *Physica E*, 7:641–645, 2000.

[9] T. M. Hall, A. Wagner, and L. F. Thompson. Beam exposure characteristics of resists. *J. Vac. Sci. Technol. B*, 16(6):1889–1892, Nov/Dec 1979.

[10] V. N. Astratov, M. S. Skolnick, S. Brand, T. F. Krauss, O. Z. Karimov, R. M. Stevenson, D. M. Whittaker, I. Culshaw, and R. M. De La Rue. Experimental technique to determine the band structure of two-dimensional photonic lattices. *IEE Proc.-Optoelectron.*, 145(6):398–402, December 1998.

[11] J. D. Joannopoulos, R. D. Meade, and J. N. Winn. *Photonics Crystals, Molding the Flow of Light.* Princeton University Press, Princeton, 1995.

[12] G. Feiertag, W. Ehrfeld, H. Freimuth, H. Kolle, H. Lehr, M. Schmidt, Sigalas, C. M. Soukoulis, G. Kiriakidis, T. Pedersen, J. Kuhl, and W. Koenig. Fabrication of photonic crystals by deep x-ray lithography. *Appl. Phys. Lett.*, 71:1441–1443, September 1997.

[13] M. Kamp, M. Emmerling, S. Kuhn, and A. Forchel. Nanolithography using a 100kV electron beam lithography system with a Schottky emitter. *J. Vac. Sci. Technol. B*, 17(1):86–89, January/February 1999.

[14] C. Gahn. The Bosch silicon micromachining foundry service. *Proc. Eurosensors*, 16, September 2002.

[15] M. Soljačić, S. G. Johnson, S. Fan, M. Ibanescu, E. Ippen, and J. D. Joannopoulos. Photonic-crystal slow-light enhancement of nonlinear phase sensitivity. *J. Opt. Soc. Am. B*, 19(9):2052–2059, September 2002.

[16] B. D'Urso, O. Painter, J. O'Brien, T. Tombrello, A. Yariv, and A. Scherer. Modal reflectivity in finite-depth two-dimensional photonic-crystal microcavities. *J. Opt. Soc. Am. B*, 15(3):1155–1159, March 1998.

[17] R. Ferrini, D. Leuenberger, M. Mulot, M. Qiu, J. Moosburger, M. Kamp, A. Forchel, S. Anand, and R. Houdré. Optical study of two-dimensional InP-based photonic crystals by internal light source technique. *IEEE J. Quantum Electron.*, 38(7):786–799, July 2002.

[18] M. Mulot, S. Anand, M. Swillo, M. Qiu, B. Jaskorzynska, and A. Talneau. Low-loss InP-based photonic-crystal waveguides etched with Ar/Cl_2 chemically assisted ion beam etching. *J. Vac. Sci. Technol. B*, 21(2):900–903, March/April 2003.

[19] D. J. Heason and A. G. Spencer. Infra-red interference patterns for new capabilities in laser end point detection. *J. Phys. D.*, 36:1543–1549, June 2003.

[20] E. D. Palik. *Handbook of Optical Constants of Solids II.* Academic Press Inc., 2nd edition, 1991.

Chapter 3

Theoretical considerations

3.1 Introduction

In this Chapter the theoretical considerations of this project are presented. These can broadly be divided into modelling techniques and data analysis.

The procedure for designing photonic crystals will be discussed in Section 3.2. The Section also contains a review of common tools for modelling PhC devices. An overview of the planar waveguide design process is given in Section 3.3, followed by a description of the `FWave` modelling tool. These two Sections contain all the modelling techniques used to design the structures that were the subject of this project.

In Section 3.4 Fourier Transform Analysis is introduced in as a powerful data analysis tool. Expressions for the transmitted and reflected intensities are derived and compared to numerically obtained results. It is demonstrated that loss coefficients associated with propagation in waveguides as well as structural information of the waveguide can be extracted conveniently by representing data in the Fourier domain.

3.2 Designing photonic crystals

Periodicity is not a fundamental requirement for photonic bandgap structures. Non-periodic structures can also give rise to photonic bandgaps. The authors of Ref. [1] demonstrated clear photonic bandgap (PBG) effects arising from Fibonacci sequence structures. However, it is much more convenient to work with periodic, finite structures, particularly with view to fabrication issues. The periodicity of photonic crystals can occur in one, two or three dimensions. It was decided to study two-dimensional (2D) PhC structures, due to the relative ease of fabrication compared to 3D structures. Patterns of circular air holes in semiconductor are the most obvious shape to consider, again with fabrication issues in mind. Furthermore, it has been shown that the largest absolute bandgaps are achieved for circular cross sections [2] and triangular

structures of holes in dielectrics [3]. Polarization dependent photonic bandgaps can occur in structures with periodically varying dielectric constants, with larger dielectric constant contrast giving rise to larger bandgaps. We define transverse electric (TE) and transverse magnetic (TM) polarizations as shown in Fig. 3.1.

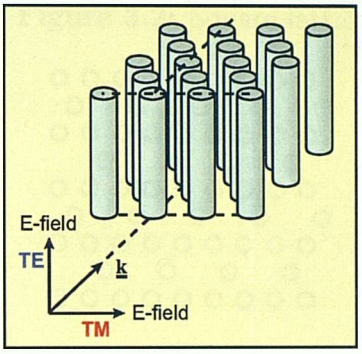


Figure 3.1: Definition of polarization

3.2.1 Pattern geometry

Patterns with air and GaAs exhibit extremely large dielectric constant variations ($\epsilon_{air} \approx 1$, $\epsilon_{GaAs} \approx 11.4$). To achieve this contrast over the shortest possible distance several pattern geometries are possible.

Square lattices (Fig. 3.2) are not the most suitable arrangement for creating large photonic bandgaps and do not offer the possibility of omnidirectional, complete bandgaps, i.e. PBG behaviour over specific frequency range for any propagation direction perpendicular to the hole-centre axes, and both for TE and TM-polarized light.

Patterns based on the hexagonal lattice are more promising in that respect. Three variants of this lattice geometry that have been studied in the past are the triangular [3], Kagomé [4] and graphite [5] lattice, shown in Fig. 3.3 a,b and c, respectively.

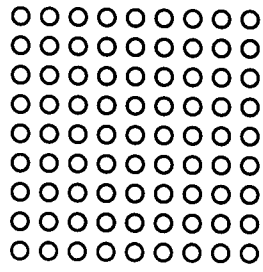


Figure 3.2: Square lattice

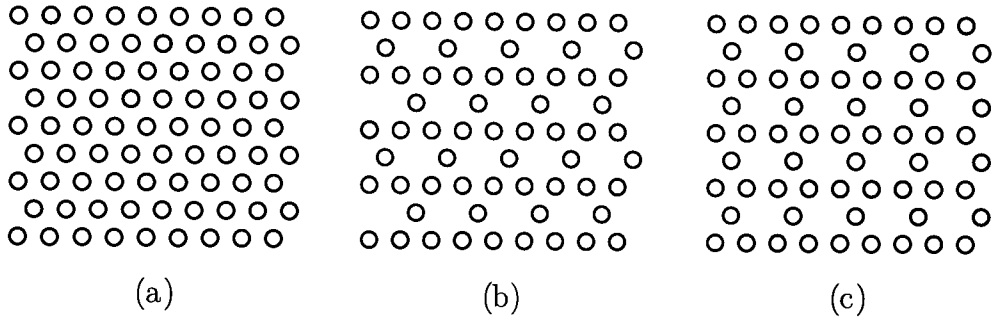


Figure 3.3: a) Triangular, b) Kagomé, c) Graphite lattice

Triangular lattice Brillouin zone

The real space lattice is a periodic function where the position of all lattice points can be described by a Fourier series, which in two dimensional space is a function of the unit vectors $\hat{x}$ and $\hat{y}$ as well as the lattice spacing a. Drawing on the analogy with crystal structures, reciprocal space (or k space) can be constructed from real space. Reciprocal lattice points are funcions of the unit vectors and $2\pi/a$ and these points give the allowed terms of the Fourier series used to represent the real space lattice [6]. Figure 3.4a shows the reciprocal lattice superimposed onto a real lattice. The two coordinate systems were scaled such that the real and reciprocal lattice points coincide.

The first Brillouin zone is the smallest volume entirely enclosed by planes that are the perpendicular bisectors of the reciprocal lattice vectors drawn from the origin. It is of special importance in the theory of solids, particularly with respect to diffraction conditions [6]. In the first Brillouin zone there are three high symmetry points, Γ, M and K, which we will use to unambiguously define propagation directions inside the

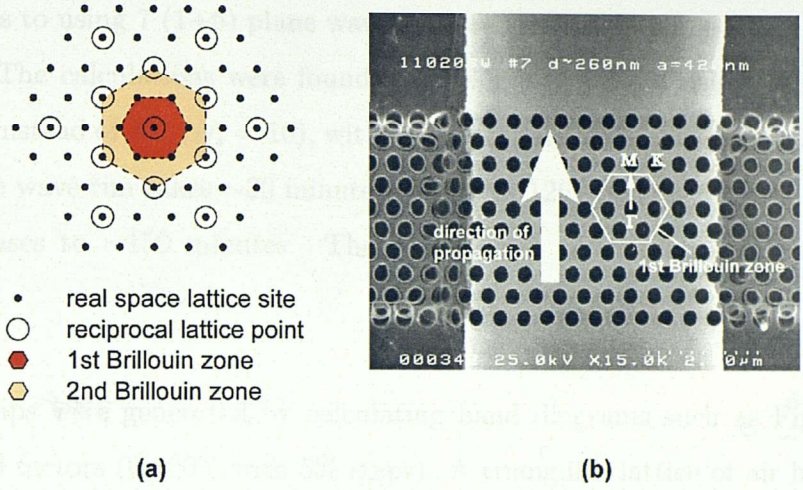


Figure 3.4: a) The real space and reciprocal lattices are superimposed. The lattice vector lengths were chosen so that the real and reciprocal lattice points overlap. b) Reciprocal lattice nomenclature. ΓM was always designed to be along the direction of light propagation, i.e. parallel to the ridge waveguide.

real space crystal lattice, as shown in Fig. 3.4b. In this project all photonic crystal structures were designed with the ΓM crystal direction along the direction of propagation.

3.2.2 Band structure calculation

The photonic band structures for triangular and graphite lattices were calculated using plane wave expansion algorithms [7] to solve for the Bloch modes in Maxwell's equations. Plane wave expansion modelling is described in Section 3.2.3. The model assumes an infinite 2D lattice of cylinders, which also extends to infinity along the cylinders' central axes.

Band diagrams were typically generated for air cylinders in a GaAs environment, with the refractive index of GaAs set to $n_{GaAs} = 3.38$. The accuracy of the plane wave expansion method depends largely on the number of plane waves included in the expansion. A useful way to specify this number is to consider, in reciprocal space, the number of shells (N_s) around a reciprocal lattice point [8]. For example, $N_s = 2$

corresponds to using 7 (1+6) plane waves. $N_s = 3$ means 13 plane waves (1+6+6) are included. The calculations were found to converge to ~0.6% using 721 plane waves ($N_s = 15$) instead of 331 ($N_s = 10$), with moderate calculation times. On a DEC Alpha a 721 plane wave run takes ~30 minutes, and with 1261 plane waves the computation time increases to ~150 minutes. The convergence of the calculations is shown in Fig. 3.5.

Gap maps were generated by calculating band diagrams such as Fig. 3.5a for a range of fill factors (0-100% with 5% steps). A triangular lattice of air holes in GaAs was considered and the plane wave expansion method was used. The gap maps indicate the positions of *complete* photonic bandgaps, i.e. gaps across the entire Brillouin zone. Figure 3.6 is a gap map for TE and TM-polarized light in an infinite plane of air holes in GaAs.

Large photonic bandgaps can occur in triangular lattices of air holes in GaAs for TM-polarized light, as shown in Fig. 3.7. This geometry was chosen for the experimental investigation of 2D photonic crystals embedded in ridge waveguides, the main part of this project. As the TM bandgap is very large, fabrication tolerances are quite relaxed. For instance, the width of the TM bandgap for a lattice with a fill factor of 50% and lattice constant $a = 420$ nm is ~ 640 nm, or equivalently, for a mid-gap wavelength of 1550 nm and fill factor of 50% the lattice parameter can be $370 < a < 580$ nm.

The PhC in the ridge waveguide were designed to operate around a central wavelength of 1550 nm. A triangular lattice with a fill factor of 40% was chosen and for the TM bandgap the mid-gap normalized frequency of $a/\lambda = 0.271$ thus dictated a lattice constant of $a = 420$ nm. Given the required fill factor $f = 40\%$ and $a = 420$ nm the hole diameter (d) was calculated using

$$d = \sqrt{\frac{2\sqrt{3}f}{\pi}}\, a$$

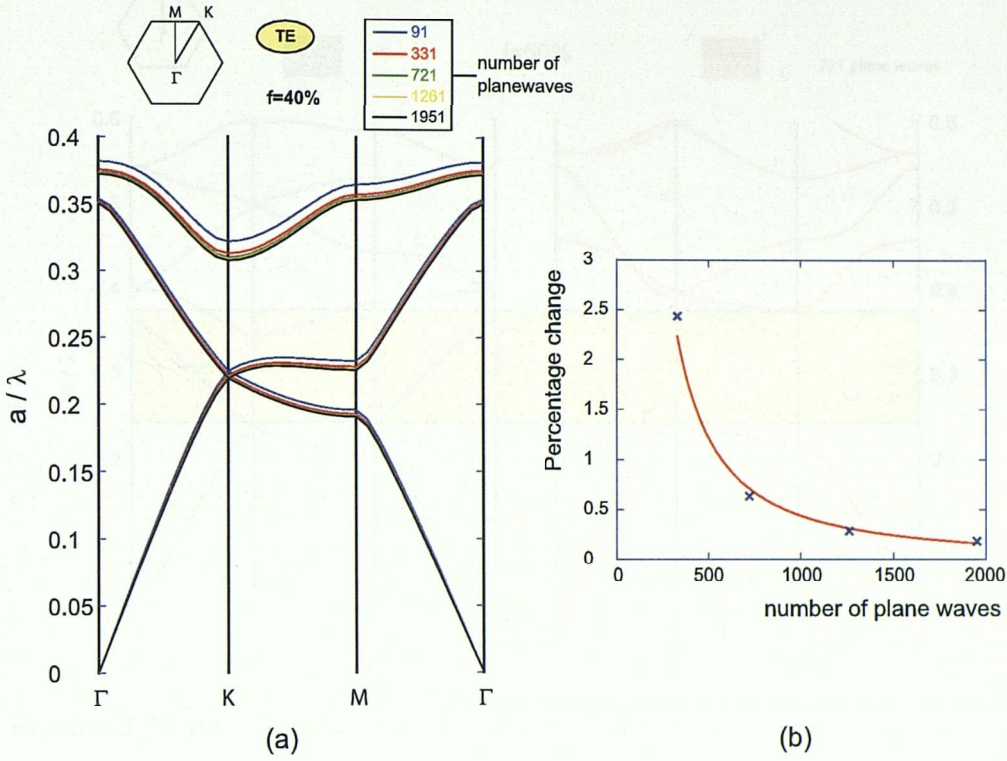


Figure 3.5: a) Band diagram for TE polarized light in a triangular lattice PhC calculated using plane wave expansion. Satisfactory accuracy is achieved with 721 plane waves. Beyond that a large increase in computing time is required to achieve a small increase in accuracy, as shown in b), which is calculated for the second band at the M point of the Brillouin zone.

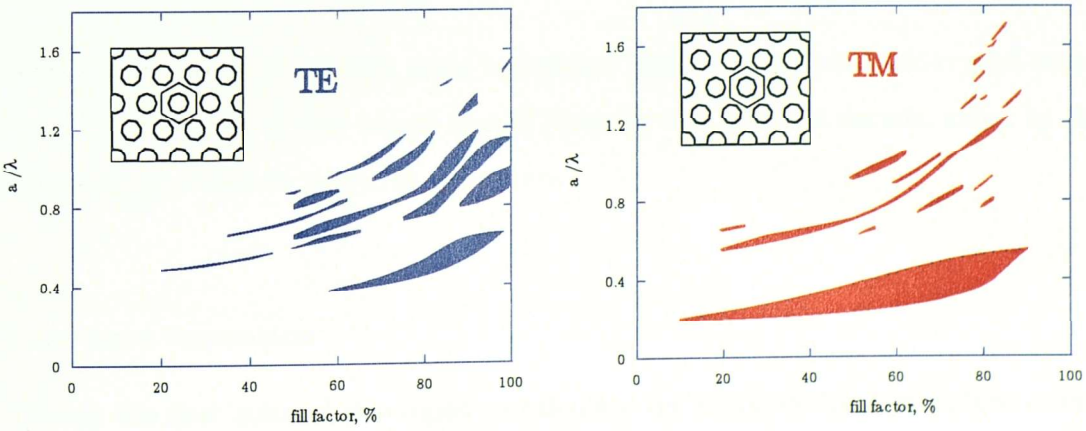


Figure 3.6: Gap map for triangular lattice of air holes. Shaded regions indicate complete bandgaps that span the entire Brillouin zone. Large complete bandgaps occur at moderate fill factors (~40 %) for TM-polarized light.

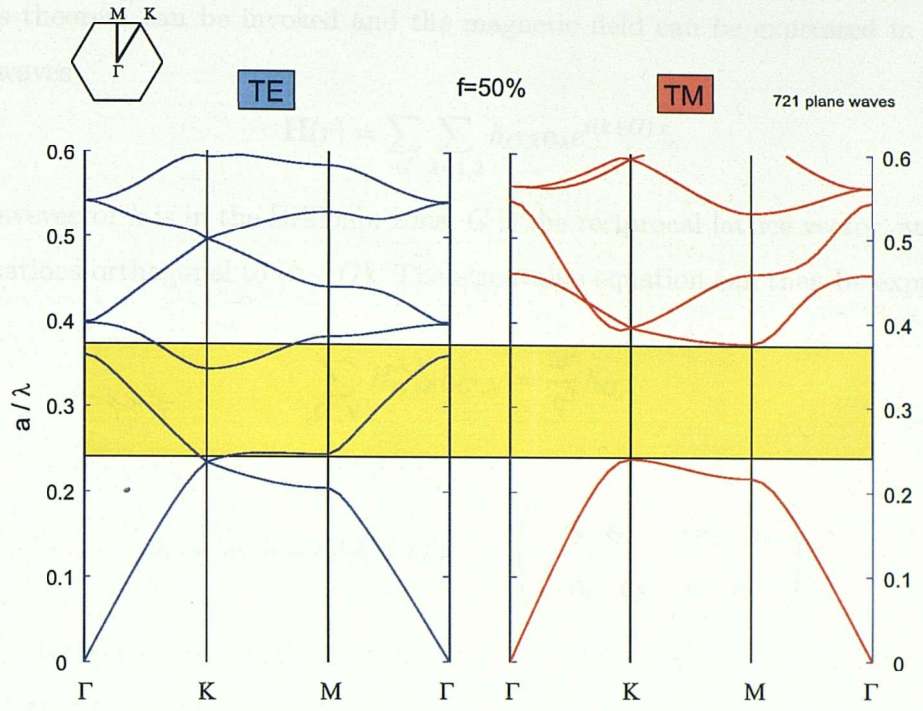


Figure 3.7: Band structure for f=50%, air holes in GaAs, triangular lattice

to be $d = 280$ nm. These parameters were convenient for fabrication using a combination of electron beam lithography and plasma etching techniques, as outlined in Chapter 2.

3.2.3 Device modelling

In this Section we will highlight some techniques used to model photonic crystal structures. This has been a very active area of research over the past decade, aided by the availability of evermore powerful computers.

Plane wave expansion

This was the first method developed to calculate the photonic band structure of two and three dimensional periodic structures [9, 10]. Briefly, Maxwell's equations can be rearranged to yield the eigenvalue equation $\nabla \times [1/\epsilon(r)\nabla \times]\mathbf{H} = (\omega^2/c^2)\mathbf{H}$, where $\mathbf{H}(r)$ is the magnetic field. Due to infinite periodicity in the crystal along the x and y axes,

Bloch's theorem can be invoked and the magnetic field can be expressed in terms of plane waves

$$\mathbf{H}(r) = \sum_{G} \sum_{\lambda=1,2} h_{G,\lambda} \mathbf{e}_{\lambda} e^{i(k+G)\cdot r}$$

The wavevector k is in the Brillouin zone, G is the reciprocal lattice vector, and $\mathbf{e}_{\lambda}$ are polarizations orthogonal to $(k+G)$. The eigenvalue equation can then be expressed as

$$\sum_{G',\lambda'} H^{\lambda,\lambda'}_{G,G'} h_{G',\lambda'} = \frac{\omega^2}{c^2} h_{G,\lambda}$$

with

$$H_{G,G'} = |k+G||k+G'|\epsilon^{-1}_{G,G'} \begin{pmatrix} \mathbf{e}_2 \cdot \mathbf{e}_2 & -\mathbf{e}_2 \cdot \mathbf{e}_1 \\ -\mathbf{e}_1 \cdot \mathbf{e}_2 & \mathbf{e}_1 \cdot \mathbf{e}_1 \end{pmatrix}$$

and $\epsilon^{-1}_{G,G'}$ is the Fourier transform of the dielectric function $\epsilon(r)$. The real eigenvalues of ω are plotted to produce band diagrams such as Fig. 3.7. These correspond to allowed, propagating modes in the crystal. The imaginary solutions correspond to waves that decay inside the crystal. The computational time grows as N^3, where N is the size of the system, i.e. the number of plane waves used.

Finite element method

The structure under investigation is divided into discrete, finite elements [11, 12, 13]. An inverse relationship exists between the mesh size and the accuracy, as well as computation time (small mesh size, high accuracy and long computation time). In the finite element method (FEM) the solution is approximated with a superposition of functions, each of which is localized to a small patch within the computational domain. Solutions to Maxwell's equations can be found effectively with the assistance of the Floquet-Bloch theorem, by considering, for instance, a unit cell of the material and imposing periodic boundary conditions [14].

FEM works in frequency space rather than k-space and can be used to model

inhomogeneous media with a complex spatial dependence of the dielectric function, including discontinuities. The discontinuities in dielectric constant, which are a feature of most of the photonic bandgap materials being produced today, and which plague plane wave methods through the Gibbs phenomenon, are trivially and exactly represented in the FEM. A generalized eigenvalue problem with sparse matrices has to be solved, which is significantly faster to compute than the plane wave expansion method.

Finite difference time domain

Finite difference time domain (FDTD) is a versatile technique for modelling EM waves interacting with complex, inhomogeneous media [15]. It is based around a discretization of Maxwell's equations in time and space. The electric or magnetic field amplitudes are evaluated at each grid point at finite time intervals. At the boundary of the finite computational domain special boundary conditions, such as the perfectly matched layer method (PML) [16] or absorbing boundary conditions (ABC), are implemented. For a fixed total number of time steps the computational time is proportional to the number of discretization points in the computation domain, i.e. the FDTD algorithm is of order N. The matrices involved in the computation are sparse and only nonzero elements need to be stored. The eigenvalues can be found from direct root search routines, which avoids the initial guess for each eigenvector required for iterative methods.

A number of commercial modelling packages employing the FDTD technique have been developed in recent years and have become very popular. The primary reasons are that the programs allow a graphical representation of the computation domain and are very user-friendly. The user can easily create complex photonic crystal systems with defects, which would be extremely difficult to implement with other modelling techniques. On the other hand it, as this tool works in the frequency domain it is usually awkward to study dispersive systems, where the dielectric constants is frequency dependent [17].

Scattering losses in photonic crystals can be investigated using 3 dimensional FDTD [18, 19, 20]. This is of particular interest in this project - see Section 5.3.3, Page 205. Although the computational power required is considerable, this method provides the opportunity of accurately modelling devices.

Transfer matrix, Scattering matrix, RCWA

The transfer matrix method (TMM) and scattering matrix method (SMM) have been used to study the interaction of EM waves with two and three dimensionally periodic dielectric structures [21, 22, 23]. These methods can be used effectively in cases where the dielectric constant is frequency dependent or has a large imaginary part, thus accounting for dispersion and absorption. Convergence of solutions with TMM is more sensitive to the spatial discretization used, than SMM.

Rigorous Coupled Wave Analysis (RCWA) was used in our group to model 2D photonic crystal structures. Software codes were written by P. N. Stavrinou. The structure under investigation is analysed in a layer-by-layer fashion. The electric field amplitudes are calculated for each layer and scattering mattrices are used to propagate the field amplitudes through the structure. Material dispersion and absorption can be incorporated easily, as RCWA calculations are performed in k-space.

3.3 Waveguide design

In order to study two dimensional photonic crystal structures in a controlled and systematic way it was decided to embed them in ridge waveguides containing a planar waveguide structure. This provides vertical and lateral confinement to electromagnetic waves of certain wavelengths. The strength of the confinement depends on a number of factors, which are reviewed in this Section.

The design challenge can be formulated as follows: What structure can guide an electro-magnetic wave without loss along a straight path? A number of special criteria emerge, which allow one to fabricate such a structure as has been proven for many decades.

Figure 3.8 is a simplified picture of a region of space, which is divided into three layers: I - cladding, II - core or guiding layer and III - substrate. The direction of an arbitrary plane wave with freespace propagation constant k_o is indicated by a ray-diagram. Layers I and III are assumed to extend to infinity and the interfaces (I/II and II/III) are assumed to be perfectly reflecting.

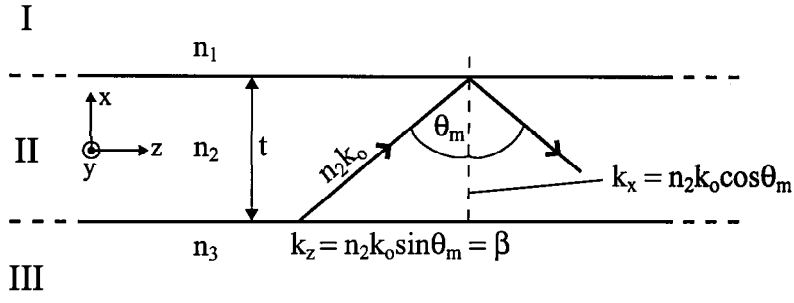


Figure 3.8: Ray diagram of general slab waveguide

In free space the propagation constant of a wave is given by

$$k_o = 2\pi/\lambda_o$$

For material of refractive index n_i, where $i \in [1, 2, 3]$, the following relations are true:

$$\text{group velocity,} \quad v_i = c/n_i$$
$$\text{wavelength,} \quad \lambda_i = \lambda_o/n_i$$
$$\text{propagation constant,} \quad k_i = n_i k_o$$

In a ray-optics picture the wave propagates along the slab in the z-direction while undergoing reflections at the slab interfaces. Therefore, unless the wave propagates

parallel to the slab interfaces the propagation constant has components in the x and z-directions. For propagation in the guiding layer ($n = n_2$)

$$k_x = n_2 k_o \cos\theta_m$$
$$k_z = n_2 k_o \sin\theta_m \equiv \beta$$

β is the effective mode propagation constant and is commonly used in place of k_z. It has units of $[m^{-1}]$.

The wave-guiding condition [24] at the layer interfaces require that

$$\theta_m = \sin^{-1}\left(\frac{m\lambda_o}{2t}\right) \qquad \text{for} \quad m = 1, 2, 3... \tag{3.1}$$

where m is an integer corresponding to the mode number, t is the slab thickness. There are clearly discrete values of θ_m for which a wave can propagate in the slab. For all other values of θ_m destructive interference between reflected waves at the slab interface and non-reflected parts would cause the wave to eventually disappear. Therefore, propagation inside slab waveguides occurs in discrete modes, each with its own propagation constant and reflection angle.

A mode in the waveguide experiences an effective refractive index of $n_2 \sin\theta_m$. Accepting this picture one can then drop the idea of a wave bouncing along inside the slab, but instead picture it as propagating right along its centre, parallel to the interfaces with an effective refractive index of $n_2 \sin\theta_m$. Every mode clearly has a different β and $n_2 \sin\theta_m$. An interesting consequence of this is that each mode propagates with a different group velocity in the waveguide. Modal (or chromatic) dispersion is a serious problem in long-distance optical communication [25, 26].

3.3.1 The wave equation

The aim of this Section is to derive the conditions under which a wave will be perfectly guided inside the guiding layer of a generic asymmetric waveguide. For an in-depth discussion the refer to Refs. [25, 26]. In the following Section we will assume a source-free, current-free environment. Faraday's law can be expressed as

$$\nabla \times E = -\mu_0 \frac{\partial H}{\partial t}$$

where μ_0 is the permeability of freespace. Performing the *curl* operation on both sides of the equation gives

$$\begin{aligned} \nabla \times \nabla \times E &= -\mu_0 \nabla \times \frac{\partial H}{\partial t} \\ &= -\mu_0 \frac{\partial}{\partial t}(\nabla \times H) \end{aligned}$$

Substituting the Ampère-Maxwell equation on the RHS results in

$$\nabla \times \nabla \times E = -\mu_0 \frac{\partial}{\partial t}\left(\epsilon_0 \frac{\partial E}{\partial t}\right) \tag{3.2}$$

where ϵ_0 is the freespace permittivity. The vector identity $\nabla \times \nabla \times E = \nabla(\nabla \cdot E) - \nabla^2 E$ can be used to rewrite the LHS of Eqn. 3.2. Therefore,

$$\nabla^2 E = \epsilon_0 \mu_0 \frac{\partial^2 E}{\partial t^2} \tag{3.3}$$

This is the Helmholtz, or time-harmonic wave equation [27]. The standard solutions are of the form

$$E(r,t) = E_o(x,y)e^{\pm i(\omega t - \beta z)}$$

where β = propagation constant = k_z. Substituting this general solution into Eqn. 3.3 gives

$$\left[\frac{\partial^2}{\partial x^2} + \frac{\partial^2}{\partial y^2}\right] E - \beta^2 E = -\epsilon_0 \mu_0 \omega^2 E$$

By definition $\epsilon_0\mu_0 = \left(\frac{n_i}{c}\right)^2$ and $\omega/k_o = c$. Therefore,

$$\left[\frac{\partial^2}{\partial x^2} + \frac{\partial^2}{\partial y^2}\right] E + (k_o^2 n_i^2 - \beta^2)E = 0$$

An ideal slab waveguide is infinite along the y-direction, so the electric field has no y-dependence, i.e. $E_0(x,y) = E_0(x)$, i.e. $\frac{\partial^2 E}{\partial y^2} = 0$. Thus,

$$\frac{\partial^2 E}{\partial x^2} + (k_o^2 n_i^2 - \beta^2)E = 0 \tag{3.4}$$

The nature of the solution depends on the coefficient of the second term and for a fixed frequency ω, the solution is determined by the propagation constant β. For a typical asymmetric guide $n_2 > n_3 > n_1$. We will analyze the requirements for having guided modes in a planar waveguide structure.

First of all there are two distinct types of solution to Eqn. 3.4. If $k_o^2 n_i^2 > \beta^2$, then the solutions are of the form

$$E \propto e^{\pm i k_{x_i} x}$$

where k_{x_i} is the x-component of the propagation constant in layer i. This says that under these conditions the electric field can propagate in region i, as shown by its sinusoidal form. If $k_o^2 n_i^2 < \beta^2$, the E-field decays exponentially in region i, i.e. it is of the form

$$E \propto e^{\pm k_{x_i} x}$$

Therefore, the only set of conditions for which the E-field can propagate in region 2 and decay exponentially elsewhere is that

$$k_o n_1 < \beta, k_o n_2 > \beta, k_o n_3 < \beta$$

The electric field and its gradient must match at the layer interfaces. This requirement allows one to construct a picture of the field distribution inside the structure, such as in Fig. 3.9.

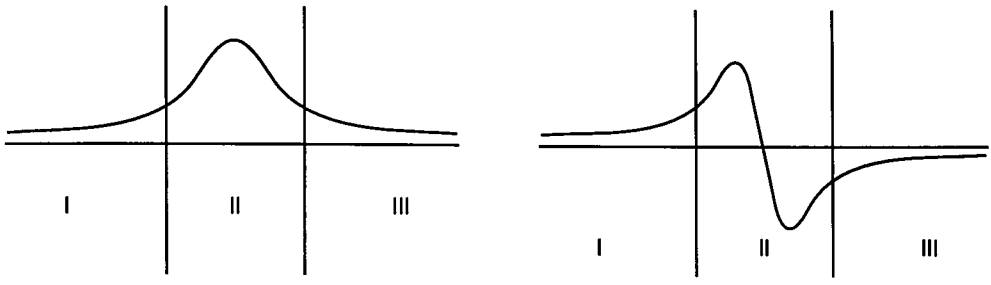


Figure 3.9: Schematic illustration of the electric field distribution of the first and second guided modes in a slab waveguide.

In this case the E-field is confined to the vicinity of the guiding layer and distinct guided modes can be supported. The allowed values of β are discrete and this is the origin of the discrete nature of guided modes. The number of confined modes depends on a range of factors, such as the thickness of the guiding layer, the frequency of the radiation and the values of n_1, n_2 and n_3. (nb. At least the fundamental mode is always guided in an ideal planar waveguide structure.)

If $k_o n_{2,3} > \beta > k_o n_1$, only in region I does the electric field decay exponentially. Propagating wave solutions exist in the guiding layer and the substrate (regions II and III). These are often called substrate radiation modes, as modes are 'lost' into the substrate region. Figure 3.10 depicts this case.

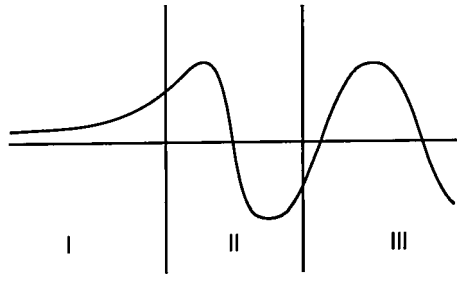


Figure 3.10: Wave propagating in the guiding layer and the substrate.

Finally, if $k_o n_i > \beta$, propagating solutions exist throughout the structure and the wave is not guided at all.

3.3.2 MultiLayer

The program `MultiLayer` by Randy Geels [28] was used to model planar waveguide structures and find the optimum parameters for an experimental study of photonic crystals in a waveguide environment.

It was decided to use Gallium Arsenide substrates and grow (Al,Ga)As epilayers to provide a waveguide environment. The tightest modal confinement in the waveguide core is achieved by having the highest possible refractive index contrast between the core and cladding layers. This would mean having AlAs/GaAs/AlAs layers atop the substrate. However, this is impractical as $Al_xGa_{1-x}As$ material with an aluminium content higher than approximately 90% oxidises rapidly in air [29], which is undesirable. The lower cladding was designed to be very thick in order to provide sufficient isolation from the high index substrate to avoid leakage into the substrate. Figure 3.11 shows the wafer structure that was found to give good modal confinement in the GaAs waveguide core in the wavelength region around 1550 nm.

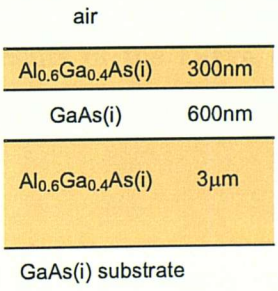


Figure 3.11: Planar waveguide structure. The aluminium component was 60% and all materials were undoped.

3.3.3 Ridge waveguide

One of the aims of this study was to experimentally investigate the effect of mode confinement on scattering losses in photonic crystals. Embedding photonic crystals in ridge waveguides has the distinct advantage of knowing precisely the shape of the mode incident on the PhC. The mode shape can be changed by varying the final processing steps described in Chapter 2. The ridge width can be changed by using a different mask and the ridge height is very easily adjusted by choosing the appropriate etch duration. This flexibility in the fabrication process offers a high degree of control over the mode shape, which affects the loss properties of the photonic crystal region.

To model the effect of etching ridge waveguides into a planar waveguide, the software package `FWave` was used. It is a finite element mode solver, which calculates the electric or magnetic field in a ridge waveguide. Table 3.1 summarizes the parameters used in the model, where the refractive index values are for λ=1550 nm [30].

$n(Al_{0.6}Ga_{0.4}As)$	3.13
n(GaAs)	3.37
ridge width	4.5 μm
ridge height	0.6 μm, 1.4 μm

Table 3.1: Parameters used for `FWave` simulation

Figures 3.12a,b show the results of the `FWave` calculations for the fundamental modes in two different ridge waveguide structures. The concentric circles are 10% lines of the electric field magnitude.

The mode shown in Fig. 3.12a is less tightly confined than that in Fig. 3.12b, although the difference is small. For both ridge heights the effective refractive index for TE-polarized light was calculated using `FWave` and in both cases it was found to be $n_{eff} \simeq 3.278$ [1]. Varying the ridge height is therefore a convenient way of studying the effect of the mode shape on the properties of the device. In practice this is easily

[1]The effective refractive index for TM modes is slightly lower. For the structure shown in Fig. 3.12b `FWave` was used to calculate n_{eff} for the fundamental TM mode. At 1550 nm it was found that $n_{eff} \simeq 3.268$.

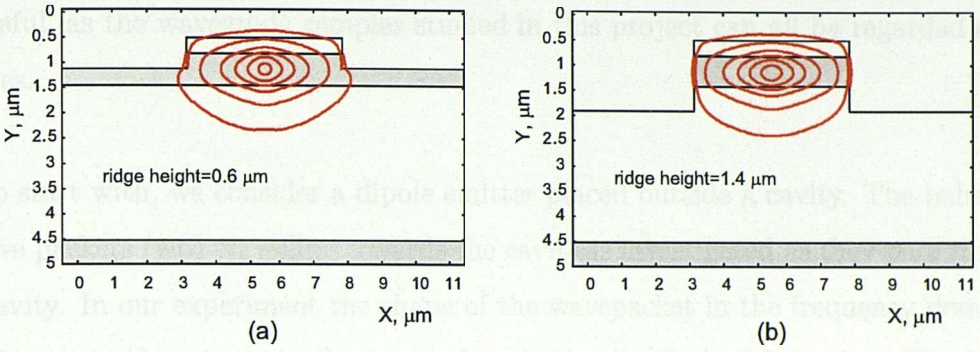


Figure 3.12: `FWave` simulation of the fundamental TE modes at 1550 nm of two different ridge heights: a) 0.6 μm b) 1.4 μm.

accomplished, as outlined in Section 2.4.2 on Page 81.

3.4 Fourier Analysis

Fourier analysis is a data analysis tool that is rarely used in the context of optical characterization of photonic crystals. Reference [31] is a noteworthy exception. This powerful technique is highly suitable for waveguide structures, where Fabry-Pérot-type resonances commonly occur. We will rigorously develop Fourier analysis, starting with Fourier decomposition of a signal in a single cavity. Fourier transformations of frequency-domain signals will be shown to produce a useful way of representing data in the Fourier domain. The features in the Fourier domain will be shown to give access to a number characteristic sample parameters, such as the waveguide loss coefficient, all from a single frequency scan of a sample.

3.4.1 Decomposition of transmission signal in a single cavity

In this Section we show how the transmission signal through a single Fabry-Pérot (FP) cavity can be decomposed into Fourier series [32]. A deeper understanding of this will

be useful, as the waveguide samples studied in this project can all be regarded as FP cavities.

To start with, we consider a dipole emitter placed outside a cavity. The behaviour of wave packets (wp) travelling towards the cavity is investigated as they pass through the cavity. In our experiment the shape of the wavepacket in the frequency domain is a very narrow Gaussian, ideally a delta function at the desired frequency. Figure 3.13 is an illustration of the system under investigation, highlighting that in this case we are only interested in transmission properties of the cavity. The loss coefficient, α', is included to account for the propagation loss inside the cavity [33].

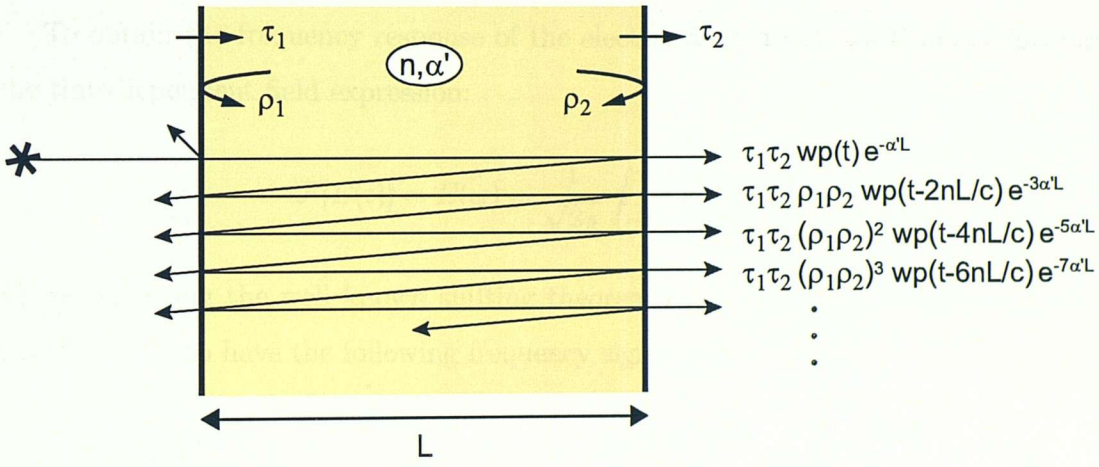


Figure 3.13: Diagram of Fabry-Pérot cavity - Transmission

The transmitted electric field, $E_T(t)$ is given by

$$\begin{aligned} E_T(t) &= \tau_1\tau_2 \mathrm{wp}(t)e^{-\alpha' L} + \tau_1\tau_2\rho_1\rho_2 \mathrm{wp}\left(t - \frac{2nL}{c}\right) e^{-3\alpha' L} \\ &\quad + \tau_1\tau_2(\rho_1\rho_2)^2 \mathrm{wp}\left(t - \frac{4nL}{c}\right) e^{-5\alpha' L} \\ &\quad + \tau_1\tau_2(\rho_1\rho_2)^3 \mathrm{wp}\left(t - \frac{6nL}{c}\right) e^{-7\alpha' L} + \ldots \end{aligned} \tag{3.5}$$

where τ_i and ρ_i are the Fresnel transmission and reflection coefficients, respectively, at the cavity walls, n=refractive index inside cavity, L=cavity length, t=time and

c=speed of light. The refractive index outside the cavity was assumed to be 1. Let $\tau = \tau_1\tau_2$ and $\rho = \rho_1\rho_2$. Therefore,

$$\begin{aligned} E_T(t) &= \tau \mathrm{wp}(t)e^{-\alpha' L} + \tau\rho \mathrm{wp}\left(t - \frac{2nL}{c}\right)e^{-3\alpha' L} \\ &\quad + \tau\rho^2 \mathrm{wp}\left(t - \frac{4nL}{c}\right)e^{-5\alpha' L} + \tau\rho^3 \mathrm{wp}\left(t - \frac{6nL}{c}\right)e^{-7\alpha' L} + \ldots \\ &= \tau e^{-\alpha' L}\left[\mathrm{wp}(t) + \rho \mathrm{wp}\left(t - \frac{2nL}{c}\right)e^{-2\alpha' L}\right. \\ &\quad \left. + \rho^2 \mathrm{wp}\left(t - \frac{4nL}{c}\right)e^{-4\alpha' L} + \rho^3 \mathrm{wp}\left(t - \frac{6nL}{c}\right)e^{-6\alpha' L} + \ldots\right] \end{aligned} \tag{3.6}$$

The expression $\mathrm{wp}(t-T)$ simply corresponds to a delay in $\mathrm{wp}(t)$ by a time T. These delay terms can be thought of as echoes of the original wave packet, $\mathrm{wp}(t)$.

To obtain the frequency response of the electric field, $E(\omega)$, we Fourier-transform the time-dependent field expression:

$$\mathcal{F}[E(t)] = E(\omega) = \frac{1}{\sqrt{2\pi}}\int_{-\infty}^{+\infty} E(t)e^{-i\omega t}dt \tag{3.7}$$

Therefore, using the well known shifting theorem [33] a wave packet delayed by $\frac{2nL}{c}$ can be shown to have the following frequency signature:

$$\begin{aligned} \int_{-\infty}^{+\infty} \mathrm{wp}\left(t - \frac{2nL}{c}\right)e^{-i\omega t}e^{-i\omega\frac{2nL}{c}}dt &= e^{-i\omega\frac{2nL}{c}}\int_{-\infty}^{+\infty} \mathrm{wp}\left(t - \frac{2nL}{c}\right)e^{-i\omega t}dt \\ &= e^{-i\omega\frac{2nL}{c}}\mathrm{wp}(\omega) \end{aligned} \tag{3.8}$$

Fourier-transforming Eqn. 3.6 thus results in

$$\begin{aligned} E_T(\omega) &= \tau e^{-\alpha' L}\left[1 + \rho e^{-i\omega\left(\frac{2nL}{c}\right)}e^{-2\alpha' L}\right. \\ &\quad \left. + \rho^2 e^{-i\omega\left(\frac{8nL}{c}\right)}e^{-4\alpha' L} + \rho^3 e^{-i\omega\left(\frac{6nL}{c}\right)}e^{-6\alpha' L} + \ldots\right]\mathrm{wp}(\omega) \end{aligned} \tag{3.9}$$

Equation 3.9 clearly shows that at frequency ω the electric field contains a constant (DC) term as well as frequency dependent terms, which have the common factor $\rho e^{-i\omega\left(\frac{2nL}{c}\right)}e^{-2\alpha' L}$.

The intensity, $I(\omega)$, is given by

$$I(\omega) = E(\omega)E^*(\omega) \tag{3.10}$$

The notation I_T is used from now on to represent the transmitted intensity. We substitute Eqn. 3.9 into Eqn. 3.10 to obtain

$$\begin{aligned} I_T(\omega) &= \tau^2 e^{-\alpha L}\left[\left(1+\tilde{\rho}e^{-i\phi}+\tilde{\rho}^2e^{-2i\phi}+...\right)\right. \\ &\quad \left.\times\left(1+\tilde{\rho}e^{+i\phi}+\tilde{\rho}^2e^{+2i\phi}+...\right)\right]|\mathrm{wp}(\omega)|^2 \end{aligned} \tag{3.11}$$

where the substitutions $\alpha = 2\alpha'$, $\phi = \frac{2nL\omega}{c}$ and $\tilde{\rho} = \rho e^{-\alpha L}$ were made. Here, α is the propagation loss in *power* units. This equation is a product of two polynomials. Expanding this expression gives

$$\begin{aligned} I_T(\omega) &= \tau^2 e^{-\alpha L}\left[\left(1+\tilde{\rho}^2+\tilde{\rho}^4+\tilde{\rho}^6+...\right)\right. \\ &\quad +\left(\tilde{\rho}+\tilde{\rho}^3+\tilde{\rho}^5+...\right)e^{-i\phi}+\left(\tilde{\rho}+\tilde{\rho}^3+\tilde{\rho}^5+...\right)e^{+i\phi} \\ &\quad +\left(\tilde{\rho}^2+\tilde{\rho}^4+\tilde{\rho}^6+...\right)e^{-2i\phi}+\left(\tilde{\rho}^2+\tilde{\rho}^4+\tilde{\rho}^6+...\right)e^{+2i\phi} \\ &\quad \left.+...\right]|\mathrm{wp}(\omega)|^2 \end{aligned} \tag{3.12}$$

To simplify this further we use the identity

$$e^{i\phi}+e^{-i\phi} = 2\cos\phi$$

and therefore Eqn. 3.12 becomes

$$\begin{aligned} I_T(\omega) &= \tau^2 e^{-\alpha L}\left[\left(1+\tilde{\rho}^2+\tilde{\rho}^4+\tilde{\rho}^6+...\right)\right. \\ &\quad +2\left(\tilde{\rho}+\tilde{\rho}^3+\tilde{\rho}^5+...\right)\cos\phi \\ &\quad +2\left(\tilde{\rho}^2+\tilde{\rho}^4+\tilde{\rho}^6+...\right)\cos(2\phi) \\ &\quad \left.+...\right]|\mathrm{wp}(\omega)|^2 \end{aligned}$$

$$= [I_0 + I_1 \cos\phi + I_2 \cos(2\phi) + ... + I_k \cos(k\phi) + ...] \, |\mathrm{wp}(\omega)|^2$$
$$= \sum_{m=0}^{\infty} I_m \cos(m\phi) |\mathrm{wp}(\omega)|^2 \quad (3.13)$$

This expression is the Fourier *cosine* series expansion for transmission through a single Fabry-Pérot cavity and I_m are the Fourier coefficients. I_0 is the constant, DC component of the signal and all other terms of the series are frequency-dependent. Figure 3.14 is an illustration of the decomposition of spectral data into Fourier components.

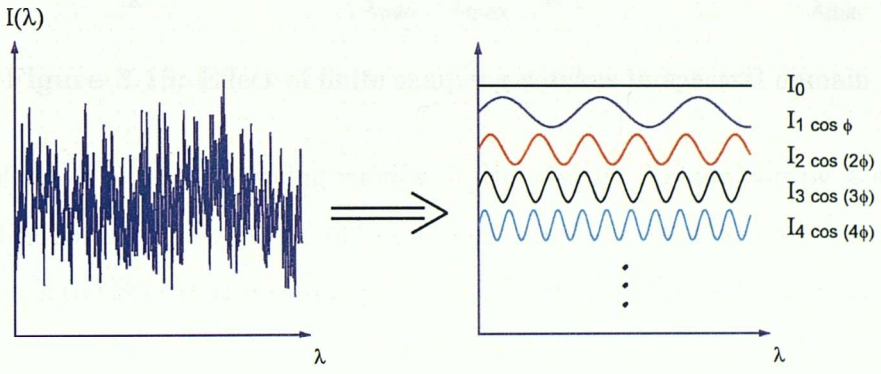
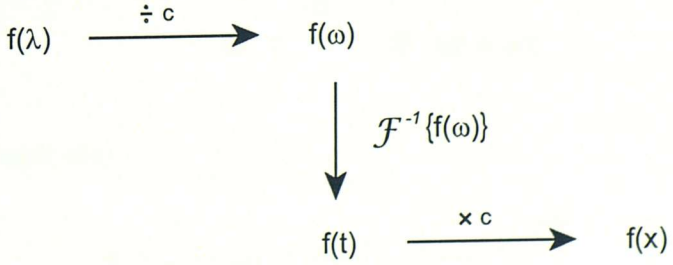


Figure 3.14: Decomposition of spectral data into Fourier components.

3.4.2 The Fourier Transform

Optical characterization of samples was carried out by performing frequency scans with a tuneable laser. This spectral data was Fourier-transformed using an inverse Fourier transform to represent the data in the Fourier domain. This process is schematically shown below.



As the wavelength range of the measured data is limited by the tuning range of the laser source, the signal can be thought of as an infinitely long spectral signal multiplied by a step function, see Fig. 3.15.

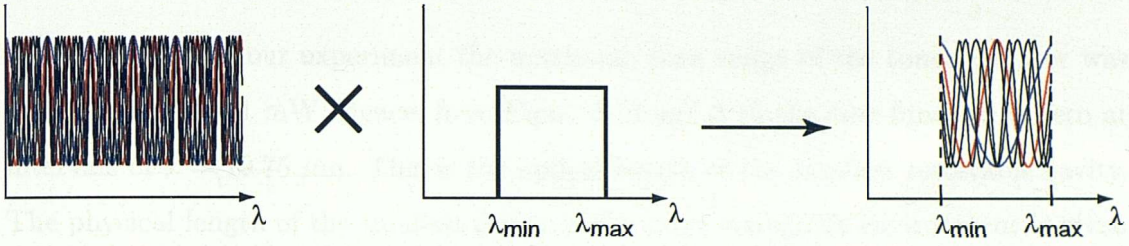


Figure 3.15: Effect of finite sampling window in spectral domain.

The effect of a finite sampling window in the Fourier domain can be described as follows: the Fourier transformed infinitely long signal is convolved with a *sinc* function, which is the Fourier transform of a *rect* function [32]. This is depicted in Fig. 3.16.

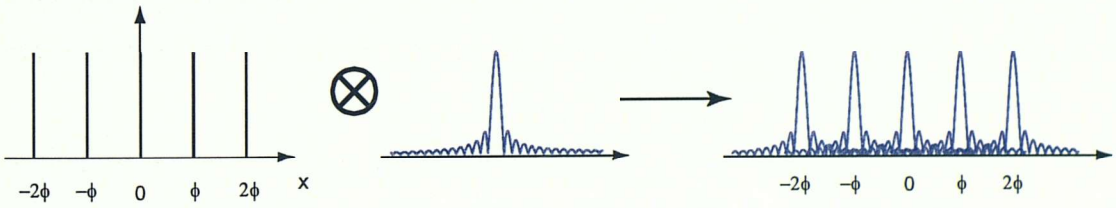


Figure 3.16: Effect of finite sampling window in Fourier domain.

The zeros of this *sinc* function determine the resolution limit of this technique. It is true that

$$\begin{aligned} f(x) &= \frac{\sin(ax)}{ax} \\ &= 0 \qquad \text{if} \quad ax = n\pi \end{aligned} \tag{3.14}$$

where n is an integer and

$$a = \frac{1}{2c}(\omega_{max} - \omega_{min}), \quad \omega_{max} = \frac{2\pi c}{\lambda_{min}} \tag{3.15}$$

Therefore the resolution is entirely determined by the size of the sampling window! The larger the scan range, the shorter the spacing of the zeros of the above *sinc* function, the higher the resolution in the Fourier domain. This highlights the need for a source with a large tuning range.

In the case of our experiment the maximum scan range of the tuneable laser was 1510-1635 nm at 1 mW. Hence, from Eqns. 3.14 and 3.15 the *sinc* function is zero at intervals of $x = 19.75\ \mu$m. This is the optical length of the smallest resolvable cavity. The physical length of the smallest cavity in the ridge waveguide environment is given by

$$\begin{aligned} 19.75 &= 2nL \\ \rightarrow L &\simeq 3.01\ \mu\text{m} \end{aligned}$$

An effective refractive index of $n = 3.278$ was used (see Section 3.3.3). This resolution limit also gives the maximum accuracy with which structural information of the device can be extracted from the Fourier representation of wavelength scans.

A number of issues require special attention.

Spatial coherence length

The largest spatial coherence length [33] (cavity length), x_s, that can be detected by a discretized frequency signal is given by

$$x_s = \frac{c}{\Delta\nu} = \frac{c}{\left(\frac{c}{\lambda_{min}} - \frac{c}{\lambda_{max}}\right) \times \frac{1}{n_s}} \tag{3.16}$$

where c is the speed of light in vacuum, n_s is the number of sample points, $n_s = (\lambda_{max} - \lambda_{min}) \div \Delta\lambda + 1$ and $\Delta\lambda$ = step length of wavelength scan. However, x_s is the length of the entire Fourier range, going from $-x_{max}$ to $+x_{max}$. Therefore,

the largest physical cavity detectable by a discretized frequency signal is given by

$$\frac{x_s}{2} = x'_s$$

It is worth noting that the step length of scans is the main factor in determining x'_s. The values corresponding to the measurements described in Section 4.3 on Page 155 are shown in Table 3.2.

scan range	1510-1635 nm
step length	0.05 nm
$\rightarrow n_s$	2501
$\Rightarrow x'_s$	~24.70 mm

Table 3.2: Spatial coherence length data

The largest cavity that is detectable in our experiment is therefore ~24.7 mm long, which is well within the coherence length of the laser (laser linewidth $\approx$ 100 kHz $\rightarrow$ coherence length $\simeq$ 3 km!). Devices were never longer than ~1 mm, but many other unwanted optical 'cavities' in the set-up are shorter than 24.7 mm, such as inside the microscope objectives, the beamsplitter or the polarizer. The signatures of these cavities will appear in the Fourier representation of the measured data.

Fast Fourier Transform

The fast Fourier Transform (FFT) is an algorithm that performs discrete Fourier transforms very efficiently [34]. Greatest efficiency is achieved if the number of data points to be transformed is an integer power of two.

Preparing the data correctly prior to performing the FFT is the key to obtaining correct results. The data in the frequency domain, $I(\omega)$, must be evenly spaced, which was accomplished by linear interpolation between the data points.

Zero-padding was carried out. This numerical trick is often used with Fourier transformations to match the Nyquist frequency [35] to the spatial coherence length. The Nyquist frequency can be described as follows. If a signal $f(t)$ has no frequency components at values greater than a frequency value ν_N then this signal can be uniquely represented by its equally spaced samples if the sampling frequency ν_s is greater than or equal to $2\nu_N$. The minimum required sampling frequency is $\nu_s = 2\nu_N$, where ν_N is known as the Nyquist frequency. Thus

$$\nu_N = \frac{\nu_s}{2} \tag{3.17}$$

For our characterization set-up the highest sampling frequency is $\nu_s = c/1510$ nm, so $\nu_N \approx 1 \times 10^{14}$ Hz. *Aliasing* is a phenomenon that occurs when one samples a signal that contains frequency components above the Nyquist frequency [32].

3.4.3 Single Fabry-Pérot cavity

Figure 3.17 is the Fourier representation of a transmission spectrum for a Fabry-Pérot cavity and was calculated using Eqns. B.1 (Page 246) and 3.10. The parameters used in this calculation are listed in Table 3.3.

n	3.278
λ	1510-1635 nm
$\Delta\lambda$	50 pm
L	700 μm

Table 3.3: Parameters for FP-cavity transmission calculation.

Resonance peaks occur every $2nL$ length units, because at these intervals the *cosine* functions in Eqn. 3.13 equal 1, leaving only the Fourier coefficients of the series. These coefficients, I_p, describe the sum of amplitudes of the $+p$ and $-p$ resonance peaks. Analytical expressions for the Fourier coefficients are derived in the following Section.

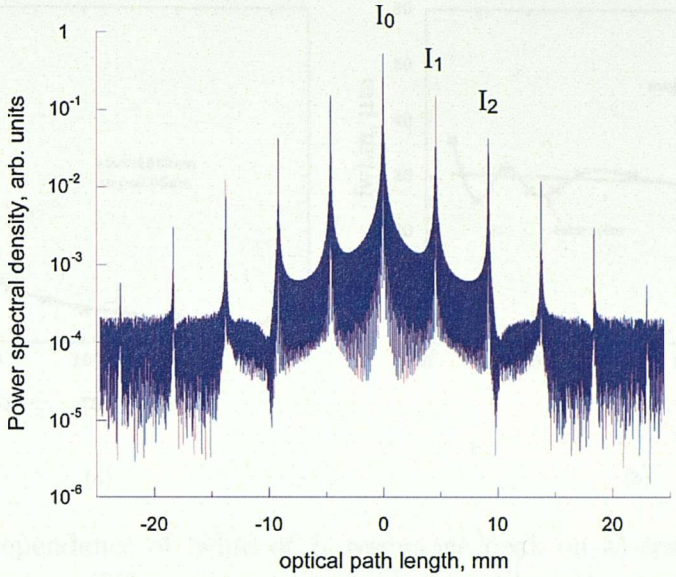


Figure 3.17: Fourier representation of transmission spectrum for FP cavity

The effect of varying the scan range and step length on the features in Fourier representation was studied. The full width half maximum (fwhm) of the I_1 peak in the Fourier representation of transmission measurements was compared and the results are shown in Figs. 3.18.

From Fig. 3.18a it is evident that the width of the resonance peaks is sensitive to the scan range, as expected from Section 3.4.2. The larger the scan range, the narrower the peaks, i.e. the more accurate the resolution in the Fourier domain. On the other hand the fwhm is rather insensitive to variations in the step length of scans, as shown in Fig. 3.18b.

3.4.4 Derivation of Fourier coefficients in Transmission

Single cavity case

The Fourier coefficients are the constant factors in the terms of the Fourier series shown in Eqn. 3.13. We will start by developing an analytical expression for the DC term, I_0, then derive equations for I_1 and I_2 and finally obtain the general expression for I_p,

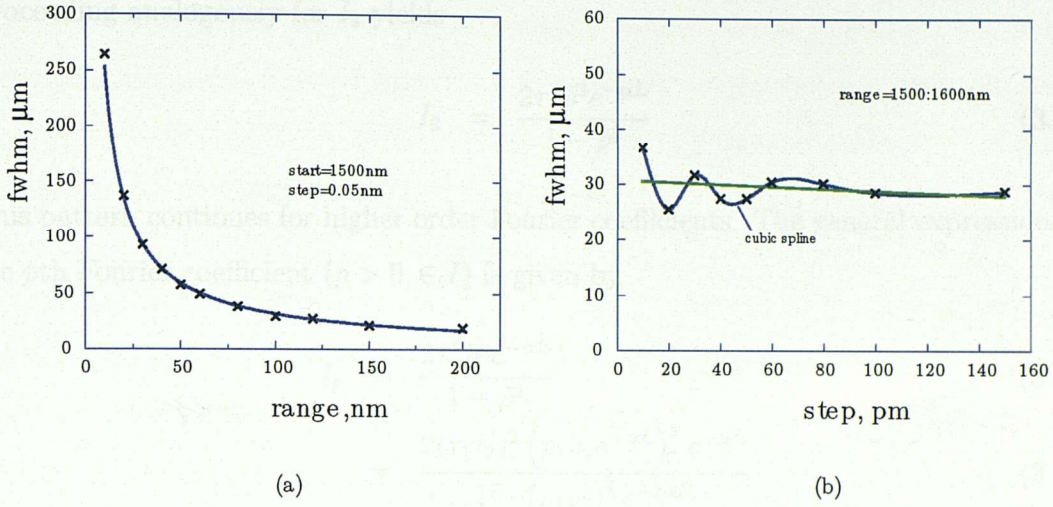


Figure 3.18: Dependence of fwhm of I_1 resonance peak on a) scan range, b) step length. In both cases a 700 μm long cavity with refractive index n=3.278 surrounded by air was used.

where p is an integer.

From Eqn. 3.12 the zero-order Fourier coefficient is obtained.

$$I_0 = \tau^2 e^{-\alpha L}\left(1+\tilde{\rho}^2+\tilde{\rho}^4+\tilde{\rho}^6+...\right) \tag{3.18}$$

This is a geometric progression and can be written as

$$I_0 = \frac{\tau^2 e^{-\alpha L}}{1-\tilde{\rho}^2} \tag{3.19}$$

Similarly, I_1 is given by

$$\begin{aligned} I_1 &= 2\tau^2 e^{-\alpha L}\left(\tilde{\rho}+\tilde{\rho}^3+\tilde{\rho}^5+...\right) \\ &= 2\tau^2\tilde{\rho}e^{-\alpha L}\left(1+\tilde{\rho}^2+\tilde{\rho}^4+...\right) \\ &= \frac{2\tau^2\tilde{\rho}e^{-\alpha L}}{1-\tilde{\rho}^2} \end{aligned} \tag{3.20}$$

Proceeding analogously for I_2 yields

$$I_2 = \frac{2\tau^2\tilde{\rho}^2 e^{-\alpha L}}{1-\tilde{\rho}^2} \tag{3.21}$$

This pattern continues for higher order Fourier coefficients. The general expression for the pth Fourier coefficient ($p > 0, \in I$) is given by

$$I_p = \frac{2\tau^2\tilde{\rho}^p e^{-\alpha L}}{1-\tilde{\rho}^2} \tag{3.22}$$

$$= \frac{2(\tau_1\tau_2)^2\left(\rho_1\rho_2 e^{-\alpha L}\right)^p e^{-\alpha L}}{1-(\rho_1\rho_2)^2 e^{-2\alpha L}} \tag{3.23}$$

This concise and highly general expression can be used to extract the propagation loss coefficient, α. This can be accomplished by taking the ratio of two consecutive Fourier coefficients, i.e. the values of the resonance peaks in the Fourier representation of the data, such as Fig. 3.17. Using Eqn. 3.23 this leads to

$$\frac{I_{p+1}}{I_p} = \rho_1\rho_2 e^{-\alpha L} \tag{3.24}$$

$$\rightarrow \alpha = -\frac{1}{L}\ln\left(\frac{I_{p+1}}{I_p}\frac{1}{\rho_1\rho_2}\right) \tag{3.25}$$

In practice it is convenient to use the I_0 and I_1 coefficients to extract the propagation loss, giving the following expression

$$\frac{I_1}{I_0} = 2\rho_1\rho_2 e^{-\alpha L} \tag{3.26}$$

As mentioned before, I_1 is the sum of the resonance peak value at $-2nL$ and $+2nL$, which stems from the $e^{\pm i\phi}$ terms in Eqn. 3.12. It is convenient to only regard one of these peaks and take this into account in the above equation. Using $I_1' = I_1/2$ Eqn. 3.25 is rearranged to give

$$\alpha = -\frac{1}{L}\ln\left(\frac{I_1'}{I_0}\frac{1}{\rho_1\rho_2}\right) \tag{3.27}$$

The above equation is an accurate analytical expression for extracting the propagation loss in a single Fabry-Pérot cavity from Fourier-transformed transmission measurements. In Section 3.4.4 we will derive a similar expression for the loss coefficient associated with propagation through a photonic crystal region inside a Fabry-Pérot cavity.

The accuracy of extracting the waveguide propagation loss using Eqn. 3.27 was analyzed numerically. Single FP cavities with different loss coefficients were modeled using `MultiLayer`. Care was taken to use the same scan parameters (wavelength range, step length) that occur in the characterization set-up described in Section 4.3 on Page 155, to mimic the experiment. Transmission spectra were Fourier-transformed and the values of the I_0 and I_1 peaks were used to extract α. Figure 3.19 shows the accuracy of the extracted α with respect to the α set in the model. Using the parameters in Table 3.3 the accuracy of this method was found to be better than 3%.

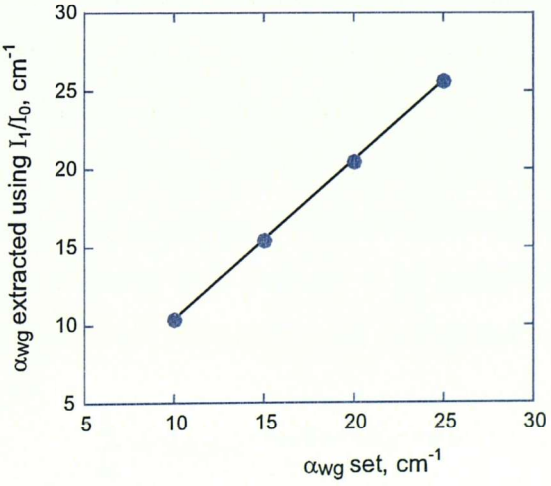


Figure 3.19: Extraction of waveguide loss from simulated data. Good agreement was observed between the set and extracted α_{wg}.

Photonic crystal patterned waveguide

The case of a waveguide that contains a photonic crystal pattern is somewhat different. With the introduction of the PhC region the ridge can be regarded as consisting of three distinct regions: two, usually uneven, waveguide sections of length L_s (short) and L_l (long) with loss coefficient α_{wg} and a photonic crystal region of length L_p and loss coefficient α_p. These different regions act as coupled cavities with their characteristic resonance peaks in the Fourier representation of transmission and reflection. Figure 3.20 was generated by Fourier-transforming a transmission spectrum of a lossless structure, calculated using `MultiLayer`. The photonic crystal region was represented as having an effective refractive index[2].

The overall propagation loss inside the ridge is described by

$$e^{-\alpha L} \rightarrow e^{-\alpha_{wg}(L_s+L_l)} e^{-\alpha_p L_p} \tag{3.28}$$

As a reminder, we are only interested in losses for light outside the photonic bandgap. Ideally the photonic crystal region would be perfectly transparent and the waveguide:PhC interface would have zero reflectivity. This is unrealistic, as the PhC patterned region has a different effective refractive index from the unpatterned waveguide region, leading to Fresnel-type reflection coefficients. Nonetheless, as a first approximation these reflection coefficients were assumed to be negligible. Following Eqn. 3.26 the expression for the normalized resonance peak corresponding to the overall cavity, I_t, is given by

$$\frac{I_t}{I_0} = 2\rho_1\rho_2 e^{-\alpha_{wg}(L_s+L_l)} e^{-\alpha_p L_p} \tag{3.29}$$

where $\rho_{1,2}$ are the reflection coefficients of the front are rear waveguide facets. This can be rearranged to give an expression for the propagation loss coefficient inside the photonic crystal:

$$\alpha_p = -\frac{1}{L_p}\ln\left(\frac{I_t'}{I_0}\frac{1}{\rho_1\rho_2}\right) - \frac{\alpha_{wg}(L_s+L_l)}{L_p} \tag{3.30}$$

[2]The first order approximation of the PhC region's effictive index was calculated as $n_{eff}(phc) = f \cdot n(air) + (1-f) \cdot n_{eff}(wg)$, with $f = 0.3$.

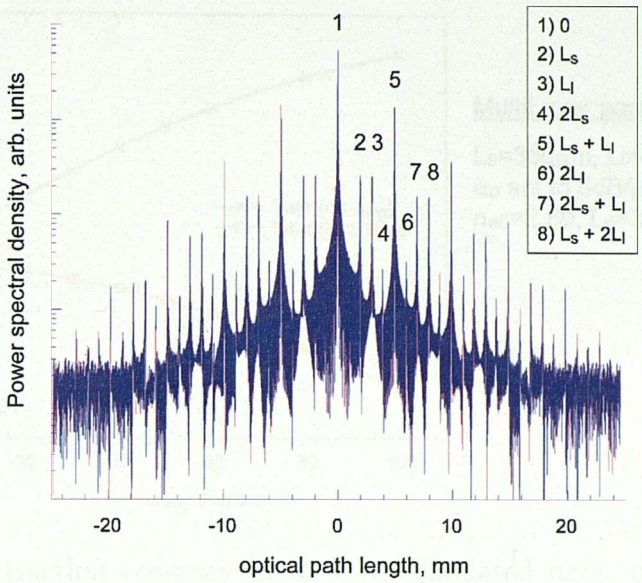


Figure 3.20: Modelled FT-transmission spectrum of waveguide with PhC. The following parameters were used to calculate this Figure: $L_s = 300$ μm, $L_l = 460$ μm, $L_p = 3.6$ μm, $n_{eff}(wg) = 3.24$, $n_{eff}(phc) = 2.59$, $\alpha_{wg} = \alpha_p = 0$. The physical length corresponding to the first eight peaks is given in the box.

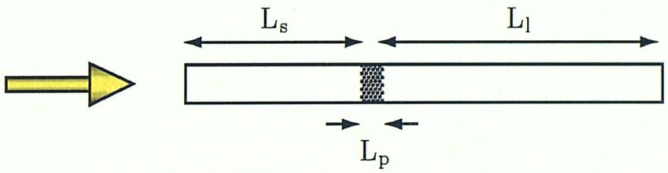


Figure 3.21: Schematic representation of ridge with PhC.

where $I_t' = I_t/2$.

Shown in Fig. 3.22 is a comparison of two methods of extracting α_p from data calculated with `MultiLayer`. $\alpha_p = 5$ dB/μm was chosen, because some of the highest losses we observed were of this order of magnitude. The two methods are **a**) ignoring losses due to waveguide propagation (Eqn. 3.27) and **b**) including waveguide loss effects (Eqn. 3.30).

The accuracy of α_p is seen to be improved by taking the waveguide loss into account. At $\alpha_{wg} = 60$ dB/cm, which is typical for our ridges, method **a** yields ~18% accuracy and method **b** ~9%. At other α_{wg}-values the accuracy of method **b** is also

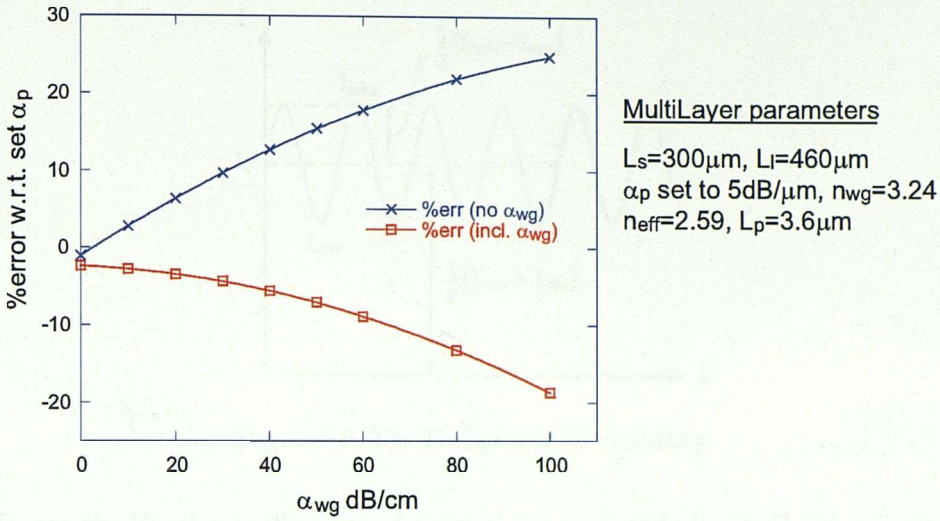


Figure 3.22: Extraction accuracy of α_p from simulated data, using two different approximations.

$\sim$2 times better than method **a**. It is worth noting that method **a** overestimatest the true value of α_{wg}, and method **b** underestimates it.

Visibility

The concept of visibility is useful for characterizing resonance fringe patterns, such as those due to transmission through Fabry-Pérot cavities discussed in Section 3.4.1. The quality of fringes produced by any interferometric system can be described quantitatively by the visibility, also called contrast or modulation [27], given generally by

$$V = \frac{I_{max} - I_{min}}{I_{max} + I_{min}} \tag{3.31}$$

Figure 3.23 is an illustration of the quantities in Eqn. 3.31. I_{max} and I_{min} are the maximum and minimum signal intensities, respectively. For a time-varying signal these can be expressed, using Eqn. 3.13, as

$$I(\omega)_{max} = I_0 + I_1 + I_2 + I_3 + I_4 + ...$$
$$I(\omega)_{min} = I_0 - I_1 + I_2 - I_3 + I_4 + ...$$

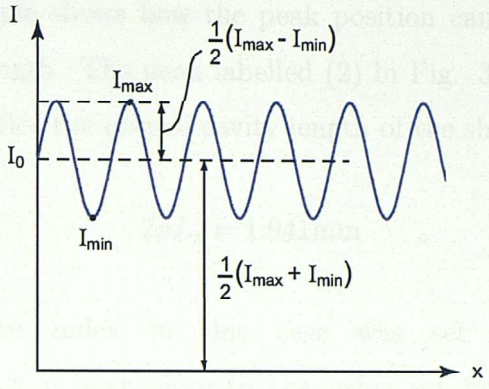


Figure 3.23: Definition of visibility.

where I_m are the Fourier coefficients of a signal decomposed into its Fourier components. Therefore,

$$\begin{aligned} V &= \frac{2\,(I_1 + I_3 + I_5 + ...)}{2\,(I_0 + I_2 + I_4 + ...)} \\ \rightarrow V &\approx \frac{I_1}{I_0} \end{aligned} \tag{3.32}$$

Equation 3.32 is the first-order approximation of the visibility. This is a good approximation, because the values of successive Fourier coefficients decreases rapidly, as given by Eqn. 3.24. For instance, for a 700 μm long unpatterned waveguide with $\alpha_{wg} = 60$ dB/cm we calculate $I_{n+1}/I_n \sim 0.27$, so $I_{n+2} \sim 0.073 I_n$.

3.4.5 Extracting cavity dimensions from the Fourier picture

The Fourier representation of transmission measurements has been shown to be very useful due to the relationships between resonance peak heights and loss coefficients. This makes use of the y-axis of graphs such as Fig. 3.20. The x-axis bears all the structural information of the device under investigation. Resonance peaks occur at positions along the x-axis, which correspond to particular cavities or their harmonic resonances. Therefore, a resonance peak is a clear signature of a cavity and it can be used to calculate the physical dimensions of that cavity.

The following example shows how the peak position can be used to extract the corresponding cavity length. The peak labelled (2) in Fig. 3.20 occurs at 1.941 mm, which corresponds to twice the optical cavity length of the short cavity; see Fig. 3.21.

$$2nL_s = 1.941\text{mm}$$

The effective refractive index in this case was set to 3.24. Therefore, $L_s = 299.54$ μm, which is very close to the value set for L_s in the calculation, $L_s = 300$ μm. The accuracy of the cavity length obtained by looking at the x-value of the resonance peak position was always found to be as good as in this example.

When working with measured data from real devices there was an uncertainty in the effective refractive index of the waveguide. This was obtained using `FWave`.

Furthermore, the interface between the PhC region and the waveguide region is not clear in real structures. There is no hard boundary and the electromagnetic waves penetrate into the PhC region a certain distance known as the penetration depth. This varies from one PhC structure to another with fill factor, hole depth and other factors. Therefore, the cavity lengths obtained from Fourier-transformed 'real' data contain larger errors than with modelled data.

3.5 Conclusion

The issues surrounding the theoretical modelling of photonic crystals in waveguide structures were presented in this Chapter. It is intended as an overview of the various modelling techniques and tools. The key points addressed are:

Design of photonic crystals. A range of possible pattern geometries were introduced, limitations and approximations were discussed.

Techniques used to model complete photonic crystal systems were highlighted, strengths and weaknesses were summarized.

Design of planar waveguide structures. This is the foundation for the entire experimental work. Well-established techniques were used to design (Al,Ga)As wafers.

Fourier Analysis (FA) was introduced as a powerful tool for characterizing Fabry-Pérot-type cavity structures, such as the devices created in this project. The importance of preparing spectral data correctly prior to Fourier analyzing it was highlighted. It was demonstrated that FA is a convenient tool for obtaining waveguide and photonic crystal propagation loss coefficients, as well as accurate structural information of the device. This technique is used in Chapter 5 as a measurement tool for assessing the losses of photonic crystals in ridge waveguide structures.

Bibliography

[1] L. Dal Negro. Light transport through the band-edge states of Fibonacci quasicrystals. *Phys. Rev. Lett.*, 90(5):55501, February 2003.

[2] R. Padjen, J. M. Gérard, and J. Y. Marzin. Analysis of the filling pattern dependence of the photonic bandgap for two-dimensional systems. *J. Mod. Opt.*, 41(2):295–310, 1994.

[3] D. Cassagne, C. Jouanin, and D. Bertho. Hexagonal photonic-band-gap structures. *Phys. Rev. B*, 53(11):7134–7142, March 1996.

[4] J. B. Nielsen, T. Sondergaard, S. E. Barkou, A. Bjarklev, J. Broeng, and M. B. Nielsen. Two-dimensional Kagomé structure, fundamental hexagonal photonic crystal configuration. *Electron. Lett.*, 35(20), September 1999.

[5] D. Cassagne, C. Jouanin, and D. Bertho. Optical properties of two-dimensional photonic crystals with graphite structure. *Appl. Phys. Lett.*, 70(3):289–291, January 1997.

[6] C. Kittel. *Introduction to Solid State Physics.* John Wiley & Sons, 7th edition, 1996.

[7] plane wave expansion codes provided by P. N. Stavrinou, Imperial College London.

[8] private communications with P. N. Stavrinou at Imperial College London.

[9] R. D. Meade, K. D. Brommer, A. M. Rappe, and J. D. Joannopoulos. Existence of a photonic band gap in two dimensions. *Appl. Phys. Lett.*, 61(4):495–497, July 1992.

[10] K. M. Leung and Y. F. Liu. Full vector wave calculation of photonic band structures in face-centred-cubic dielectric media. *Phys. Rev. Lett.*, 65(21):2646–2649, November 1990.

[11] J. Jin. *The finite element method in electromagnetics.* Wiley, 1993.

[12] G. Bao, D. C. Dobson, and J. A. Cox. Mathematical studies in rigorous grating theory. *J. Opt. Soc. Am. A*, 12(5), May 1995.

[13] B. P. Hiett. *Photonic crystal modelling using finite element analysis.* PhD thesis, University of Southampton, December 2002.

[14] D. H. Beckett, S. J. Cox, J. M. Generowicz, B. P. Hiett, M. Molinari, and K. S. Thomas. Application of finite element methods to photonic crystal modelling. *IEE CEM*, Ref.2002/063, April 2002.

[15] K. S. Yee. Numerical solution of initial boundary value problems involving Maxwell's equations in isotropic media. *IEEE Trans. Antennas Propag.*, 14:302–307, May 1966.

[16] J.-P. Berenger. A perfectly matched layer for the absorption of electromagnetic waves. *J. Comput. Phys.*, 114:185–200, 1994.

[17] A. J. Ward. Light on a lattice. *Contemp. Phys.*, 40(2):117–137, 1999.

[18] Y. Tanaka, T. Asano, Y. Akahane, B.-S. Song, and S. Noda. Theoretical investigation of a two-dimensional photonic crystal slab with truncated cone air holes. *Appl. Phys. Lett.*, 82(11):1661–1663, March 2003.

[19] M. Lončar, D. Nedeljkovič, T. P. Pearsall, J. Vučkovič, A. Scherer, S. Kuchinsky, and D. C. Allan. Experimental and theoretical confirmation of Bloch-mode light propagation in planar photonic crystal waveguides. *Appl. Phys. Lett.*, 80(10):1689–1691, March 2002.

[20] B. D'Urso, O. Painter, J. O'Brien, T. Tombrello, A. Yariv, and A. Scherer. Modal reflectivity in finite-depth two-dimensional photonic-crystal microcavities. *J. Opt. Soc. Am. B*, 15(3):1155–1159, March 1998.

[21] J. B. Pendry and A. MacKinnon. Calculation of photon dispersion relations. *Phys. Rev. Lett.*, 69(19):2772–2774, November 1992.

[22] M. M. Sigalas, C. M. Soukoulis, C. T. Chan, and K. M. Ho. Electromagnetic-wave propagation through dispersive and absorptive photonic band-gap-materials. *Phys. Rev. B*, 49(16):11080–11087, April 1994.

[23] D. M. Whittaker and I. S. Culshaw. Scattering-matrix treatment of patterned multilayer photonic structures. *Phys. Rev. B*, 60(4):2610–2618, July 1999.

[24] A. J. Baden Fuller. *Microwaves.* Pergamon, 2nd edition, 1979.

[25] R. G. Hunsperger. *Integrated Optics.* Springer, 4th edition, 1995.

[26] A. Yariv. *Optical Electronics in Modern Communication.* Oxford University Press, 5th edition, 1997.

[27] E. Hecht. *Optics.* Addison-Wesley, 2nd edition, 1987.

[28] provided by M. Whitehead, with permission of R. Geels at University of California, Santa Barbara.

[29] private communications with B. Poole, Sharp Laboratories of Europe.

[30] M. A. Afromowitz. Refractive index of Ga(1-x)Al(x)As. *Solid State Commun.*, 15:59–63, 1974.

[31] A. Talneau, M. Mulot, S. Anand, and Ph. Lalanne. Compound cavity measurement of transmission and reflection of a tapered single-line photonic-crystal waveguide. *Appl. Phys. Lett.*, 82(16):2577–2579, April 2003.

[32] A. D. Poularikas and S. Seely. *Signals and Systems.* PWS Engineering, 1985.

[33] M. Klein and T. Furtak. *Optics.* Wiley, 2nd edition, 1986.

[34] W. H. Press, B. P. Flannery, S. A. Teukolsky, and W. T. Vetterling. *Numerical Recipes in Pascal.* Cambridge University Press, 1990.

[35] F. G. Stremler. *Introduction to communication systems.* Addison-Wesley, 2nd edition, 1982.

Chapter 4

Characterization

4.1 Description of problem

Photonic crystals (PhC) were embedded into ridge waveguides, as described in Chapter 2. The PhCs have photonic bandgaps (PBG) for certain photon energies and polarizations. The central wavelength of a PBG is a function of, primarily, the geometry of the PhC, the lattice spacing, the fill factor and the refractive index contrast of the two media that make up the photonic crystal. Therefore, the central wavelength of the PBG is a key design parameter.

For photonic crystals with large refractive index contrast as in air:GaAs systems and central wavelengths around 1550 nm, the main focus of this study, the first TM bandgap is typically several hundreds of nanometers [1]. Ideally one would like to characterize the properties of the PhC over the entire bandgap.

The band structure of a photonic crystal is highly polarization-dependent [2]. This fundamental property can be exploited to make ultra-compact polarizers, out-of-plane couplers [3] and other essential components for future optical integrated circuits. The polarization-dependence must be studied experimentally. A number of groups have reported on the characterization of these structures in only one polarization; see for instance Ref. [4]. For the applications that those authors had in mind this may have been sufficient, but it is an incomplete result as other applications of PhCs are envisaged, which specifically utilize the polarization-dependence of the photonic crystals.

4.1.1 Requirements for characterization set-up

The primary demand was to have a system, which would allow focusing of light into a 4.5 μm wide ridge waveguide and collect light emerging at the output facet. The optical power detected would be very low, since the available sources have low power outputs.

The photonic crystal structures were designed to have a large bandgap in TM polarization, centred around 1550 nm, which is the wavelength region of choice in telecommunications applications. To characterize the photonic band structure of the samples over a wide spectral range would require a source with a large tuning range. There are a number of sources which can be used to cover a large spectral range.

Temporally short pulses can be used to probe the structures, as these have a large frequency (wavelength) spectrum. A white light source ideally emits light over several 1000s of nanometres. In practice this is unrealistic and a good white light source emits strongly over <1000 nm. A tuneable laser source is another possible source, whose long coherence length is a necessity in certain experiments. We characterized samples using a white light source and a semiconductor tuneable laser.

A key requirement for our experiments was to select the polarization state of light as it enters the sample, as the highly polarization-dependent nature of photonic crystals was investigated. Furthermore, the set-up needed to be sufficiently accurate and reliable to produce repeatable measurements.

4.2 White light spectroscopy

A white light source emits over the entire visible range of the electromagnetic spectrum and usually well beyond it. This type of source would be well suited for spectral characterization of optoelectronic devices, which typically operate in the near infrared (NIR) part of the spectrum. The white light sources that are available exhibit a number of problems, which render this type of experiment nearly prohibitively delicate. This Section is an account of the work undertaken in setting up a characterization experiment based around a white light source.

4.2.1 The Source

The white light source used here was a Xenon arc lamp (Oriel Xenon arc lamp 60064) that has a very broad range of emission from UV to NIR. As the trace in Fig. 4.1 shows, the Xe arc lamp has a very inhomogeneous emission spectrum, with the strongest emission peaks in the range 810-1000 nm. The power output at maximum intensity was recorded as $\sim$190 nWnm^{-1}, which is rather low compared to conventional semiconductor laser sources ($\sim$10 mW) but it is still amongst the most powerful white light sources available.

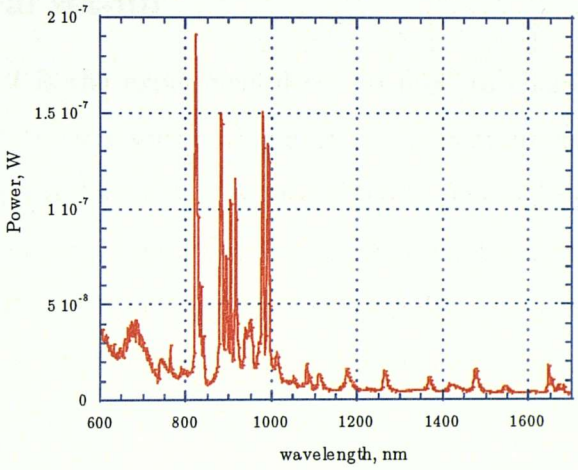


Figure 4.1: Emission spectrum of the Xenon arc lamp, as measured with the set-up shown in Fig. 4.2.

It was found that the source took about one hour to stabilise to achieve repeatable measurements. One major advantage of using an arc lamp as opposed to a conventional incandescent filament light source is that the light originates in a gap between two arc-shaped electrodes, which creates a very small source. As the source's emission spectrum was very inhomogeneous any effects due to the EM waves interaction with the device under investigation was not easily detectable. The recorded signal needed to be normalized. For this two possibilities were considered:

1. normalization with respect to the source spectrum

2. normalization with respect to measurements from a reference sample. In the case of the patterned ridge waveguides the transmission spectrum measured from an unpatterned ridge served as the reference spectrum.

Both cases were investigated. Normalization is typically carried out with respect to an unpatterned sample [4, 5, 6].

4.2.2 General set-up

Shown in Fig. 4.2 is the experimental set-up used to characterize ridge waveguide samples with a white light source. Light from a Xenon arc lamp was focused into an optical fibre using a microscope objective (MOG). The light emerging from the fibre was collimated, polarized and focused into the waveguide structure under investigation. Several methods of collecting light at the waveguide's output end were investigated. All optical components were mounted on nanopositioning stages, which had three axes of freedom and positioning resolution of 50 nm. In the following Section a detailed description of the various components of the set-up is given.

The Xenon arc lamp was the key component of this experiment. A condenser lens and a UV filter were mounted in front of the opening of the Xe lamp. The UV filter was merely a safety precaution. The emerging light was directed onto the back of a microscope objective, which was used to focus the beam of light onto the core of an FC/PC connector-fitted optical fibre. The MOG used had a numerical aperture (NA) = 0.50, magnification $\times 25$, focal length (f) = 7.2 mm and working distance (wd) = 0.44 mm. (Melles Griot cat.♯ 04 OAS014).

Two types of optical fibre were investigated: single-mode (SMF) and multi-mode (MMF) fibre. The fibres were not polarization-maintaining. The SM fibre used had

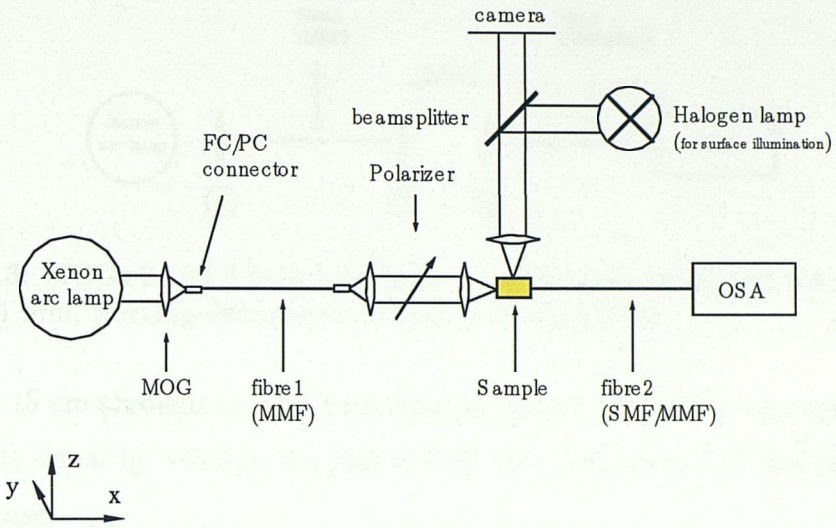


Figure 4.2: First set-up for white light characterization.

core/cladding diameters 8/125 μm, and the MM fibre had the dimensions 62.5/125 μm. The fibres had FC/PC connectors at both ends. Connectors with metal jackets were found to be much more robust and reliable than ones with plastic jackets.

To measure the output of the Xe lamp directly, the light was launched into an optical fibre using the MOG described above. The other end of the fibre was connected directly to the OSA. The device under test was designed to operate around 1300 nm. The wavelength range 1150-1350 nm was primarily focused on, because the source's emission power dropped off quickly beyond ~1350 nm. There is a peak in the Xe lamp's emission spectrum near 1267 nm. Using MMF the maximum power at that peak was measured to be ~35±2 nWnm^{-1}. With SMF the max. power was ~1.0±0.1 nWnm^{-1}. The losses when using SM fibre in this way are significantly greater than with MM fibre due to coupling losses.

The coupling efficiency in and out of optical fibre was investigated using the set-up shown in Fig. 4.3. Using MM fibre to collect the maximum amount of light from the source, the maximum power measured with MMF as fibre 2 was 12±1 nWnm^{-1} and 500±10 pWnm^{-1} with SMF as fibre 2. Hence, collimating light out from the MM fibre,

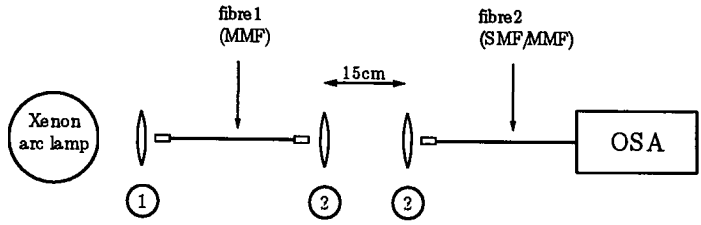


Figure 4.3: MOGs 2 and 3 both have large magnification (×63) and NA (0.85), focal length=3.1 mm, working distance=0.14 mm (♯ 04 OAS 018)

sending it 15 cm through air and back into an optical fibre using appropriate MOGs reduced the signal by ~2/3 in the case of MM fibre and about 1/2 the light is lost in the SMF case.

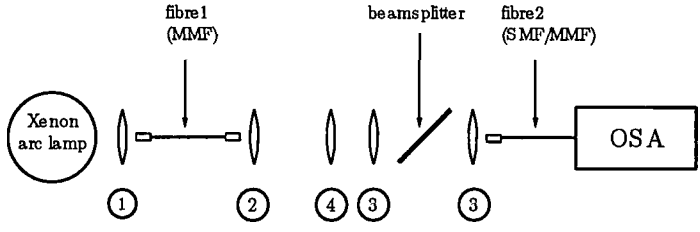


Figure 4.4: Layout with two further MOGs added. MOGs 4 and 5 have long working distances of 8.7 mm, NA=0.55 and ×50 magnification.

Two more MOGs (♯4 and 5) were added to the set-up as shown in Fig. 4.4. MOGs 4 and 5 have a long working distance (8.7 mm). The sample was later inserted between them. To obtain the minimum beam waist and spot size beyond MOG 4 and thus optimal focusing, the incident beam on MOG 4 must be perfectly collimated, as explained below. Perfect collimation does not exist in reality, as it would require perfectly planar wavefronts, which is impossible to achieve with finite optical components. Nonetheless, it is important not to focus onto the back of MOG 4, but instead 'fill' the back of MOG 4 completely by expanding the beam sufficiently with MOG 2. Without the sample in place the beam was focused by MOG 4 to a point in midair from where it was 'collected' by MOG 5. Using a MM fibre connected to the OSA the maximum power recorded at 1267 nm was 950±10 $pWnm^{-1}$ and with SMF it was 76±5 $pWnm^{-1}$. Both of these were without the beamsplitter (BS) in place. Compared

to the previous results, the loss in power due to MOGs 4 and 5 is ~92% for MM and ~85% for SM fibre. Adding a BS was found to reduce the signal in both cases by ~2/3.

4.2.3 Spot size

Focusing the light beam onto the back of MOG 4 produced a minimum spot size of 50±2 μm on the input facet of the sample, measured as explained below. Filling the back of MOG 4 completely to assure the beam was collimated reduced the spot size to 6±2 μm. A collimated beam of light produces the minimum spot size. This is depicted in Fig. 4.5, where MOG 4 is taken to be a single bi-convex lens.

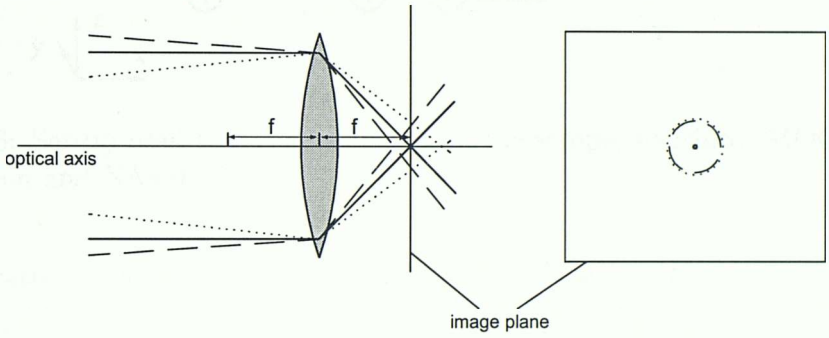


Figure 4.5: This diagram demonstrates how important it is to have a collimated input beam in order to achieve the minimum spot size when focusing through a convex lens.

Classically the diffraction limited spot diameter, ϕ_D, is given by

$$\phi_D = \frac{1.22\lambda}{\mathrm{NA}} \tag{4.1}$$

Therefore, the diffraction limited spot diameter for MOG 4 (NA=0.55), which was used to focus light into the waveguide, for monochromatic light at 1300 nm is 2.88 μm. This is significantly smaller than what was observed (~ 6±2 μm), probably due to poor beam collimation.

Samples consisted of planar AlGaAs/GaAs/AlGaAs waveguides grown by MBE

on top of an intrinsic GaAs substrate. The plane of the layers is the x-y plane. Free-standing ridges were etched to provide confinement lateral (y-direction) to the direction of propagation (x-direction).

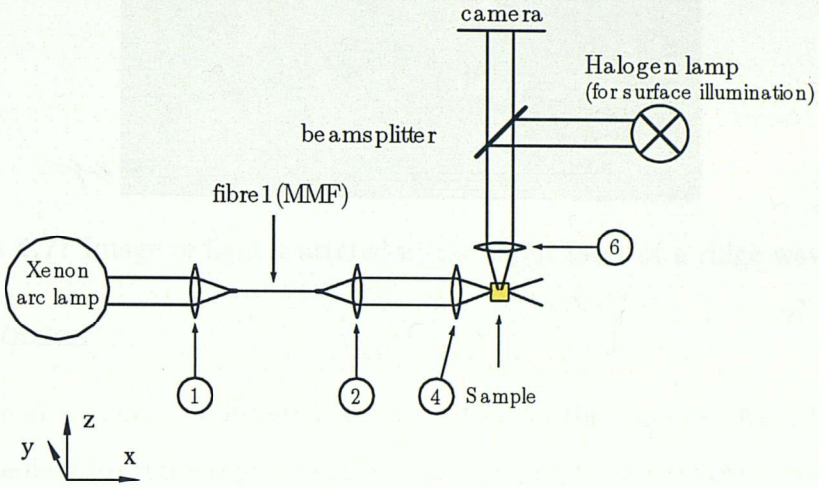


Figure 4.6: Set-up used to record an image of the sample's surface. MOG 6 has $\times 10$ magnification and NA=0.17.

Light scattered as it impinged on the input facet. The top of the sample was imaged using a charge coupled device (CCD) camera with a silicon detector, shown in Fig. 4.6. The image captured with the CCD camera was recorded using a frame grabber, which produced a digital image as in Fig. 4.7. The input beam was moved along z-dir. of the sample using the controls on MOG 4 until the largest spot size was seen. This was then minimised by focusing MOG 4. Using the known ridge width of 4.5 μm for comparison, the spot size could be measured on the recorded image. This measurement was rather crude and the true value is likely to be smaller than what was measured. The scattered light was very bright and it was difficult to determine exactly what area it originates from. Thus the stated spot diameter should be taken as the upper limit.

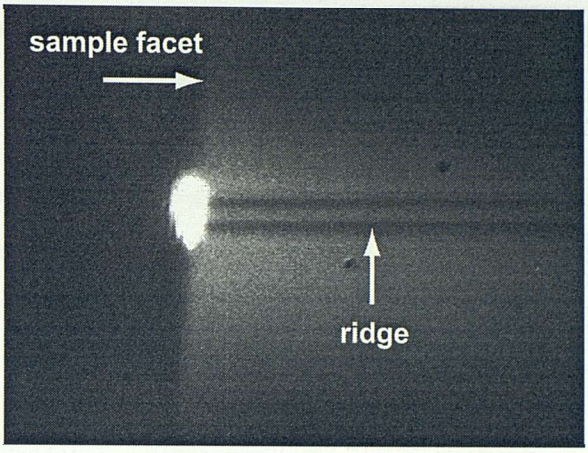


Figure 4.7: Image of light scattered at the input facet of a ridge waveguide.

4.2.4 Losses

Light was focused onto the input facet of a ridge on the sample. At a boundary of dielectric media with refractive indices of ~1.0 (air) and ~3.3 (GaAs) about 30% [1] of the EM radiation is expected to get reflected. At the output facet the same applies and again ~30% of the guided light is reflected internally. Without anti-reflection coating at most 50% of the incident light can be transmitted through a perfect GaAs-based waveguide. How significant is the loss due to reflection into and out of optical fibres? Assuming an air:silica interface at each end of the fibre one must expect about 3% reflection at each facet - approx. 96% overall transmission. The loss here is quite low due to the relatively small difference in refractive indices of the two media (n_{silica} ~1.45). It is worth stressing that every interface between dielectric media affects the transmission and reflection properties of the whole system, which is essentially a series of lossy coupled cavities. The overall transmission decreases with every added interface. Exactly how lossy each of the MOGs, beamsplitters, polarizers, etc. is, was investigated and is discussed in Section 4.4.

Coating the waveguide facets with anti-reflection coating would significantly reduce the coupling losses, but this would have been prohibitively expensive. The application

[1] Fresnel reflection coefficient for plane wave at normal incidence: $r = \frac{n2-n1}{n2+n1}$, $Reflectance = r^2$

of index-matching gel was considered in order to reduce the coupling losses, but due to the particular layout of the experiment this option was not pursued.

The ridge waveguides were 4.5 μm wide and 0.6-2 μm high. With a minimum spot size of $\sim$6 μm diameter a significant portion of the light could not be coupled into the waveguide. The waveguide core was 600 nm thick. Some of the light escaped over the top of the structure; another fraction was lost into the substrate. Figure 4.8 shows an image of the output facet of the waveguide.

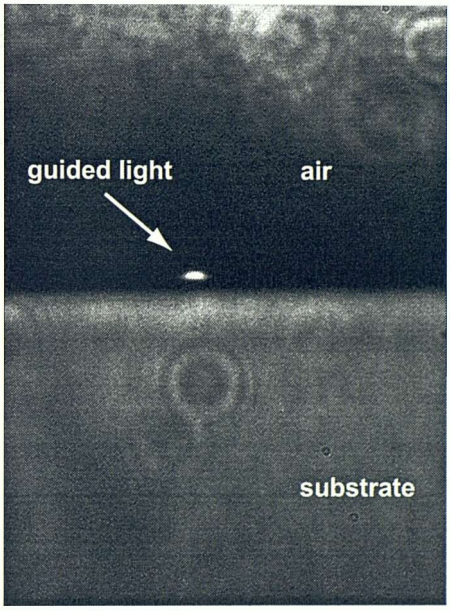


Figure 4.8: CCD camera image of the output facet.

The guided light is seen clearly. A ridge on the surface of the sample has the effect of confining the light to a 'channel' along the guiding layer. The light areas above and below the dark central region are due to light going over the top of the sample and through the substrate, respectively.

4.2.5 Output facet

Three options were considered for collecting light emerging from the output facet of the waveguide.

1. Microscope objective
2. Multi-mode fibre
3. Single-mode fibre

Using a high magnification MOG the emerging light at the rear end of the waveguide was collimated and directed onto a CCD camera to produce a real-time image of the rear facet. This enabled the alignment of the sample in the beam of light to be carried out with relative ease. Once the image showed guided light of maximum intensity, the collimated light was directed onto a MOG, which focused the light into the core of a MMF. This fibre was connected to the OSA - see Fig. 4.9.

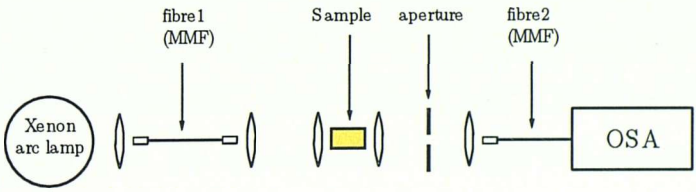


Figure 4.9: Set-up for white light measurements with MOG at output facet.

It was found that with this set-up the signal recorded at the OSA was too low to distinguish from the noise. As seen in Fig. 4.8 a significant amount of light that did not travel through the ridge waveguide emerges at the output facet. With a minimum spot diameter of $\sim$6 μm for the MOG at the output facet the guided light cannot be isolated from this light 'noise'. Attempts were made to clean up the collected light by inserting a spatial filter between the two MOGs at the output end of the sample, but these failed to produce the desired results.

Option 2 involved using a multi-mode fibre to collect light directly out of the sample. This was as shown in Fig. 4.2 with a MMF for fibre 2. The FC/PC connector at one end of a typical MMF was cut off. The fibre was stripped of all insulation and cladding, and the remaining core was cleaved vertically. The bare fibre was held in a collet fibre chuck (Melles Griot cat.♯ 17 HFC005). To ensure that the sample was well aligned with the beam of light the output facet was imaged in real-time using a high magnification MOG and a CCD camera - see Fig. 4.10.

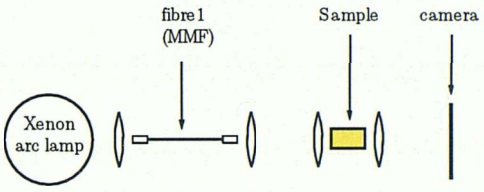


Figure 4.10: Imaging the output facet.

Once optimum alignment was achieved the MOG was removed and the cleaved fibre tip was brought to within less than ~5 μm of the output facet. In order to monitor the alignment process the top surface of the sample was imaged using the halogen lamp, MOG, CCD camera set-up described earlier. To facilitate the alignment, light from the Xe arc lamp was focused into the connector-fitted end of the cleaved MM fibre. The spot of light emerging from the cleaved end of the fibre was seen very clearly on the output facet of the sample. Once the cleaved end was in line with the ridge waveguide on the sample and as close to the facet as possible without actually touching it, the connector-fitted end of the fibre was connected to the OSA and the light was launched into fibre 1.

The transmitted signal was measured at various positions perpendicular to the output facet, i.e. along the x-direction. The result is shown in Fig. 4.11. If only guided light was collected by the fibre, then the measured intensity would be expected to decrease rapidly away from the output facet, as the tightly confined guided modes diverge strongly at the output facet. The result, however, shows that the light intensity

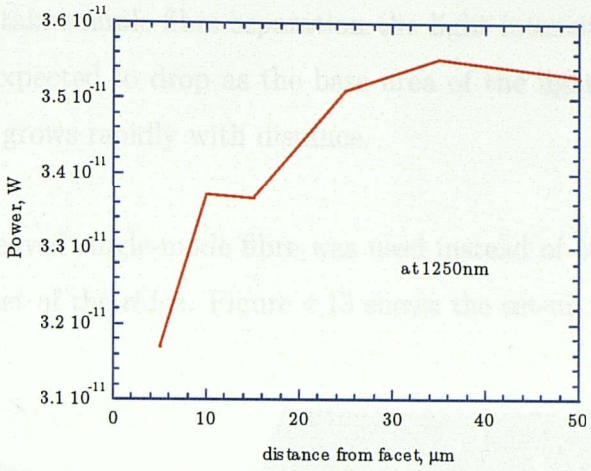


Figure 4.11: Variation of transmission signal with distance of fibre to output facet.

increased the further away from the facet the fibre was moved, until a separation of about 35 μm, beyond which the measured intensity dropped. This indicates that most of the collected light, even when the fibre nearly touched the facet, passed through the substrate rather than the guiding layer. As the fibre was moved further away from the facet, even more light from the substrate and the air was collected, because the area of the fibre is relatively large. This situation is depicted schematically in Fig. 4.12. The part of the light cone going over the top of the sample has a larger solid angle than the part going through the substrate, because the light is refracted towards the 'normal' upon entering a higher refractive index medium.

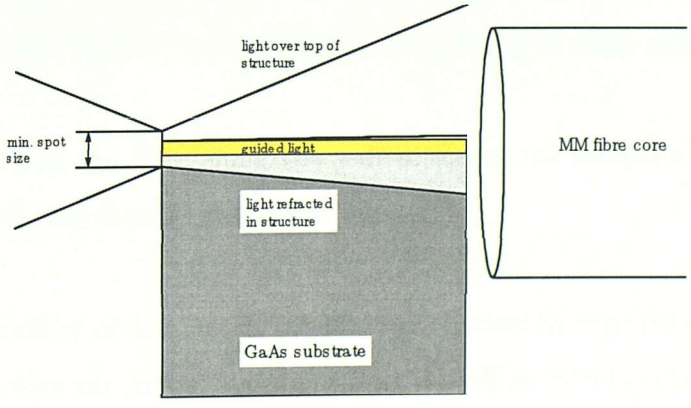


Figure 4.12: As the minimum spot size of the input beam is larger than the ridge area some light escapes through the substrate or over the top of the sample.

Beyond a certain sample-fibre separation the light intensity per unit area of fibre facet would be expected to drop as the base area of the light cones originating from the output facet grows rapidly with distance.

Option 3: Cleaved single-mode fibre was used instead of MMF to couple light out of the output facet of the ridge. Figure 4.13 shows the set-up and is drawn to scale.

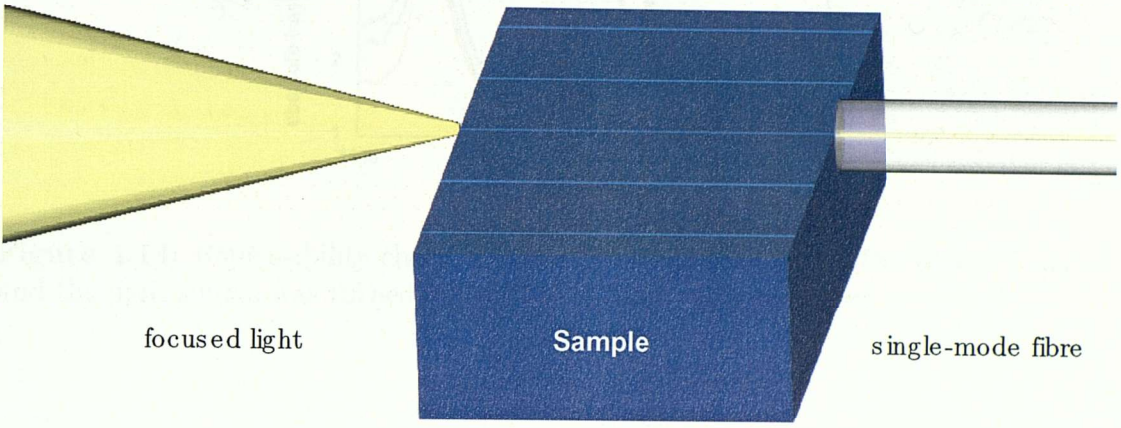


Figure 4.13: Illustration of set-up with SMF at output facet, to scale.

In general the signal due to the transmitted light was much weaker than with MMF. However, as the diameter of the cleaved core of the SMF was only 8 μm, far less of the spurious light was collected. As before, the fibre was brought in line with the output facet of the ridge and adjusted to maximise the recorded signal. The signal was weaker than with MMF, but 'cleaner' in the sense that the signal to noise ratio is much higher.

Moving the tip of the fibre along the y-direction of the sample's output facet the signal dropped off very rapidly away from the ridge.

The reproducibility of the measurements was checked by repeating a measurement after moving the fibre end in and out of position, as well as switching the light source off for 2 hours and turning it back on. The data was normalised with respect to the direct source measurements is shown in Fig. 4.14. It can be seen that the general features

do not vary much from one recording to the next. It is mainly their magnitude that changes.

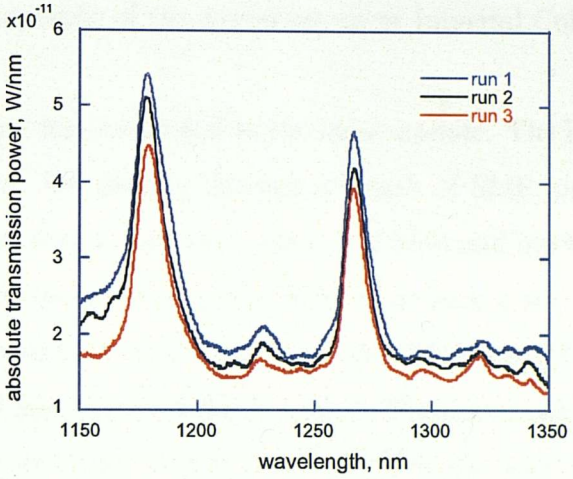


Figure 4.14: Repeatability check of white light measurements. The fibre was moved and the light source was turned off and on between measurements.

4.3 Laser-based characterization

Following the insight gained with the white light set-up the experiment was modified to employ a tuneable laser source. The following Section describes this set-up in detail.

4.3.1 Description of laser

The laser source was the Agilent Technologies solid-state tuneable laser module 81642A. It is based on an InGaAsP Fabry-Pérot cavity. The tuning range is 1509-1641 nm. This covers most of the International Telecommunications Union's (ITU) S band and all of the C and L bands, which are of particular interest for telecommunications applications. The output wavelength accuracy is ± 0.015 nm. The linewidth of the output is stated as 100 kHz, which corresponds to a coherence length of $\sim 3 \times 10^3$ m! The maximum power output occurs at 1595.0 nm and is 5.665 mW. In order to achieve constant output power across the scan range, the power level of the laser can be fixed. The laser can produce ≥ 1 mW in the range 1510-1635 nm.

4.3.2 Experimental set-up

Figure 4.15 shows the layout of the laser-based characterization experiment. Figures 4.16a and b are photographs of the actual set-up at Imperial College London.

A single mode fibre was connected to the laser module. The laser output occurs in one polarization state. On passing through a length of SMF, polarization mode dispersion (PMD) occurs due to imperfections in the fibre and mechanical strain, among other factors. The mechanical strain was induced in such a way that the light at the end of the SMF was unpolarized, i.e. approximately 50% TE, 50% TM-polarized. The beam was collimated and passed through a Glan-Thompson polarizer with which the polarization state for the light entering the waveguide was selected.

Some of the polarized light was deflected onto a detector using a beamsplitter. It is extremely useful to monitor the input light. Small changes to the strain induced in the above mentioned optical fibre result in significant changes in PMD and therefore cause large changes in the transmitted TE:TM ratio. These variations were corrected by normalizing the recorded transmission, reflection, or scattering measurements with respect to the power measured at the input detector. It was found that the transmission:reflection ratio of the beamsplitter was not 50:50 and that the behaviour was polarization-dependent. These effects were accounted for as part of the normalization.

The light that passed straight through the beamsplitter was focused into the input facet of a ridge using a long working distance, $\times 50$ magnification microscope objective with a numerical aperture of 0.55. An identical MOG was used to collect light emerging from the rear facet of the ridge. The light was directed onto a Germanium detector (accuracy of $\pm 3\%$ in tuning range of laser) and connected to a power meter. The Ge detector was used to record optical power transmitted through the ridge. Light reflected from the sample was directed onto a detector using the same beamsplitter that tapped off a part of the input light.

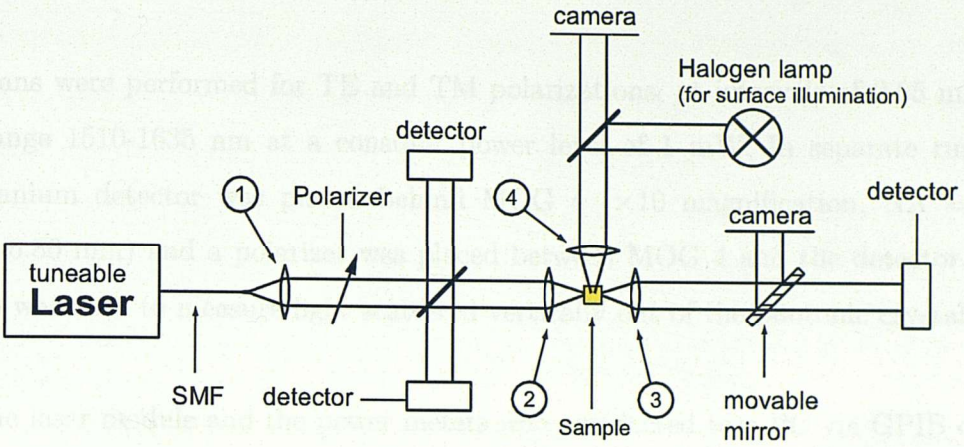


Figure 4.15: Set-up for laser-based characterization.

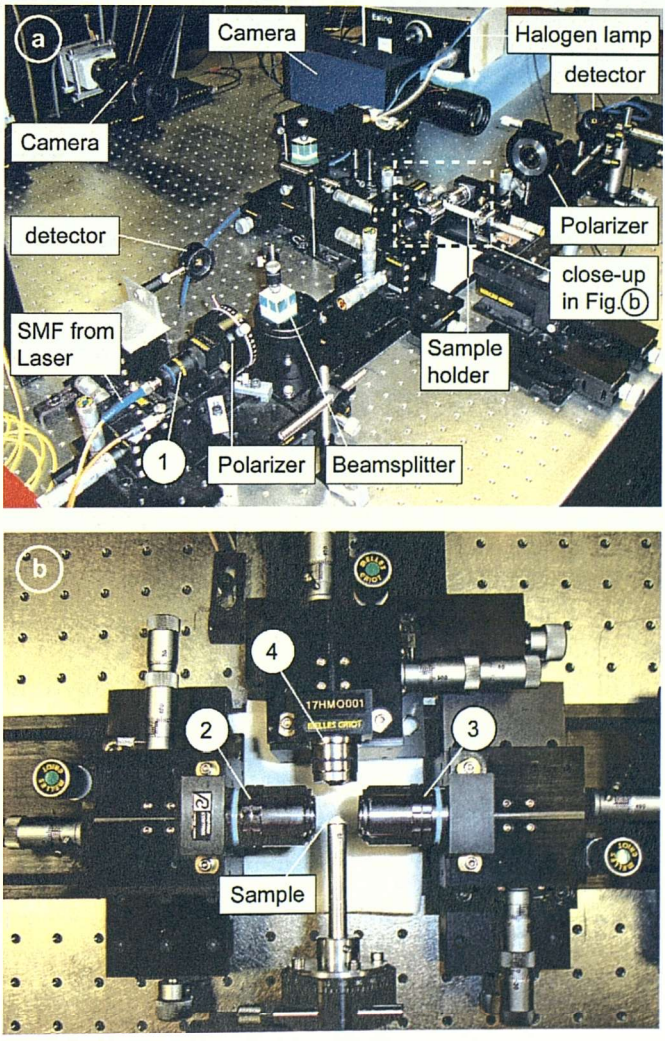


Figure 4.16: Photographs of the characterization set-up. a) All components are shown (cf. Fig. 4.15), b) close-up around the sample.

Scans were performed for TE and TM polarizations, at intervals of 0.05 nm over the range 1510-1635 nm at a constant power level of 1 mW. In separate runs the Germanium detector was placed behind MOG 4 (×10 magnification, NA = 0.17, wd = 6.80 mm) and a polarizer was placed between MOG 4 and the detector. This set-up was used to measure light scattered vertically out of the photonic crystal.

The laser module and the power meters were connected to a PC via GPIB cables. LabView VI's were used to synchronize and operate the components remotely from the PC.

4.3.3 Polarizer

A polarizer was used to select one of the two orthogonal linear polarizations, so that the state of the light incident on the sample was known exactly. Polarization can be achieved in several different ways, such as reflection at Brewster's angle, scattering, selective absorption of one polarization (dichroism) and birefringence.

Birefringence, also called double refraction, occurs in optically anisotropic media, that is, media having optical properties that depend on direction. Different refractive indices exist depending on the orientation of the incident electromagnetic wave. A birefringent crystal will divide an incident beam of monochromatic light into two beams of orthogonal polarization. Using a generalization of Huygens' principle, the propagation of waves inside birefringent media can be described as a spherical (ordinary) wave plus a wave that is an ellipsoid of revolution (extraordinary wave) - see Ref.[7], p.599-604. The **o** wave and **e** wave have refractive indices n_o and n_e, respectively. These parameters are important in the design of polarizers.

A number of polarizers exist, which all have a birefringent crystal at their hearts. Calcite, a rhombohedral crystalline form of calcium carbonate, is a birefringent mate-

rial commonly used to make polarizers. Examples are the Nicol prism, Rochon prism, Wollaston prism, Glan-Taylor prism and the Glan-Thompson prism. They each have strengths and weaknesses and the right choice of polarizer depends on the experiment. A Glan-Thompson (GTh) prism was used. This polarizer has a relatively large acceptance angle (typically ~20°) and the beam does not suffer parallel displacement.

Figure 4.17 shows a typical GTh polarizing prism. It consists of two prisms, which are cemented together. The entrance and exit facets are designed to be normal to the incident beam. The most commonly used cement is n-butyl methacrylate, which is a low refractive index polymer. The prism angle is cut so that the o wave suffers total internal reflection at the first prism and is absorbed by the prism housing. The refractive index of the cement is matched to n_e, which reduces losses due to Fresnel reflection.

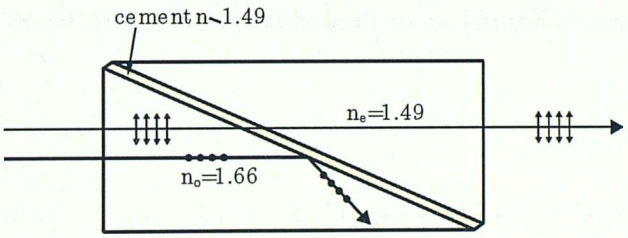


Figure 4.17: Glan-Thompson polarizing prism.

The GTh polarizing prism has a useable wavelength range of 350-2300 nm. Typical extinction ratio (transmission through two such prisms rotated by 90° to each other) is $<1\times10^{-5}$. Transmission through one GTh prism (ratio of total output to total unpolarized input) is quoted as 36%. This represents quite a significant loss to the overall system.

Such prisms typically have a number of imperfections, which lead to a performance below the ideal values quoted in the product catalogue. These fall into two categories: material and fabrication imperfections.

Material imperfections:

- Lattice defects as well as trace amount of chemical impurities in the calcite can occur and these change the absorption.
- Dislocations in the crystal lattice are not uncommon and result in streaked fluctuations in the refractive index of calcite. This can cause distortion of a light wavefront passing through the crystal.
- Small inclusions within the calcite crystal are a source of scatter. These may be small cracks or small bubbles. This would reduce the extinction ratio of the polarizer.
- The cement layer may be inhomogeneous.

All of these factors occur and will certainly lead to an overall transmission below 36%.

Fabrication imperfections:

- The optic axes of the two halves of the prism may not be exactly parallel. As a consequence, when the polarizer is rotated the axial beam would be displaced. This defect is known as *squirm* [8].
- If the two facets of the prisms are not parallel, the axial beam will be deviated.

The GTh polarizing prism is a commonly used polarizer as it has superior performance over most other polarizers in many aspects. Nonetheless, despite the impressive data sheet provided by the manufacturer actual performance of this component will be somewhat worse than the data suggests, due to the imperfections mentioned above.

4.3.4 Scattering measurements

One of the primary loss mechanisms in light interaction with photonic crystals is scattering out of the PhC. When light propagates in a waveguide and encounters a PhC, some of it is scattered vertically out of the waveguide by the PhC. Exactly how much light is lost in that way was the subject of a series of measurements performed on a photonic crystal-patterned ridge waveguide sample.

The samples under investigation were of the type shown in Fig. 2.53 on Page 97. The experimental set-up used to measure the scattered light is shown in Fig. 4.18. The MOG used to collect the light over the PhC was the same as the one used previously to illuminate the surface of the sample. It had to have a long working distance due to physical constraints close to the sample. The MOG that was used had a working distance of ~14 mm , ×10 magnification and NA of 0.17. These parameters are not very spectacular, but it was the best available equipment and it proved to be sufficiently good to provide interesting results.

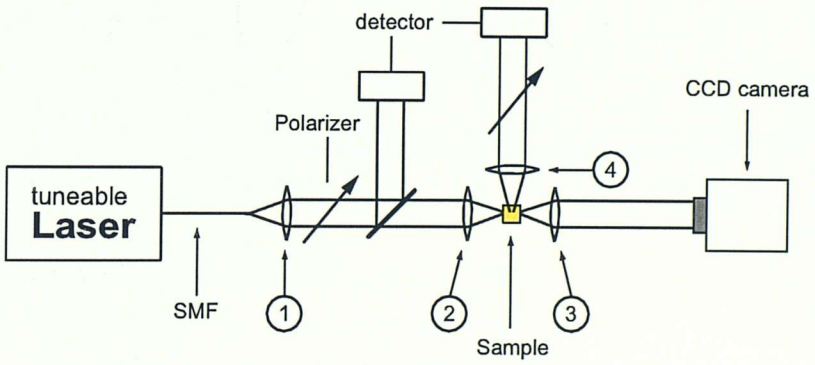


Figure 4.18: Experimental set-up for measuring light scattered vertically out of the PhC pattern.

The laser was set to produce 5.0 mW at 1570 nm. A Germanium detector was placed 14±0.5 cm behind MOG 4 and a polarizer inserted between the MOG and the detector. The transmitted light was imaged on a CCD camera. In that way optimum transmission was monitored in real-time, while the scattered light was measured. In

order to verify that the recorded light was indeed scattered out of the PhC, MOG 4 was moved along the ridge and the power recorded at fixed intervals.

Prior to setting up the Ge detector behind MOG 4, the top surface of the sample was imaged. The micrometer readings at which the left and right ends of the waveguide were in the centre of the screen were noted, to within ~50 μm. The Ge detector was set up and MOG 4 was approximately lined up with the 'left' edge of the ridge waveguide containing the PhC pattern. The recorded power was seen to increase more than tenfold near the centre of the ridge compared to the edge. On the 'far side' of the ridge the power decreased again gradually away from the centre of the ridge. The results of the scan are plotted in Fig. 4.19.

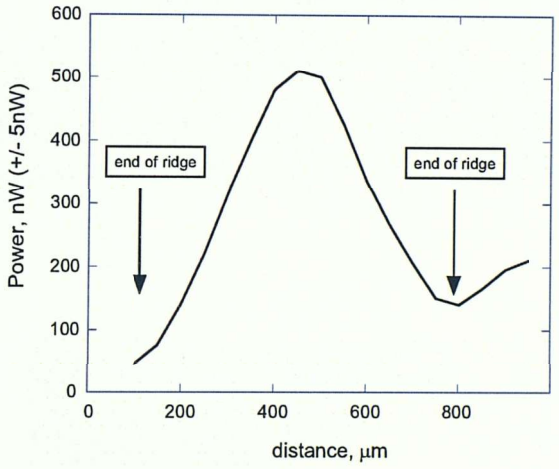


Figure 4.19: Scan along top of ridge waveguide with PhC pattern.

The peak in the plot is quite broad, with a FWHM ~400 μm. One reason may be that the spot size of a MOG with such a low NA is quite large. At best, i.e. at the diffraction limit, the minimum spot diameter of a 0.17 NA microscope objective at 1570 nm is ~11 μm. Sub-optimal focusing may also be a reason for the broad peak in Fig. 4.19. Nonetheless, the scan in Fig. 4.19 shows clearly that most of the scattered light was collected over the PhC. The set-up needs to be improved to accurately measure light scattered out the PhC.

It is worth pointing out that the overall scattering loss out of the PhC must be quite substantial, as the solid angle covered by the MOG is small compared to the solid angle that the light can scatter into as depicted in Fig. 4.20.

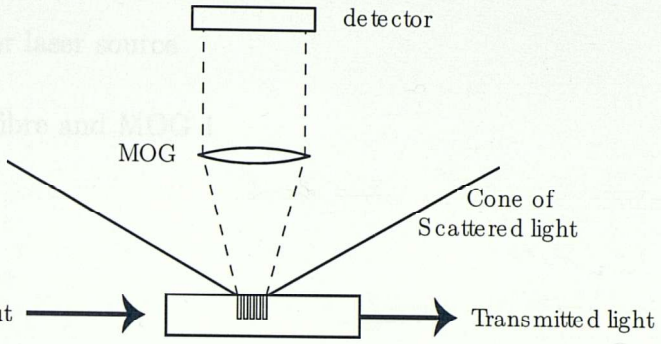


Figure 4.20: Limit of scattered light detection. The solid angle subtended by the MOG is clearly much smaller than the scattered light cone.

Light is not only scattered out of the top surface of the waveguide, but also out of the sides, due to the poor pattern termination as part of the fabrication processes - see Fig. 4.21. It was not possible to measure the light scattered out of the sidewalls of the pattern.

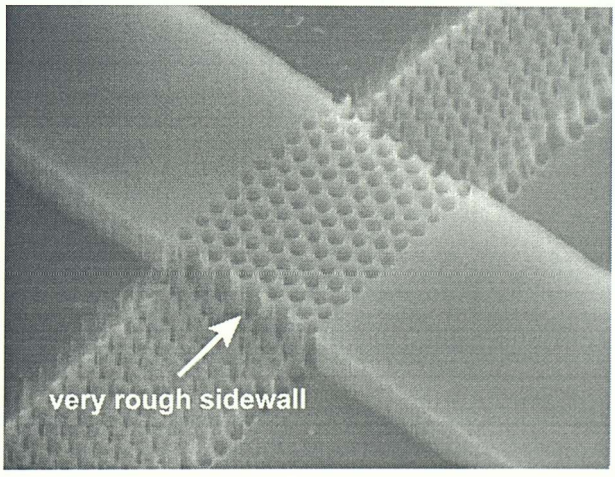


Figure 4.21: Scattering loss due to poor PhC termination.

4.4 Loss analysis of characterization set-up

Figure 4.22 shows the typical set-up used to characterize ridge waveguide samples. In order to perform a loss analysis the set-up was divided into sections, which were treated separately.

1. Semiconductor laser source
2. Single mode fibre and MOG 1
3. Polarizer
4. Beamsplitter
5. MOG 2
6. Sample
7. (a) MOG 3

   (b) cleaved single mode fibre
8. Germanium detector

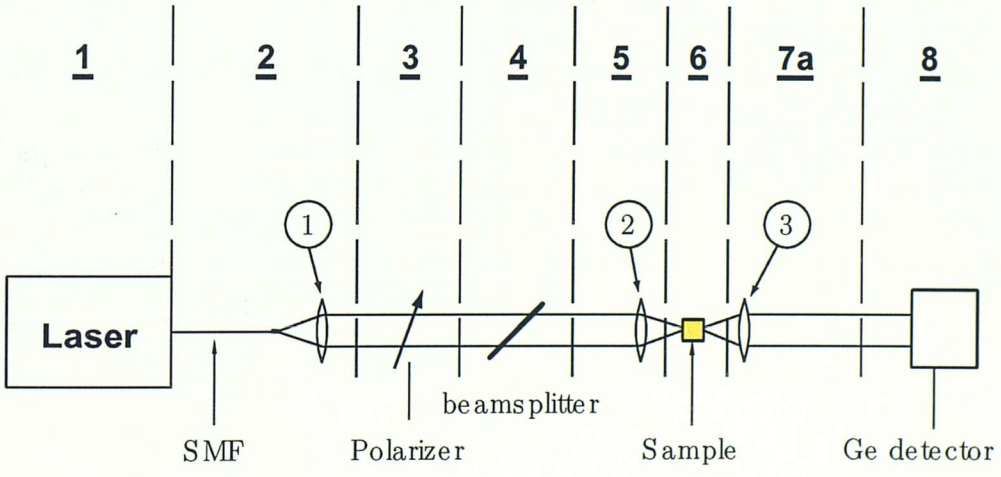


Figure 4.22: Characterization set-up as used in the loss analysis.

At every interface between media with different dielectric constants the transmitted signal is reduced due to Fresnel reflections. This is unavoidable. The effect is more

significant the larger the dielectric constant contrast of the two media. Other factors that reduce the overall transmission are discussed in the following Section.

4.4.1 Details

1) The laser was set to output 1 mW of power over the large range of 1510-1635 nm. According to the manufacturer's manual and calibration certificate the power stability is better than ±0.03 dB (or ~0.7%) over 24 hours, so the nominal value of 1 mW was assumed to emerge at the output of the laser.

2) The SM fibre used had a core diameter of 8 μm and cladding diameter of 125 μm, length = 3 m. It was fitted with FC/PC connectors at both ends. MOG 1 had ×63 magnification and a numerical aperture of 0.85. Losses can occur in a number of places in this section:

- coupling into the SM fibre at the laser output
- propagation loss through the SM fibre
- coupling out of SM fibre
- losses at MOG

With the laser set to output 1 mW, an average power of 0.3 mW was measured with a Germanium detector placed behind MOG 1. Therefore, the losses in section 2 are approximately 70% (-1.5 dB). Aprroximately 30% (-5.2 dB) of the input power is transmitted.

3) The Glan-Thompson polarizing prism used had a maximum transmission of 36% (-4.4 dB) according to the manufacturer's catalogue. A detailed description of the polarizer is given in Section 4.3.3.

4) The beamsplitter was not anti-reflection coated and therefore reflections occurred at every dielectric media interface, leading to reduced transmission and deflection performance. Figure 4.23 shows the set-up used to characterize the beamsplitter. The transmission and deflection coefficients obtained from these measurements were used to normalize the final measurements. The beamsplitter can therefore be regarded as a lossless component.

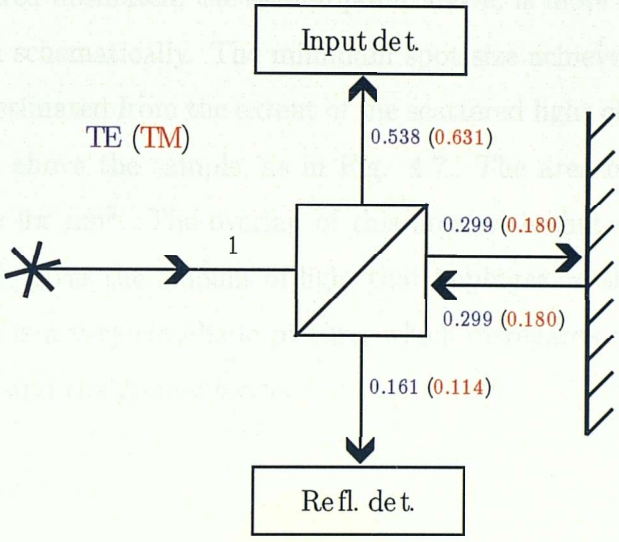


Figure 4.23: Set-up for beamsplitter characterization.

5) MOG 2 had NA=0.55 and ×63 magnification. Some light is lost in propagation through this MOG due to Fresnel reflections and material imperfections of the lenses. These losses were neglected in this loss estimation, as the losses occurring in other parts of the set-up are far greater.

6) Most of the light was lost on coupling into and out of the sample. The reasons can be summarised as follows:

- Fresnel reflection at input facet due to large dielectric constant difference between air and GaAs (~1:12)

- area mismatch between focused spot produced by MOG 2 and guided mode area
- propagation loss in waveguide due to imperfections in waveguide, such as scattering at walls, as they are not perfectly smooth
- coupling out of waveguide at back facet

Using the Fresnel equation for a plane wave at normal incidence a reflection coefficient of ~30% is calculated for an air:GaAs interface, i.e. approximately 70% is transmitted. The area mismatch, the second point above, is more serious. Figure 4.24 shows the situation schematically. The minimum spot size achieved with MOG 2 was ~6 μm. This was estimated from the extent of the scattered light observed at the input facet, imaged from above the sample, as in Fig. 4.7. The area of the focused beam was therefore $A_s \approx 9\pi$ μm^2. The overlap of this area with that of the guided mode inside the waveguide gives the amount of light that impinges on the front facet of the guiding layer. This is a very simplistic picture, which disregards the Gaussian profile of the focused spot and the guided mode.

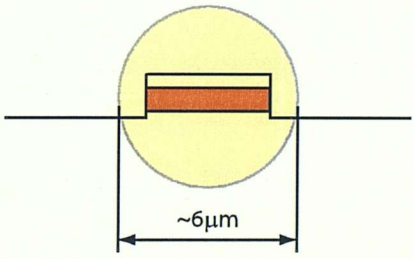


Figure 4.24: Area mismatch between the focused spot on the input facet of the waveguide and the area of the guided mode.

The guided mode inside the ridge waveguide was tightly confined to the guiding layer. The modal area was therefore approximated by $A_m \approx 4.5 \times 1 = 4.5$ μm^2, as the waveguide was 4.5 μm wide and the guiding layer was 0.6 μm thick. The fraction of the focused spot that overlapped the mode area was only ~$4.5/28 \approx 0.16$. Merely ~16% of the input light can possibly be coupled into the waveguide. Taking the losses due to Fresnel reflection into account, only about $0.70 \times 0.16 \approx 0.11$, i.e. only 11%

(-9.6 dB) of the light is coupled into the waveguide. This is a very lossy process!

How can it be improved? Tighter focusing would increase the overlap of the spot area with the guiding layer of the waveguide. What is the performance limit of the MOG? Ideally the MOG would focus the light to a spot of diffraction limited diameter, ϕ_D, given by

$$\phi_D = \frac{1.22\lambda}{\mathrm{NA}}$$

At $\lambda = 1.55$ μm and NA $= 0.55$, the diffraction limit of the spot is $\sim$3.5 μm. This spot would give an overlap of nearly 50% with the guided mode area in the ridge, an improvement of a factor of 3 to what was actually achieved. To use the MOG at the diffraction limit the aperture of the MOG must be filled with a perfectly collimated beam. This is difficult to achieve, especially as the beam passed through a polarizer and a beamsplitter before impinging on MOG 2. Therefore, it is believed that the described set-up was operating very close to what was practically possible with the given polarizer, beamsplitter and MOG 2.

At the output facet there was again a large difference in dielectric constant (GaAs:air) and hence a transmission of about 70% from the guiding layer into air. Two different set-ups were investigated for transporting the light from the output facet to the detector.

7a) MOG 3 was positioned with its focal plane on the sample's output facet. As the minimum spot size was always larger than the guided mode area it was assumed that all the light that emerged from the waveguide was collected by MOG 3. Reflection and scattering losses occurred as the light propagated through the MOG. These losses would be of the same magnitude as in 5) and were also be neglected.

7b) A stripped, vertically cleaved single-mode fibre was lined up with the ridge

waveguide and brought to within ~5 μm of the output facet. The fibre had a core diameter of 8 μm and cladding diameter of 125 μm. The following losses occurred:

- Fresnel reflection at the input and output facets of the fibre accounted for ~4% losses and was ignored.
- Propagation losses inside the SM fibre were also minimal and were ignored.
- A special adaptor was used to position the FC/PC connector-fitted end of the SM fibre in front of the detector; see Fig. 4.25. The fibre facet was less than 10 mm away from the detector chip, which had an active circular area of 3 mm diameter. These dimensions mean that even though the light spread out when it emerged from the SM fibre, it still fell entirely onto the detector chip.

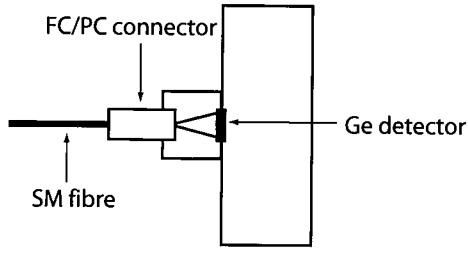


Figure 4.25: Adaptor for positioning the FC/PC connector-fitted end of the SM fibre in front of the detector.

8) The Germanium detector had a wavelength-dependent responsivity function, data for which was supplied by the manufacturer. Losses in this unit as well as the power meter, which the detector feeds into were assumed to be negligible.

4.4.2 Estimation of overall losses

For the set-up shown in Fig. 4.22 the overall losses can be estimated given the above component descriptions. It was assumed that MOGs 2 and 3, i.e. sections 5 and 7a were lossless. Using α_{wg} as the propagation loss in an unpatterned waveguide in the sample, section 6, the overall losses were follows:

$$1 \times 10^{-3} \times 0.30 \times 0.36 \times 0.11 \times e^{-\alpha_{wg}L} \times 0.70 \approx 2.0 \times 10^{-6}$$

2.0×10^{-6} W was the maximum power measured through an unpatterned ridge, with MOG 3 at the output facet. The waveguide length L was $\sim$700 μm. Therefore,

$$\begin{aligned} e^{-\alpha_{wg}L} &\approx 0.24 \\ \alpha_{wg} &\approx 20/\text{cm} = 87\ \text{dB/cm} \end{aligned}$$

This is a crude approximation to a complicated system comprising many components. The analysis may be somewhat oversimplified, but it is useful in that it highlights the main sources of losses. Coupling the light into the waveguide is the most expensive part of the set-up. There seems to be no way this can be improved significantly. The analysis also revealed that the waveguide propagation loss is quite severe, but direct measurements of the waveguide propagation loss using Fourier transform analysis (Section 3.4, Page 118) also showed values of typically $10 < \alpha_{wg} < 20$ /cm - see Section 5.1.4 on Page 189. This may be due to fabrication issues or a poor waveguide design. Both of these factors can be improved.

4.4.3 Other difficulties

In order to couple the maximum amount of light of minimum spot size $\sim$5 μm into the 4.5 μm waveguide one needs to obtain alignment accuracy better than $\sim$0.5 μm. One factor that affected measurements results was the amount of mechanical vibration induced in the optical components. Ideally the equipment would be set up on a 'floated' optical bench. This, however, was not available. As a consequence the vibrations resulting from pumps running nearby or doors slammed in the vicinity of the laboratory were clearly picked up by the experiment. This lead to uncharacteristic glitches in the recorded spectra.

A further factor, which adversely affected the experiment was the unexpected behaviour of the Melles Griot nanopositioning stages used in this experiment. It was found that these were not as mechanically stable as the manufacturer claimed. Certain thumbscrews were found to gradually slip and slowly move the top-mounting platform. To quantify this instability the power transmission through a typical ridge waveguide was recorded at one-minute intervals for one hour. The laser was set to output 1 mW at 1570 nm and TE polarization was chosen. Figure 4.26 shows the obtained data.

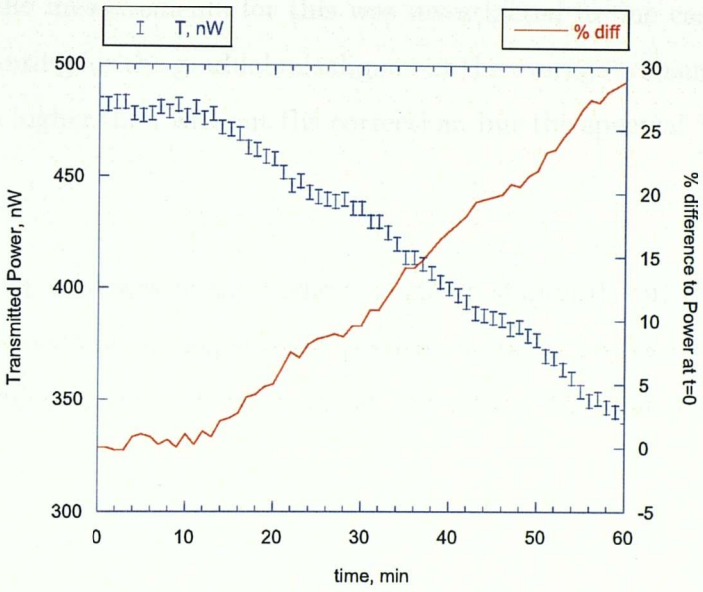


Figure 4.26: Stability test. Transmission through an unpatterned ridge waveguide recorded at 1 min intervals.

Clearly the set-up suffers from mechanical instability to some degree. After 15 minutes the transmitted power dropped to ~97% of its initial value, and ~90% after 30 minutes. After one hour the measured power in transmission was ~71% of the initial power. This apparently non-linear behaviour can be explained as follows. Focusing on the nanopositioning stage which holds the MOG that focuses the light into the waveguide, we see that a movement of the drive that controls motion perpendicular to the waveguide plane will move the focused spot perpendicular to the waveguide. Assuming a constant movement of the drive, then as the focused spot slowly

drifts the amount of transmitted light only changes slightly initially as there is still a large overlap of the focused spot with the waveguide core. At some point the overlap decreases rapidly, leading to a significant reduction in transmitted light, as seen in Fig. 4.26. This investigation indicated a limit to how long scans over all wavelengths (1510-1635 nm) could take before the system became too misaligned.

A typical scan took 30 minutes, by which time, according to the findings shown in Fig. 4.26 only ~90% of light was transmitted, compared with the optimal alignment case. It was assumed that this was a systematic effect, present at every scan. The effect of normalising the measurements for this was investigated in one case. It was found that when accounting for the gradual misalignment the average transmitted power over a scan was ~5% higher than without the correction, but the spectral features were unaffected.

The equipment used was of the highest available standard, but the extremely demanding requirements of the experiment pushed the performance of the components to their limits, which occasionally exposed flaws such that of the nanopositioning stages.

4.5 Conclusion

A great deal was learned about performing optical characterization over the three years that this project took. The set-up constantly evolved and must continue to do so in order to improve the accuracy and reliability of measurements.

It is believed that the potential for using white light as the source for characterizing passive structures is great. The main difficulties with the type of source used here were identified as the inhomogeneous emission spectrum and the very low output power levels at long wavelengths (>1300 nm). Further research with an arc lamp-type of source should concentrate on reducing losses in the system by, for instance, directing light from the source into the sample through free space, rather than coupling light in and out of an optical fibre. Also, further work must be carried out to ensure that only the light guided inside the sample is recorded and no other light 'noise'.

The set-up based on the tuneable laser source worked very well and gave excellent results. Improvements can be achieved by reducing the overall susceptibility to vibrations by floating the optical bench. It is also necessary to check the mechanical stability of all positioning stages to avoid beam drifts over time. This would open the possibility of running longer wavelength scans, which means the step length of the scans could be reduced. Using Fourier analysis discussed in Section 3.4 on Page 118 this would lead to an increase in the detectable optical distance. Alternatively the longer scan time can be utilized to improve the measurement accuracy by averaging several measurements at each wavelength.

It was clearly demonstrated that with the set-up described in Section 4.3 we were able to perform accurate, repeatable optical measurements of passive optical components with micron-sized dimensions.

Bibliography

[1] D. Cassagne, C. Jouanin, and D. Bertho. Hexagonal photonic-band-gap structures. *Phys. Rev. B*, 53(11):7134–7142, March 1996.

[2] R. D. Meade, A. M. Rappe, K. D. Brommer, and J. D. Joannopoulos. Nature of the photonic band gap: some insights from a field analysis. *J. Opt. Soc. Am. B*, 10(2):328–332, February 1993.

[3] D. Taillaert, W. Bogaerts, P. Bienstman, T. F. Krauss, P. Van Daele, I. Moerman, S. Verstuyft, K. De Mesel, and R. Baets. An out-of-plane grating coupler for efficient butt-coupling between compact planar waveguides and single-mode fibers. *IEEE J. Quantum Electron.*, 38(7):949–955, July 2002.

[4] S. Y. Lin, E. Chow, S. G. Johnson, and J. D. Joannopoulos. Demonstration of highly efficient waveguiding in a photonic crystal slab at the 1.5μm wavelength. *Opt. Lett.*, 25(17):1297–1299, September 2000.

[5] N. Kawai, K. Inoue, N. Carlsson, N. Ikeda, Y. Sugimoto, K. Asakawa, and T. Takemori. Confined band gap in an air-bridge type of two-dimensional AlGaAs photonic crystal. *Phys. Rev. Lett.*, 86(11):2289–2292, March 2001.

[6] E. Chow, S. Y. Lin, S. G. Johnson, P. R. Villeneuve, J. D. Joannopoulos, J. R. Wendt, G. A. Vawter, W. Zubrzycki, H. Hou, and A. Alleman. Three-dimensional control of light in a two-dimensional photonic crystal slab. *Nature (London)*, 407:983–986, October 2000.

[7] M. Klein and T. Furtak. *Optics.* Wiley, 2nd edition, 1986.

[8] W. G. Driscoll and J. M. Bennett. *Handbook of Optics.* McGraw-Hill, 1978.

Chapter 5

Optical characterization results

5.1 Presentation of key results

This Section is the culmination of all the work described thus far. Due to the large amount of data generated over the past two years we can only show the most significant results. The observation of photonic bandgap (PBG) effects will be demonstrated unambiguously in the first part of this Section, followed by various interesting results in the spectral domain and finally results from Fourier-transformed data will be presented. Key observations will be discussed in detail and conclusions will be drawn.

5.1.1 Observation of PBG-effect

Photonic bandgap effects were shown unambiguously with 2D photonic crystal patterns in a ridge waveguide environment. As described in Section 3.2.2 on Page 104 triangular lattices of air holes in GaAs were designed to have a photonic bandgap for TM-polarized light over the scan range of our laser source, and allow uninhibited propagation for light with TE polarization. The ΓM symmetry of the crystal lattice was chosen to lie along the direction of propagation. Figure 5.1 shows a typical structure used in this study, which was fabricated in the manner described in Chapter 2.

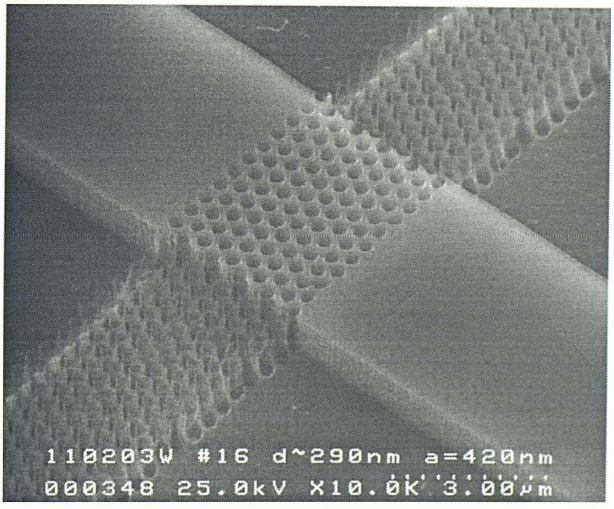


Figure 5.1: SEM image of 10 row PhC in a ridge waveguide.

Figure 5.2a shows the band structure of an infinite lattice with a fill factor of 50%, calculated using plane wave expansion code [1](see Section 3.2.3, Page 107). Figure 5.2b was calculated using RCWA [2] (see Section 3.2.3, Page 110) and shows the transmission behaviour of a 10 row photonic crystal for light propagation along the ΓM symmetry axis.

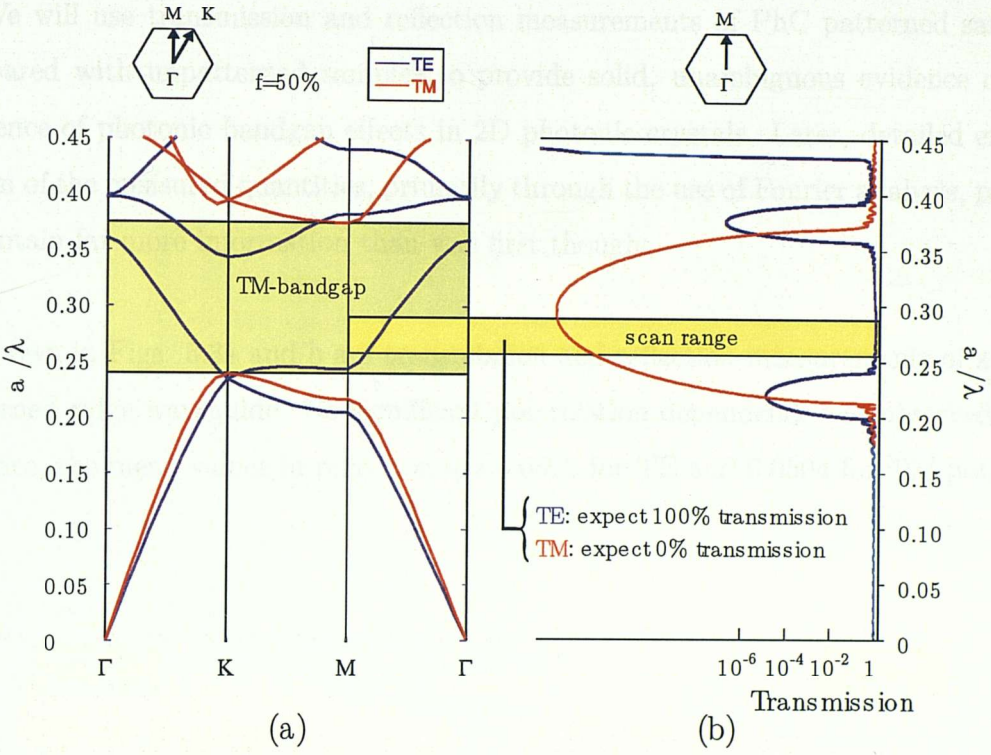


Figure 5.2: a) Photonic band structure for infinite 2D lattice of air holes in GaAs, fill factor 50%, calculated using plane wave expansion code, b) Theoretical transmission behaviour of 10 row PhC along ΓM, calculated using RCWA.

A key question to answer was whether the behaviour expected from the type of results shown in Fig. 5.2 would be seen in a ridge waveguide environment, which the calculations neglected. Previous work [3, 4, 5] differed from this approach in several aspects. Internal sources (quantum dots or quantum wells) had been used, whereas our structures are entirely passive. No ridges were used, and hence there was no lateral confinement. A series of samples (up to 8) were fabricated with different lattice parameters and the transmission measurements stitched together to show the appearance

of photonic bandgaps. No reflection measurements were reported. Chow *et al* [6] used 2D PhCs in passive ridge waveguides, but only showed transmission measurements. Moderate transmission in TE[1] and none in TM polarization was reported. The fact that no TM-polarized light is observed in transmission does not prove unambiguously the existence of a photonic bandgap!

We will use transmission and reflection measurements of PhC patterned samples compared with unpatterned samples to provide solid, unambiguous evidence of the existence of photonic bandgap effects in 2D photonic crystals. Later, detailed examination of the measured quantities, primarily through the use of Fourier analysis, proved to contain far more information than was first thought.

Shown in Figs. 5.3a and b are transmission and reflection measurements of an unpatterned ridge waveguide. No significant polarization dependence was observed. For instance, the mean values in reflection are 0.0523 for TE and 0.0504 for TM polarization.

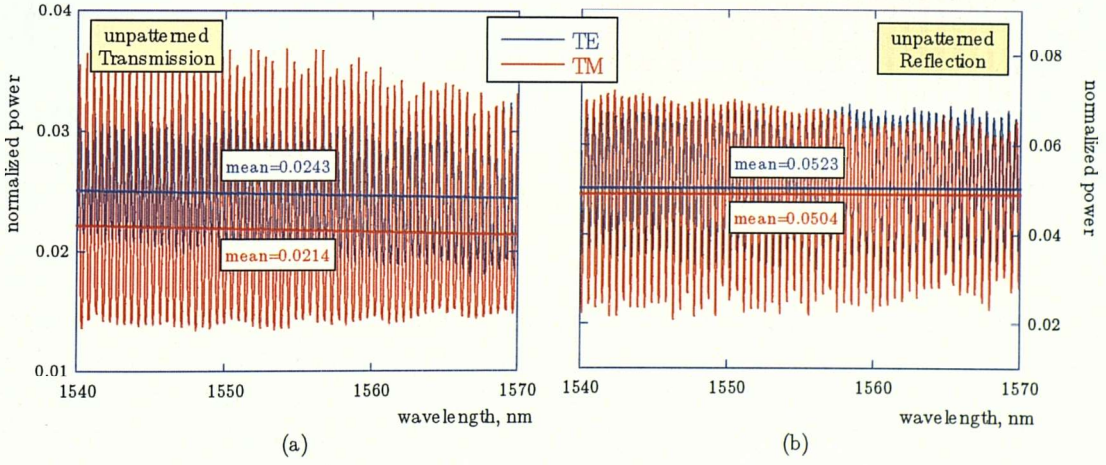


Figure 5.3: a) Transmission and b) Reflection measurements of an unpatterned ridge waveguide on sample 260203A. No significant polarization dependence is seen.

[1]The authors in Ref. [6] used the reverse of our notation, i.e. TE is referred to as TM in their article.

A sample containing a 10 row photonic crystal pattern in a ridge waveguide, as in Fig. 5.1, was studied in transmission (Fig. 5.4c) and reflection (Fig. 5.4d). The theoretical transmission behaviour of such a structures was calculated over a large spectral range using RCWA [2] (see Section 3.2.3 on Page 110), where care was taken to use the same lattice parameters as for the real sample, measured in an SEM.

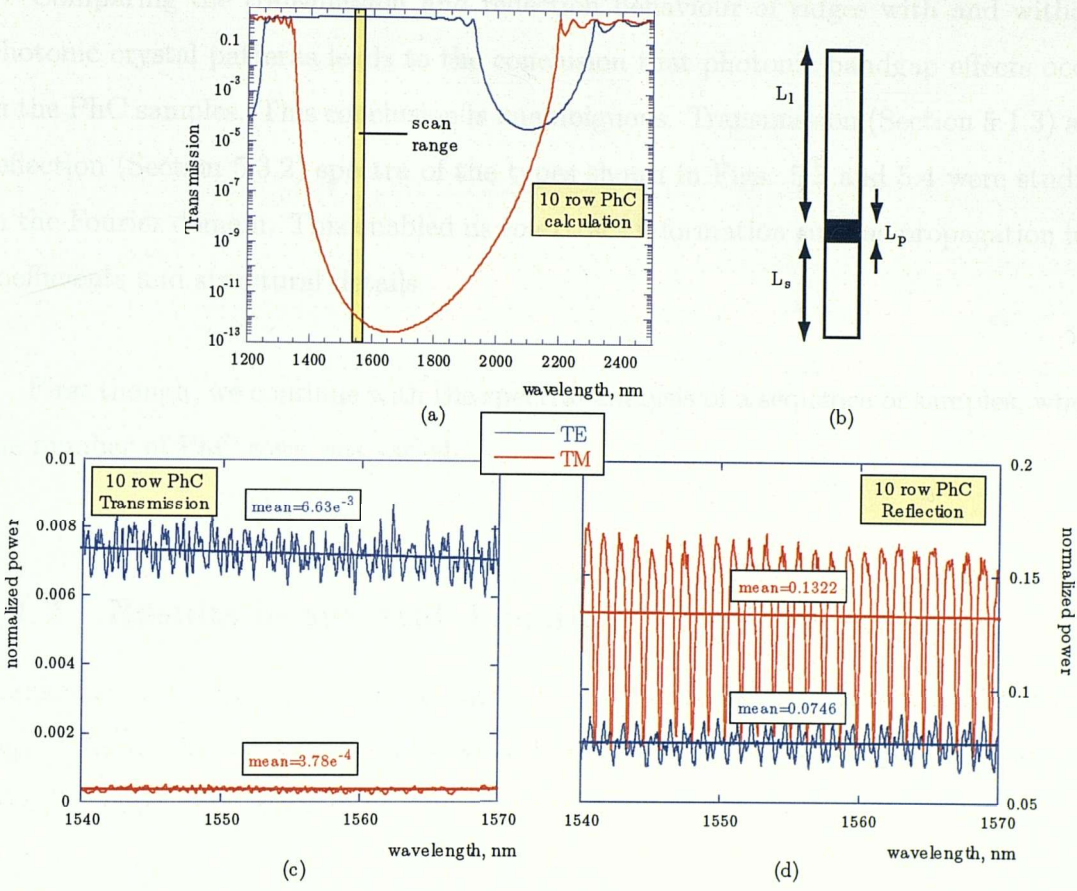


Figure 5.4: Experimental demonstration of PBG effect. a) Transmission calculation for 10 row PhC with the same lattice parameters as the measured sample, b) Schematic representation of patterned sample, c) Transmission, d) Reflection measurements for 10 row PhC in a ridge waveguide, sample 260203A. Strong polarization discrimination is seen in c), which is reversed in d).

Strong polarization discrimination is seen in Fig. 5.4c, with TM-polarized light being strongly suppressed. This is expected from the band structure calculations explained in Section 3.2.2 on Page 104, where a large TM bandgap is predicted to occur

for the lattice parameters used here. Polarization discrimination is also observed in reflection measurements. TM-polarized light is reflected more strongly by the PhC than TE due the presence of a photonic bandgap, but the discrimination is less pronounced than in transmission due to large specular reflection off the front waveguide facet (see Chapter 3).

Comparing the transmission *and* reflection behaviour of ridges with and without photonic crystal patterns leads to the conclusion that photonic bandgap effects occur in the PhC samples. This conclusion is unambiguous. Transmission (Section 5.1.3) and reflection (Section 5.3.2) spectra of the types shown in Figs. 5.3 and 5.4 were studied in the Fourier domain. This enabled us to extract information such as propagation loss coefficients and structural details.

First though, we continue with the spectral analysis of a sequence of samples, where the number of PhC rows was varied.

5.1.2 Results in spectral domain

Transmission spectra for 5 and 20 rows of PhC with ΓM orientation are shown in Figs. 5.5a and b, respectively. The two ridges were on the same sample and therefore have the same ridge dimensions.

Several features are noteworthy. For the 5 row pattern in Fig. 5.5a the polarization discrimination is quite constant across the entire spectral range, with an average value of 20 dB. However, at certain wavelengths (e.g. 1632.0 nm) the polarization discrimination is as large as 27 dB. As this structure consists of merely 5 rows of air holes and extends over ~1.8 μm, it is a significant effect, i.e. 15 dB/μm polarization discrimination! For the 20 row pattern the polarization discrimination is seen to decrease at the long wavelength end of the spectrum. This spectral dependence of the PBG effect was unexpected. The spectral dependence of various parameters was inves-

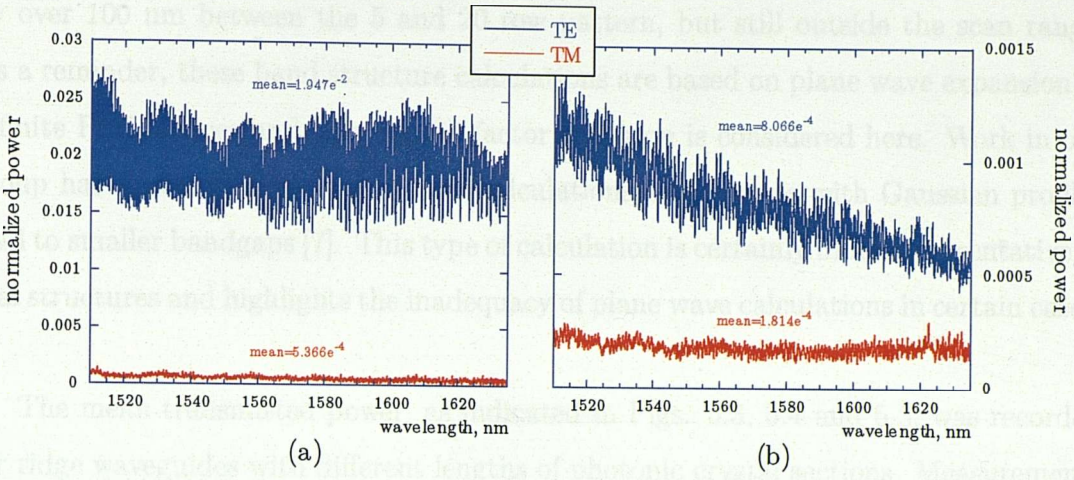


Figure 5.5: Measured transmission spectra for a) 5 row PhC, b) 20 row PhC embedded in ridge waveguides.

tigated by Fourier-analyzing small spectral windows at either end of the scan range. The size of the sampling window only affects the resolution in the Fourier domain and not the position of resonance peaks, as described in Section 3.4.2 on Page 122. Results are listed in Table 5.1, where the average TE power and the polarization discrimination (TE power/TM power) are compared across three different spectral windows of Fig. 5.5b.

	1515-1545 nm	1600-1630 nm	1510-1635 nm
avg. TE power	1.01×10^{-3}	6.25×10^{-4}	8.07×10^{-4}
TE/TM power ratio	5.13	3.47	4.45

Table 5.1: Transmission results for 20 row PhC structure, highlighting the spectral dependence of the PBG effect in this particular sample.

One possible reason for this drastic difference in transmission behaviour between the 5 row and 20 row sample could be a consequence of the proximity effect discussed in Section 2.3.3 on Page 61. As a result of this effect the hole diameters across the 20 row pattern are slightly larger than for the 5 row pattern, giving the 20 row pattern a larger fill factor (f $\sim$ 27%) than the 5 row pattern (f $\sim$ 21 %). In Section 3.2.2, Page 104 it was discussed how the photonic band structure is a function of the pattern's fill factor. As a consequence, the lower edge of the second TE band (see Fig. 5.2) shifts

by over 100 nm between the 5 and 20 row pattern, but still outside the scan range. As a reminder, these band structure calculations are based on plane wave expansion in infinite PhC lattices and only the fill factor variation is considered here. Work in our group has shown that band structure calculations using waves with Gaussian profiles lead to smaller bandgaps [7]. This type of calculation is certainly more representative of real structures and highlights the inadequacy of plane wave calculations in certain cases.

The mean transmitted power, as indicated in Figs. 5.3, 5.4 and 5.5, was recorded for ridge waveguides with different lengths of photonic crystal sections. Measurements were normalized with respect to an unpatterned ridge on the same sample. The results are displayed in Fig. 5.6.

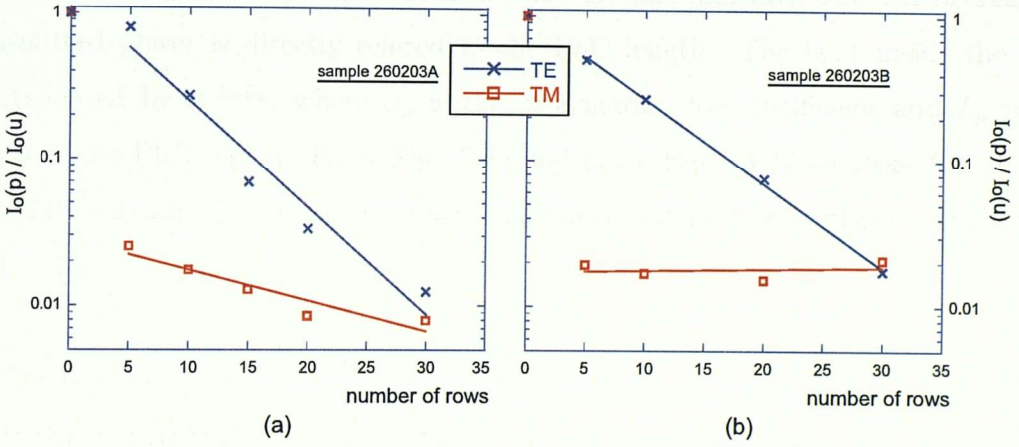


Figure 5.6: Normalized average transmitted power for different PhC lengths. a) average fill factor, f~25%, b) f~30%. Sample details are shown in Table 5.2.

Table 5.2 shows the physical details of the samples used to produce Fig. 5.6. The two samples were produced with different nominal hole diameters for the PhC patterns, which resulted in the two samples having different fill factors. Ideally the fill factor for each pattern on the same sample would be constant. However, as previously mentioned the proximity effect resulted in fill factor variation between patterns of the same sample.

The average power transmitted in TE polarization drops at an exponential rate

set	no. of rows	hole diameter nm	fill factor %	hole depth nm
A	5	200	21	850
	10	210	23	860
	15	220	25	870
	20	230	27	890
	30	240	30	900
B	5	220	25	870
	10	250	32	950
	20	260	35	970
	30	270	37	1000

Table 5.2: Physical parameters of two PhC samples, 260203A and B, obtained from measurements in an SEM. Lengths have an accuracy of ± 5 nm.

as the length of the photonic crystal region increases. Given that the ridge lengths are identical in each set (samples 260203A and B) this indicates that the decrease in transmitted power is directly related to the PhC length. The light inside the PhC is attenuated by $e^{-\alpha_p L_p}$, where α_p is the propagation loss coefficient and L_p is the length of the PhC region. From Fig. 5.6a and using Eqn. 3.27 on Page 129 we find $\alpha_p \approx 2.01$ dB/μm. This value is later verified using alternative methods - see Section 5.2.1.

The observation that the transmitted TE power drops as the PhC length increases, contradicts the findings reported in Ref. [6], where a similar structure was investigated. The authors reported that the transmission properties of light outside of the PBG, i.e. TE-polarized light with our nomenclature, were insensitive to the length of the PhC region.

There is one complication which means that a direct comparison between the five different patterns must be done with care. As mentioned above, the proximity effect causes the average hole diameter per pattern to increase with the pattern length for these structures, particularly between 5 and 20 rows. As described in Section 2.4.2 on Page 75 larger holes get etched deeper under constant etch conditions, which leads to

the result that the holes of the larger patterns are deeper than those of the smaller ones. The overlap of the PhC pattern with the waveguide mode differs between the two samples (see Section 5.2.3).

The power of transmitted TM-polarized light is nearly two orders of magnitude lower than TE light for the shortest photonic crystal. For longer PhC structures the transmitted TM light is seen to decrease, but at a rate which would suggest a smaller propagation loss coefficient than for TE polarization. This is not the true! First of all, the power levels of transmitted TM light are very close to the noise floor, rendering these measurements more inaccurate than for TE light due to a lower signal to noise ratio. Secondly, as described in Section 4.2.5 on Page 151 some of the light collected by the microscope objective at the output facet did not pass through the waveguide, and thus represents optical noise. In the spectral domain this noise will increase the overall power level measured. In the Fourier representation it will only contribute to the zero-order peak! This fact could be used to calculate the noise level in a transmitted signal. Also, it highlights the fact that the nonzero resonance peaks in the Fourier domain are entirely free of spurious background light. Thirdly, it was found that polarization mixing occurs for TM-polarized light, as described in Section 5.1.2.

Polarization mixing

Mixing between pure TE and TM-polarized light may occur as light passes through a photonic crystal region. The vector nature of electromagnetic radiation is always disregarded in band structure calculations. Scalar models assume that perfectly polarized light interacts with the PhC structure, but in real structures this is very difficult to ensure. Polarization mixing was considered as a possible explanation for the small nonzero transmitted power in TM polarization through PhC regions. This was found to be a significant effect in Ref. [6]. The characterization set-up shown in Fig. 4.15 on Page 157 was used for this investigation. A polarizer was placed in front of the transmission power detector. Figure 5.7 summarizes the results obtained for a

set of waveguides with 0(plain) - 30 PhC rows, sample 260203A. The measurements were carried out at 1570 nm.

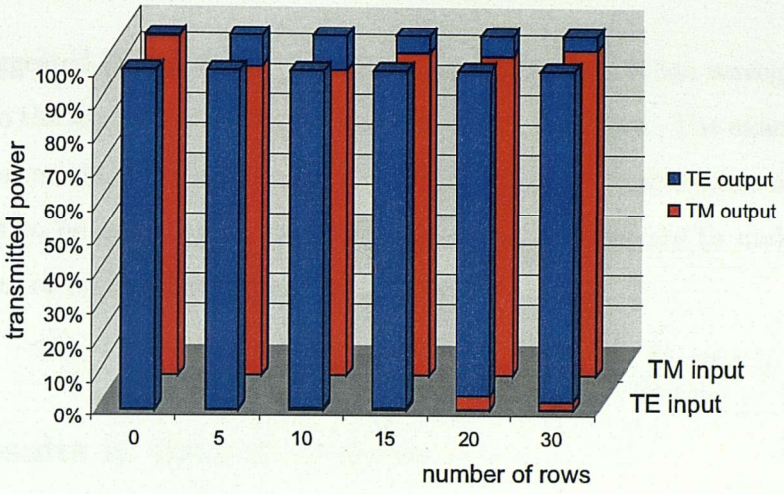


Figure 5.7: Results from polarization mixing tests. Input polarization was varied and the polarization state of transmitted light was analyzed with the aid of a second polarizer. Errors are of the order of 2% for TM input results, and <1% with TE input.

As in Ref. [6] we find that for TM-polarized input a significant amount of light is converted to TE polarization, up to 10% for the 10 row sample. There is nearly no polarization mixing for TE input light. The absolute values of the recorded polarization mixing effects are affected by the characterization set-up. At the given power levels there are quite substantial errors associated with the measurements, particularly for TM-polarized input light. Nonetheless, we have shown some evidence that polarization mixing does occur for propagation through photonic crystal structures.

These results suggest that looking back at Fig. 5.6, part of the light measured for TM transmission was actually converted to TE-polarized light after propagating through the PhC region. The polarization state of transmitted light was not analyzed for the measurements displayed in Fig. 5.6. Unfortunately the obvious question of whether this polarization effect depends on the PhC length, can not be conclusively answered. The polarization mixing effect peaks at the 10 row sample and decreases for longer PhC lengths. The mixing effect may be masked, as the effectiveness of the PBG

structure increases with length and depth of the PhC patterns across that set of samples, as mentioned in Section 5.1.2. The losses in the PhC region scale exponentially with increasing pattern length.

It was suggested in Ref. [6] that polarization mixing in a ridge waveguide environment is due to the asymmetry of the planar waveguide structure. The exact dependence of polarization mixing on PhC length, hole depth, waveguide structure and other factors will need to be investigated carefully if photonic crystals are to make their mark as components of optical integrated circuits.

5.1.3 Results in Fourier domain

Following the presentation of the spectral results, we now turn to their representation in the Fourier domain. As was discussed in Section 3.4 on Page 118 a great deal of information is contained in the Fourier-transformed data, which usually remains inaccessible in the spectral domain. Using the techniques discussed in Section 3.4.2 on Page 122 the spectral data shown in Fig. 5.8a was Fourier-transformed to produce Figs. 5.8b and c, which respectively show the TE and TM transmission spectra for a 5 row photonic crystal sample in the Fourier domain. The Fourier representation is rich in features. Following the discussions in Section 3.4 the majority of features of the Fourier pictures can be explained. Information such as propagation loss coefficients, visibility, average power and structural properties are readily accessible using the Fourier representation, as will be shown in Section 5.2.

From Figs. 5.8b and c one can immediately see the mean transmitted power, which is the value of the I_0 peak. The I_0 values of the TE and TM Fourier plots agree well with the mean calculated from in the spectral picture by taking the numerical average over all data points, e.g. for TE(spectral): $I_0 = 0.01947$, TE(Fourier): $I_0 = 0.01945$. I_s and I_l are the resonance peaks corresponding to the "short" and "long" cavities of the sample, respectively. Their position along the x-axis, L'_s and L'_l, are the optical lengths

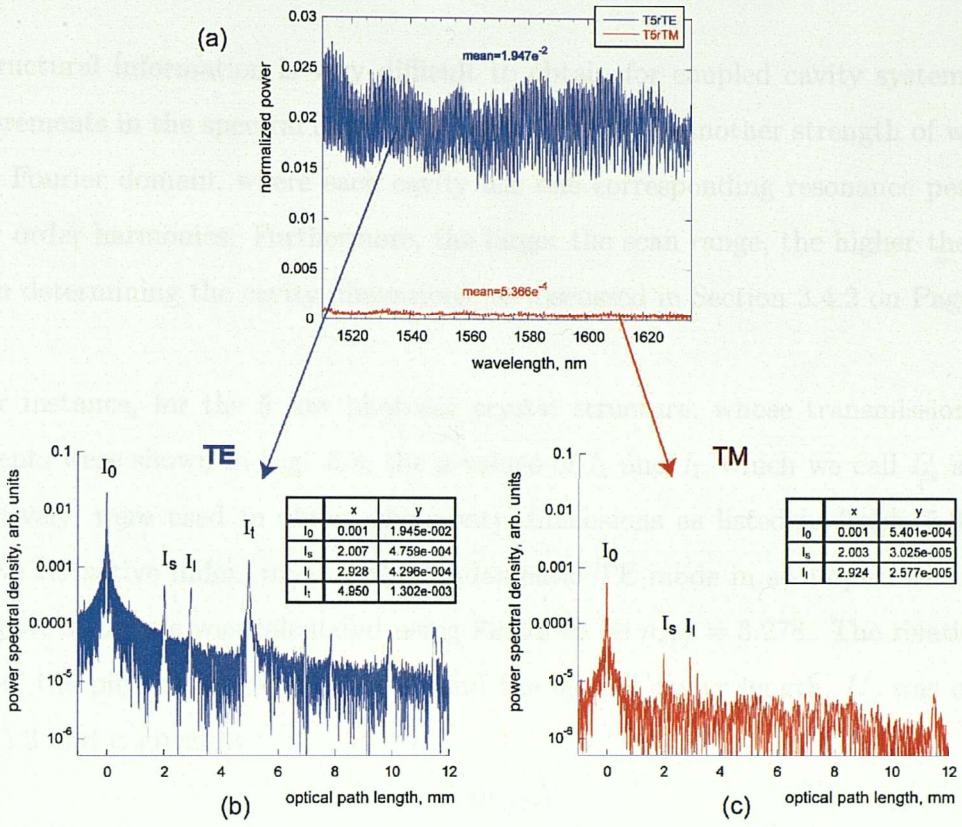


Figure 5.8: a) Spectral transmission results for a 5 row PhC structure, b) Fourier representation of TE trace in a), c) Fourier representation of TM trace in a). High transmission is expected for TE-polarized light, low for TM.

of the short and long cavity and can be used to accurately determine the sample's physical structure, as explained in the following Section.

Structural information

Information about the physical structure of the sample under investigation can be derived from the Fourier representation of transmission and reflection measurements. This is easily done, as the optical distance is a natural unit in the Fourier domain. The optical distance of the various cavities in the structure can be converted to the physical cavity length once the effective refractive index of the waveguide structure is known. Computational tools such as `FWave` described in Section 3.3.3 on Page 117 can be used for this task.

Structural information is very difficult to obtain for coupled cavity systems with measurements in the spectral domain. This highlights yet another strength of working in the Fourier domain, where each cavity has one corresponding resonance peak and higher order harmonics. Furthermore, the larger the scan range, the higher the accuracy in determining the cavity dimensions, as discussed in Section 3.4.2 on Page 122.

For instance, for the 5 row photonic crystal structure, whose transmission measurements were shown in Fig. 5.8, the x-values of I_s and I_l, which we call L'_s and L'_l, respectively, were used to obtain the cavity dimensions as listed in Table 5.3. The effective refractive index, n_{eff}, of the fundamental TE mode in an unpatterned ridge waveguide structure was calculated using `FWave` to be $n_{eff} = 3.278$. The relationship between the physical cavity length, L, and the optical cavity length, L', was used in Table 5.3 and is given by

$$L = 2n_{eff}L'$$

L'_s (mm)	L'_l (mm)	L_s (μm)	L_l (μm)
2.007	2.928	306	447

Table 5.3: Cavity lengths of 5 row sample extracted from Fourier picture of TE transmission. $L_s(L_l)$ is the physical length of the "short" ("long") cavity. The effective refractive index for the fundamental TE mode was calculated using `FWave`.

The following test of the characterization technique was carried out. Transmission and reflection measurements were recorded for a PhC patterned sample in the usual manner described in Section 4.3, Page 155. The sample was then reversed and the reflection measurement was repeated. The Fourier representation of all three measurements (TE polarization only) is shown in Fig. 5.9, where the traces have been offset for clarity. The position of all major resonance peaks agrees across all measurements, as expected from the invarience of Maxwell's equations under time reversal, which highlights the high accuracy and reproducibility of these measurements. The change in peak heights corresponding to the front and rear cavities are explained in Section 5.3.1.

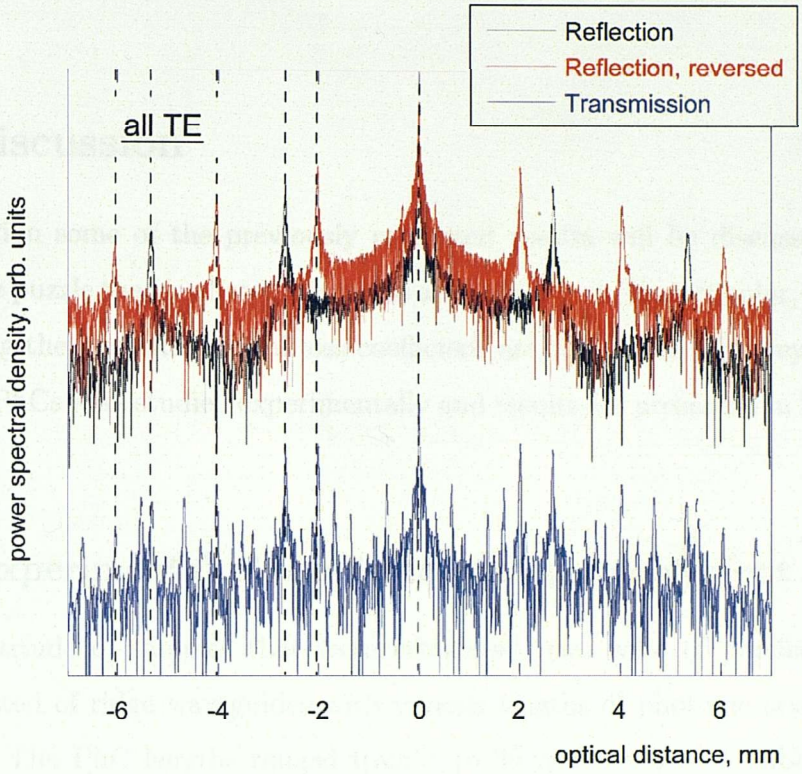


Figure 5.9: Fourier representation of transmission and reflection for normal and reversed 20 row PhC sample showing excellent reproducibility of resonance peak positions. The traces are offset for clarity.

5.1.4 Waveguide propagation losses

A number of ridges were left unpatterned on each processed sample, so that the waveguide propagation loss coefficient α_{wg} could be extracted. This was carried out using the technique outlined in Section 3.4.4, Page 127. Typical values obtained for α_{wg} were of the order of 60 dB/cm (14 /cm), which seemed rather high [8, 9]. However, some of the fabrication issues outlined in Section 2.5.7 on Page 93 have detrimental effects on the transmission properties of the ridges and ways of reducing them were suggested. Nonetheless, as our structures were always <1000 μm long, this loss value is not prohibitively large.

Several samples with unpatterned ridges of various heights were characterized and no correlation between the propagation loss coefficient and the ridge height was found.

5.2 Discussion

In this Section some of the previously presented results will be discussed and more pieces to the puzzle that is photonic crystals are introduced. In particular, two methods for obtaining the photonic crystal loss coefficient are compared. The key components to losses in PhCs were studied experimentally and results are presented in Section 5.2.3.

5.2.1 Experimental photonic crystal loss coefficient results

Of the multitude of samples that were fabricated, two were of particular interest. They consisted of ridge waveguides with various lengths of photonic crystal patterns embedded. The PhC lengths ranged from 5 to 30 rows - refer to Table 5.2 for the samples' physical parameters. The loss coefficients for propagation inside the PhC region, α_p, were calculated for each sample using two different methods: using Fourier representation (outlined in Section 3.4.4, Page 131) and using the spectral picture (the conventional way of determining the PhC loss coefficient). These two methods are compared in Section 5.2.2. Values of α_p obtained with both techniques are plotted in Figs. 5.10a and b.

The lowest loss coefficient was found in the 5 row structure of sample A and was $\alpha_p \approx 0.6$ dB/μm. The average α_p value for other samples of the same set were of the order of 1.8 dB/μm, which is three times as high as the best result. This agrees well with the value of α_p obtained from Fig. 5.6 in Section 5.1.2 ($\alpha_p \approx 2.01$ dB/μm), which essentially represents an average over all samples of that particular set. It must be stressed here that similar results were obtained using two different, independent approaches for calculating the photonic crystal loss coefficient. A number of factors render the direct comparison of the loss coefficient across samples difficult. These are all related to the fill factor variation across each set and are discussed in Section 5.2.3.

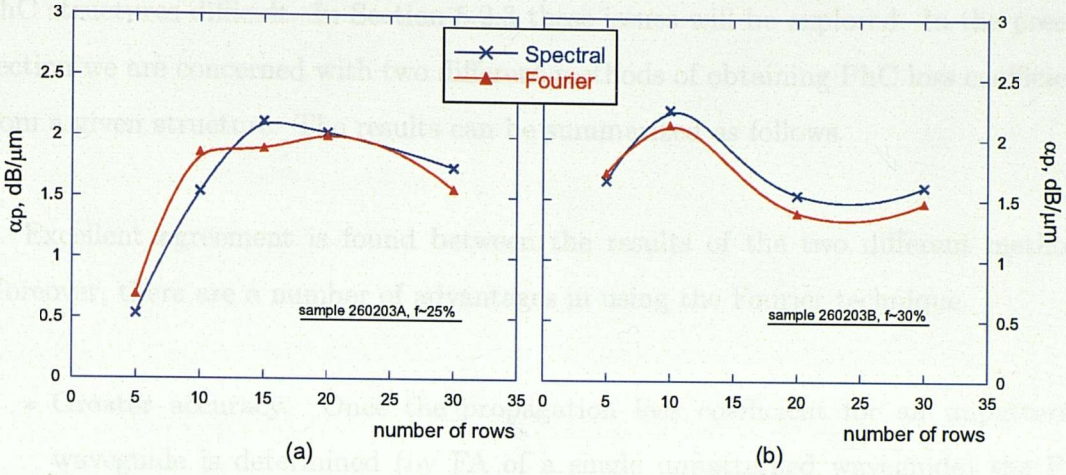


Figure 5.10: Photonic crystal loss coefficients extracted from various photonic crystal lengths using two different techniques. a) Sample with average fill factor ~25%, b) f~30%.

5.2.2 Comparing two methods for extracting the PhC loss coefficient

The accuracy with which the photonic crystal propagation loss is extracted from experimental data is compared for two techniques. The conventional method to obtain α_p is to normalize the mean of the transmitted power spectrum of a patterned waveguide with that of an unpatterned one. The alternative method proposed here utilizes Fourier analysis (FA) of the transmission spectra through a patterned waveguide. The simplifying approximation, that the waveguide:PhC interface has no reflection coefficient, was made, as mentioned in Section 3.4.4 on Page 131. Figures 5.10a and b show the results for two different samples. Each sample consists of a series of ridge waveguides with PhC patterns of various lengths. The main difference between the two samples is that the fill factor of sample A is ~25% and ~30% for sample B. The fill factor variation also leads to a variation of another important physical parameter, the etch depth. Reasons for why the fill factor is closely related to the etch depth for a given etch duration were discussed in Section 2.4.2, Page 75. A multitude of factors contribute to the overall performance of PhCs, which renders comparisons of

PhC structures difficult. In Section 5.2.3 these issues will be explored. In the present Section we are concerned with two different methods of obtaining PhC loss coefficients from a given structure. The results can be summarized as follows.

Excellent agreement is found between the results of the two different methods. Moreover, there are a number of advantages in using the Fourier technique.

* Greater accuracy. Once the propagation loss coefficient for an unpatterned waveguide is determined (by FA of a single unpatterned waveguide) the PhC loss coefficient is obtained with high accuracy.

* Improved reproducibility. The results of obtaining α_{wg} and α_p using FA are much less sensitive to experimental factors, such as the alignment and focusing, which significantly affect the spectral measurements.

* Potentially self-consistent. It is theoretically possible to extract α_{wg} and α_p with the FA technique from a single measurement of a patterned waveguide, as explained in Section 5.3.1. This will never be possible with the conventional spectral method.

* Structural information, such as cavity dimensions. FA gives insight into the physical structure of the sample with great accuracy (see Section 5.1.3). This is impossible in the spectral domain with coupled cavity structures.

* Easy comparison with modelled structures. Calculated transmission spectra are awkward to compare directly with measurements in the spectral domain.

* Visualization of sample quality. The rate at which higher order harmonics of a cavity resonance peak decay are a clear and convenient indication of the loss characteristics of the structure.

* Direct measure of visibility - see Section 3.4.4, Page 127.

Figures 5.10a and b show clearly that the FA technique, although used in a simplified form, yields results which closely match those obtained by the more error prone conventional method. The above points are further examples of the strength of the Fourier analysis technique used in this context.

5.2.3 Key factors of losses in photonic crystals

At this point we will carry out a systematic study of the losses that occur in photonic crystal structures. These can broadly be classified as intrinsic and extrinsic losses. Intrinsic losses occur in the case where holes have no imperfections and are infinitely deep. Extrinsic losses are primarily due to imperfections or inadequacies in the fabrication process. These can potentially be reduced as better control over the fabrication processes is gained. We will focus on losses as a function of fill factor, hole depth and modal confinement. For each study it was attempted to keep all other factors constant. This proved to be impossible, as mentioned in the following subsections.

Hole depth

It has been shown theoretically that the hole depth is an important contributing factor of losses in 2D photonic crystals [10, 11, 12, 13]. Much of that work focused on 2D PhC structures consisting of air holes in indium phosphide. Dry etching of InP has different characteristics to AlGaAs etches. Deeper etches are routinely achieved in InP than in AlGaAs. However, the hole profiles are typically 'carrot-shaped' (anisotropic) in InP [14], whereas vertical profiles are easier to realize in AlGaAs structures. Anisotropy seems to be a significant contribution to PhC losses [13, 15, 16], but as we were working exclusively with AlGaAs, it is not a problem we were faced with.

The hole depth and vertical mode confinement due to the planar waveguide structure determine the overlap of the mode with the photonic crystal. According to the

work presented in Refs. [10, 12], the larger the overlap, the lower the propagation losses inside the PhC region. The limited experimental data on 2D PhC losses in the literature [12, 14] suggests indeed that out-of-plane losses are lower for structures with a larger confinement factor. Due to the lack of experimental verification of these relationships at the outset of this project it was decided to investigate them by creating PhC patterns of different depths, embedded in a ridge waveguide structure, as described in Section 2.4.2, Page 81. Figure 5.11 shows the relationship of the photonic crystal loss coefficient with hole depth obtained from several different samples (110203A,B, 190203A, 260203B, 270203B, 110303A,B) listed in appendix C on Page 248. α_p was calculated using the Fourier analysis technique described in Section 3.4.4, Page 131.

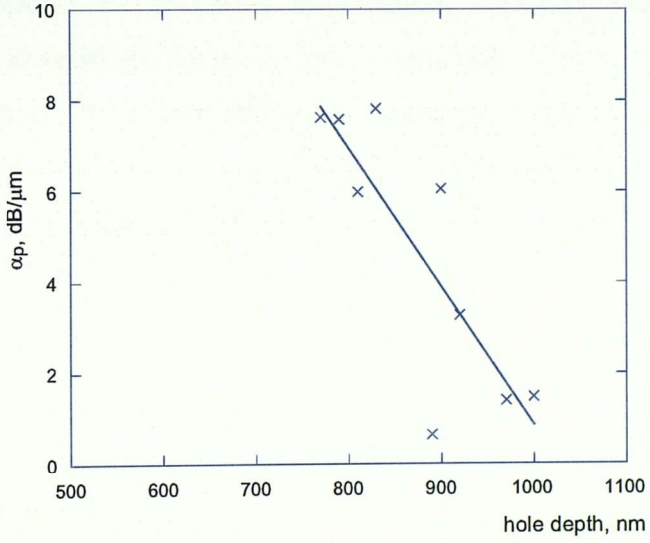


Figure 5.11: PhC loss coefficient as a function of hole depth. Losses can be reduced significantly by etching holes sufficiently deep. Samples 110203A,B, 190203A, 260203B, 270203B, 110303A and B were used to generate this plot. Hole depths are accurate to ±5 nm.

The relationship between the hole depth and α_p over the range shown in Fig. 5.11 loosely follows a linear trend. This would suggest that for holes deeper than ~1050 nm the losses would disappear. We do not believe that this linear trend is sustainable. We expect the losses to decrease ever more slowly beyond a certain depth. It was not possible to investigate the exact nature of this relationship, due to difficulties

in etching deep high quality hole patterns. Improvements in the fabrication technique were proposed in Chapter 2, which can be used to increase the etch depth for a given hole diameter. However, from the range of samples that were successfully fabricated we must conclude that the deeper the holes, the smaller the propagation losses inside the PhC region, which verifies the propositions in Refs. [12, 13]. α_p is certainly very sensitive to the hole depth of PhC patterns.

Ideally in this investigation one would look at a range of samples with varying hole depths and constant hole diameter (fill factor). This was unrealistic given the available time and resources. Therefore, out of all fabricated samples, the ones with hole diameter, d=280±20 nm, were included in the study. With a lattice constant of 420 nm this corresponds to a fill factor of f=40±6%. Restricting the range of samples to d=280±10 nm reduces the available data points from 9 to 4, but yields the same trend as in Fig. 5.11. It is very difficult to construct a fair test across samples, as many factors govern the behaviour of photonic crystals and it is a huge technological challenge to keep them constant at will!

Fill factor

The fill factor is a parameter in the design of photonic crystals. In Section 3.2 on Page 101 it was shown how the photonic band structure is a direct function of the fill factor, from which the hole diameter and lattice constant for a PhC pattern are calculated. Throughout this study of PhC patterns in ridge waveguides the lattice constant was kept fixed at 420 nm. Due to the nature of the techniques used to fabricate the photonic crystals, described in Chapter 2, and particularly the electron beam lithography process used to write the pattern (Section 2.3, Page 50), the lattice constant could be controlled to an accuracy of ±5 nm. Much poorer control was possible over the hole diameters, primarily due to the proximity effect discussed in Section 2.3.3, Page 61. Hence, fill factor variations occurred across different patterns. It has been suggested that the fill factor is also a factor that affects photonic crystal losses [3, 17]. To inves-

tigate this we selected successfully fabricated samples, which had hole depths greater than 850 nm. This was considered sufficiently deep to minimize depth-dependent PhC loss effects. α_p was extracted using the Fourier analysis method described in Section 3.4.4 on Page 131 and results are shown in Fig. 5.12.

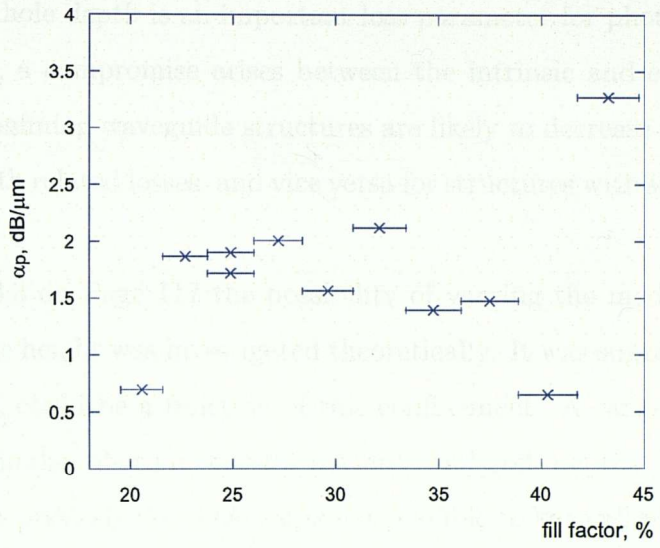


Figure 5.12: PhC loss coefficient as a function of fill factor. All patterns used here have hole depth >850 nm. Errors in the fill factor are quite large, ~4.5%, due to the accuracy with which hole diameters can be measured in an SEM (±5 nm).

A weak trend is observed in Fig. 5.12, whereby lower loss coefficients are expected for smaller fill factors. This really is a very weak trend. Leaving out the three most extreme data points gives a picture, where the loss coefficients are similar for a fill factor range from ~20-40%. In any case, it can be said that the fill factor is not a significant parameter that influences the loss characteristics of photonic crystals, contradicting the findings of Refs. [3, 17].

Modal confinement

Modal confinement is an intrinsic loss parameter, as it is not related to fabrication limitations. It is a prerequisite for real devices, where the very nature of guided electromagnetic waves means that modal confinement occurs.

It was suggested that in Ref. [10] that the intrinsic losses are a function of the square dielectric constant step of the waveguide, $(\Delta\epsilon)^2$, which is one of the key parameters that determine the modal confinement. The lower the dielectric constant step, the lower the intrinsic losses, according to Refs. [3, 10, 18]. As discussed in Section 5.2.3 the hole depth is an important loss parameter for photonic crystal structures. Therefore, a compromise arises between the intrinsic and etch-depth induced losses. Weakly confining waveguide structures are likely to decrease intrinsic losses but increase etch-depth related losses, and vice versa for structures with strong confinement.

In Section 3.3.3 on Page 117 the possibility of varying the modal confinement by changing the ridge height was investigated theoretically. It was suggested that the PhC loss coefficient α_p could be a function of this confinement. A range of structures was fabricated with similar photonic crystal patterns and etch depths, but different ridge heights. As in the previous Sections it was not possible to keep all physical parameters of the PhC structures constant while only varying the ridge height. Out of all processed structures the ones with hole diameters $d = 280\pm20$ nm and hole depths >800 nm were included in this study. The results are shown in Fig. 5.13.

No correlation between the ridge height and the PhC loss coefficient was found. It is believed that the structural variations across the samples, particularly hole depth, had a significant effect on the loss coefficient and masked the contributions due to modal confinement variations. Therefore, Fig. 5.13 does not present an unbiased study of α_p as a function of modal confinement. Given the available time and equipment it was not possible to produce samples to the required specifications with sufficient accuracy. We do believe, nonetheless, that varying the ridge height in this type of structure is a convenient way of adjusting the mode confinement in order to minimize scattering losses in the photonic crystal region.

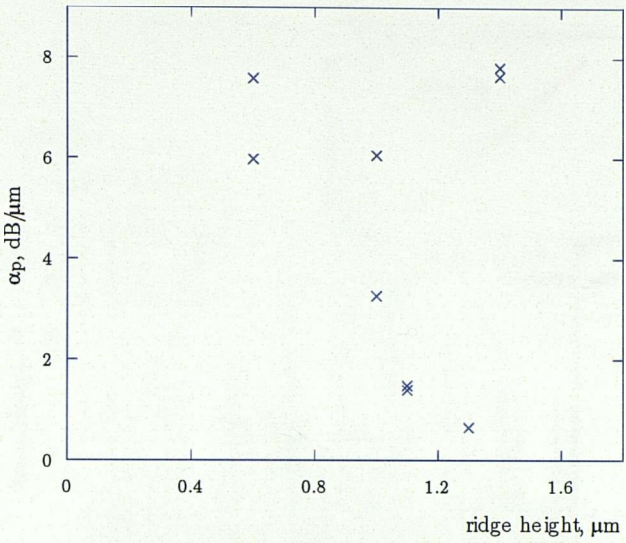


Figure 5.13: PhC loss coefficient as function ridge height. No correlation was found.

5.2.4 Linear response

Linear power response is a desirable property for many opto-electronic components. Over the moderate power range available with our laser system it was verified that the photonic crystal devices studied in this project had a linear response to power. Figure 5.14 shows the results for transmission in TE polarization at different input power levels.

Maximum transmission was observed at 5.0 mW with peak intensity of $\sim$1.2 $\times 10^{-6}$ W. Typical Fabry-Pérot fringes are visible. The fine structure of the transmission spectra is evident at all power levels. The background noise level was very low, at $\sim$3 nW. The power response of the peak at 1588.30 nm is shown in the inset of Fig. 5.14. A linear fit to the data shows that the transmission response of the 20 row photonic crystal component is indeed linear at these power levels, as expected. We can therefore be confident that at the power levels used for all measurements the samples had a linear power response.

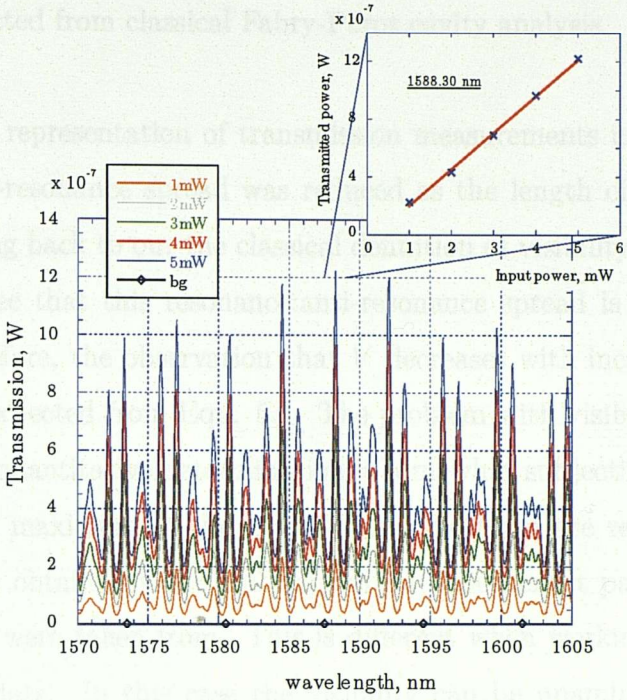


Figure 5.14: Transmission spectra for different input powers through a 20 row PhC. The inset shows the transmitted power for different input powers at a fixed wavelength.

5.2.5 Quantitative analysis of visibility

The concept of visibility was defined in the context of transmission through photonic crystal patterned waveguides in Section 3.4.4, Page 127. The visibility, V, is taken to be (see Eqn. 3.29, Page 131)

$$V \approx \frac{I_t}{I_0}$$

where I_t and I_0 are obtained from Fourier analysis such that I_t is the resonance peak corresponding to the cavity defined by the front and rear ridge facets, and I_0 is the DC term. Equation 3.29 stated that

$$\frac{I_t}{I_0} = 2\rho_1\rho_2 e^{-\alpha_{wg}(L_s+L_l)} e^{-\alpha_p L_p}$$

Therefore, the visibility clearly depends on the photonic crystal propagation loss, as

$$V \propto e^{-\alpha_p L_p} \tag{5.1}$$

which is also expected from classical Fabry-Pérot cavity analysis.

In the spectral representation of transmission measurements it was observed that the resonance:anti-resonance spread was reduced as the length of the PhC region is increased. Referring back to our the classical definition of visibility given in Eqn. 3.31 on Page 133 we see that this resonance:anti-resonance spread is a direct indication of visibility. Therefore, the observation that V decreases with increasing PhC length confirms what is expected from Eqn. 5.1. The problem with visibility in the spectral domain is that its quantitative determination is somewhat subjective. Only one intensity minimum and maximum of the transmission spectrum are required to calculate the visibility. The obtained value will depend on which exact part of the spectrum the measurements were taken from. This is different when working with the Fourier representation of data. In this case the visibility can be unambiguously defined as the ratio of the I_t to I_0 peaks, albeit these consist of averages over a large spectral range. The fact that the Fourier representation removes any ambiguity in the determination of the visibility allows for a rigorous, meaningful quantitative comparison of visibility between different samples. The result of such a comparison is plotted in Fig. 5.15.

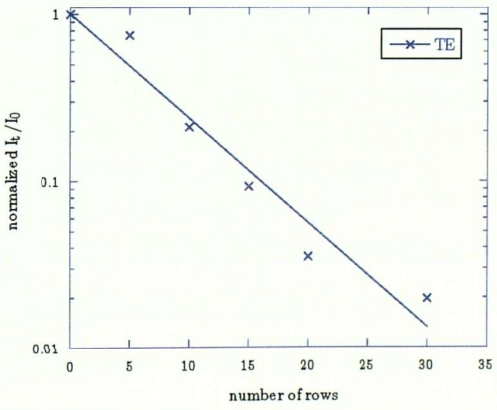


Figure 5.15: Visibility, defined here as I_t/I_0, as a function of PhC length.

Comparing Fig. 5.15 to the TE trace in Fig. 5.6 shows clearly that as the length of the PhC section increases, the visibility is seen to decrease rapidly, in part due to

the average transmitted power decreasing.

The visibility for TM-polarized light could not be computed from the Fourier picture, because the I_t peaks are not visible. This is due to the PBG effect, which strongly suppresses the transmission of light with TM polarization.

5.3 Other issues

We have shown how Fourier analysis is a powerful tool for analysing waveguide structures, in particular waveguides with embedded photonic crystal patterns. In this Section we will go further and explore how far this technique can be pushed to obtain the maximum amount of information about a structure.

5.3.1 Richness of Fourier representation

It was noted in Section 5.1.3 how rich in features the Fourier representation is, as shown in Fig. 5.8. Why is such a multitude of resonance peaks visible at all?

To answer this question we will take a step back and ask what the Fourier-transformed transmission measurements for an ideal photonic crystal structure would look like. The ideal PhC structure, as outlined in Section 3.2 on Page 101, would allow TE-polarized light to propagate uninhibited (100% transmission) and reflect all TM light (0% transmission). In the TE case the overall structure would behave like a single Fabry-Pérot cavity and exhibit evenly spaced FP fringes in the spectral domain and resonance peaks and harmonics corresponding to the overall cavity length. If perfect modal matching between the waveguide sections and the PhC region were possible, no resonance peaks due to the front and rear cavities would appear at all! In the case of TM-polarized light no light would be transmitted at all, in which case only noise would be recorded in transmission.

To return to the original question, the fact that resonance peaks for the front and rear cavities and their harmonics are visible is a first indication that 100% TE transmission is highly unrealistic in real structures. From a purely classical picture it is known that any interface between dielectric media with different dielectric constants gives rise to Fresnel-type reflection [19]. The effective refractive index of the photonic crystal region is necessarily different to that of the plain waveguide section. Hence there are nonzero Fresnel reflection coefficients associated with the waveguide:PhC interface. This gives rise to Fabry-Pérot cavities between the waveguide end facets and the PhC region, which have characteristic resonance peaks in the Fourier domain.

In the Fourier representation of transmission measurements for a number of structures we noticed that the peaks corresponding to the short and long cavity, I_s and I_l respectively, have different heights. This was unexpected from the modelled structure shown in Figs. 3.21 and 3.20. However, no waveguide losses (α_{wg}) and no photonic crystal loss coefficients (α_p) were included in that model. As mentioned in Section 5.1.4 our structures had quite substantial waveguide losses and significant propagation losses in the photonic crystal region. When these were included in the model it was found that particularly the value of α_{wg} affected the relative heights of I_s and I_l. It ought to be possible to extract α_{wg} from I_s and I_l. The height difference between the I_s and I_l peaks is certainly a qualitative indication of the loss coefficient of the plain waveguide regions.

We believe that it is possible to extract all relevant loss parameters of a PhC pattern in a ridge waveguide environment from a single wavelength scan in transmission. This one-shot measurement approach will be an invaluable characterization tool, which would certainly benefit the photonic crystal community. It would set a standard way of evaluating measurements, which would allow results to be verified more readily and generally render results more credible.

5.3.2 Reflection measurements

Reflection measurements on photonic crystal structures can complement the information obtained from transmission measurements, as shown in Fig. 5.4. Analytical expressions for the Fourier coefficients can be found for the reflection case. The analysis is complicated slightly with respect to the transmission case, due to specular reflection from the front facet.

Figure 5.16 shows Fourier-transformed reflection measurements for a sample containing a 10 row photonic crystal section. Five harmonics of the resonance peak corresponding to the front cavity are visible. This fact on its own is testament to the high reflection coefficients of the boundaries that confine the front cavity.

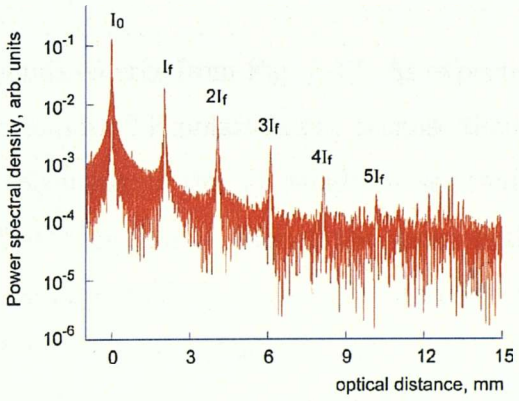


Figure 5.16: Fourier representation of TM reflection from 10 row PhC.

Carrying on from the discussion in Section 5.3.1 of reflection from photonic crystal structures, it is found that this effect can be studied thoroughly by carrying out reflection measurements. Samples with various PhC lengths were characterized. As the visibility is a function of the reflection coefficients that define the Fabry-Pérot cavity under investigation, we have plotted the visibility of reflection measurements in Fig. 5.17. We define the visibility in this case as

$$V = \frac{I_f}{I_0}$$

where I_f is the resonance peak corresponding to the front cavity with respect to the input facet of the waveguide and I_0 is the DC component of the signal.

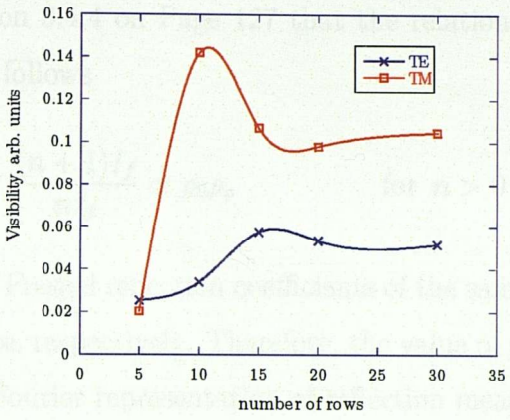


Figure 5.17: Visibility from reflection measurements, defined here as I_f/I_0, as a function of PhC length. The increasing TE visibility is significant.

Several interesting points emerge from Fig. 5.17. As expected the visibility for TM-polarized light is higher than for TE polarization, because there is a photonic bandgap for TM-polarized light. Focusing on the TE result we see that the visibility increases with the length of the PhC region, even though the wavelength range lies outside the bandgap. This is can be explained by drawing a comparison to distributed Bragg reflectors (DBR) [20], for which the reflectivity increases with the number of layers. For structures with more than 15 rows of holes the TE visibility is seen to level off. This is most likely due to the large loss coefficients associated with propagation inside the PhC region. This nonzero TE reflection is one of the loss mechanisms outlined in Section 5.3.3.

All structures were designed to have a photonic bandgap for light with TM polarization and were therefore expected to reflect TM light efficiently. This was indeed found to be the case. Maximum visibility was found for the 10 row structure, where it was $\sim$7 times the higher than for the 5 row structure. Beyond 10 rows the visibility was found to drop to $\sim$5 times the value for the 5 row structure. This again can be attributed to the large losses for propagation inside the PhC structure.

The Fresnel reflection coefficients of the PhC interface discussed in Section 5.3.1 can potentially be obtained from reflection measurements. It can be shown by analogy with the steps in Section 3.4.4 on Page 127 that the relationship between I_f and its harmonics in Fig. 5.16 follows

$$\frac{(n+1)I_f}{nI_f} \propto \rho_0 \rho_p \qquad \text{for } n > 0$$

where ρ_0 and ρ_p are the Fresnel reflection coefficients of the sample's front facet and the waveguide:PhC interface, respectively. Therefore, the value of ρ_0 could also potentially be extracted from the Fourier representation of reflection measurements.

5.3.3 Loss mechanisms

Various loss mechanisms occur in the two dimensional photonic crystals that were studied in this project. Some of these losses are general problems with this type of structure, others are particular to the sample used in this study. Figure 5.18 is an illustration of the major loss mechanisms that occur in our structures.

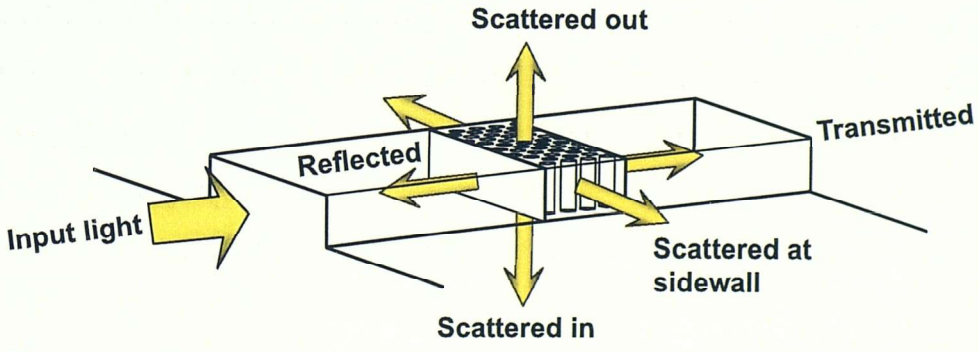


Figure 5.18: Schematic representation of loss mechanisms inside photonic crystal structures.

Out-of-plane scattering

This is believed to be the main source of losses, which affects all 2D photonic crystals. Light scattered into the substrate is essentially undetectable. Our measurements of light scattered vertically out of the sample (see Section 4.3.4, Page 161) showed that there is a significant amount of light lost through this path. A thorough quantitative analysis of was found to be difficult, due to technical limitations of the characterization set-up and the generally low power levels.

Attempts were made by a number of groups to study this effect [12, 13], although most of the work has been of a theoretical nature. It is now accepted that the hole depth of a PhC pattern is a key parameter that critically affects the propagation losses inside photonic crystals. This is also what we found, as was shown by the experimental evaluation of the α_p vs. hole depth relationship presented in Section 5.2.3. To minimize this loss the hole pattern needs to be etched deep enough to reach sufficient overlap between the unperturbed waveguide mode and the hole pattern [16].

Scattering at ridge sidewalls

Any 2D photonic crystal structures with finite lateral extent in the waveguide plane potentially suffer from losses through this mechanism. In our structures this type of loss is likely to be particularly large, as the PhC is as wide as the ridge. The poor termination of the PhC on the ridge's sidewalls presents large scattering sites, as outlined in Section 4.3.4 on Page 161 and shown clearly in Fig. 4.21 on Page 163. This loss can only be reduced by redesigning the overall structure, perhaps to the design used in Ref. [6]. The problem with that design, though, is that the independence of hole depth and ridge height is lost. This is true, because the ridge then has to be defined during the same electron beam lithography step as the hole pattern and the holes and ridge can no longer be etched separately.

The amount of light lost through this mechanism can not be measured with our experimental set-up, but is estimated to be smaller than the losses due to out-of-plane scattering and reflection.

Reflection

The reflection measurements discussed in Section 5.3.2 demonstrate clearly that reflection at the PhC interface occurs for TE-polarized light and that this effect depends to some extent on the length of the photonic crystal region. The mismatch between the waveguide modes and the allowed modes inside the PhC can potentially be reduced by gradually increasing the strength of the PBG effect through tapering [11], where the hole diameter is increased gradually from zero to the intended diameter. This has never been demonstrated experimentally with the type of PhC structures investigated here, i.e. where propagation occurs *through* the PhC region. With the current state of technology it would be prohibitively difficult to fabricate structures with gradually varying hole diameters and constant etch depth, due to the etch depth:hole diameter relationship described in Section 2.4.2, Page 75. In photonic crystal defect waveguides it has been shown experimentally that careful considerations of matching bulk waveguide modes and photonic crystals waveguide modes can lead to much improved coupling and hence reduced reflection losses [21, 22].

It will be difficult to reduce reflection losses at PhC interfaces due to fundamental physics problems as well as fabrication problems. The reduction in overall PhC losses achievable by optimizing these reflection losses, however, is smaller and more difficult to attain than the possible gains from reducing out-of-plane scattering.

This summarizes the key factors that contribute to the propagation loss inside photonic crystals. Ways of reducing them have been highlighted. We believe that much can be achieved by optimizing the design of the PhC structures, but a relatively larger reduction in losses will come about through advances in the fabrication technology used

in creating these devices. This has been demonstrated by the tremendous improvements in the quality of photonic crystals over the past decade. As this trend continues and people become more aware of the factors that govern the behaviour of these devices, large improvements in the loss reduction are bound to be achieved.

Bibliography

[1] plane wave expansion codes provided by P. N. Stavrinou, Imperial College London.

[2] calculations by P. Caillaud, based on source code by P. N. Stavrinou.

[3] H. Benisty, C. Weisbuch, D. Labilloy, M. Rattier, C. J. M. Smith, T. F. Krauss, R. De La Rue, R. Houdré, U. Oesterle, C. Jouanin, and D. Cassagne. Optical and confinement properties of two-dimensional photonic crystals. *J. Lightwave Technol.*, 17(11):2063–2077, November 1999.

[4] D. Labilloy, H. Benisty, C. Weisbuch, T. F. Krauss, D. Cassagne, C. Jouanin, R. Houdré, U. Oesterle, and V. Bardinal. Diffraction efficiency and guided light control by two-dimensional photonic-bandgap lattices. *IEEE J. Quantum Electron.*, 35(7):1045–1052, July 1999.

[5] M. Rattier, H. Benisty, C. J. M. Smith, A. Béraud, D. Cassagne, C. Jouanin, T. F. Krauss, and C. Weisbuch. Performance of waveguide-based two-dimensional photonic crystal mirrors studied with Fabry-Perot resonators. *IEEE J.Quantum Electron.*, 37(2):237–243, February 2001.

[6] E. Chow, S. Y. Lin, S. G. Johnson, P. R. Villeneuve, J. D. Joannopoulos, J. R. Wendt, G. A. Vawter, W. Zubrzycki, H. Hou, and A. Alleman. Three-dimensional control of light in a two-dimensional photonic crystal slab. *Nature (London)*, 407:983–986, October 2000.

[7] work by P. Caillaud and P. N. Stavrinou, Imperial College London.

[8] J. Wang, B. Smith, X. Xie, X. Wang, and G. T. Burnham. High-efficiency diode lasers at high output power. *Appl. Phys. Lett.*, 74(11):1525–1527, March 1999.

[9] P. Millar, R. M. De La Rue, T. F. Krauss, J. S. Aitchison, N. G. R. Broderick, and D. J. Richardson. Nonlinear propagation effects in an AlGaAs Bragg grating filter. *Opt. Lett.*, 24(10):685–687, May 1999.

[10] H. Benisty, D. Labilloy, C. Weisbuch, C. J. M. Smith, T. F. Krauss, D. Cassagne, A. Béraud, and C. Jouanin. Radiation losses of waveguide-based two-dimensional photonic crystals: Positive role of the substrate. *Appl. Phys. Lett.*, 76(5):532–534, January 2000.

[11] M. Palamaru and Ph. Lalanne. Photonic crystal waveguides: Out-of-plane losses and adiabatic modal conversion. *Appl. Phys. Lett.*, 78(11):1466–1468, March 2001.

[12] H. Benisty, Ph. Lalanne, S. Olivier, M. Rattier, C. Weisbuch, C. J. M. Smith, T. F. Krauss, C. Jouanin, and D. Cassagne. Finite-depth and intrinsic losses in vertically etched two-dimensional photonic crystals. *Opt. Quantum Electron.*, 34:205–215, 2002.

[13] R. Ferrini, B. Lombardet, B. Wild, R. Houdré, and G.-H. Duan. Hole depth- and shape-induced radiation losses in two-dimensional photonic crystals. *Appl. Phys. Lett.*, 82(7):1009–1011, February 2003.

[14] R. Ferrini, D. Leuenberger, M. Mulot, M. Qiu, J. Moosburger, M. Kamp, A. Forchel, S. Anand, and R. Houdré. Optical study of two-dimensional InP-based photonic crystals by internal light source technique. *IEEE J. Quantum Electron.*, 38(7):786–799, July 2002.

[15] Y. Tanaka, T. Asano, Y. Akahane, B.-S. Song, and S. Noda. Theoretical investigation of a two-dimensional photonic crystal slab with truncated cone air holes. *Appl. Phys. Lett.*, 82(11):1661–1663, March 2003.

[16] R. Ferrini, R. Houdré, H. Benisty, M. Qiu, and J. Moosburger. Radiation losses in planar photonic crystals: two-dimensional representation of hole depth and shape by an imaginary dielectric constant. *J. Opt. Soc. Am. B*, 20(3):469–478, March 2003.

[17] T. F. Krauss, R. De La Rue, and S. Brand. Two-dimensional photonic-bandgap structures operating at near-infrared wavelengths. *Nature (London)*, 383:699–702, October 1996.

[18] W. Bogaerts, P. Bienstman, D. Taillaert, R. Baets, and D. De Zutter. Out-of-plane scattering in photonic crystal slabs. *IEEE Phot. Technol. Lett.*, 13(6):565–567, June 2001.

[19] M. Born and E. Wolf. *Principles of optics: electromagnetic theory of propagation, interference and diffraction of light.* Cambridge University Press, 6th edition, 1997.

[20] H. A. Macleod. *Thin-film optical filters.* IoP, 3rd edition, 2001.

[21] P. Lalanne and A. Talneau. Modal conversion with artificial materials for photonic-crystal waveguides. *Opt. Express*, 10(8):354–359, April 2002.

[22] A. Talneau, M. Mulot, S. Anand, and Ph. Lalanne. Compound cavity measurement of transmission and reflection of a tapered single-line photonic-crystal waveguide. *Appl. Phys. Lett.*, 82(16):2577–2579, April 2003.

Chapter 6

Other photonic bandgap structures

The primary focus of this project was the investigation of 2D photonic crystals embedded in ridge waveguides, combining conventional, well-established ridge waveguide technology with PhC structures. This is a logical approach to studying this new class of materials. However, the novel and unique properties of photonic crystals may require a more radical approach, whereby entirely new designs need to be considered. We have carried out work in that direction, which is reported in the present Chapter.

6.1 Large fill factor work

For a long time, spontaneous emission (SE) was believed to be an intrinsic material property. In 1946 Purcell [1] demonstrated theoretically that SE can be tailored by changing the environment of the emitter. That work was carried out in the microwave regime. Purcell predicted that an atom radiating on-resonance with the modes of a high finesse wavelength size cavity can radiate much faster than in free space. Off-resonance, SE will be suppressed. The Purcell factor, F_P, describes the magnitude of SE enhancement and is given by

$$F_P = \frac{3}{4\pi^2}\left(\frac{\lambda}{n}\right)^3 \frac{Q}{V_m}$$

where λ is the wavelength, n is the refractive index of the cavity with quality factor Q and mode volume V_m. Therefore, for an experimental realization of spontaneous emission control it is important to achieve a high Q-factor and a small mode volume.

The first experimental work on suppression and enhancement of spontaneous emission was carried out in the microwave regime [2]. At optical frequencies, experiments involving SE control have employed nanocavities including micropillars [3], microdiscs [4], AlO_x-apertured vertical cavities [5] and photonic crystal defect cavities [6, 7, 8, 9, 10, 11, 12, 13]. In particular the PhC-based devices seem to offer a great deal of design fiexibility and superior functionality compared to the other structures.

Very high Q-factors of the order of 30000 and small mode volumes of the order of $V_m \sim 2(\lambda/2n)^3$ have been proposed theoretically [6, 11]. The highest experimentally measured Q-factor is ~3000 [11].

Photonic crystals were first proposed as a way to modify the optical radiation from emitters within crystals, by Yablonovitch [14] and John [15]. This work marked the beginning of the research into photonic crystals, merely 16 years ago. It is interesting to note how many different applications have been envisaged for PhCs, as outlined in Section 1.3 on Page 21. The original aim of using PhCs for ultra-high field localization is still pursued actively today and it is with this idea in mind that the work on large fill factor structures was carried out. Ultimately, this work can lead to a large range of interesting applications, such as ultra-low threshold lasers [14, 16], high modulation rate light-emitting diodes [17] and quantum cryptography [18, 19].

6.1.1 Rationale for large fill factors

In Section 3.2 on Page 101 the band structure of 2D PhCs was shown to be crucially dependent on the fill factor. This is particularly well-illustrated in the gap maps shown in Fig. 3.6 on Page 106, which indicate regions where complete bandgaps occurs, i.e. forbidden frequency ranges over the entire first Brillouin zone. Triangular lattices of air holes in GaAs exhibit a large first photonic bandgap in the fill factor range ~30-85% for TM-polarized light. This bandgap overlaps with the bandgap in TE polarization for fill factors greater than 60%. Therefore, 2D photonic crystals with fill factors greater than 60% are predicted to have complete photonic bandgaps over in both polarizations over the entire Brillouin zone. A photonic crystal 'defect' cavity can be created by not etching holes in the desired locations, as in Fig. 6.1. This destroys the homogeneity of the PhC pattern and can therefore be regarded as a defect. Cavities of the order of the emission wavelengths of the internal source are realized, for example, by leaving out a single hole. The defect cavities are labelled following the convention used by Benisty *et al* [20]. For example, a 'circular' defect cavity with a 3 row diameter is labelled H3.

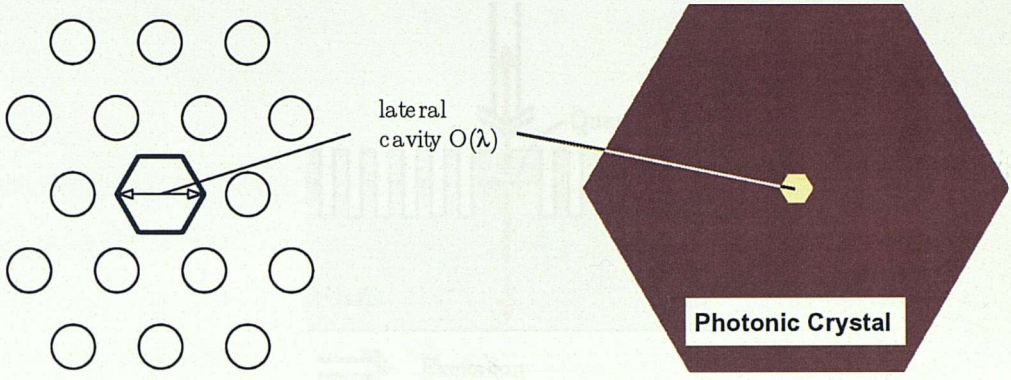


Figure 6.1: Diagram of a H1 photonic crystal defect cavity. Cavities of the order of the emission wavelength are easily created.

Quantum dots (Qdots) are highly suitable emitters that can be placed inside high Q-factor microcavities. Qdots have the ability to efficiently capture and localize photo-excited free carriers, have negligible re-absorption and a wide spectral bandwidth for emission due to inhomogeneous broadening, which is a result of size fluctuations during the growth process [9]. Qdots are atom-like structures that, following excitation, emit photons of random polarization in all directions [21]. In a photonic crystal environment this emission can be made to be

1. more directional

2. more efficient

Figure 6.2 shows the structure that was envisaged for the study of quantum dots in high Q photonic crystal defect cavities. Emission in the plane normal to the holes would be forbidden by the photonic bandgaps that exist for TE and TM polarization if the PhC's fill factor is sufficiently large. Studies of out-of-plane propagation in triangular lattice PhCs has shown that bandgaps are shifted to higher frequencies as as the out-of-plane angle increases [22, 23]. In Ref. [23] it was shown that for TE polarization the first (lowest frequency) ΓK bandgap (see Section 3.2, Page 101) in an air:GaAs triangular lattice of holes persists for light incident up to $\sim 25^\circ$ away from the normal. Emission into the remaining space where no photonic bandgaps exist, would be enhanced.

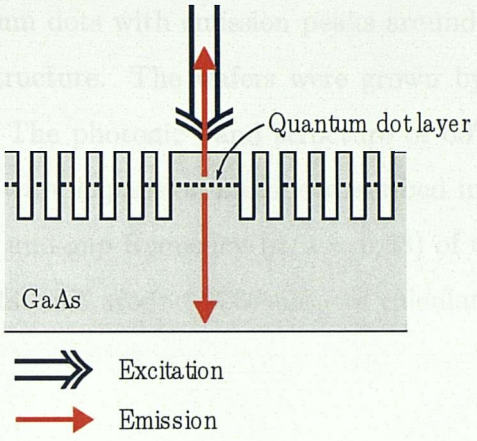


Figure 6.2: Proposed experiment to characterize the behaviour of quantum dots in a PhC defect cavity.

The lifetime of spontaneously emitted photons would be affected by confining the emitter inside a high Q and small mode volume cavity. The rate of spontaneous emission, Γ, is given by Fermi's Golden Rule [24]:

$$\Gamma(r) = \frac{2\pi}{\hbar}\langle(d \cdot E(r))\rangle^2 \rho(\omega) \tag{6.1}$$

where d is the electric dipole of transition, $E(r)$ is the local zero-point root-mean-square electric field, and $\rho(\omega)$ is the density of electromagnetic modes. In a PBG the density of EM modes is zero. The spontaneous emission rate is related to the lifetime (τ) as follows

$$\Gamma = \frac{1}{\tau}$$

Therefore, as the number of available radiation modes is reduced by the presence of a photonic bandgap, $\rho(\omega)$ decreases, which means the lifetime τ increases. This can be verified experimentally by performing time-resolved photoluminescence [25]. As in Fig. 6.2 the cavity containing Qdots would be pumped optically by a suitable laser source and the lifetime of emitted photons would be measured.

6.1.2 Fabrication of large fill factor 2D photonic crystals

Self-assembled InAs quantum dots with emission peaks around 1250 nm were embedded in a GaAs/AlGaAs structure. The wafers were grown by Christine Roberts at Imperial College London. The photonic band structure of 60% fill factor PhCs was calculated using the plane wave expansion method described in Section 3.2.2 on Page 104. Using the normalized mid-gap frequency ($a/\lambda = 0.38$) of the lowest TE bandgap and the fact that the Qdots emit around 1250 nm, we calculated the required lattice constant to be ~480 nm.

Two dimensional photonic crystals with fill factor ~60% were fabricated as described in Section 2.4.2 on Page 79. Using Eqn. 2.2 on Page 48 we see that for PhC structures with a lattice constant of 420 nm and a fill factor of 60% the walls between neighbouring holes must be just less than 80 nm thick. This is difficult to accomplish with a high degree of accuracy and repeatability. Nonetheless, some excellent patterns were fabricated as shown in Fig. 6.3, which shows a highly uniform PhC pattern produced by electron beam lithography (EBL) of PMMA and reactive ion etching into silica. This acts as a mask during the plasma etch whereby the pattern is transferred into the underlying epilayers.

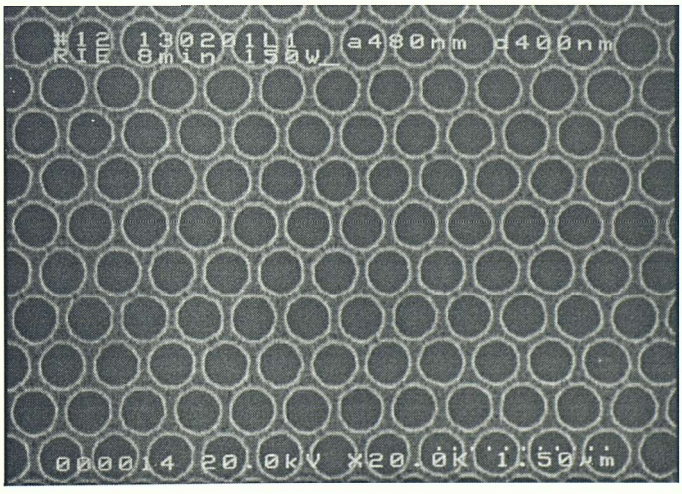


Figure 6.3: SEM image of large fill factor SiO_2 mask with excellent uniformity.

Producing a high quality mask is one of two key steps to fabricating large fill factor patterns. The other is the pattern transfer into the epilayers. The etch conditions must be controlled in such a way as to ensure vertical etching. Excessive lateral etch components can lead to holes overlapping, as shown in Figs. 2.38, 2.39 and 2.40.

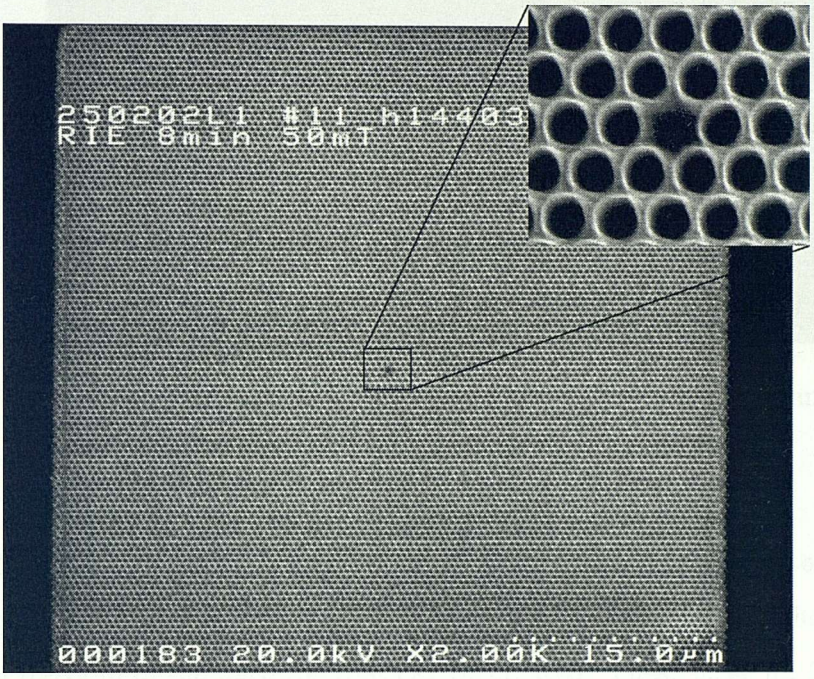


Figure 6.4: SEM image of one-hole cavity (H1) in 50x50 μm pattern.

Electron beam lithography is a highly versatile tool. Patterns can contain any imaginable 2D feature. Defect cavities can easily be patterned and patterns can be altered arbitrarily from one pattern to the next. This degree of flexibility is not available with other exposure techniques, such as holographic imaging [26]. One of the drawbacks of EBL is the size of area that can be exposed with high resolution. We found that regions of 50×50 μm could be patterned homogeneously with a high quality PhC pattern. Figures 6.4 and 6.5 show 50×50 μm fields of large fill factor photonic crystals with small central defect cavities.

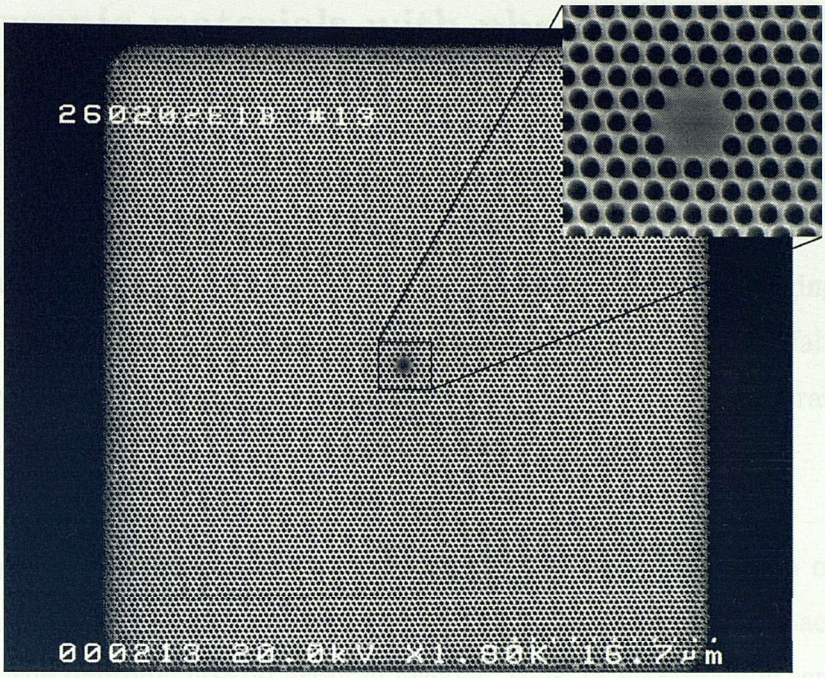


Figure 6.5: SEM image of three-hole cavity (H3) in 50×50 μm pattern.

6.1.3 Conclusions of large fill factor work

The fabrication of high fill factor 2D photonic crystals was shown to be possible for use with emitters of near infrared radiation. The techniques used here offer a large degree of freedom in the patterns that can be created. These large fill factor structures represent a significant technological challenge and pushed the available equipment to its limit. The smallest feature sizes that were successfully fabricated were ~30 nm.

Optical characterization of the fabricated structures was not carried out. This was due to time constraints as well as due to a refocusing of the project goals. Nonetheless, we believe that photonic crystals can be used in this context to create compact new devices operating with unprecedented efficiency.

6.2 Organic materials with photonic crystals

Photonic crystals and organic polymers are two exotic branches of solid-state physics, which have received a great deal of attention over the past decade. However, at the beginning of this project there had been little overlap of these two areas. The few articles that were published on that subject [27, 28, 29, 30] were seen as encouraging and led us to investigate this exciting area of research. Based on our experience of fabricating 2D photonic crystal lattices we chose to investigate the possibility of incorporating organic gain material in these structures to produce a laser resonator.

An inorganic host was patterned with a photonic crystal structure consisting of air holes into which the organic substance was introduced. Strong feedback was to be provided by the photonic crystal array of organic 'rods' in an inorganic semiconductor environment, resulting in strong interaction with the gain medium. The device was designed to be optically pumped and emit from the surface. Figure 6.6 is a diagrammatic representation of the proposed device.

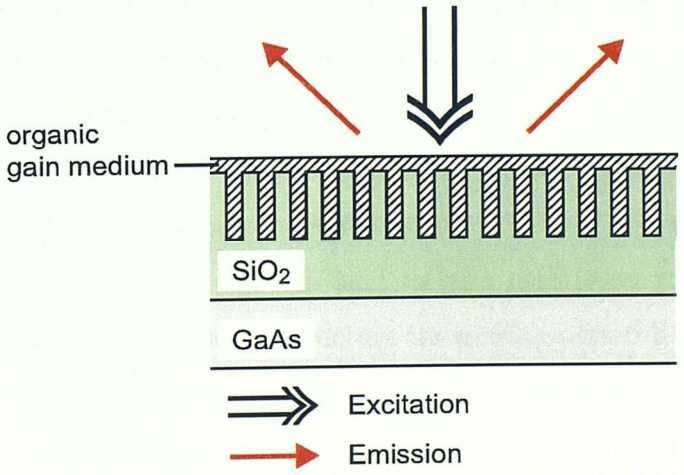


Figure 6.6: Diagram of a photonic crystal with organic gain material. Emission from optically pumped organic material is amplified at certain wavelengths dictated by the PhC lattice.

The organic material was applied to the PhC structures by M. Ramon at Imperial College London, who was also involved in the optical characterization of these devices.

6.2.1 Fundamentals

Traditional distributed feedback (DFB) lasers are based on periodic refractive index modulation in one dimension. The feedback necessary for lasing to occur is provided in one spatial direction by the grating structure. Improved performance of these devices seems possible if spontaneous emission is controlled over the entire plane [27]. 2D photonic crystals are ideally suited for this task, as they provide compact periodic refractive index modulation over the entire plane.

Organic materials are an interesting gain medium for 2D PhCs. Organic dyes and polymers are commercially available (for example, see Refs. [31, 32]) and typically emit in the visible part of the electromagnetic spectrum. They can easily be applied to a PhC-patterned surface, simply by spin coating in the way PMMA was applied prior to electron beam lithography, described in Section 2.2.2, Page 44.

An optically excited organic polymer[1] de-excites by spontaneously emitting photons. In a resonator environment such as that provided by a 2D PhC structure, some of the emitted light is fed back into the system. This feedback, which results from Bragg reflections induced by the periodic refractive index and gain variation, is the basis of DFB lasers [33]. Continuous coherent backscattering from the periodic perturbation provides strong feedback and can lead to laser oscillation without the benefit of end reflectors [34]. In a 1D grating structure the grating period a induces coupling between the forward and backward propagating waves at Bragg frequencies $\omega_B = N\pi c/a$ (N is an integer), which in turn creates bandgaps around ω_B [27]. This concept can be extended to 2D photonic crystals, where bandgaps occur at certain lattice period-related frequencies - see Section 3.2 on Page 101.

It was found in Ref. [35] that the gain (g) of an active 'gain rod' in a 2D PhC

[1]This discussion also applies to organic dyes.

lattice is uniquely determined by the product of the time (t) for light to pass a gain rod and the electric field confinement (Γ) in the gain rod. But $t = 2r/v_g$, where r is the radius of the rod and v_g is the group velocity of the emitted radiation. Thus,

$$g \propto \frac{\Gamma}{v_g} \tag{6.2}$$

The group velocity can be expressed as $v_g = d\omega/dk$, where k is the wavevector [36]. On a dispersion diagram such as the band structures plots discussed in Section 3.2.2 on Page 104 the group velocity is given by the gradient of the photonic bands. At a photonic band edge the group velocity tends to zero. A remarkable increase in gain enhancement in the vicinity of photonic band edges was reported in Ref. [35]. Photonic crystals operating near photonic bandgaps are therefore highly suitable structures for increasing the interaction of light with the gain medium.

In Ref. [37] laser action in 2D PhCs with optical gain material was studied experimentally. Successful operation was explained to be due to feedback mechanisms that occur at photonic band edges, in analogy with the coupling mechanism of two counter-propagating waves in a 1D DFB laser [33]. 2D or 3D photonic crystal lasers have a variety of feedback mechanisms due to their extended degree of freedom [37], which can be utilized to create more efficient and more compact laser structures than the one dimensional devices.

6.2.2 Design considerations

In order to design a suitable photonic crystal structure the most important parameters to consider are the emission wavelength of the active material, the geometry of the lattice structure and the type of material to be used as the host, i.e. the material into which holes will be etched.

The organic polymer that was to be used is a Dow Chemical Company [32] pro-

prietary red emission copolymer, known as Dow Red F. It absorbs strongly in the UV and has its peak emission around 670 nm. Another possible polymer emits in the blue part of the spectrum, around 460 nm. The emission was not expected to be polarized [38].

Regarding the host material, GaAs would make an unsuitable host for this application. With a bandgap energy of ~1.42 eV [39, 40], which corresponds to a cutoff wavelength of ~870 nm, it would absorb the radiation emitted by the polymer. Adding aluminium during the growth of GaAs increases the bandgap energy. A 70% aluminium content composition, AlGaAs(70), has a refractive index of ~3.33 at 670 nm and bandgap energy of ~2.37 eV [39], which corresponds to a cutoff wavelength of ~525 nm. This would make it suitable for work with the red emitting polymer, but not with the blue emitting one. Fused silica, SiO_2, has a large bandgap energy of ~9 eV (cutoff wavelength ~135 nm) and would therefore not absorb the radiation emitted by either the red or blue polymer. However, the refractive index of silica is very low, $n_{SiO_2} = 1.46$ [27], which provides very little contrast to that of the polymer ($n_{poly} = 1.65$).

Taking these factors into consideration, the band structures for four cases was calculated:

1. polymer in SiO_2 with a triangular lattice
2. polymer in SiO_2 with a graphite lattice
3. polymer in AlGaAs(70) with a triangular lattice
4. polymer in AlGaAs(70) with a graphite lattice

In cases 1 and 2 the gain material is of higher refractive index than the host material. In cases 3 and 4 it is the host material, which has the higher refractive index. Another important difference between cases 1,2 and 3,4 is the refractive index contrast. The polymer and SiO_2 have very similar refractive indices, giving low contrast. For

AlGaAs(70) and the polymer the refractive index contrast is large, ~3.33:1.65.

In previous publications the SiO_2:polymer case was considered with an underlying square photonic crystal lattice [30], triangular lattice [28] and graphite lattice [27]. Using a plane wave expansion program [41] (see Section 3.2.3, Page 107) the effect of changing the lattice structure (triangular vs. graphite) and changing the host material (SiO_2 vs. AlGaAs(70)) was investigated.

6.2.3 Band structures

With the dielectric constants and the lattice geometry fixed, the only other factor to be set for the calculations is the radius (r) of rods relative to the lattice constant (a), the nearest-neighbour centre-to-centre rod separation. In the case of the triangular lattice it is convenient to define the fill factor (f) as the percentage of the lattice unit cell occupied by rod-material, as defined in Section 2.2.3 on Page 46. $f = 0\%$ is the case where the rod diameter is 0, i.e. the host material is unpatterned. $f = 100\%$ corresponds to all of the unit cell occupied by rod material. When $r/a = 0.5$ the rods touch and the host lattice ceases to be fully connected. For the triangular lattice this corresponds to a fill factor of $f \sim 91\%$. However, fabrication difficulties usually limit the maximum fill factor to less than 60%, or $r/a \sim 0.4$.

Table 6.1 summarizes the structural requirements for the four cases described in the previous Section. These requirements were obtained by calculating the photonic band structures in each case using the plane wave expansion algorithm [41] with 721 plane waves for lattices with fill factor 50%. Calculations were performed with the following refractive index values (at 670 nm): $n_{polymer} = 1.65$, $n_{SiO_2} = 1.46$ and $n_{AlGaAs(70)} = 3.33$. The midgap frequency of the first bandgap for TM polarization was determined. If no complete bandgap was found to occur, then the first ΓK bandgap was considered. Using the obtained value of the midgap frequency and the emission peak wavelength, $\lambda = 670$ nm, the required lattice constant was calculated. For example, if

$$
\begin{aligned}
a/\lambda &= 0.372 \\
\rightarrow a &= 0.372 \times 670 \\
&= 249 \text{ nm}
\end{aligned}
$$

		triangular			graphite		
	all in nm	a	d	w	a	d	w
λ_{red}	SiO_2	249	185	64	168	134	34
	AlGaAs(70)	173	128	45	82	66	16
λ_{blue}	SiO_2	171	127	44	115	92	23
	AlGaAs(70)	118	88	30	57	46	11

Table 6.1: Structural parameters for PhC with organic material. a=lattice constant, d=hole diameter, w=(a-d)=smallest wall width between adjacent holes. Band structure calculations were based on structures with a 50% fill factor.

Bandgaps are typically wider in structures with AlGaAs(70) due to the large refractive index contrast between the host and the polymer. Complete bandgaps also occur in that configuration, but not with a SiO_2 host. A further advantage of AlGaAs(70) structures is the occurrence of significant higher order bandgaps. Designing photonic crystals to operate around the second complete bandgap in the case of the red-emitting polymer in AlGaAs(70) with a graphite lattice, for example, would change the required lattice parameters to a=143 nm, d=115 nm, w=28 nm. This would be a more realistic structure to fabricate with current technology. Smaller lattice dimensions are required for a PBG around λ_{blue} than around λ_{red} (see Section 2.2.3, Page 46).

6.2.4 Fabrication of 2D photonic crystals with active organic materials

From a practical point of view the lattice parameters presented in Table 6.1 are very demanding and difficult to fabrication using the available technology (see Section 2.3.2, Page 57). The one structure that is readily realizable consists of a SiO_2 host with a triangular lattice, for red-emitting material, which is the same configuration used in

Ref. [30]. Only a small bandgap (~34 nm) exists along the ΓK direction (see Section 3.2.1, Page 103) for TE-polarized light. We successfully patterned 50 × 50 μm areas with triangular lattices in SiO_2 with the lattice parameters a=240 nm, d=180 nm.

A ~400 μm thick layer of silica was deposited on a GaAs substrate using PECVD. The PMMA photoresist was spun on and electron beam lithography was carried out to expose patterns of triangular holes in the photoresist. The hole patterns were transferred to the silica layer by reactive ion etching (RIE). These processing steps were described in detail in Sections 2.2, 2.3 and 2.4.1.

Numerous difficulties arose due to the small hole sizes required. The largest field that could be exposed while maintaining the required resolution to assure smooth features was approximately 50×50 μm. Apart from the reduction in resolution, the onboard memory of the signal generator card that controls the electron beam writer (see Section 2.3, Page 50) was insufficient to handle larger pattern files. More than 65000 holes make up a typical 50×50 μm pattern with 180 nm diameter holes and lattice constant 210 nm. This resulted in pattern file sizes close to the maximum allowed by the hardware. Also, it was difficult to accurately control the etch depth during RIE etches. However, the hole depth in these structures was not such a critical parameter, unlike in the PhC structures in ridge waveguides (see Section 5.2.3 on Page 193).

The time required to write a typical 50×50 μm pattern of more than 65000 holes was approximately 15 minutes.

Due to unforeseen difficulties it was not possible to use the Dow Red F polymer as the gain material. This was substituted by an organic fluorescent dye known as DCM (see for example Ref. [42, 43]), which has its emission peak at 620 nm. It absorbs strongly in the range 420-510 nm. This dye was applied to the PhC-patterned sample by spin coating.

6.2.5 Optical characterization

The first set-up used was similar to the scattering measurements set-up described in Section 4.3.4, Page 161 and depicted in Fig. 4.18. An Argon-ion laser was used in continuous wave (CW) mode to pump the sample.

We failed to observe lasing from the sample, or even amplified spontaneous emission (ASE). Two main reasons for this failure were identified. 1) Alignment. It was difficult to know whether the patterned area (50×50 μm) was actually hit. 2) Power. The output of the laser was likely to have been too low and the set-up was not suited to deliver sufficient power to the sample.

The sample was then used in a different set-up, based around an optical parametric oscillator (OPO) laser. This is pumped by a Nd:YAG laser and generates 10 ns wide pulses with 600 μJ/pulse at a repetition rate of 10 Hz, at 526 nm. Again we failed to observe lasing or ASE. The difficulties with this particular set-up were: 1) Alignment. Again, it was difficult to monitor which part of the sample we focused on. 2) Spot size. A large cylindrical lens and a variable slit aperture were used to produce a small spot. However, we estimated the minimum spot size to be >500 μm wide.

Another problem may be that the size of the PhC area was too small to generate sufficient feedback for lasing (or ASE) to occur. Also, due to small fabrication inaccuracies (see Section 2.3.2, Page 57) the photonic crystal lattice may have had a slightly different photonic band structure than expected (see Section 3.2 on Page 101 for a discussion of the factor that affect the band structure of PhCs). The fabricated structures may therefore have bandgaps away from the emission peak of the gain material.

6.2.6 Conclusion from work with organic materials in photonic crystals

This investigation highlighted some of the difficulties involved in combining two very different branches of solid-state physics. The use of organic materials in a photonic crystal environment is a rapidly developing field, which shows a great deal of promise [37]. We have shown that although the design of these structures is feasible, their realization requires the current state of fabrication technology to be pushed to its limits. Optical characterization is a delicate task that requires carefully designed, dedicated set-ups. We believe that the experience gained from this first generation of samples has shown that the incorporation of organic gain material into 2D photonic crystals to create functional active devices is not beyond our technical ability and work should continue to pursue this goal.

6.3 Photonic crystal microcavity in ridge waveguides

One further structure that was investigated was based on a one-dimensional microcavity defined by two-dimensional photonic crystal 'mirrors'. Control of the behaviour light inside optoelectronic devices has been studied for many decades [34]. Examples include DFB and DBR lasers as well as fibre Bragg gratings. These devices tend to be quite long (typically >100 μm), because they use small refractive index modulations ($\Delta n \sim 10^{-2}$ [44]) to minimize modal mismatch and scattering losses. Photonic crystals offer the possibility of significant size reduction for these applications. Compact lasers have been created with highly reflective PhC mirrors [45, 46, 47], because large photonic bandgaps can be achieved with a small number of periods [48]. Photonic crystal microcavities can act as narrow bandpass filters, whereby only modes sustained by the cavity can propagate. The characteristics of the filter can be controlled by varying the PhC parameters and the separations of the two 'mirrors'. It is easy to envisage how

this type of device could form an integral part of complex photonic circuits.

The PhC structure was embedded in a conventional ridge waveguide with a planar waveguide structure following the procedures described in Chapter 2. A cavity was created inside the PhC region by 'removing' a certain number of rows of holes from an otherwise perfect crystal lattice. A similar structure was previously investigated [44, 49] and encouraging results were obtained, which clearly showed the existence of cavity modes. In those structures, however, quantum dots were used as an internal light source and the PhC regions were not embedded in ridge waveguides. Figure 6.7 shows one of our fully processed samples with two 20 row PhC regions with a 6 row gap.

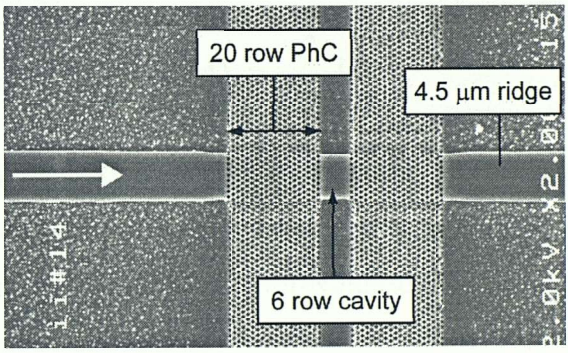


Figure 6.7: SEM image of 1D photonic crystal microcavity. A 6 row cavity is defined by two 20 row photonic crystals.

6.3.1 Fabrication

The fabrication of these structures was described in Chapter 2. The only difference to the 'single' PhC structures was the pattern design. For example, to create the pattern shown in Fig. 6.7 a large pattern consisting of 46 rows of holes was created. From this the central 6 rows were removed, leaving two 20 row patterns separated by a 6 row gap.

6.3.2 Cavity design

An analogy can be drawn between photons in a microcavity defined by PhC mirrors and a symmetrical Fabry-Pérot interferometer [50]. Photons of wavelength λ inside a single cavity defined by two mirrors interfere constructively at normal incidence under the condition that

$$\begin{aligned} (2nL) \times (2\pi/\lambda) &= 2m\pi \\ \rightarrow 2nL &= m\lambda \end{aligned} \tag{6.3}$$

where n is the refractive index of the cavity, L is the cavity length and m is an integer that corresponds to the order of consecutive fringes. Rearranging Eqn. 6.3 and differentiating λ with respect to m leads to the following expression:

$$\delta\lambda = \frac{\lambda^2}{2nL}\delta m \tag{6.4}$$

With δm set to 1 this equation gives the change in wavelength required to observe consecutive constructively interfering fringes. This is commonly known as the free spectral range (FSR). As a first order approximation Eqn. 6.4 was used to calculate the expected FSR for a cavity defined by two PhC mirrors. Put another way, the cavity dimensions required to obtain transmission peaks of a particular FSR can be calculated using Eqn. 6.4. For example, a free spectral range of 20 nm around a wavelength of 1570 nm, for a cavity with refractive index 3.38 (GaAs) would require a 50 row 'defect' in a ΓM-oriented photonic crystal with a lattice constant of 420 nm. For this structure we would expect to observe approximately 6 resonance peaks corresponding to the microcavity, over the scan range of our laser source (125 nm). A structure consisting of two 10 row photonic crystals separated by a 50 row gap is shown in Fig. 6.8.

This first order approach could be refined by taking the following into consideration. First of all, the PhC:waveguide interface is not a 'hard' boundary as a classical mirror would be. The electromagnetic waves penetrate a certain length into the PhC,

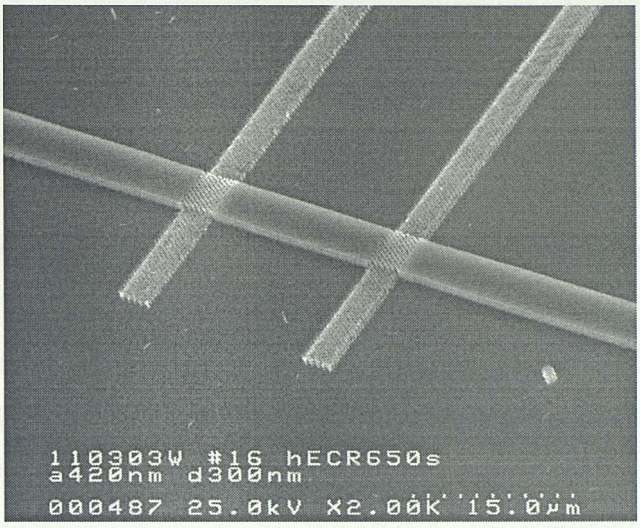


Figure 6.8: SEM image of 50 row 'defect' PhC cavity. Two 10 row PhC patterns were used to define the cavity.

although it was argued in Ref. [44] that this penetration depth is negligible. Secondly, the effective refractive index of the ridge waveguide section must be calculated carefully using tools such as `FWave` described in Section 3.3.3 on Page 117. Taking the thus obtained refractive index value of $n_{eff} = 3.24$ into account in the above calculation, we find an expected FSR of ~21 nm. These points do not result in a significant deviation from the first order approximation result (FSR = 20 nm), but would need to be considered carefully in real devices based on this type of structure.

6.3.3 Optical characterization

Photonic crystal microcavity samples were optically characterized using the set-up described in Section 4.3, Page 155. Transmission and reflection spectra were recorded for TE and TM-polarized input light. Unfortunately there was little evidence of the expected resonance peaks. Several reasons can help to explain this.

The results in Chapter 5 indicated severe propagation losses inside the photonic crystal, of the order of 1 dB/μm. The total length of the 'mirror' sections in the cavity

structures investigated here is ~7 μm, corresponding to a total power of at least 7 dB due to the PhC section alone, which is substantial.

The samples were purely passive structures with a large PBG for TM polarization. As TM-polarized light enters the waveguide it is effectively reflected by the first PhC mirror (expected from Sections 3.2 and 5.1.1). This was apparent in reflection measurements, where the reflected TM power was higher than TE. TE-polarized light passes through the first PhC mirror and experiences scattering losses in the process. The second mirror is identical to the first and hence does not reflect much of the TE light. Instead, the TE-polarized light traverses the second PhC region with more scattering losses occurring. This structure is only truly functional with gain material inside the cavity.

6.3.4 Conclusions from 1D PhC microcavity work

It does not require 10 rows of PhC to produce a strong PBG effect. In Section 5.1.2 on Page 180 we reported strong PBG effects in the form of polarization discrimination up to 27 dB with only 5 row photonic crystals. Therefore, no more than 5 rows should be used as cavity boundaries. Quantum dots appear to be highly suitable as internal light sources [13] and should be incorporated into future microcavity PhC devices.

Bibliography

[1] E. M. Purcell. Spontaneous emission probabilities at radio frequencies. *Phys. Rev.*, 69(11,12):681–681, 1946.

[2] P. Goy, J. M. Raimond, M. Gross, and S. Haroche. Observation of cavity-enhanced single-atom spontaneous emission. *Phys. Rev. Lett.*, 50(24):1903–1906, June 1983.

[3] J. M. Gérard, D. Barrier, J. Y. Marzin, R. Kuszelewicz, L. Manin, E Costard, V. Thierry-Mieg, and T. Rivera. Quantum boxes as active probes for photonic microstructures: The pillar microcavity case. *Appl. Phys. Lett.*, 69(4):449–451, July 1996.

[4] B. Gayral and J. M. Gérard. Strong Purcell effect for InAs quantum boxes in high-Q wet-etched microdisks. *Physica E*, 7:641–645, 2000.

[5] D. G. Deppe, L. A. Graham, and D. L. Huffaker. Enhanced spontaneous emission using quantum dots and apertured microcavity. *J. Quantum Electron.*, 35(10):1502–1508, October 1999.

[6] O. J. Painter, J. Vučković, and A. Scherer. Defect modes of a two-dimensional photonic crystal in an optically thin dielectric slab. *J. Opt. Soc .Am. B*, 16(2):275–285, February 1999.

[7] O. J. Painter, A. Husain, A. Scherer, P. T. Lee, I. Kim, J. D. O'Brien, and P. D. Dapkus. Lithographic tuning of a two-dimensional photonic crystal laser array. *IEEE Phot. Technol. Lett.*, 12(9):1126–1128, September 2000.

[8] M. Boroditsky, T. F. Krauss, R. Coccioli, R. Bhat, and E. Yablonovitch. Light extraction from optically pumped light-emitting diode by thin-slab photonic crystals. *Appl. Phys. Lett.*, 75(8):1036–1038, August 1999.

[9] C. Reese. Photonic crystal microcavities with self-assembled InAs quantum dots as active emitters. *Appl. Phys. Lett.*, 78(16):2279–2281, April 2001.

[10] T. Yoshie, A. Scherer, H. Chen, D. Huffaker, and D. Deppe. Optical characterisation of two-dimensional photonic crystal cavities with indium arsenide quantum dot emitters. *Appl. Phys. Lett.*, 79(1):114–116, July 2001.

[11] T. Yoshie, A. Scherer, H. Chen, D. Huffaker, and D. Deppe. High quality two-dimensional photonic crystal slab cavities. *Appl. Phys. Lett.*, 79(26):4289–4291, December 2001.

[12] C. J. M. Smith, H. Benisty, D. Labilloy, U. Oesterle, R. Houdré, T. F. Krauss, R. M. De La Rue, and C. Weisbuch. Near-infrared microcavities confined by two-dimensional photonic bandgap crystals. *Electron. Lett.*, 35(3):228–230, February 1999.

[13] T. D. Happ, I. I. Tartakovskii, V. D. Kulakovskii, J.-P. Reithmaier, M. Kamp, and A. Forchel. Enhanced light emission of In(x)Ga(1-x)As quantum dots in a two-dimensional photonic crystal defect microcavity. *Phys. Rev. B*, 66(R):041303(R)–1–4, July 2002.

[14] E. Yablonivitch. Inhibited spontaneous emission in solid-state physics and electronics. *Phys. Rev. Lett.*, 58(20):2059–2062, May 1987.

[15] S. John. Strong localization of photoncs in certain disordered dielectric superlattices. *Phys. Rev. Lett.*, 58(23):2486–2489, June 1987.

[16] Y. Yamamoto, S. Machida, and G. Björk. Microcavity semiconductor laser with enhanced spontaneous emission. *Phys. Rev. A*, 44(1):657–668, July 1991.

[17] L. A. Graham, D. L. Huffaker, and D. G. Deppe. Spontaneous lifetime control in a native-oxide-apertured microcavity. *Appl. Phys. Lett.*, 74(17):2408–2410, April 1999.

[18] A. Imamoglu, D. D. Awschalom, G. Burkard, D. P. DiVincenzo, D. Loss, M. Sherwin, and A. Small. Quantum information processing using quantum dot spins and cavity QED. *Phys. Rev. Lett.*, 83(20):4204–4207, November 1999.

[19] P. Michler, A. Kiraz, C. Becher, W. V. Schoenfeld, P. M. Petroff, L. Zhang, E. Hu, and A. Imamoglu. A quantum dot single-photon turnstile device. *Science*, 290:2282–2284, December 2000.

[20] H. Benisty, C. Weisbuch, D. Labilloy, M. Rattier, C. J. M. Smith, T. F. Krauss, R. De La Rue, R. Houdré, U. Oesterle, C. Jouanin, and D. Cassagne. Optical and confinement properties of two-dimensional photonic crystals. *J. Lightwave Technol.*, 17(11):2063–2077, November 1999.

[21] private communication with R. Murray, Imperial College London.

[22] A. A. Maradudin and A. R. McGurn. Out of plane porpagation of electromagnetic waves in a two-dimensional periodic dielectric medium. *J. Mod. Opt.*, 41(2):275–284, 1994.

[23] P. A. Rigby. *A critical appraisal of the design, fabrication and assessment of photonic structures in III-V semiconductors.* D. Phil., St. Cross College, Oxford University, 1998.

[24] M. Boroditsky, R. Vrijen, T. F. Krauss, R. Coccioli, R. Bhat, and E. Yablonovitch. Spontaneous emission extraction and Purcell enhancement from thin-film 2-D photonic crystals. *J. Lightwave Technol.*, 17(11):2096–2112, November 1999.

[25] B. Pal and A. S. Vengurlekar. Time-resolved excitonic coherent polarization dynamics in GaAs multiple quantum wells. *Phys. Rev. B*, 68:205331–1:6, 2003.

[26] E. W. Ward. *Advanced technologies for optoelectronic integrated circuits.* Ph.D., Imperial College, University of London, 2004.

[27] A. Mekis, M. Meier, A. Dodabalapur, R. E. Slusher, and J. D. Joannopoulos. Lasing mechanism in two-dimensional photonic crystal lasers. *Appl. Phys. A*, 69:111–114, 1999.

[28] M. Meier, D. Dodabalapur, J. A. Rogers, R. E. Slusher, A. Mekis, A. Timko, C. A. Murray, R. Ruel, and O. Nalamasu. Emission characteristics of two-dimensional organic photonic crystal lasers fabricated by replica molding. *J. Appl. Phys.*, 86(7):3502–3507, October 1999.

[29] K. Yoshino, S. Tatsuhara, Y. Kawagishi, and M. Ozaki. Amplified spontaneous emission and lasing in conducting polymers and fluorescent dyes in opals as photonic crystals. *Appl. Phys. Lett.*, 74(18):2590–2592, May 1999.

[30] M. Berggren, D. Dodabalapur, R. E. Slusher, Z. Bao, A. Timko, and O. Nalamasu. Organic lasers based on lithographically defined photonic-bandgap resonators. *Electron. Lett.*, 34(1):90–91, January 1998.

[31] Exciton Inc., *www.exciton.com.*

[32] The Dow Chemical Company, *www.dow.com.*

[33] H. Kogelnik and C. V. Shank. Stimulated emission in a periodic structure. *Appl. Phys. Lett.*, 18:152–154, February 1971.

[34] A. Yariv. *Optical Electronics in Modern Communication.* Oxford University Press, 5th edition, 1997.

[35] S. Nojima. Optical-gain enhancement in two-dimensional active photonic crystals. *J. Appl. Phys.*, 90(2):545–551, July 2001.

[36] E. Hecht. *Optics.* Addison-Wesley, 2nd edition, 1987.

[37] M. Notomi, H. Suzuki, and T. Tamamura. Directional lasing oscillation of two-dimensional organic photonic crystal lasers at several photonic band gaps. *Appl. Phys. Lett.*, 78(10):1325–1327, March 2001.

[38] private communications with members of the Organic Materials division of the Experimental Solid State physics group at Imperial College London.

[39] M. A. Afromowitz. Refractive index of Ga(1-x)Al(x)As. *Solid State Commun.*, 15:59–63, 1974.

[40] S. Kayali, G. Ponchak, and R. Shaw. GaAs MMIC reliability assurance guideline for space applications. *Jet Propulsion Laboratory publication*, 96-25:1–221, December 1996.

[41] plane wave expansion codes provided by P. N. Stavrinou, Imperial College London.

[42] X. Peng, L. Liu, J. Wu, Y. Li, Z. Hou, L. Xu, W. Wang, F. Li, and M. Ye. Wide-range amplified spontaneous emission wavelength tuning in a solid-state dye waveguide. *Opt. Lett.*, 25(5):314–316, March 2000.

[43] V. G. Kozlov, V. Bulović, and S. R. Forrest. Temperature independent performance of organic semiconductor lasers. *Appl. Phys. Lett.*, 18(3):2575–2577, November 1997.

[44] C. J. M. Smith, R. M. De La Rue, H. Benisty, U. Oesterle, T. F. Krauss, D. Labilloy, C. Weisbuch, and R. Houdré. In-plane microcavity resonators with two-dimensional photonic bandgap mirrors. *IEE Proc.-Optoelectron.*, 145(6):373–378, December 1998.

[45] J. O'Brien, O. Painter, R. Lee, C. C. Cheng, A. Yariv, and A. Scherer. Lasers incorporating 2D photonic bandgap mirrors. *Electron. Lett.*, 32(24):2243–2244, November 1996.

[46] T. D. Happ, A. Markard, M. Kamp, A. Forchel, and S. Anand. Single-mode operation of coupled-cavity lasers based on two-dimensional photonic crystals. *Appl. Phys. Lett.*, 79(25):4091–4093, December 2001.

[47] S. Mahnkopf, M. Kamp, and A. Forchel. Tunable distributed feedback laser with photonic crystal mirrors. *Appl. Phys. Lett.*, 82(18):2942–2944, May 2003.

[48] D. Labilloy, H. Benisty, C. Weisbuch, T. F. Krauss, R. M. De La Rue, V. Bardinal, R. Houdré, U. Oesterle, D. Cassagne, and C. Jouanin. Quantitative measurement of transmission, reflection, and diffraction of two-dimensional photonic band gap structures at near-infrared wavelengths. *Phys. Rev. Lett.*, 79(21):4147–4150, November 1997.

[49] M. Rattier, H. Benisty, C. J. M. Smith, A. Béraud, D. Cassagne, C. Jouanin, T. F. Krauss, and C. Weisbuch. Performance of waveguide-based two-dimensional photonic crystal mirrors studied with Fabry-Perot resonators. *IEEE J.Quantum Electron.*, 37(2):237–243, February 2001.

[50] M. Klein and T. Furtak. *Optics.* Wiley, 2nd edition, 1986.

Chapter 7

Conclusions

The aim of this project was to design, fabricate and assess two dimensional photonic crystals (2D PhCs) in a GaAs/AlGaAs environment, for operation in the near infrared part of the spectrum. 2D PhCs embedded in free standing ridge waveguides were the structures that were studied most intensely.

7.1 Summary

In Chapter 2 we presented our approach to the fabrication of 2D photonic crystals consisting of air holes in GaAs/AlGaAs with hole diameters in the range 200-300 nm. High quality lattices with excellent cross-sectional profiles were fabricated using a combination of electron beam lithography (EBL), reactive ion etching (RIE) and electron cyclotron resonance (ECR) etching. A large range of difficulties in the more than 50 processing steps was overcome to produce a number of high quality samples with variations in fill factor, hole depth and ridge height.

The theoretical foundations for the operation of photonic bandgap (PBG) devices were shown in Chapter 3. The design of photonic crystals was discussed and a range of modelling tools was reviewed. Waveguide structures were designed using well-established techniques. In the second half of Chapter 3 we discussed data analysis techniques and introduced Fourier analysis (FA) in the context of PhC-patterned waveguides. When we initially considered Fourier analysis as a possible method for treating our measurements, we immediately realized the great potential of this technique. Much work went into establishing a method of deducing waveguide and photonic crystal characteristics from transmission data represented in the Fourier domain (Section 3.4, Page 118). The unpatterned waveguide case was shown to be solvable analytically. We used certain simplifying assumptions to obtain a first order approximation of PhC loss coefficients from PhC patterns in waveguides. A rigorous study of FA showed it to be a powerful data analysis tool, which can be applied to the measurements of many different types of structures.

In Chapter 4 a detailed description of our optical characterization set-up was given. Various attempts to use a white light source to characterize the samples were reported, highlighting the potential of this approach. The second set-up was based around a tuneable semiconductor laser and was shown to give accurate, repeatable measurements for wavelength scans with 50 pm steps. The difficulties involved in optically characterizing waveguides with dimensions of the order of 4 μm were discussed.

Results from the optical characterization of 2D PhCs in ridge waveguides were presented in Chapter 5. PBG effects were clearly demonstrated. Results from treating transmission data in the spectral domain and Fourier domain were discussed. Waveguide propagation losses were shown to be easily obtainable using Fourier analysis and for our unpatterned ridge waveguides we typically found loss coefficients of $\sim$60 dB/cm ($\sim$14 /cm). FA was used with transmission measurements to extract photonic crystal loss coefficients. The lowest recorded PhC loss coefficient was $\sim$0.6 dB/μm ($\sim$1400 /cm). Loss mechanisms for propagation through 2D PhCs were analyzed and the hole depth was confirmed to be a significant factor.

Chapter 6 was a collection of other work on 2D photonic crystals that we carried out.

* The possibility of fabricating large fill factor PhCs was demonstrated. It was shown that ultra-small 2D microcavities can be fabricated to potentially provide high confinement of light in very small volumes.

* Samples with small features were produced and combined with optically emitting organic semiconductors, which act as active gain material.

* One-dimensional microcavities were defined by 2D PhCs in a ridge waveguide configuration.

7.2 Conlusions

This project has been a success in many ways. We met all the objectives set at the start of the project, that is to design, fabricate and analyze 2D PhCs. Over the past three years we have learned a great deal, particularly about the fabrication and analysis aspects of photonic crystal structures.

We learned to appreciate the intricacies of fabricating sub-micron structures and succeeded in producing high quality samples. Electron beam lithography is an excellent tool for writing sub-micron patterns, as outlined in Section 2.3 on Page 50. It is highly suitable to a research environment as it allows great flexibility in the pattern design. We believe that the particular equipment we used is capable of producing smooth, uniform patterns with ~100 nm diameter holes. The disadvantages we encountered were

- small field of view at high resolution
  → can not pattern areas larger than ~50×50 μm at the required resolution

- too small onboard memory of e-beam control card
  → restricts the number of object a pattern can contain, to ~65000

- slow - approximately 15 min to write a single 50×50 μm pattern with 65000 holes
  → this rules out electron beam lithography for large scale production

ECR etching was used to transfer the PhC pattern into the GaAs/AlGaAs epilayers. This technique enabled us to produce holes with excellent profiles and vertical walls. A multitude of process parameters govern the ECR behaviour (see Section 2.4.2, Page 74). We did not optimize this process due to time constraints. As a result we 'only' succeeded in etching holes (diameter ~280 nm) in GaAs/AlGaAs to a depth of ~1 μm. This will need to be improved as the results in Section 5.2.3 on Page 193 showed the critical dependence of PhC losses on the hole depths. We estimate that by optimizing the ECR process, the etch depth can be increased to ~1.5 μm without increasing the

thickness of the silica layer.

ECR etching is a good tool to be used in a research environment. ICP (see Section 2.4.2, Page 74) is a very similar etching tool. It can produce equally high density plasmas but is much more user-friendly than ECR and seems to be a more promising candidate for large volume industrial etching of 2D photonic crystals.

The two-stage process we employed of separately etching the PhCs and ridges proved to be advantageous. We showed that PhC structures can be combined with conventional waveguide processing technology. It also allowed us to vary hole depth and ridge height independently, which is impossible if the PhCs and ridges are written and etched together. We are not aware of any other group that also uses this two-stage method. Varying the ridge height changes the modal confinement (Section 3.3.3, Page 117), which is believed to be related to PhC losses (Section 5.2.3, Page 193).

Fourier analysis proved to be a robust, unambiguous way of determining loss characteristics of waveguides and photonic crystals. The credibility that this method lends to loss measurements has so far been missing in the photonic crystal community. We believe that correctly applied Fourier analysis can become a valuable tool to be used with many different structures commonly used in the optoelectronics community.

Our characterization efforts using a white light source highlighted the difficulties of work at very low power levels. The rewards for successfully using such a relatively cheap, large bandwidth source are tremendous. We believe that the set-up can be optimized to work with an arc lamp-type source, though perhaps not beyond 1300 nm, where the power output drops substantially.

The laser-based set-up was a great success. The laser itself was very reliable, accurate and user-friendly. Mechanical instabilities in the system were located and minimized where possible. In order to improve the system's performance vibrations must

be eliminated. They were minimized by carrying out experiments in the evening or on weekends, but vibrations are generally expected to be felt on an un-floated optical bench on the 10th floor of a building in central London.

Large fill factor PhCs can potentially be used in conjunction with quantum dots to create highly efficient light sources and we have shown that we can produce high quality large fill factor structures.

The work we carried out on combining PhCs with organic gain material was regarded as an encouraging start to more thorough studies of this type of device. Although no positive results can be reported, we have learned a great deal about the design, fabrication and assessment of these structures. This knowledge would be an excellent starting point for the second generation of such devices.

We proved our ability to fabricate high quality 1D microcavities using 2D PhCs. The transmission losses proved to be too severe to obtain positive results, but we are convinced that this type of structure can be used as a suitable filter for optical integrated circuits or to create highly compact inplane lasers.

The losses associated with light propagation through photonic crystals are a serious concern and need to be reduced before PhCs can one day be the indispensable component of integrated optoelectronic circuits, which we believe they will. Improvements in the fabrication techniques will lead to lower losses. However, more experimental data is required to verify the key loss factors. The work here presented is a step towards firmly establishing the loss levels currently experienced throughout the PhC community, as it shows how Fourier analysis is an unambiguous, unbiased, robust tool. This is a necessary step before conquering them, one day.

7.3 Future work

Loss mechanisms in photonic crystal structures must be further investigated if PhCs are to become components of integrated optical circuits. We would like to continue to explore the loss dependence on the hole depth of PhC patterns. This will require optimization of the dry etching techniques.

More work on Fourier analysis is required. The simple approximation of zero reflection losses at the waveguide:PhC interface must be improved upon. As mentioned in Section 5.3.1 on Page 201 the relative height of certain resonance peaks is closely related to the propagation loss in the unpatterned waveguide sections. This relationship is worth exploring, because it offers the possibility of performing complete, self-consistent, one-shot optical characterization with a single wavelength scan.

There are a number of improvements to the optical characterization set-up that we envisage. Focusing light into the waveguide is very delicate and the movement control on the nanopositioning stages was barely adequate (see Section 4.4.3 on Page 170). Ideally one would mount all components on piezo-controlled positioning stages. This is prohibitively expensive, but may be possible with one or two critical positioning stages. The optical bench should be floated. This would reduce the susceptibility to vibrations during measurements. Also, two more detectors should be acquired so that the input power, transmission, reflection and scattering can all be measured simultaneously. This would significantly speed up the time required to characterize samples.

Optical characterization using a white light source should continue to be attempted. Losses in the set-up due to coupling in an out of optical fibre, for example, must be minimized. Light could be focused down and into the waveguide directly, eliminating the need for the initial optical fibre (see Section 4.2.2 on Page 144). Spatial filtering should be employed to clean up the light emerging from the waveguide. The beam drift due to mechanical instability of certain components of the set-up must be elim-

inated (Section 4.4.3, Page 170). With the laser-based set-up this would allow longer wavelength scans to be run. This could be utilized by decreasing the step length of scans, which in the Fourier domain would increase the largest detectable optical distance (Section 3.4, Page 118). Longer scan times could also be used to improve the measurement accuracy by averaging several measurements at each wavelength.

Polarization mixing in PhCs reported in Section 5.1.2 on Page 184 should be further investigated. This effect must be well-understood before PhCs can be used in optical integrated circuits.

Using the experience gained from the large fill factor work it would be interesting to investigate how far these structures can be developed to produce high modal confinement in wavelength-sized microcavities with quantum dots as an internal light source.

We believe the combination of active organic material with inorganic PhCs offers the possibility of creating exciting new devices. This will require optimization of the sample design and improvements in the EBL patterning process.

The true potential of photonic crystals has not been unlocked yet and a killer application remains illusive. We believe that some of the recent work on using PhCs to create compact waveguides is certainly interesting, but does not take advantage of the strengths and unique characteristics of photonic crystals. The highly dispersive nature of these structures should be exploited. The opportunity to engineer the photonic band structure of photonic crystals should be exploited to design more applications such as dispersion compensators or superprisms. The highly dispersive behaviour of PhCs requires light propagation *through* the crystals, which with today's fabrication technology and as reported in this thesis is a very lossy process. Progress in the understanding and management of losses needs to continue for the PhC industry to develop out of its baby shoes.

Appendix A

Processing steps for fabrication of 2D Photonic Crystals in ridge waveguides

Preparation for EBL
clean with acetone-methanol-DI water-N_2 blow dry
SiO_2 deposition with PECVD - 260nm=10min
if necessary remove by HP-dip, A-M-DIW-N_2
spin on PMMA, 0.2μm filter, 4500rpm, 30s
if film not homogenous remove with A-M-DIW-N_2
bake on hotplate for 90s @ 180°C
e-beam lithography
Post EBL treatment
develop in MIBK for 60s
rinse immediately MIBK:IPA (1:3) for 30s, N_2 blow dry
check under microscope
RIE, 8min, 50mT, APC angle 0°, 150W
3min in A in ultrasonic bath, lowest power, M-DIW-N_2
check in SEM
mount on graphite plate using graphite paste
with plate on hotplate, ramp up to 110°C with max power
bake on hotplate for 5min @ 110°C
ECR etch
remove from graphite plate, clean in A-M-DIW-N_2
check in SEM
cleave through test patterns, mount edge-on, check in SEM

Table A.1: Processing steps for deposition of masking layers, EBL and transfer of patterns into epilayers

Ridge lithography & etch
clean with A-M-DIW-N_2 blow dry
RIE, 2min, 50mT, APC angle 0°, 150W
with sample on spinner, apply drop of HMDS, spin ~5s
immediately apply S1813, 0.45μm filter, 4000rpm, 40s
if film not homogenous remove with A-M-DIW-N_2
bake on hotplate for 60s @ 109°C
UV exposure using 4.5μm mask, 2.8s
post-bake on hotplate for 10min @115°C
if film not homogenous remove with A-M-DIW-N_2
develop in 351 developer for 45s,45s, DIW, N_2 blow dry
mount on graphite plate using graphite paste
with plate on hotplate, ramp up to 110°C with max power
bake on hotplate for 5min @ 110°C
ECR etch
remove from graphite plate, clean in A-M-DIW-N_2
RIE O_2 descum for 10min
check in SEM

Table A.2: Processing steps for creating ridge waveguides

Thinning the substrate
melt wax on glass slide (>150°C), mount sample face down
soak in A for 3min + clean back surf. with cotton bud
rinse with A-M-DIW, N_2
measure sample thickness
mix H_20(15ml), H_2O_2(120ml), H_2SO_4(15ml) in that order
place on cold stirrer, add magnet + sample
stir @ 400rpm for 5min to remove ~100μm
rinse in DIW in beaker, then tap DIW + N_2
measure sample thickness
heat glass slide to at least 150°C, slide sample off
soak in A for 3min, rinse with A-M-DIW, N_2
cleave into strips

Table A.3: Processing steps for thinning the substrate by wet etching

Appendix B

Fabry-Pérot Equation

In this Section we show how the equations for transmission amplitudes developed in Section 3.4 on Page 118 can be used to derive the general Fabry-Pérot (FP) transmission equation for a single cavity.

The starting point is the general form of the transmitted electric field in the frequency domain, $E_T(\omega)$, as in Eqn. 3.9 on Page 120. This follows a geometric progression and can be expressed as

$$\begin{aligned} E_T(\omega) &= \tau e^{-\frac{\alpha}{2}L} \sum_{m=0}^{\infty} \left(\rho e^{-i\phi} e^{-\alpha L}\right)^m \\ &= \frac{\tau e^{-\frac{\alpha}{2}L}}{1 - \rho e^{-i\phi} e^{-\alpha L}} \end{aligned} \tag{B.1}$$

using the same symbol definitions as in Chapter 3. The factor $\mathrm{wp}(t)$ has been dropped for convenience. Equation B.1 is inserted into the expression $I(\omega) = E(\omega)E^*(\omega)$ to give the transmitted intensity spectrum, $I_T(\omega)$.

$$\begin{aligned} I_T(\omega) &= \frac{\tau e^{-\frac{\alpha}{2}L}}{1 - \rho e^{-i\phi} e^{-\alpha L}} \times \frac{\tau e^{-\frac{\alpha}{2}L}}{1 - \rho e^{+i\phi} e^{-\alpha L}} \\ &= \frac{\tau^2 e^{-\alpha L}}{1 - \rho e^{-\alpha L}\left(e^{-i\phi} + e^{+i\phi}\right) + \rho^2 e^{-2\alpha L}} \end{aligned}$$

$$
\begin{aligned}
&= \frac{\tau^2 e^{-\alpha L}}{1 - 2\rho e^{-\alpha L}\cos\phi + \rho^2 e^{-2\alpha L}} \\
&= \frac{(\tau_1\tau_2)^2 e^{-\alpha L}}{1 - 2\rho_1\rho_2 e^{-\alpha L}\cos\left(\frac{2nL\omega}{c}\right) + (\rho_1\rho_2)^2 e^{-2\alpha L}}
\end{aligned}
\tag{B.2}
$$

This is the standard FP transmission equation for a single cavity.

Appendix C

Sample catalogue

ID	Wafer	a nm	d nm	hd nm	rh μm	w μm	pattern types
waveguide samples							
020402E2	QT1598UP	-	-	-	3.20		plain
170402	QT1598UP	-	-	-	2.00		plain
020402E3	QT1598UP	-	-	-	1.40		plain
180402	QT1598UP	420	280	550	1.20		20r, 20r3d', 20r6d
270602	QT1598UP	420	280	1000	0.65		20r, 20r3d', 20r6d
050702	QT1598UP	420	280	1000	1.30		20r, 20r3d', 20r6d
010802	QT1598UP	350	200	850	2.80		10r, 10r10, 10r30
190203'	QT1598D	-	-	-	1.20		plain
110203A	QT1598D	420	290	920	1.00	4.8	10r, 50r10
110203B	QT1598D	420	260	850	1.00	4.8	10r, 50r10
260203A	QT1598D	420	240	870	1.10	5.0	5r,10r,15r,20r,30r
260203B	QT1598D	420	270	950	1.10	5.0	5r,10r,20r,30r
190203A	QT1598D	420	300	890	1.30	4.4	10r,50r10
110303A	QT1598D	420	300	830	1.40	4.45	10r,50r10
110303B	QT1598D	420	220	740	1.40	4.45	10r,50r10
270203A	QT1598D	420	200	700	0.60	4.5	10r,50r10
270203B	QT1598D	420	270	800	0.60	4.5	10r,50r10
organic dye samples							
080102	SiO_2/GaAs	280	210	100			
210102	SiO_2/GaAs	280/210	240/180	90/100			

Table C.1: Catalogue of fabricated samples. a=lattice constant, d=hole diameter, hd=hole depth, rh=ridge height, w=ridge width. Indicated diameters are an approximate value for the mean hole diameter of all patterns found on that sample. Lattice constants were measured with an accuracy of ± 5 nm.

Appendix D

Publications

Refereed articles

- S. Klengel, P.N. Stavrinou, R.F. Oulton, P. Caillaud, G. Parry, B. Poole, J. Heffernan, "Experimental study of transmission and reflection properties of passive 2D photonic crystals", Appl. Phys. Lett., in preparation

Oral presentations

- S. Klengel, P.N. Stavrinou, P. Caillaud, G. Parry, B. Poole, J. Heffernan, "Spectral analysis of 2D Photonic Crystals in ridge waveguides", Young Researchers in Optics 2003, IOP, London, 24 September 2003
- S. Klengel, P.N. Stavrinou, R.F. Oulton, G. Parry, B. Poole, J. Heffernan, "Novel characterisation techniques and loss measurements for passive 2D photonic crystals in GaAs/AlGaAs at 1.55 μm", PREP 2003, Exeter, UK, 14-16 April 2003
- S. Klengel, P.N. Stavrinou, G. Parry, B. Poole, J. Heffernan, "Fabrication of Photonic Crystal structures in free-standing GaAs/AlGaAs ridge waveguides", Dry Etching - Advances and Trends, IOP, London, 22 January 2003
- S. Klengel, P.N. Stavrinou, G. Parry, B. Poole, J. Heffernan, "Photonic Crystals in conventional ridge waveguides", UPC technical meeting, Bristol, September 2002
- S. Klengel, P.N. Stavrinou, G. Parry, B. Poole, J. Heffernan, "Fabrication of 2D Photonic Crystals", UPC technical meeting, Glasgow, September 2001

Poster presentations

- "Fabrication of Photonic crystal strutures in GaAs/AlGaAs", Workshop and European Optical Society topical meeting on 2D Photonic Crystals, Ascona, Switzerland, 25-30 August 2002
- "Detailed spectral analysis of 2D photonic crystal structures embedded into ridge waveguides", Conference on Lasers and Electro Optics (CLEO), Baltimore, MD, USA, 1-6 June 2003